University of Warsaw

Faculty of Physics

Doctoral School of Exact and Natural Sciences

Feshbach Spectroscopy of Potassium-Cesium Mixtures

Doctoral Dissertation

Author: Mateusz Bocheński

Supervisor: Prof. Paweł Kowalczyk

Co-supervisor: Dr Mariusz Semczuk

Warsaw, 2025

Abstract

In this thesis, we present the construction of an experimental apparatus enabling the cooling of ^{39}K, ^{40}K, ^{41}K, and ^{133}Cs atoms, as well as their mixtures, to temperatures in the range of $5-20$ µK. The key components of the setup are discussed, including the vacuum system, laser systems, and magnetic field coils.

Cooling in the apparatus is realized using several laser-cooling techniques: magneto-optical trapping, compression, sub-Doppler gray molasses cooling, and trapping in either a magnetic trap or an optical dipole trap.

The developed cooling procedures were successfully applied to all of the above isotopes, achieving efficiencies comparable to, and in some cases exceeding, the best results reported worldwide. A particularly notable achievement is the cooling of the fermionic isotope ^{40}K. To the best of our knowledge, this represents the first demonstration of sub-Doppler cooling and magnetic trapping of ^{40}K in a single-chamber vacuum system without the use of isotopically enriched dispensers.

The high efficiency of the implemented procedures also enabled the production of a cold ^{39}K-^{133}Cs mixture in an optical dipole trap and the performance of Feshbach spectroscopy on this system. Although this mixture had previously been realized and investigated by H. C. Nägerl's group in Innsbruck, the results presented here reveal a number of previously unexplored aspects, including several spectroscopic resonances observed for the first time.

In addition, we report the first realization of ^{39}K-^{40}K and ^{41}K-^{133}Cs mixtures, together with the methodology for their preparation and their observed collisional properties. For the heteronuclear mixture of two potassium isotopes, the obtained results also served as a benchmark for the efficiency and reliability of the modular laser system developed in this work.

The creation of the ^{41}K-^{133}Cs mixture constituted the main objective of this thesis, and its characterization has therefore been carried out in the greatest detail. We present measured three-body loss coefficients, compare them with those of the ^{39}K-^{133}Cs mixture, and report the first observations of Feshbach resonances in ^{41}K-^{133}Cs.

This characterization represents an important milestone toward the creation for the first time of ultracold ^{41}K-^{133}Cs molecules, whose properties appear highly promising in the context of quantum simulations.

Streszczenie

W pracy prezentujemy konstrukcję układu doświadczalnego umożliwiającego chłodzenie atomów ^{39}K, ^{40}K, ^{41}K oraz ^{133}Cs, jak również ich mieszanin, do temperatur rzędu $5-20$ µK. Omówione zostały kluczowe elementy eksperymentu, w tym układ próżniowy, układy laserowe oraz cewki wytwarzające pola magnetyczne.

Chłodzenie w przedstawionym układzie realizowane jest za pomocą metod chłodzenia laserowego: pułapkowania magnetooptycznego, kompresji, chłodzenia w szarych melasach optycznych oraz pułapkowania w pułapce magnetycznej i optycznej pułapce dipolowej.

Opracowane procedury chłodzenia zostały zastosowane do wszystkich wymienionych izotopów i atomów i osiągnęły wydajność porównywalną, a niekiedy przewyższającą najlepsze istniejące na świecie eksperymenty. Przykładem rekordowej efektywności jest przedstawione w pracy chłodzenie fermionowego izotopu potasu ^{40}K. Zgodnie z naszą wiedzą, po raz pierwszy udało się schłodzić go do temperatur sub-dopplerowskich i pułapkować magnetycznie w układzie próżniowym typu single-chamber, bez wykorzystania wzbogaconych izotopowo dyspenserów.

Osiągnięta wydajność procedur umożliwiła również wytworzenie zimnej mieszaniny ^{39}K-^{133}Cs w optycznej pułapce dipolowej oraz przeprowadzenie spektroskopii Feshbacha. Choć mieszanina ta była wcześniej badana w grupie H. C. Nägerla w Austrii, przedstawione w niniejszej pracy wyniki ujawniają szereg wcześniej niedyskutowanych aspektów, w tym wiele przejść spektroskopowych zaobserwowanych po raz pierwszy.

Poza tym w pracy po raz pierwszy zaprezentowano mieszaniny ^{39}K-^{40}K oraz ^{41}K-^{133}Cs, metodykę ich uzyskania oraz obserwowane własności zderzeniowe. W przypadku heterojądrowej mieszaniny dwóch izotopów potasu uzyskane wyniki posłużyły dodatkowo jako dowód wysokiej wydajności oraz niezawodności stworzonego modułowego układu laserowego.

Wytworzenie mieszaniny ^{41}K-^{133}Cs stanowiło główny cel niniejszej rozprawy, dlatego jej charakterystyka została przeprowadzona w najbardziej szczegółowy sposób. Przedstawiamy zmierzone współczynniki strat trójciałowych, porównanie z miesza-

niną ^{39}K-^{133}Cs oraz pierwsze obserwacje rezonansów Feshbacha w układzie ^{41}K-^{133}Cs.

Przeprowadzona charakterystyka stanowi istotny krok w kierunku wytworzenia po raz pierwszy ultrazimnych cząsteczek ^{41}K-^{133}Cs, których właściwości wydają się szczególnie obiecujące w kontekście zastosowań w symulatorach kwantowych.

Acknowledgments

It is customary for doctoral dissertations to include a section of acknowledgments, to thank all those who contributed, directly or indirectly, to their completion. Yet if I were to provide a full list, this work would no longer resemble a scientific dissertation, but rather a phone book. And with so many people to thank, one must ask: what would be the proper order?

Perhaps it is best to start with those who had to endure the collateral damage of my research. For this reason, I would first like to thank my partner, Kasia, who – despite sharing a home with me – spent many lonely hours waiting while I was occupied with long measurement sessions. She always showed immense understanding, and in difficult moments, the very awareness that someone was waiting for me gave me the strength to endure even the hardest days filled with setbacks.

Following the chronology of life, I should begin by thanking my entire family, who supported me at every step along this long and winding road. Among them are aunts and uncles; cousins; and, most importantly, my grandparents; my brother, his wife, and their daughter; and, above all, my wonderful parents. Regardless of the circumstances, they always gave me unwavering support, often guiding my actions in the right direction.

If, however, I shift from the chronology of life to that of my scientific journey, my first thanks must go to Dr. M. Semczuk, who guided me for nearly a decade, introducing me to the field of cold-atom physics and patiently walking me through the intricacies of experimental work. And while many PhD students might value such knowledge the most, above all I am grateful for his patience and perseverance in shaping the way I think as an experimental physicist, through countless – and often very spirited – discussions.

Within the specific chronology of this doctoral project, my deepest gratitude goes to Prof. P. Kowalczyk, the supervisor of this dissertation, who oversaw every stage of its preparation and whose guidance was invaluable. Without his support and mentorship, this work could not have been completed.

In such a chronology, however, it is difficult to assign a precise place to my friends,

as they accompanied me at many different stages of life and work. Nevertheless, their presence was crucial – especially Michał A., Mateusz G., Artur K., Maciek R., Kuba, and Martyna W., and many others, who often reminded me that life cannot consist of work alone.

Alongside these lifelong friendships, there is another group deserving special mention – those with whom I had the privilege of working side by side. I am grateful to Paulina R.-M., with whom I spent many late evenings during measurements, filling the time with conversations ranging from funny memes to politics and theology. These ten-minute breaks – often devoted to collectively lamenting the ways of the world – gave me strength in moments of doubt. I thank Kuba D., with whom I spent countless hours in the lab and during conferences in many countries. His knowledge – spanning physics, music, gastronomy, and countless other topics – ensured that even long waits, whether for a flight or for a measurement result, became an enjoyable experience. I am also grateful to Paweł A., from whom I learned a great deal about engineering and physics. Beyond that, our frequent conversations were a constant source of support, always giving me hope and strength to persevere and ultimately complete this dissertation. I am equally thankful to Natalia K. for the unwavering support she showed me throughout my scientific journey. Thanks to these people, many difficult moments in the laboratory were easier to endure, and their ability to move seamlessly from serious scientific discussions to the most absurd stories was an invaluable source of joy.

Finally, beyond family, mentors, and friends, I wish to thank many others whose support was invaluable throughout this journey: the heads of the optics division, Prof. Cz. Radzewicz and Prof. P. Fita; the administrative director, Ms. Beata G.; Ms. Gosia M. from the financial section; and the ever-reliable staff of the dean's office – Ms. Iwona and Ms. Gosia. I am also grateful to Ms. Halina P., the secretary of the optics division, for her kind assistance and warm conversations, as well as the skilled technicians of the division – Mr. Marek, Mr. Andrzej, and Mr. Sławek. Lastly, I thank the entire UQG laboratory team – Koray, Jorge, Kuba, and Om – for their support and collaboration.

Ultimately, the list of those to whom I am indebted is far too long to name everyone. To all who made this journey possible: **thank you**.

Contents

Chapter 1

Introduction

The physics of cold gases has attracted the attention of both experimentalists and theorists for decades. It is difficult to pinpoint the exact moment in the history of physics when this interest began. One could argue that it truly started with the work of A. Einstein and S. N. Bose (1924), who laid the foundations of quantum statistics and introduced the possibility of reaching what we now call quantum degeneracy in a system of bosons. However, these theoretical considerations were only the beginning, as such regimes remained well beyond experimental reach at that time.

This theory, together with the development of laser spectroscopy and technology of laser construction, defined a central objective: to find methods of cooling atoms in order to reduce thermal broadening of spectral lines and to explore novel quantum effects that could potentially emerge in low-energy samples.

Undoubtedly, an experimental breakthrough came with the development of the first magneto-optical traps (MOTs) for neutral atoms (1987 [1]) and the realization of the first degenerate quantum gases (1995 [2]). These milestones opened an entirely new chapter in experimental physics, as recognized by the Nobel Committee through the awarding of Nobel Prizes, but also demonstrated by the vast number of cold-atom experiments conducted since then.

These achievements - the production of the first cold and ultracold samples of rubidium and sodium motivated researchers to cool other alkali atoms: cesium (1990 [3]), potassium isotopes (1995 [4]), lithium (1998 [5]), francium (2003 [6], thereby demonstrating laser cooling of all alkali atoms. In subsequent years, traps for atoms from other groups were developed as well, including strontium (1999 [7]), ytterbium (1999 [8]), erbium (2008 [9]), and many others.

The motivation for cooling new species was not a race between research groups to increase atomic complexity, but rather stemmed from the broad range of scientific

opportunities and applications. Since the first demonstrations, cold neutral atoms have been used to investigate fundamental phenomena such as the emergence of new quantum phases and the observation of superfluidity in ultracold gases [10], [11]. At the same time, many groups developed practical applications of cold atoms, including frequency standards and atomic interferometers [12], [13]. This diversity of directions continues to motivate new experiments, and a natural next step in this progress was to cool not only individual atomic species but also their mixtures. Although such experiments are considerably more complex, they hold enormous promise for potential applications—for instance, at the interface of condensed matter and AMO physics.

To show an advantage of ultracold mixtures over single species scenario, consider for example, interfering laser beams that form an interference pattern in space. Depending on the relative propagation directions, one can create square optical lattices—by arranging beams at right angles and retroreflecting them on themselves. In this case, the spacing between sites (the maxima or minima of the light intensity) is uniform, producing a lattice configuration analogous to a simple cubic (sc) crystal [14]. By changing the geometry to beams intersecting at 60°, it becomes possible to create a honeycomb (graphene-like) lattice [15]. Already these two examples demonstrate the enormous flexibility laser beams provide in engineering systems that can closely mimic crystalline structures typical of condensed matter physics. The crucial difference is that, in cold-atom physics, the lattice geometry is not determined by the material itself, but rather by the relative arrangement of laser beams, offering great tunability.

There are, of course, technological limitations. To generate such optical lattices, one needs highly stable laser beams, both in intensity and spatial profile, since vibrations can cause heating that prevents long trapping times. Furthermore, the choice of laser wavelength is critical: atomic interactions are short-ranged and occur at length scales much smaller than the spacing between interference fringes of high-power lasers at 1064 nm or 532 nm.

Instead of relying on different laser wavelengths, a more advantageous approach is to create heteronuclear molecules from mixtures of cold atoms. Such systems exhibit long-range dipole interactions, with interaction ranges larger than the lattice spacing. Moreover, by applying an external electric field, the relative orientation of dipole moments can be tuned, allowing direct control of the interaction strength. Ultracold molecules in optical lattices, therefore, provide a platform for quantum simulations—systems capable of reproducing condensed-matter phenomena but with tunable lattice constants, geometries, and interactions.

For this to be possible, however, ultracold molecules must first be created. In

recent years, experiments aimed at laser cooling of molecules have achieved their intended goal, enabling efficient cooling to sub-Doppler temperatures [16], [17]. Nevertheless, the typical approach still relies on preparing mixtures of cold or ultracold atoms and subsequently forming molecules from them. The procedure is complex and requires developing cooling techniques for different atomic species, trapping them, characterizing collisional properties, identifying Feshbach resonances for magneto-association, transferring metastable molecules to the ground state (via STIRAP), minimizing molecular losses, and finally loading them into an optical lattice.

Many of these methods have been developed for different mixtures, such as ^{85}Rb-^{87}Rb, ^{87}Rb-^{133}Cs, ^{23}Na-^{41}K, ^{7}Li-^{133}Cs, ^{39}K-^{133}Cs, and many more [18]–[22]. However, it is not obvious which mixture possesses the most favorable properties. In fact, before performing detailed studies of each system, it is impossible to predict which one will be optimal for a given experimental goal.

In this dissertation, we present an experimental apparatus designed to cool ^{39}K, ^{40}K, ^{41}K, and ^{133}Cs, and to study their mixtures. To the best of our knowledge, this is one of very few experiments—if not the only one—where a methodology for cooling all these atoms has been developed.

We have also investigated mixtures of these species. In some cases, we reproduced earlier results from another group (e.g. ^{39}K-Cs), but we also performed the first cooling and studies of previously unexplored mixtures (^{39}K-^{40}K, ^{41}K-^{133}Cs). To present the development of the apparatus and the obtained results in a structured way, this thesis is divided into the following chapters:

- Chapter 1, **Potassium and cesium properties**, discusses the relevant properties of potassium and cesium atoms, including a brief theoretical overview of atomic interactions and their tunability through Feshbach resonances.

- Chapter 2, **Laser cooling, pumping, and imaging of potassium and cesium atoms**, describes the methods of laser cooling, optical pumping, and detection. Alongside the theoretical background, we emphasize the experimental perspective, including several practical insights gained during the preparation of this work.

- Chapter 3, **Ultracold atoms experiment at UW**, presents the experimental apparatus. We describe the vacuum system, magnetic-field sources and their characterization, as well as the implemented laser stabilization techniques and the development and characteristic of optical dipole trap. A significant part of our know-how, acquired during the preparation of the experiment, is included here, with references to numerous challenges encountered in practice.

- Chapter 4 is our first publication **Sub-Doppler laser cooling and magnetic trapping of natural-abundance fermionic potassium.**, focusing on laser cooling. We present the applied techniques and their implementation, culminating in what we believe to be the first sub-Doppler cooling of fermionic potassium in a single-chamber setup without enriched dispensers. The work concludes with the demonstration of magnetic trapping of these atoms in our system.

- Chapter 5, also based on a publication, **Magnetic trapping of an ultracold ^{39}K-^{40}K mixture with a versatile potassium laser system**, describes our modular laser system for potassium cooling. The setup is capable of cooling all three natural potassium isotopes and can be easily adapted for metastable isotopes. To demonstrate its novelty and efficiency, we report laser cooling of ^{41}K and the first cooling of the ^{39}K-^{40}K mixture, which we subsequently transfer to the magnetic trap. Phenomenologically, we demonstrate the heteronuclear interactions through the observation of lifetime reduction.

- Chapter 6 is the publication **Sub-Doppler cooling of potassium-cesium mixtures: optical trapping, Feshbach spectroscopy, and loss analysis**. At the time of submission, this work was under review in a journal. Here, we present the laser system for cesium cooling and characterize cooling of all previously discussed bosonic species. We also report Feshbach spectroscopy of the ^{39}K-Cs mixture, where we observed several previously unreported resonances, and we analyze three-body losses in ^{39}K-Cs and ^{41}K-Cs mixtures by measuring lifetimes in the optical dipole trap.

- Chapter 7, **Feshbach spectroscopy of ^{41}K-Cs mixtures**, presents what is arguably the most important study of this dissertation: the first Feshbach spectroscopy of this new mixture. We show that theoretical predictions of resonance positions deviate significantly from experimental observations, indicating that essential elements of the interaction potential remain unaccounted for—an important direction for future research.

- Chapter 8 concludes the dissertation, summarizing the main results and briefly mentioning several aspects that were studied but not fully described within thesis.

The structure of the dissertation reflects the novelty of the research: the development of a new experimental apparatus, the cooling of two previously unexplored mixtures (^{39}K-^{40}K and ^{41}K-Cs), and Feshbach spectroscopy of a new ^{41}K-Cs mixture

and a known system (^{39}K-Cs), where we observed many new resonances relevant for refining interaction potentials. For clarity and coherence, we begin with the properties of the studied atoms.

Chapter 2

Potassium and cesium properties

In experimental atomic physics, the choice of atomic species fundamentally shapes both the experimental methodology and the scope of possible investigations. For example, to study the fermionic nature of matter, especially in the strongly interacting regime, one is limited to working with ^{6}Li or ^{40}K [23], [24]. Among many studies, these species have been recently used to observe the role of the Pauli principle in blocking spontaneous emission or light scattering on the atomic cloud [25], [26]. When working with fermions, one needs to circumvent limitations imposed by the Pauli principle and either use a spin mixture to enable collisions needed for a temperature reduction during evaporative cooling [27] or use another species (usually a bosonic atom) as a coolant [28], [29]. Experiments that require clouds of quantum degenerate bosons can choose from a vastly larger pool of candidate species. Some of them, like ^{23}Na, ^{87}Rb, or to too large an extent ^{41}K are known to be rather easy to bring into the quantum degenerate regime, particularly because they can be efficiently evaporated using an RF-knife in a magnetic trap even to the temperatures and densities that allow for reaching quantum degeneracy [2], [30], [31].

Evaporative cooling in a magnetic trap is relatively slow and limits the ability to prepare atoms in arbitrary magnetic sublevels. Additionally, even for magnetically trappable states of some species like ^{39}K or ^{133}Cs [32], [33], evaporation might be impossible due to unfavorable collisional properties. An alternative approach is to use optical dipole traps, where trapping is not sensitive to the magnetic moment of an atom and it is possible to tune collisional cross-section and inelastic losses with magnetic field, enabling efficient evaporation. This approach was essential to create Bose-Einstein condensates of ^{133}Cs and ^{39}K [32], [33].

For certain studies it is vital to have the ability to introduce and, ideally, to tune long-range interactions [34], [35]. In the typical case of atoms in optical lattices,

the range of dipolar interaction is too short for their effect to be observable. To present that we can introduce the so-called dipole length a_{dd}, which characterizes the absolute strength of dipolar interactions [36]. It depends on the particle mass m and the dipolar coupling constant C_{dd}, and is defined as

$$a_{dd} = \frac{C_{dd} m}{12\pi\hbar^2}.$$

For systems with a fixed magnetic dipole moment μ, the coupling constant is $C_{dd} = \mu_0\mu^2$, where μ_0 is the vacuum magnetic permeability. In the case of electric dipole interactions with dipole moment d, the coupling constant is $C_{dd} = d^2/\epsilon_0$, where ϵ_0 denotes the vacuum electric permittivity.

In this context, one can compare a dipole length with the distance between lattice sites generated by the 1064 nm or 532 nm light. For atoms with large magnetic moments, such as lanthanides, e.g., ^{164}Dy, ^{166}Er, the (magnetic) dipole length still remains small, reaching only 3-7 nm [37], [38]. Moreover, in these systems it is not possible to 'switch off' interactions. An alternative approach is to use heteronuclear molecules with large electric dipole moments in their respective rotational and vibrational singlet ground states, such as KCs (d = 1.9 D, a_{dd} = 3.09 µm), LiRb (d = 4.1 D, a_{dd} = 7.86 µm), AgCs (d = 9.75 D, a_{dd} = 114 µm) [39], [40].

In our laboratory, we focus on cesium atoms (^{133}Cs) and three natural isotopes of potassium (^{39}K, ^{40}K, ^{41}K). This set of atoms could be used for studies requiring fermions (^{40}K), bosons (^{39}K, ^{41}K, ^{133}Cs), bosonic and fermionic mass-imbalanced mixtures, heteroisotopic molecules as well as homo- and heteronuclear molecules. The cooling methods and results that we have obtained are mainly dictated by the properties of these atoms, which are discussed in the remainder of this chapter.

Let's begin with a short description of physical properties of potassium and cesium, which in the case of heteronuclear mixtures significantly reduces the efficiency of some processes. For example, cesium and potassium atoms placed in a large-volume dipole trap with a shallow trapping potential can spatially separate due to their mass difference, an effect typically called a gravitational sag. This reduces the number of collisions and may decrease evaporation efficiency or the association of molecules. The masses of cesium atoms and three natural potassium isotopes based on Ref. [41], [42] are presented in Table 2.1.

Another aspect important from the perspective of the experiment, or rather from the perspective of the methods used to stabilize the frequency of cooling lasers, is the vapor pressure as a function of temperature. It defines the pressure exerted by atoms in a gaseous state in a closed system when the gas phase is in thermodynamic equilibrium with the liquid or solid phase [43]. In simpler terms, we can consider

it to be a value that indicates 'how many' atoms are in the gas phase depending on the temperature. This affects spectroscopy in hot vapors both in terms of the visibility of transitions and in terms of the collisional broadening of spectral lines. For cesium atoms, the vapor pressure at room temperature is $p_{Cs}^{293K} = 1.00 \times 10^{-6}$ mbar, as calculated from equation (1) in Ref. [41], while for potassium atoms at the same temperature, the vapor pressure is almost two orders of magnitude lower and reaches $p_K^{293K} = 1.3 \times 10^{-8}$ mbar. This justifies the need, described in the further part of this thesis, to heat the glass cell with potassium atoms to $T = 60^o$C in order to perform saturation spectroscopy, and obtain a signal allowing for the reliable stabilization of the frequency of cooling lasers. According to formula (1) from Ref. [42], at $T = 60^o$C the vapor pressure reaches $p_K^{333K} = 1.03 \times 10^{-6}$ mbar, similar to the cesium vapor pressure at the room temperature.

The number of neutrons in the atomic nucleus determines if a given potassium isotope has a fermionic or a bosonic nature. For the isotopes discussed in this thesis, a summary of these values, the resulting nuclear spin, the division into isotopes, and their abundance in natural sources is presented in Table 2.1.

	Protons	Neutrons	Mass (u)	Statistic	Abundance	Nuclear spin I
^{39}K	19	20	38.96	Boson	93.26	3/2
^{40}K	19	21	39.96	Fermion	0.012	4
^{41}K	19	22	40.96	Boson	6.73	3/2
^{133}Cs	55	78	132.91	Boson	100	7/2

Table 2.1: Summary of the key physical properties of the potassium and cesium atoms relevant from the perspective of this work. The table shows the number of protons, neutrons, the mass in atomic units, quantum statistics, its abundance in a natural source and the nuclear spins [41], [42].

From the perspective of laser cooling, trapping, detection, and optical pumping, the physical properties of atoms are important, but the electronic structure is fundamental, as it largely determines the applicable techniques and their efficiency. Although comprehensive descriptions of potassium and cesium properties can be found in the literature [41], [42], this chapter summarizes only some sections of these works, and focuses on the aspects relevant to the scope of this thesis. In the first part, we will focus on the properties of potassium and establish symbols that will be used in the rest of the work. The second part of the chapter presents the properties relevant to the cooling of cesium atoms. In the third part, we will discuss interactions between potassium and cesium atoms from the perspective of molecular potentials.

2.1 Electronic structure of potassium atoms

For cooling methods applied in the thesis in the case of potassium atoms, the relevant electronic states are ${}^2S_{1/2}$ (the ground state of K atom), ${}^2P_{1/2}$, and ${}^2P_{3/2}$, denoted as ${}^{2S+1}L_J$, where S is the total spin of the electrons, L is the orbital angular momentum, and J is the total electronic angular momentum. The optical transitions between these levels define the D lines: the D1 line corresponds to the ${}^2S_{1/2} \rightarrow {}^2P_{1/2}$ transition which for the ${}^{39}K$ isotope has a central frequency of $f = 389.286059$ THz (770.11 nm), and the D2 line to the ${}^2S_{1/2} \rightarrow {}^2P_{3/2}$ with the frequency of $f = 391.016170$ THz (766.70 nm). The isotopic shift of the frequency of both D1 and D2 lines in potassium is relatively small in the order of 100-250 MHz.

These transition frequencies are crucial during the laboratory setup phase, particularly when selecting lasers with appropriate central wavelengths. They also play a key role at the stage of selection of experimental procedures, particularly in applications involving laser beams that are detuned far from resonance, as in the case of dipole trap, where the depth of the trap depends strongly on the detuning from the transition (see chapter 3).

In the context of laser cooling and related techniques, the coupling between the electronic angular momentum J and the nuclear spin I must also be considered, as it gives rise to a hyperfine structure. The resulting energy levels are labeled by the total atomic angular momentum F, which can take values in the range $|J-I| \leq F \leq J+I$. The hyperfine structure of levels involved in the D1 and D2 transitions is presented in Fig. 2.2. As can be seen in the graph, the separation between the energy levels of the excited state ${}^2P_{3/2}$ for bosonic isotopes is small, especially compared to the natural linewidth of the D2 line ($\Gamma_{\mathrm{D2}} = 6.035$ MHz) and the D1 line ($\Gamma_{\mathrm{D1}} = 5.956$ MHz). This significantly limits the possibility of independently addressing the excited-state sublevels of the ${}^2P_{3/2}$ manifold and reduces the efficiency of laser cooling methods operating on the D2 line. Therefore, it is better to use a D1 line for cooling schemes which require well-separated excited state levels.

In the presence of a magnetic field, each hyperfine level characterized by total angular momentum F splits into $2F+1$ Zeeman (magnetic) sublevels corresponding to different projections m_{F} of F onto the quantization axis, where $m_{\mathrm{F}} \in \{-F, -F+1, \ldots, F\}$. The energy difference between successive m_{F} levels in the presence of a non-zero magnetic field is described by the Zeeman effect. For the weak magnetic field, or more precisely, if the splitting of the magnetic levels m_{F} due to the presence of the magnetic field is small relative to the energy difference between subsequent F states, the change of the energy ΔE due to the magnetic field B, for a given magnetic

	$a^{hf}_{S_{1/2}}$ ($h \times$ MHz)	$a^{hf}_{P_{1/2}}$ ($h \times$ MHz)	$a^{hf}_{P_{3/2}}$ ($h \times$ MHz)	$b^{hf}_{P_{3/2}}$ ($h \times$ MHz)	g_I ($\times 10^{-4}$)
^{39}K	230.860	27.775	6.093	2.786	-1.41935
^{40}K	-285.731	-34.523	-7.585	-3.445	1.76490
^{41}K	127.007	15.245	3.363	3.351	-0.77906
^{133}Cs	2298.158	291.920	50.275	-0.53	-3.98854

Table 2.2: Hyperfine structure constants for three isotopes of potassium, and cesium atoms. Last column represents Landé g-factor for the nuclear spin for each species.

state m_{F}, can be calculated using the formula

$$\Delta E = \mu_B m_F g_F B_z, \tag{2.1}$$

where $\mu_B = 9.27 \times 10^{-24}$ J/T is the Bohr magneton, and the hyperfine Landé g-factor is given by

$$g_{\mathrm{F}} = g_J \frac{F(F+1) - I(I+1) + J(J+1)}{2F(F+1)} + g_I \frac{F(F+1) + I(I+1) - J(J+1)}{2F(F+1)},$$

where g_J and g_I are the Landé g-factors for the total electronic angular momentum and the nuclear spin, respectively. The values of g_I for the cesium and potassium isotopes are summarized in Table 2.2. The values of g_J and the calculated values of g_{F} for each state are presented in Fig. 2.2.

For higher magnetic fields, where the linear approximation of the Zeeman effect ceases to be valid, there exists an analytical formula known as the Breit-Rabi formula, which describes the change of energy of a magnetic sublevel. For potassium and cesium atoms it can be applied only to the levels belonging to the ground state manifold. The formula is given as:

$$E^{\mathrm{hf}}(B) = -\frac{a^{\mathrm{hf}}}{4} + g_I \mu_B m_f B \pm \frac{a^{\mathrm{hf}}(I+1/2)}{2} \left(1 + \frac{4 m_f x}{2I+1} + x^2\right)^{1/2} \tag{2.2}$$

$$x = \frac{(g_J - g_I)\mu_B}{a^{\mathrm{hf}}(I+1/2)} B,$$

where a^{hf} is a hyperfine structure constant.

The Breit-Rabi formula is useful from the perspective of experimental system diagnostics. For example, it can be used to determine the frequency range in which the RF-knife must operate for efficient evaporation in the magnetic trap. Perhaps

most importantly, it can also be used for precise measurement of the magnetic field in the system and calibration of its sources (see chapter 4).

However, in systems where an optical transition is excited on the D2 or D1 line, the usefulness of the Breit-Rabi formula is limited due to the inability to apply it to the energy levels of the excited state. In such a situation, the solution is to use the entire equation, for which the Breit-Rabi formula is an analytical result that can be calculated due to the restriction to $L = 0$, $S = 1/2$. The energies can be calculated by diagonalization of the

$$\hat{H}_{\text{int}} = \hat{H}_{\text{hf}} + \hat{H}_{\text{B}}, \tag{2.3}$$

where for the magnetic field along the z-axis

$$\hat{H}_{\text{B}} = \mu_{\text{B}} \left(g_{\text{J}} \hat{J}_z + g_{\text{I}} \hat{I}_z \right) B_z,$$

$$H_{\text{hfs}} = a_{\text{hfs}} \, \boldsymbol{I} \cdot \boldsymbol{J} + b_{\text{hfs}} \, \frac{3(\boldsymbol{I} \cdot \boldsymbol{J})^2 + \frac{3}{2} \boldsymbol{I} \cdot \boldsymbol{J} - I(I+1)J(J+1)}{2I(2I-1)J(2J-1)}$$

Here, a_{hfs} and b_{hfs} are the magnetic dipole and electric quadrupole hyperfine constants, the values of which for potassium and cesium atoms are presented in Table 2.2. We use bold symbols for vector operators (e.g., $\mathbf{J}$, $\mathbf{I}$), and a hat to denote quantum-mechanical operators in general. For example, $\hat{J}_z$ denotes the z-component of $\mathbf{J}$, defined with respect to the quantization axis. The corresponding eigenvalues (e.g., m_{S}, m_{L}, m_{I}) are used only for specific energy levels.

Using the full model of the Zeeman effect, we can identify the range of validity of the linear approximation by quantifying how the error increases with the magnetic field. This behavior is illustrated for the ground state of potassium atoms in Fig. 2.1. Naturally, the usefulness of the approximation depends on the required level of precision. For example, when calibrating a magnetic field source using magnetic dipole transitions, even a deviation of approximately 100 kHz can significantly affect the outcome, due to the fact that the typical transition width observed in this calibration is lower than 20 kHz (see chapter 3). By contrast, absolute energy shifts are less important for magnetic trapping, since the slope of the energy shift as a function of the magnetic field is what truly matters, because it determines the trapping potential generated by the field gradient.

2.2 Electronic structure of cesium atoms

For experiments with cesium atoms, cooling procedures typically utilize the D2 line, which corresponds to the transition between the $^2S_{1/2}$ and $^2P_{3/2}$ states, with a res-

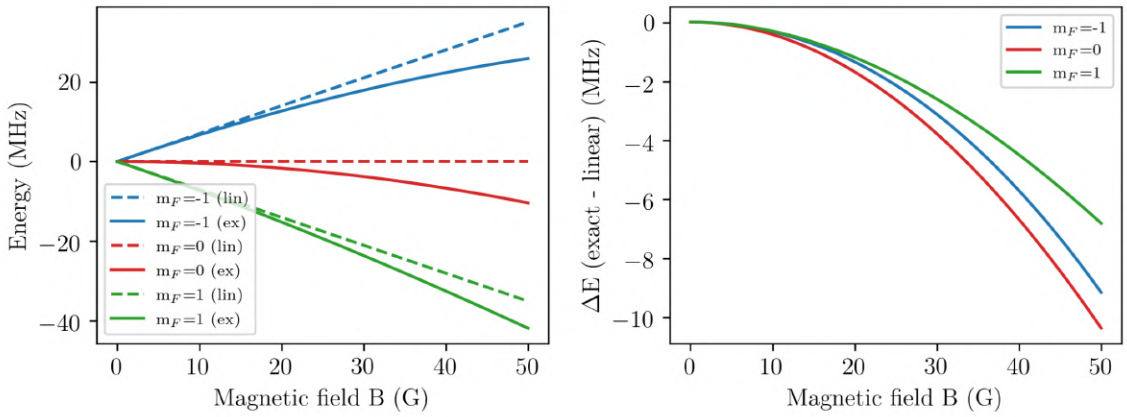

Figure 2.1: Zeeman splitting of the ground-state hyperfine levels of ^{39}K as a function of magnetic field. The left panel shows the energy levels of the $F = 1$ manifold calculated using the linear Zeeman approximation (dashed lines) and by exact diagonalization of the hyperfine-Zeeman Hamiltonian (solid lines). The right panel shows the difference between the results of exact calculations and linear approximation for energies for each magnetic sublevel m_{F}.

onant frequency of $f = 351.725718$ THz ($\lambda = 852.35$ nm). As shown in Figure 2.2, the hyperfine splitting in both the ground and excited states is significantly larger than in the case of potassium atoms. Therefore, it is not necessary to employ the D1-line cooling, as each transition can be addressed almost independently.

Situation becomes a bit more complicated if the magnetic field is introduced, as in the ground state, two hyperfine levels are available: $F = \{3, 4\}$, while in the excited state, four levels are present: $F = \{2, 3, 4, 5\}$. This results in a significantly larger number of magnetic sublevels compared to potassium atoms, which can hinder optical pumping between these states. In particular, for atoms in the lower ground state manifold, efficient optical pumping into non-stretched states becomes nearly impossible.

In the case of our experiment, we decided to attempt optical pumping in a high magnetic field, utilizing the constraints imposed by selection rules. This requires the use of the exact formula for the energy of the magnetic state (Eq. 2.3). We calculate the energy shifts of the ground and excited hyperfine levels as a function of the magnetic field, as shown in Fig. 2.3. Based on these results, we estimate the frequency and the line shape of the available transitions, assuming that each transition has a linewidth equal to the natural linewidth of the D2 line, $\Gamma = 5.22$ MHz, and that the transition probabilities are the same.

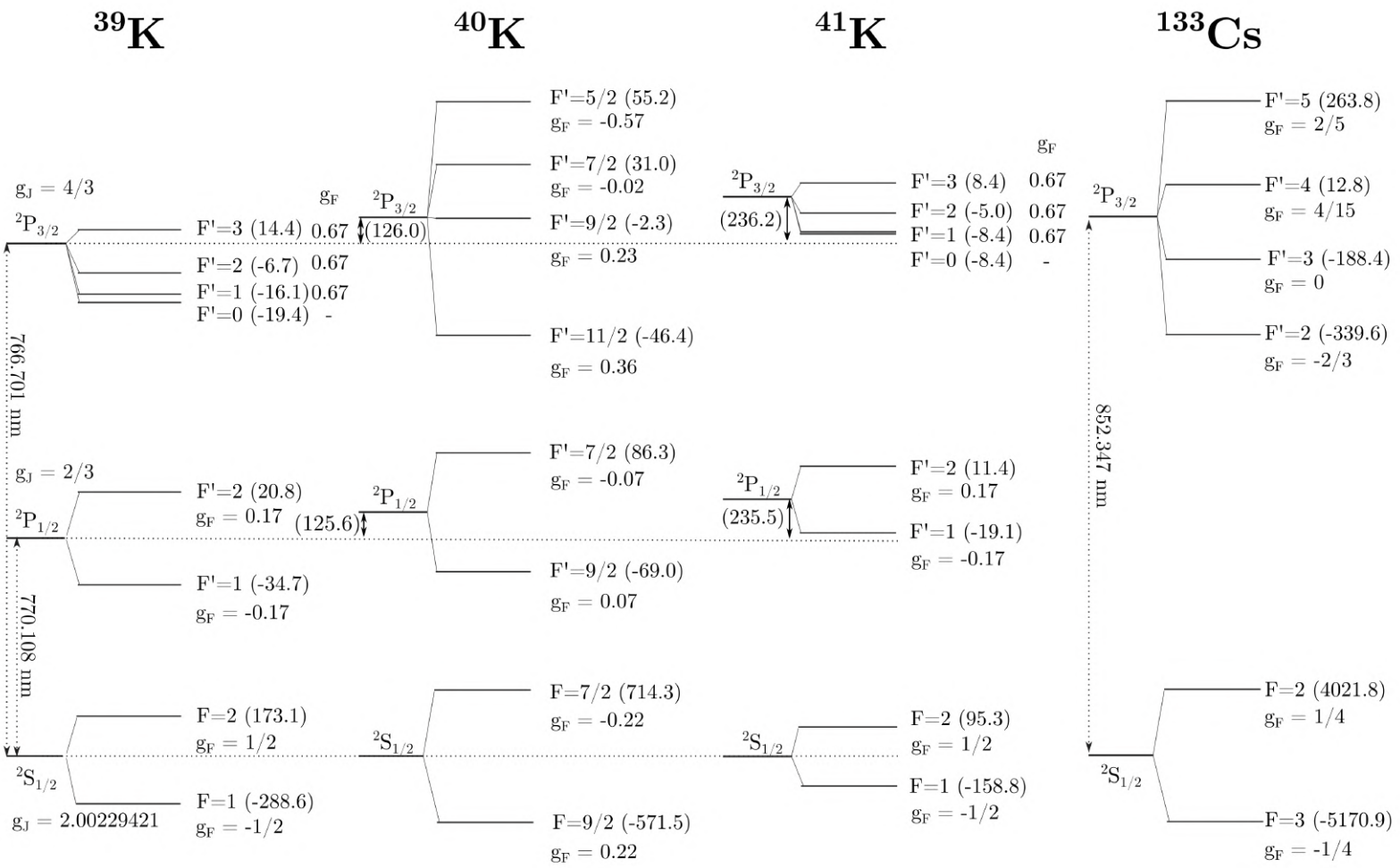

Figure 2.2: Energy level diagram of potassium and cesium atoms relevant to this work. The diagram shows the hyperfine structure of the $^2S_{1/2}$, $^2P_{1/2}$, and $^2P_{3/2}$ states of potassium isotopes. For cesium, only the $^2S_{1/2}$ and $^2P_{3/2}$ states are shown, since the $^2P_{1/2}$ state is not used in this work. For each hyperfine level F, the detuning from the corresponding fine structure level (in MHz) is indicated in parentheses. The Landé g-factors for each hyperfine level (g_F) and for each fine structure state (g_J) are also provided.

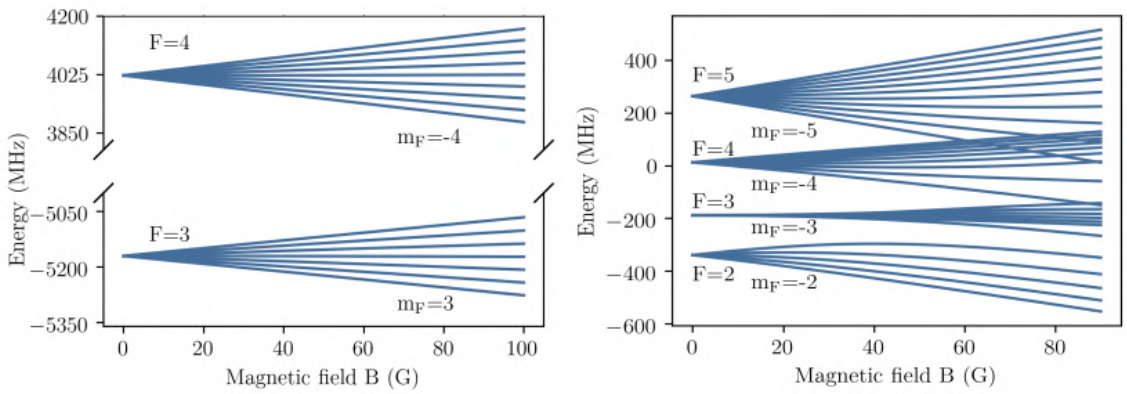

Figure 2.3: Zeeman splitting of the ground-state (left side), and excited state (right side) for hyperfine levels of ^{133}Cs as a function of magnetic field.

The simulation results for a magnetic field of 88 G are presented in Fig. 2.4. As can be seen, the spectrum of transitions becomes dense, preventing selective addressing of individual states. However, by applying selection rules and orienting the linear polarization of light along the quantization axis, with the wave vector aligned perpendicularly to the quantization axis, the only transitions allowed are those with no change in the magnetic quantum number, i.e. $\Delta m_{\mathrm{F}} = 0$ - so-called π transitions. Under these conditions, it becomes possible to isolate a $^2S_{1/2}, F = 3, m_{\mathrm{F}} = 3 \rightarrow {}^2P_{3/2}, F = 3, m_{\mathrm{F}} = 3$ transition and selectively remove atoms out of that ground state, because the closest-neighbor transition is detuned by 2.5 Γ, as illustrated on the right side of Fig. 2.4. This 'resolved' magnetic states structure, together with proper experimental procedure, can be used to obtain a sample polarized dominantly in the $^2S_{1/2}, F = 3, m_{\mathrm{F}} = 2$ state, as presented in chapter 3.

2.3 Molecular properties of potassium and cesium

Many phenomena in cold atom physics are not governed solely by the internal atomic energy structure. The relevant molecular interaction potentials may also play an important role during interatomic collisions. Let us consider, as an example, 10^8 Cs or K atoms we routinely confine in a magneto-optical trap (MOT) in an early stage of each experimental sequence. With a cloud radius of about 1 mm, the atomic density $n \approx 10^{10}$ is relatively low, and the average interatomic distance $d \sim n^{-1/3} = 10$ µm

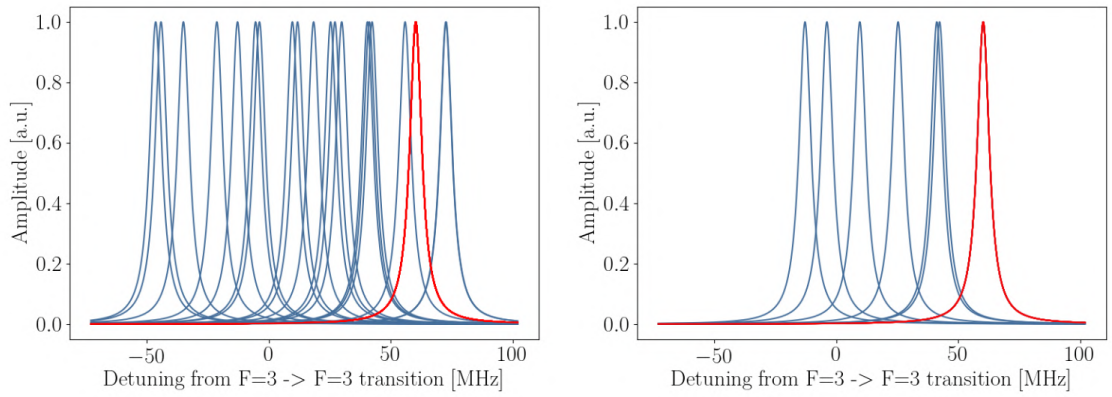

Figure 2.4: Simulation of allowed transitions on the D_2 line from the ground state $^2S_{1/2}$ in cesium atoms. Each transition is modeled using a Lorentzian profile with a full width at half maximum (FWHM) of $\Gamma = 5.22$ MHz and unit-normalized amplitude. The left panel shows all allowed transitions from the $F = 3$ ground-state manifold, while the right panel includes only π-transitions (i.e., $\Delta m_F = 0$). Transition $^2S_{1/2}, F = 3, m_F \rightarrow^2 P_{3/2}, F = 3, m_F$, which is directly relevant for the optical pumping scheme presented in the thesis, is highlighted in red.

remains large. Despite the relatively low density and the large average interatomic separation, one of the key parameters determining the system's evolution toward equilibrium is the so-called two-body loss coefficient, which value depends on the specific atomic species confined in the trap.

A well-known model that explains the source of two-body losses (commonly called light-assisted collisions) in a MOT is the Gallagher-Pritchard model, which proposes two dominant loss mechanisms [44]. In the first scenario, fine-structure changing process, red-detuned (with respect to the $P_{3/2}$ state) MOT light couples two colliding ground-state atoms into a weakly bound molecular state near the $S_{1/2} + P_{3/2}$ asymptote. Following spontaneous emission, one atom may decay into a lower fine-structure component (e.g., $^2P_{1/2}$), and the hyperfine energy is distributed between both atoms, increasing their kinetic energy, accelerating both atoms out of the trap. while the other returns to the ground state. As an example discussed in the Gallagher-Pritchard paper, the process for sodium atoms can be written as:

$$\mathrm{Na} + \mathrm{Na} + h\nu \longrightarrow \mathrm{Na}_2^*(^2P_{3/2}) \longrightarrow \mathrm{Na}^*(^2P_{1/2}) + \mathrm{Na} + \Delta E_{FS}, \tag{2.4}$$

where the asterisk indicates an excited atomic or molecular state, and ΔE_{FS} is the fine-structure energy splitting. According to the estimates, in the case of sodium

(Na) each atom gains approximately $\Delta E_{FS}/2 \approx 12$ K of kinetic energy, which is typically sufficient to remove both atoms from the MOT.

The second proposed mechanism involves the escape of atoms caused by radiative redistribution. In this process, a pair of ground-state atoms is photoassociated into an excited molecular state by absorption of a red-detuned photon. The excited molecule subsequently decays radiatively back into two free atoms, emitting a photon of different (typically lower) energy. This process results in a net kinetic energy gain equal to the photon energy difference:

$$\mathrm{Na} + \mathrm{Na} + h\nu \longrightarrow \mathrm{Na}_2^* \longrightarrow \mathrm{Na} + \mathrm{Na} + h\nu', \tag{2.5}$$

with the energy difference $\Delta E = h(\nu - \nu')$ transferred to the atoms as kinetic energy.

As can be seen, both loss mechanisms are based on the process of photoassociation of atoms into excited molecular states and thus depend sensitively on the molecular potentials. These processes are particularly relevant in the samples, where atom pairs interact under MOT light, which drives transitions near the $S_{1/2} + P_{3/2}$ asymptote.

What happens in denser samples, where light-assisted collisions become negligible due to the absence of near-resonant light? As an example, consider potassium and cesium atoms confined in a far-off-resonance optical dipole trap, such as the one formed by a laser operating at 1064 nm (i.e., 200–300 nm detuned from the D-line transitions). In such conditions, the trapping light does not induce significant resonant excitations, and the dominant collisional processes are governed by ground-state molecular interactions. The primary loss mechanism under these circumstances is typically three-body recombination, which depends sensitively on the internal quantum states of the atoms and the trap parameters [22], [45].

In three-body recombination, as the name suggests, three atoms collide simultaneously, resulting in the formation of a weakly bound diatomic molecule and the release of binding energy, which is carried away as kinetic energy by the molecule and the remaining atom. This energy release is typically sufficient to eject all three particles from the trap. The recombination process can be schematically represented as:

$$\mathrm{A} + \mathrm{A} + \mathrm{A} \rightarrow \mathrm{A}_2 + \mathrm{A} + \Delta E_{\mathrm{bind}}, \tag{2.6}$$

where ΔE_{bind} is the binding energy of the formed molecule.

Three-body losses significantly limit experiments involving ultracold dense samples. Large three-body recombination rates can drastically reduce the lifetime of atoms in the trap, preventing efficient evaporative cooling. Because the recombination rate is dependent on the local atomic density, losses predominantly occur in the center of the trap, where the density is highest. On the other hand, the center

of the trap is occupied by the coldest atoms; hence, spatially selective loss leads to a phenomenon known as anti-evaporation - removal of the coldest atoms from the sample, leading to an increase in the average temperature [46].

The implication is straightforward: a high three-body recombination rate, which depends on the short-range part of the molecular potential, can prevent efficient evaporative cooling and limit the achievable peak density. It can also hinder molecule formation or simply reduce the trap lifetime.

For potassium and cesium atoms, the three-body loss coefficient L_3 has been measured in the presence of weak magnetic fields for the lowest-energy magnetic sublevels: ${}^2S_{1/2}, F = 3, m_F = 3$ for Cs, and ${}^2S_{1/2}, F = 1, m_F = 1$ for ^{39}K and ^{41}K. The reported values are [45], [46]:

$$L_3^{\mathrm{Cs}} = 3 \times 10^{-24}\ \mathrm{cm}^6\,\mathrm{s}^{-1} \tag{2.7}$$

$$L_3^{{}^{39}\mathrm{K}} = 1 \times 10^{-29}\ \mathrm{cm}^6\,\mathrm{s}^{-1} \tag{2.8}$$

$$L_3^{{}^{41}\mathrm{K}} = 4 \times 10^{-29}\ \mathrm{cm}^6\,\mathrm{s}^{-1} \tag{2.9}$$

For the fermionic isotope ^{40}K, due to the Pauli principle, s-wave collisions between identical atoms are suppressed at low temperatures. As a result, the dominant contribution to three-body collisions arises from higher partial waves, namely p-wave interactions, which are much less probable. To the best of our knowledge, the three-body recombination rate for ^{40}K in its lowest spin state has not yet been precisely determined.

As one can see from the presented values, the three-body recombination coefficient for cesium atoms is approximately five orders of magnitude larger than for potassium atoms. In practical terms, this means that the trap lifetime of cesium at high densities can be severely limited. Consequently, experiments aiming to reach quantum degeneracy or perform molecule formation with ultracold cesium are strongly affected by this property.

As early as 2002, researchers managed to tune—or more precisely, reduce—the three-body loss coefficient in such a way that achieving a Bose–Einstein condensate of cesium became feasible [47]. In order to provide a consistent explanation for this, let us follow the approach outlined in reference [48], where the authors first consider the range of interactions between two atoms with masses m_1 and m_2, assumed to have no internal structure. These atoms have relative momentum $\hbar k$ and interact via a central molecular potential $V(R)$ that depends only on their mutual distance R. Due to the spherical symmetry of the interaction, it is convenient to expand the incoming plane wave $e^{i\mathbf{k}\cdot\mathbf{R}}$, which describes the relative motion of the atoms in the free-particle limit, into a sum over spherical harmonics $Y_{lm_l}(\hat{\mathbf{R}})$. Here, l is the

relative orbital angular momentum, m_l its projection on the z-axis, and $\hat{\mathbf{R}} = \mathbf{R}/R$ is the unit vector pointing in the direction of $\mathbf{R}$. For integer values $l \in 0, 1, 2, \ldots$, the successive partial waves are called the s-wave ($l = 0$), p-wave ($l = 1$), d-wave ($l = 2$), and so on.

The corresponding relative-motion wave function $\Psi(\mathbf{R})$ satisfies the Schrödinger equation

$$\left[-\frac{\hbar^2}{2\mu}\nabla^2 + V(R)\right]\Psi(\mathbf{R}) = E\Psi(\mathbf{R}), \tag{2.10}$$

where E is the total energy.

Because $V(R)$ is spherically symmetric, the angular dependence is fully described by the spherical harmonics $Y_{lm_l}(\hat{\mathbf{R}})$, leaving only the radial part. Writing the radial wave function as $\Psi(R) = \phi(R)/R$, the Schrödinger equation reduces to

$$\frac{-\hbar^2}{2\mu}\frac{d^2\phi(R)}{dR^2} + \left(V(R) + \frac{\hbar^2 l(l+1)}{2\mu R^2}\right)\phi(R) = E\phi(R). \tag{2.11}$$

The second term in the effective potential represents the centrifugal barrier, which vanishes for s-wave ($l = 0$) collisions. These dominate in low-energy (cold) bosonic systems. For identical fermions, s-wave scattering is forbidden by the Pauli exclusion principle, and the leading contribution comes from the p-wave ($l = 1$) channel, which is strongly suppressed at low energies.

The precise form of the interaction potential remains to be specified. Although many approximations for molecular potentials exist, prominently Lennard-Jones or Morse potentials, the interatomic separation in optical dipole traps, before evaporation, is typically relatively large (on the order of 0.1-1 μm). Therefore, the dominant contribution to the potential is the long-range van der Waals interaction, which can be expressed as

$$V(R) = -\frac{C_6}{R^6} - \frac{C_8}{R^8} - \frac{C_{10}}{R^{10}}, \tag{2.12}$$

where C_6, C_8, and C_{10} are the van der Waals coefficients. As can be seen, at large distances the contributions of the higher-order terms become increasingly negligible, and in many cases the potential can be approximated as $V(R) \approx -C_6/R^6$. In the limit of large interatomic separation, $R \to \infty$, the scattering solution for this potential is given by the wavefunction

$$\phi(R) \propto \sin(kR - \pi l/2 + \eta_l(E)), \tag{2.13}$$

where $\eta_l(E)$ is the phase shift between the incoming and outgoing wave. For the lowest partial wave ($l = 0$), the angular momentum-dependent term vanishes. Comparing this wavefunction to the one in the absence of an interaction potential $\phi(R) \propto$

$\sin(kR)$, we observe that the presence of the potential only introduces a phase shift. For van der Waals-type potentials, the phase shift can be expressed as [22]:

$$k \cot(\eta_l(E)) = -\frac{1}{a} + \frac{1}{2} r_0 k^2, \tag{2.14}$$

where r_0 is the effective range parameter describing the finite-range correction to the s-wave scattering and a is the scattering length—a key parameter used to characterize the interatomic interaction. In the low-energy limit, the elastic cross-section of identical bosons is related to a by

$$\sigma_{el} = \frac{8\pi a^2}{1 + k^2 a^2}. \tag{2.15}$$

Finally, let's return to the discussion about three-body losses introduced at the beginning of this section. It has been shown e.g. in Ref.[45] that for the homonuclear mixtures, there exists a relation between the scattering length in cold gases and the three-body loss coefficient, given by $L_3 \propto a^4$. This means that if there exists a mechanism that allows for tuning of the scattering length, it is also possible to tune, or even minimize three-body losses in the system.

2.4 Feshbach resonances

In experiments with ultracold gases, the tuning of interaction strength is most commonly achieved by exploiting the phenomenon of Feshbach resonances. However, in order to discuss this mechanism, we must move beyond the simplification introduced in the previous section, where atomic scattering was described in terms of two structureless atoms. As outlined at the beginning of this chapter, alkali atoms possess a rich internal structure that strongly affects the dynamics of scattering processes. For clarity, in the following section we describe atoms in their ground hyperfine states using Dirac notation $|F, m_{\mathrm{F}}\rangle$, following the conventions established earlier in the text.

Following again the explanation presented in Ref. [48], let us consider a pair of atoms in states $|F, m_{\mathrm{F}_1}\rangle$, $|F, m_{\mathrm{F}_2}\rangle$, colliding with total energy E_t, which includes both kinetic and internal energy contributions. This collision occurs within a molecular potential associated with these states and is energetically allowed when E_t exceeds the asymptotic potential energy E_o at large interatomic separation. In this case, the atoms can move freely and interact via so-called 'open channel'.

Due to the rich internal structure of atoms, other molecular potentials may also be involved. In particular, collisions could occur in a different channel corresponding

to states $\left|F', m'_{\mathrm{F}_1}\right\rangle + \left|F', m'_{\mathrm{F}_2}\right\rangle$. However, if the internal energy required for such a process is not accessible, i.e., if the energy of the channel $E_c > E_t$ at $R \to \infty$, this channel is so-called 'closed channel'.

At short interatomic distances, the minimum of the molecular potential of the closed channel may occur near the total collision energy. If a bound state exists in the closed channel with energy resonant with the collision energy, atoms can tunnel into the closed channel, or to be more precise—coupling between open and closed channel might occur. In other words, when the collision energy matches that of a bound molecular level in the closed channel, a Feshbach resonance can be observed—provided that the condition $M_{\mathrm{F}} = m_{\mathrm{F}_1} + m_{\mathrm{F}_2} = m'_{\mathrm{F}_1} + m'_{\mathrm{F}_2} + m_l$ is satisfied, where the m_l term vanishes for the s-wave scattering.

This naturally raises the question: what happens if there is no bound state near the collision energy? In that case, tunneling probability is negligible. However, since atoms in the open and closed channels generally occupy different magnetic sublevels, their energies might shift differently in an external magnetic field. This allows for the tuning of the resonance condition using a magnetic field. A schematic depiction of the Feshbach resonance mechanism and magnetic tuning is shown in Fig. 2.5.

Near a Feshbach resonance, the scattering length between atoms becomes tunable. If a resonance occurs at magnetic field B_0 and has a width Δ, the scattering length as a function of applied field B is given by

$$a = a_{bg}\left(1 - \frac{\Delta}{B - B_0}\right), \tag{2.16}$$

where a_{bg} is the background (non-resonant) scattering length. It is important to note that the width Δ can be defined as the distance between the resonance position and the magnetic field for which $a = 0$ is approaching from the negative scattering length side (as presented in Fig. 2.6). Thus, as in the case of homonuclear Feshbach resonances in ^{39}K, the width can be negative [48], [49].

Another crucial point is that both the magnitude and the sign of the scattering length can be tuned, corresponding to mean-field attractive interactions ($a < 0$), repulsive interactions ($a > 0$), or effectively non-interacting atoms ($a = 0$). The sign of a is determined by the position of the nearest bound molecular state relative to the scattering threshold (energy of colliding atoms E_t): a bound state just below threshold ($E_b < E_t$) gives $a > 0$, whereas a bound, virtual state just above the threshold ($E_b > E_t$) gives a$<$0. A schematic representation of the scattering length tuning around the position of the Feshbach resonance is presented in Fig. 2.6.

The final aspect of Feshbach resonances that should be discussed is the method of their detection. In a real experiment, direct measurement of the scattering length

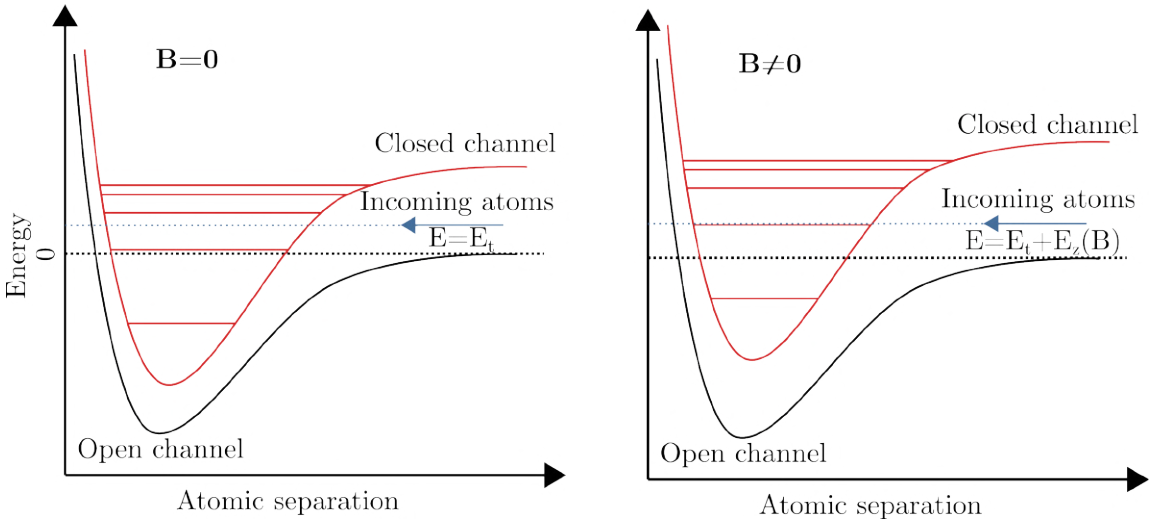

Figure 2.5: Diagram of Feshbach resonances in the coupled-channels picture: the open channel (black curve) and the closed channel (red curve). On the left side of the diagram, atoms in the open channel with a given collision energy E_t (blue arrow) do not resonate with any bound state in the closed channel in the absence of a magnetic field. On the right side, the magnetic field tunes a bound state in the closed channel into resonance with the energy of the colliding atoms. For clarity, the bound states of the open channel are omitted. Idea for the picture was taken from [48].

is rarely performed at the early stages of the experiment. Instead, one typically employs so-called loss spectroscopy. Recalling the earlier discussion on the three-body loss coefficient and its scaling with the fourth power of the scattering length, it becomes clear that in the vicinity of a resonance—where the scattering length becomes very large—atom losses will also become significantly more pronounced, provided that the measurement time and sample density are sufficient for their observation. Consequently, resonances are most commonly identified via measurements of the loss of atoms as a function of magnetic field. This also complements the earlier discussion on how it was possible to achieve Bose-Einstein condensation of cesium, despite its large three-body loss coefficient. The key was to choose an appropriate magnetic field range in which the loss coefficient could be reduced by up to three orders of magnitude, down to $L_3^{\mathrm{Cs}} \approx 10^{-27}$ cm^{6}s^{-1} [47].

Although the presented discussion of three-body losses, scattering length, and related topics may seem complicated, it still constitutes a simplified model that neglects several important phenomena, such as Efimov resonances [50]. Furthermore,

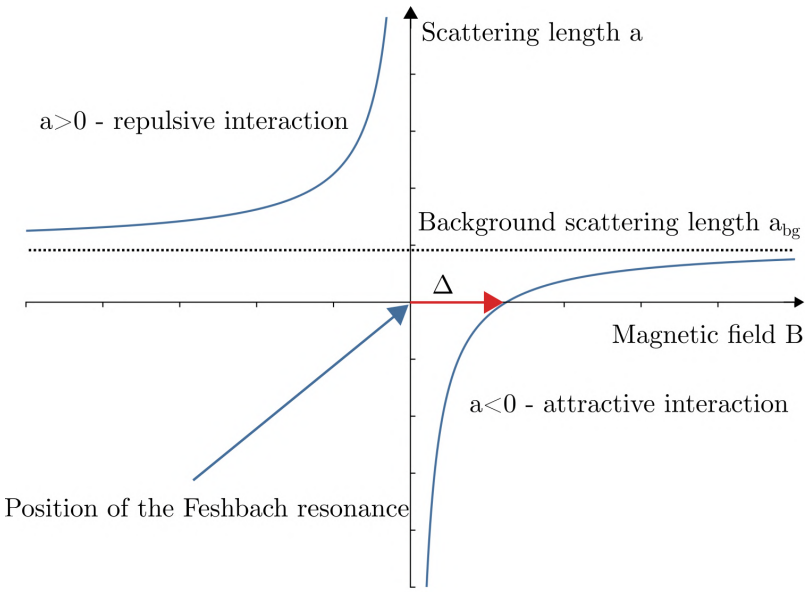

Figure 2.6: Illustration of the scattering length tuning near a Feshbach resonance. The plot shows the scattering length as a function of magnetic field. A location of a Feshbach resonance of width Δ is indicated by the blue arrow. The background (off-resonant) scattering length a_{bg} is marked with a dashed line.

this entire analysis was conducted with the specific objectives and context of the current study in mind. Nonetheless, even this simplified framework already provides a clear justification for why Feshbach resonances have become a powerful and widely used tool. Interaction tuning has become a standard technique in cold atom experiments. For efficient evaporative cooling toward quantum degeneracy, repulsive interactions must be carefully optimized to balance between minimizing three-body losses and maintaining sufficient interaction strength [47]. For molecules formation, the magnetic field should be ramped across the Feshbach resonance from the attractive interaction region towards the region with repulsive interactions. [51], [52].

Clearly, knowing the positions and properties (e.g., widths) of Feshbach resonances is essential for achieving quantum degeneracy in most atomic species. In heteronuclear atomic mixtures, the situation becomes even more crucial: Feshbach resonances are key to producing ultracold molecules and quantum-degenerate mixtures. In this work, we have made a significant step in that direction by identifying previously unobserved Feshbach resonances in the ^{39}K+Cs mixture (see chapter 7) that has been studied in the group of prof. Hans-Christoph Nägerl, University of Innsbruck and fully characterizing a novel mixture mixture of ^{41}K+Cs (see chapter 8).

The results of Feshbach spectroscopy required the preparation of cold, heteronuclear mixtures in an optical dipole trap. To make this possible, we developed efficient cooling methods, which are described in the next chapter.

Chapter 3

Laser cooling, pumping and imaging of potassium and cesium atoms

This chapter focuses on the cooling methods employed in our experiment, which largely determine the obtained results and sample properties like the number of atoms, temperature, or density. When working with new atomic species, such as in the new ultracold silver-alkali experiment currently under development, one typically selects techniques based on approaches that worked for atoms with a similar energy structure or comparable hyperfine splittings. However, even after identifying suitable methods, estimating their efficiency or achievable parameters without detailed simulations remains extremely challenging, or sometimes even impossible.

In the case of potassium and cesium, the situation is a bit easier as a wide range of cooling techniques has been demonstrated to work with these species and over time refined by many research groups. These techniques include magneto-optical traps (MOTs) [4], [53], [54], compression using light tuned to the D1 or D2 transition [31], [55], sub-Doppler cooling in gray optical molasses [56], [57], degenerate Raman sideband cooling [58]–[60] and evaporative cooling either in a magnetic or in an optical dipole trap. Such methods often represent the final stage of cooling, since they do not impose any obvious lower bound on the attainable temperature. Their efficiency has already enabled the achievement of quantum degeneracy with cesium atoms and with all stable isotopes of potassium [27], [33], [47], [61].

Although these cooling methods are well established for individual atomic species, it has to be emphasized that each experimental setup is different and the implementation of a given method is not always straightforward. Moreover, what performance can be obtained in the case of mixtures is much less predictable, as additional losses or interactions might hinder cooling with well-established methods developed in a

single-species scenario. Therefore, experiments aiming to simultaneously cool mixtures must account for the mutual influence of each cooling stage on individual species. For instance, gray molasses cooling of potassium cannot be effectively performed while cesium is being magnetically compressed, as molasses cooling efficiency strongly depends on the precise cancellation of any magnetic field that could be present in the setup.

Similar challenges arise in optical pumping and imaging. From the perspective of ultracold mixture experiments, a key question is how the procedures applied to one species affect the other, and whether it is possible to choose parameters such that the level of control over both species is maximized.

In this chapter, we present the cooling, optical pumping, and imaging techniques used in our experiment. We describe their operating principles, highlight key technical challenges, and discuss the results, with particular emphasis on their applicability to ultracold potassium–cesium mixtures. Selected experimental results for potassium and cesium are included to support the choice of the strategy of laser cooling, while a more detailed discussion of obtained parameters is provided in chapters 5, 6, 7. At the end of several sections, we include brief 'tutorials' on the application and optimization of the methods, based on the experience of the author.

In our experiment, we adopt a strategy in which each stage of the cooling sequence focuses on optimizing a specific parameter while preserving, as much as possible, the ones that have already been optimized. Furthermore, the choice of methods is partly constrained by the available optical components and laser systems, and their applicability in the case of potassium-potassium isotopic mixtures and potassium-cesium mixtures.

The atoms are initially captured in a magneto-optical trap (MOT), where the primary objective is to maximize the number of atoms. Discussion of the magneto-optical trapping principles is presented in section 3.1.

In the next stage, the atomic cloud is compressed by increasing the magnetic field gradient and adjusting the detuning of the MOT beams, in order to optimize atomic density. For potassium, we also introduce a method of compression using D2 and D1 line light simultaneously, which provides time that allows for switching between different lasers used for cooling. This transition time is necessary due to technical constraints in the system as presented in chapter 6. Further discussion is presented in section 3.2

Almost immediately after the compression of the cloud, atoms are cooled using gray optical molasses. This stage serves a dual purpose: to reduce the temperature of the atomic cloud and to facilitate efficient loading into the optical dipole trap. The theoretical background for optical molasses cooling, as well as experimental insight,

is presented in section 3.3.

At the final stage of cooling, we transfer atoms to the optical dipole trap, where spectroscopic measurements are performed. The operating principles of the dipole trap, along with a discussion of its relevance in cold atom physics, are presented in section 3.4.

The achievable results strongly depend on the population distribution among atomic and magnetic states; therefore, we describe the pumping methods between F and m_{F} states in section 3.5.

Throughout the experiment, we employ both absorption and fluorescence imaging techniques to characterize the atomic sample. These methods allow us to extract parameters such as temperature, density, or number of atoms. Additionally, we introduce several techniques to determine the distribution of atoms among magnetic sublevels. These diagnostic tools, and the methods used to extract from them the cloud properties, are presented in the final part of this chapter, namely in sections 3.6, 3.7.

To maintain clarity and logical coherence, each method is presented in the sequential order in which it appears during the experiment; initially, we detail the functioning of the magneto-optical trap.

3.1 Magneto-optical trapping

In experiments with ultracold neutral atoms, the magneto-optical trap (MOT) constitutes the first cooling stage at which one can meaningfully speak of "cold atoms". Regardless of whether the atoms originate from dispensers (as in our case) or from an atomic oven, and whether a two- or three-dimensional MOT is used, this technique enables the preparation of a localized and spatially confined atomic sample with a temperature typically not exceeding 10 mK. In some extreme cases - such as with lanthanide atoms - temperatures as low as 15 μK have been reported [62].

Although MOT operation was first demonstrated in 1987 [1], and its fundamentals have been discussed many times in the literature, we briefly summarize here its operating principles for the sake of completeness and consistency within this thesis [63]–[65].

In order to fully describe the cooling process in a magneto-optical trap (MOT), it should be noted first that the temperature of an atom is closely related to its velocity, according to equation $\frac{3}{2}k_BT = \frac{1}{2}m\langle v^2\rangle$, resulting from kinetic theory [43]. Thus, instead of discussing laser cooling in thermodynamic terms, it is possible to pose a simpler question - how to slow down atoms using laser light?

Atoms in the trap are slowed down by multiple cycles of photon absorption followed by spontaneous emission. For simplicity, let us assume an atom with mo-

mentum $\vec{p} = \{p_x, 0, 0\}$, and a counter-propagating resonant laser beam with a wave vector $\vec{k} = \{-k_x, 0, 0\}$. With each absorption, the atom gains momentum $\hbar\vec{k}$ opposite to its motion, that is, its momentum becomes $\vec{p} = \{p_x - \hbar k, 0, 0\}$. The excited atom will subsequently undergo spontaneous emission, randomly emitting a photon with momentum $\hbar\vec{k}'$, where $\vec{k}'$ is isotropically distributed.

Crucially, the absorption process is directional (anisotropic), whereas spontaneous emission is isotropic. Over many such cycles, the directional momentum kicks from absorption accumulate, while the momentum changes from spontaneous emission sum to zero. As a result, the net effect is a gradual reduction in the velocity of the atom and, therefore, its temperature. This process is illustrated in Fig. 3.1.

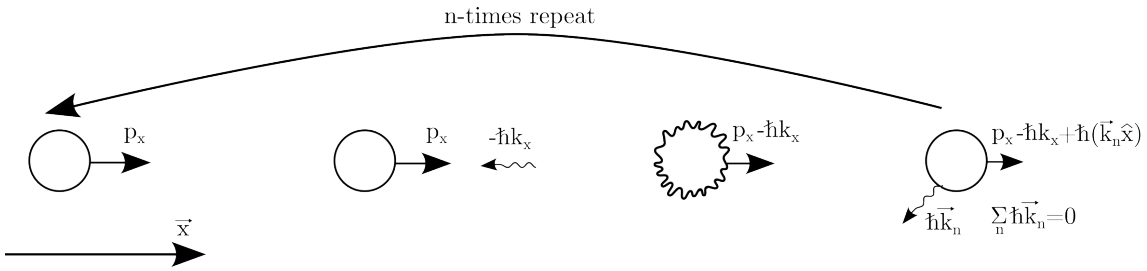

Figure 3.1: Laser cooling scheme. From left to right: an atom moving along the x-axis absorbs a counter-propagating photon, becomes excited, and subsequently emits a photon via spontaneous emission in a random direction.

However, this simplified cooling scheme does not account for several essential factors. For example, it assumes a perfect two-level cycling transition. In reality, atoms have complex internal structures, and a single-frequency laser beam is insufficient for efficient cooling. Let's assume, as an example, bosonic potassium atoms. If the cooling transition is ${}^2S_{1/2}, F = 2 \rightarrow^2 P_{3/2}, F = 3$, due to selection rules ($\Delta F = \{0, \pm 1\}$) the only possible decay channel for the excited atom is ${}^2P_{3/2}, F = 3 \rightarrow^2 S_{1/2}, F = 2$. However, atoms can be off-resonantly excited to the ${}^2P_{3/2}, F = 2$ level and from there a decay to ${}^2S_{1/2}, F = 1$ is possible, putting the population in the so-called 'dark state'- a Zeeman or a hyperfine level that does not interact with the cooling light. To avoid this, additional "repumping" lasers that bring the population back into the cooling cycle are required. For alkali atoms two frequencies are sufficient. In the case of cesium and potassium atoms, the 'cooling beam' drives the following transitions:

- ${}^2S_{1/2}, F = 4 \rightarrow {}^2P_{3/2}, F = 5$ (Cs),
- ${}^2S_{1/2}, F = 2 \rightarrow {}^2P_{3/2}, F = 3$ (^{39}K, ^{41}K),

- $^2S_{1/2}, F = 9/2 \rightarrow {}^2P_{3/2}, F = 11/2$ (^{40}K)

whereas the 'repumping beam' drives:

- $^2S_{1/2}, F = 3 \rightarrow {}^2P_{3/2}, F = 4$ (Cs),
- $^2S_{1/2}, F = 1 \rightarrow {}^2P_{3/2}, F = 2$ (^{39}K, ^{41}K),
- $^2S_{1/2}, F = 7/2 \rightarrow {}^2P_{3/2}, F = 9/2$ (^{40}K).

Importantly, the likelihood of the atom leaving the cooling cycle depends on the excited-state hyperfine splitting. In cesium and ^{40}K, where this splitting is large, the repumping beam can have a significantly lower intensity than the cooling beam, as off-resonant excitations have a low probability. In contrast, in bosonic potassium, the small excited-state splitting necessitates comparable intensities of both beams for the efficient cooling process.

The use of near-resonant light, as has been discussed above, is insufficient to create a Magneto-Optical *Trap* (MOT) because a mechanism to spatially localize or even confine the atomic cloud is also needed . This trapping process is essentially the same for all alkalis regardless of their quantum statistics; therefore, for clarity, we will focus on bosonic atoms.

The first mechanism contributing to the trapping process is velocity-selective cooling, which relies on red-detuning the laser frequency relative to the atomic transition (i.e. the energy of a cooling photon is lower than the energy of a corresponding transition). In this configuration, the Doppler effect shifts the atomic resonance closer to the laser frequency for atoms moving opposite to the propagation direction of the light. As a result, these atoms experience an increased probability of photon absorption, leading to a force that opposes their motion and slows them down. This mechanism produces a velocity-dependent force—often referred to as a friction-like or molasses force—which enables efficient cooling. In the presence of two counter-propagating beams, an atom that moves out of the central region is most likely pushed back toward it. However, this effect alone does not provide spatial confinement, as the force depends only on the atom's velocity and not on its position. Therefore, effective trapping requires an additional mechanism that introduces a position-dependent force.

The role of the Zeeman effect

As the name of the trap suggests, the presence of a magnetic field is essential for the operation of a MOT. Referring back to the atomic energy structure (see chapter 2), we

recall that in a magnetic field the hyperfine levels F split into magnetic sublevels m_{F}. It is sufficient to discuss the splitting using only the linear Zeeman effect (see Eq. 2.1). This can be done reliably, as the typical size of the cloud at this stage reaches not more than 1.5 cm, and the typical magnetic field gradient is smaller than 12 G/cm; therefore, in the case of both potassium and cesium atoms, in the area occupied by the cloud, the magnetic field is smaller than 18 G and the linear approximation still reliably reproduces the real shift of magnetic sublevels (see fig 2.1).

Let's now consider the one-dimensional cooling setup discussed previously, but with a magnetic field gradient applied along the x-axis. In this configuration, the magnetic field vanishes at the center of the trap and increases linearly with distance from the center. As a result, the magnetic sublevels become increasingly split as atoms move away from the center of the trap. This spatial variation in energy levels is the basis of the trapping mechanism.

If the cooling light is red-detuned from the $F \to F' + 1$ transition, it will become resonant with certain $m_{\mathrm{F}} \to m'_{\mathrm{F}}$ transitions at a specific distance from the trap center. Consequently, the absorption probability is highest at some distance from the center of the magnetic field $x = 0$, at position x_{res}, the atom absorbs a photon from a beam with a wavevector $\vec{k} = \{-k_x, 0, 0\}$ and is pushed back toward the center of the trap. However, due to the symmetry of the field, an atom located at $-x_{\mathrm{res}}$ would experience the same magnitude of Zeeman shift and would also absorb photons from the same beam, thus being pushed 'away' from the trap center.

To create an asymmetric scenario in which the probability of absorption of the photon is larger at x_{res} than at $-x_{\mathrm{res}}$, one can introduce circularly polarized light. Let's assume that the beam propagating in the direction of $-\vec{x}$ is right-hand circularly polarized in the beam frame, with a wavevector of $\vec{k} = \{-k_x, 0, 0\}$. Due to the quantization axis defined by the local magnetic field, this beam drives $\Delta m_F = -1$ (σ^-) transitions near x_{res}. At $-x_{\mathrm{res}}$, the same beam is only capable of driving $\Delta m_F = +1$ (σ^+) transitions, which are detuned from the resonance, and thus much less probable.

If the beam is retroreflected such that the polarization remains right-handed, but the wavevector becomes $\vec{k} = \{+k_x, 0, 0\}$, then the situation is reversed: atoms at $-x_{\mathrm{res}}$ will now preferentially absorb light and be pushed back toward the trap center. This spatially dependent scattering force provides a trapping effect in both directions, allowing the MOT to confine atoms around the zero of the magnetic field. A schematic illustration of this mechanism is shown in Fig. 3.2.

While the above description is limited to one spatial dimension, it is straightforward to generalize to two and three dimensions by arranging laser beams along Cartesian axes. The magnetic field gradient is typically generated by a single pair of

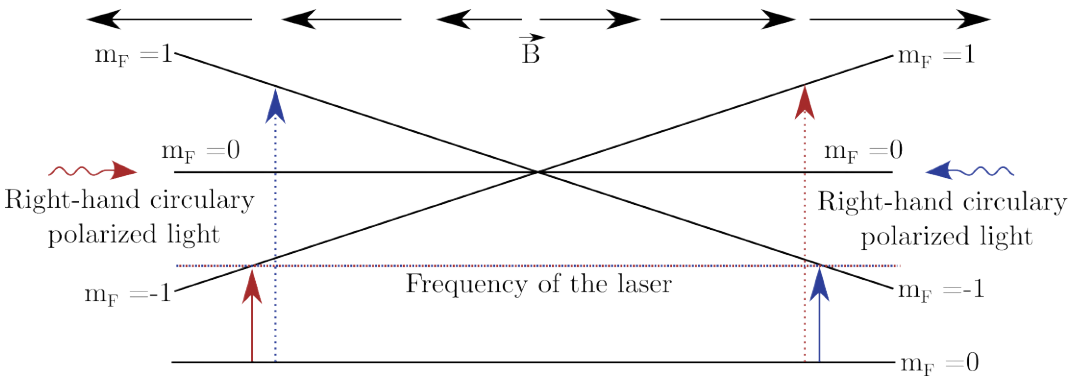

Figure 3.2: Magneto-optical trap scheme. The magnetic field strength, shown at the top of the figure, increases with distance from the trap center, leading to a shift in the energies of magnetic sublevels m_F. As a result, the laser beams from the left and right become resonant at different positions in space. The most probable absorption locations are indicated with solid vertical arrows, where the arrow color matches the color of the corresponding laser beam. Allowed transition for the beam on the other side of the magnetic field, are presented as dotted arrow.

anti-Helmholtz coils, resulting in a higher gradient along the coil axis compared to the transverse directions.

Of course, as is often the case with such 'graphical' considerations, the above discussion of laser cooling is a simplified model. In particular, it does not account for mechanisms that define the final temperature or the number of atoms that can be trapped. One fundamental limit can be easily introduced based on the discrete nature of momentum transfer during photon absorption. As the temperature of an atom approaches absolute zero, any further absorption event will impart momentum $\hbar k$ to the atom, thus increasing its velocity. This defines the so-called recoil temperature limit [66], which depends on the photon wave vector k and the atomic mass m, and is given by equation 3.1:

$$T_{\mathrm{r}} = \frac{\hbar^2 k^2}{2 m k_{\mathrm{B}}}, \tag{3.1}$$

where k_b is the Boltzmann constant. For potassium and cesium atoms, this limit is extremely low, on the order of $T_{\mathrm{r}} < 500$ nK [41], [42]. This is far below the typical temperatures achieved in a magneto-optical trap, and in practice, the recoil limit is only relevant in the context of sub-Doppler cooling methods discussed in the following chapters.

A more relevant limitation for standard cooling in magneto-optical trap arises

from the balance between cooling due to photon absorption and heating due to spontaneous emission. In the idealized description, spontaneous emission is assumed to be isotropic, resulting in a net momentum transfer that averages to zero. However, since the kinetic energy scales as $E \propto p^2$, the sum of spontaneous emissions leads to a non-negligible energy transfer - heating [66]. When the cooling rate due to absorption is equal to the heating rate from spontaneous emission, the system reaches the Doppler temperature limit given by 3.2:

$$T_{\mathrm{D}} = \frac{\hbar\Gamma}{2k_{\mathrm{B}}}, \tag{3.2}$$

where Γ is a natural linewidth of the cooling transition. For potassium and cesium atoms, this limit provides a more accurate estimate of the minimum achievable temperature using Doppler cooling alone, yielding $T_{\mathrm{D}} \approx 125$–$145$ μK for D2-line cooling in the case of both species [41], [42].

In our experiment, the temperature achieved at this stage for cesium atoms reaches $T_{\mathrm{Cs}} = 155$ μK, which is close to the Doppler limit. However, for potassium, the observed temperature depends on the isotope and for ^{41}K it typically does not go below $T_{^{41}\mathrm{K}} = 10$ mK. This significant deviation suggests the presence of additional heating mechanisms beyond the presented model.

In case of the atoms with small excited state hyperfine splitting like ^{39}K or ^{41}K, non-resonant scattering contributes significantly to the heating of the sample. In such cases, the concept of red detuning, as used in standard Doppler cooling, must be reconsidered. Let us discuss the example of the excited-state structure of the ^{39}K atom, as illustrated in Fig. 2.2. When the cooling beam is red-detuned relative to the $^2S_{1/2}, F = 2 \rightarrow {}^2P_{3/2}, F = 3$ transition, it remains close in frequency to other excited states, namely $^2P_{3/2}, F = 2$ and $F = 1$. Given the relatively large natural linewidth $\Gamma \approx 6.04$ MHz, these off-resonant transitions are still significantly excited. For a moderate detuning of $\Delta \leq 1.5\ \Gamma$, the scattering rate associated with the lower F states on the so-called 'blue side' becomes substantial, leading to increased heating. At such a small detuning, the effective trapping range is also reduced, which limits the size of the MOT.

To address this issue, a common approach is to detune the cooling beam below the entire excited-state manifold. Although this improves the selectivity of the cooled atoms, it comes at a cost: near the magnetic field minimum, the detuning is large even for the main cooling transition. This detuning leads to a significantly reduced scattering rate, thus decreasing cooling efficiency. Moreover, the probability of excitation to lower F states increases, further invalidating the two-level system (atom) approximation, which is more applicable in species with larger hyperfine splittings, such as cesium.

As a result of the small energy splitting between the excited states, the repumping beam must also be detuned below the entire manifold. It thus contributes significantly to the cooling process and must operate at an intensity comparable to that of the main cooling beam. Consequently, atoms in the MOT populate both hyperfine ground states, $^2S_{1/2}$, $F = 1$ and $F = 2$, with comparable probability.

All the effects discussed above are the fundamental reasons behind the limitations on the achievable temperatures in a magneto-optical trap (MOT) and they depend strongly on the separation of atomic energy levels. In the presented experimental system, the lowest temperatures reached at this stage are 155 μK for cesium (^{133}Cs), which has the largest excited state hyperfine splitting, 250 μK for fermionic potassium (^{40}K), and up to 2.5 mK and 10 mK for bosonic isotopes ^{39}K and ^{41}K, respectively.

Limits on the atom number in a MOT

In terms of cooling dynamics, the temperature of the atomic cloud eventually reaches a steady state, in which the cooling mechanisms are balanced by various heating processes. Similarly, there must exist processes that limit the total number of atoms that can be captured in a MOT. Typically, this number ranges from 10^5 to 10^9, set by specific loading and loss mechanisms at play, which will now be discussed [4], [53], [54].

A straightforward explanation for the limitation of the number of atoms is simply the availability of the atoms. In a vacuum system prepared for experiments with, for example, potassium or cesium, if the chamber has just been prepared, and laser beams and magnetic fields are activated, no trapping will occur if there are no atoms to capture. Although residual gases such as hydrogen, nitrogen, or oxygen, originating from outgassing, are still present, they are not trappable by the existing MOT.

This somewhat trivial example illustrates an essential limitation: the number of atoms available for trapping determines the maximum population in the trap. A practical illustration in our case is provided by the trapping of fermionic potassium. Since we use dispensers with natural isotopic composition as atom sources, only 0.012% of the emitted potassium atoms are ^{40}K [42]. Consequently, the number of fermionic potassium atoms that can be trapped is inherently low. In this context, we can define a loading rate R, which approximates the number of atoms loaded into the trap per unit of time under given vacuum conditions and is proportional to the background gas pressure of the trapped species [67].

At first glance, one might think that increasing the dispenser current to emit more

atoms would be advantageous. Indeed, doing so increases the number of trappable atoms, but also enhances the release of unwanted background atoms (e.g. from the contamination of the dispensers or simply other, more abundant potassium isotopes). These additional atoms are not efficiently cooled and contribute to an increased background of 'hot' gas. As a result, atoms in the MOT are subject to frequent collisions with background particles, which can expel them from the trapping region. The associated loss rate is characterized by the coefficient γ representing collisions with the background gas. Thus, increasing the dispenser current simultaneously increases both the loading rate R and the loss rate γ, which can lead to a balance between gains and losses, eventually resulting in a steady-state number of atoms [67].

However, there is another significant 'loss channel' that must be considered. In a dense MOT, ongoing photon scattering can result in a cooled atom absorbing a photon and then undergoing an inelastic collision with another atom in the ground state. Such two-body inelastic collisions can remove both atoms from the trap, and this process is characterized by a loss coefficient β. Notably, the loss rate due to this mechanism increases with both the number of atoms and the atomic density, introducing an additional limitation on the maximum trap population.

This gain and loss mechanism leads to a rate equation describing the time evolution of the number of trapped atoms [67]:

$$\dot{N}(t) = R - \gamma N(t) - \beta \bar{n} N(t), \tag{3.3}$$

where $\dot{N}(t)$ is the time derivative of the number of trapped atoms, $N(t)$ is the temporal number of atoms in the trap, and $\bar{n}$ is the mean density of atoms in the trap.

The situation becomes even more complex when dealing with mixtures of different atomic species. In such cases, an additional loss mechanism must be included in the model to account for the heteronuclear collisions. Here, the number of atoms of one species affects the dynamics and loss rate of the other, and the evolution of the atomic populations must be described by a system of coupled differential equations.

For atomic species A, the rate equation takes the form [68]:

$$\dot{N}_A(t) = R - \gamma N_A(t) - \beta \int_{V_A} n_A^2(\mathbf{r})\, d^3\mathbf{r} - \beta' \int_{V_A} n_A(\mathbf{r})\, n_B(\mathbf{r})\, d^3\mathbf{r}, \tag{3.4}$$

where $N_A(t)$ is the number of atoms of species A at time t, $n_A(\mathbf{r})$ and $n_B(\mathbf{r})$ are the densities of species A and B, respectively, and the integrals are taken over the volume occupied by species A. The coefficients β and β' represent the two-body intraspecies and interspecies loss rates, respectively.

An exemplary set of measured loading curves, together with fitted theoretical models based on the equations discussed above, is presented in Fig. 3.3. The figure displays three experimental datasets: the light blue curve shows the measured evolution of the number of ^{39}K atoms in the MOT as a function of time, while the black and red curves correspond to the measured loading dynamics of fermionic potassium ^{40}K in the absence and presence of ^{39}K, respectively.

From this plot, one can clearly observe that the maximum number of ^{40}K atoms is reduced in the heteronuclear case. This reduction can be attributed to the additional interspecies collision term included in Eq. 3.4. A more detailed discussion and analysis of MOT dynamics in the context of our experimental system can be found in the doctoral dissertation of J. Dobosz [69].

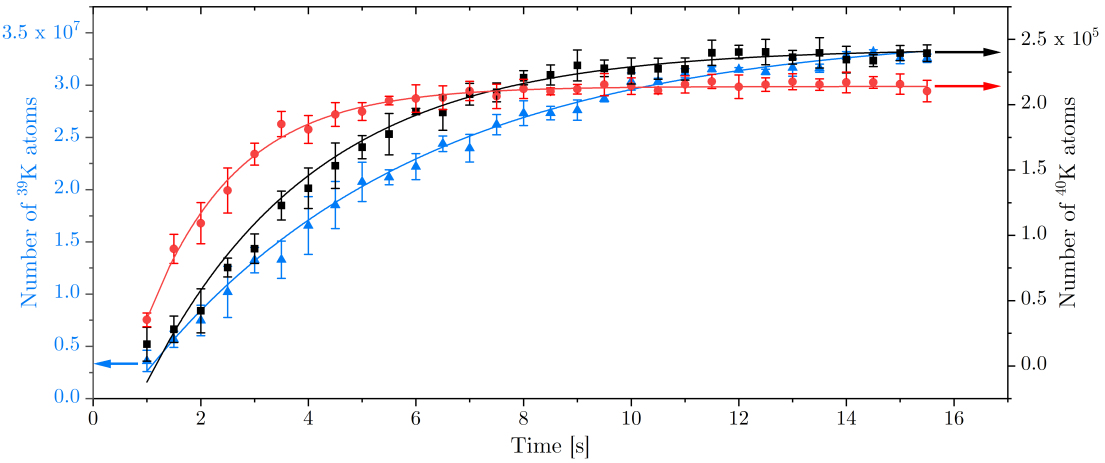

Figure 3.3: Magneto-optical trap loading curves of only ^{39}K (blue triangles), of ^{40}K atoms in the presence of ^{39}K (red circles) and of ^{40}K only (black squares), with fitted curves resulting from Eq. 3.3, 3.4.

Practical insights into MOT operation

In addition to the theoretical aspects of laser cooling already presented, we would like to discuss several practical considerations related to the operation and optimization of a magneto-optical trap (MOT). A significant part of the author's work was devoted to developing and maintaining the MOT system. Based on this experience, we would like to share several practical insights.

For the methods discussed here, it is highly beneficial to continuously monitor a fluorescence from the atoms using a camera. This real-time feedback allows one to

quickly assess the performance of the system during alignment and optimization.

A good starting point, although perhaps obvious, is to choose the laser beam parameters based on established values found in the literature. It might be that, for example, the maximum available optical power is lower than the reference value; it is advisable then to tune the laser's frequency closer to resonance in order to compensate for the reduced scattering rate. This recommendation applies particularly to the initial stage of optimizing the setup, when no fluorescence from the cold atoms is yet visible.

The second step concerns the magnetic field gradient. Initially, it can be advantageous to apply a gradient two to three times higher than the value typically recommended in the literature. While this increases two-body collisional losses and reduces the trap size, it can significantly improve visibility when loading a small number of atoms. It is especially important when the MOT beams are not yet properly aligned (e.g., they intersect at suboptimal angles or do not cross and overlap at the center of the magnetic field).

If no atomic cloud is observed in this configuration and only a small number of atoms is expected, the reverse strategy may prove helpful: the MOT can be initially loaded at a low or moderate magnetic field gradient to increase the number of trapped atoms, and the gradient is then suddenly increased after a fixed delay. In such a scenario, the atomic cloud may remain invisible during the loading phase but can become detectable through a fluorescence flash triggered by the sudden compression. Using this technique, we were able to observe laser cooled ^{40}K atoms for the first time in our setup.

Figure 3.4 shows an example of fluorescence images obtained using a simple CCD camera (*Conrad Electronic Fingerkamera DV-1910B*). In this sequence of photos, the atomic cloud is not visible during the initial loading phase (left panel). Then, the magnetic field gradient is quickly increased from 11 G/cm to 40 G/cm along the stronger axis. This causes the cloud to appear due to the increased atomic density (see middle panel). In the third panel, taken 100 ms later, the cloud is barely visible, as enhanced density increases the collision rate which dominates and results in atom loss leading to the dilution of the sample.

Of course, detecting *some* fluorescence is only the first step. Further optimization is necessary to prepare the sample for future experiments. Throughout this thesis, we use a simple diagnostic method to determine whether the MOT beams or mirrors need readjustment: we observe how the atomic cloud evolves as a function of the magnetic field gradient. With properly aligned MOT beams and the atomic cloud located at the magnetic field center, the reduction of the gradient should lead to a gradual expansion of the cloud, which should nonetheless remain trapped. If,

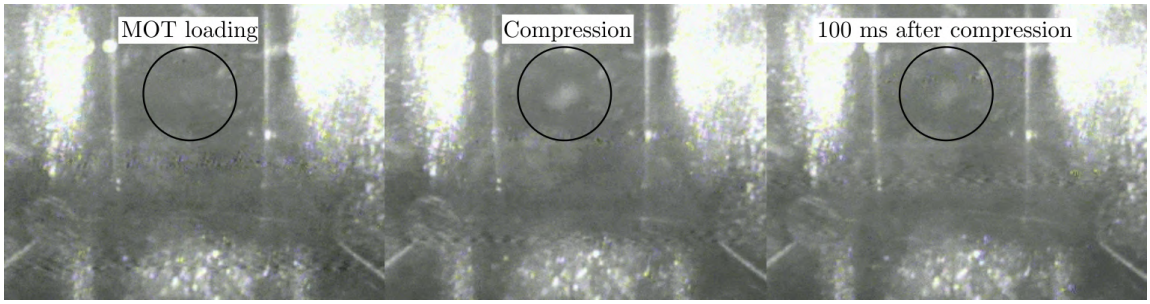

Figure 3.4: Three frames from a video recorded during the loading of the ^{40}K MOT. The left panel shows the interior of the vacuum chamber during the initial loading phase, where no atomic cloud is visible. The middle panel corresponds to the moment of magnetic compression, during which the atomic cloud becomes visible due to increased density. The right panel shows the cloud 100 ms later, where it begins to disappear as a result of enhanced collisional losses. In each panel, a circle indicates the region where fluorescence from the atomic cloud is (or should be) observed.

however, the beam intensity balance (easy to verify with a power meter) or spatial overlap are suboptimal, the cloud may shift off-center or disappear entirely. In our experiments, the typical gradient along the strongest MOT axis 11–15 G/cm. However, in a well-aligned configuration, the atomic cloud remains visible even at a gradient as low as 1 G/cm. Example fluorescence images showing the evolution of the ^{133}Cs cloud for decreasing magnetic field gradients for both properly (top) and improperly (bottom) aligned MOTs are shown in Fig. 3.5.

These methods allow us to achieve a 'good' magneto-optical trap. It is important to emphasize that, in the context of our experimental goals, 'good' refers specifically to maximizing the number of trapped atoms. At this stage, we are not concerned with optimizing the temperature or the density, as these parameters will be addressed in subsequent stages of the experiment, where the focus shifts to maximizing the atomic density, minimizing the temperature, and improving the transfer efficiency to the optical dipole trap. The results obtained for the single-species and mixtures cooling at this stage are presented in chapters 5, 6, 7.

3.2 Compressed Magneto-Optical trap

Considering the MOT loading equations (see Eqs. 3.3, 3.4), one can explore strategies to minimize loss coefficients. In both single- and multi-species MOTs, the first loss term depends on the background gas pressure (which we cannot influence at this

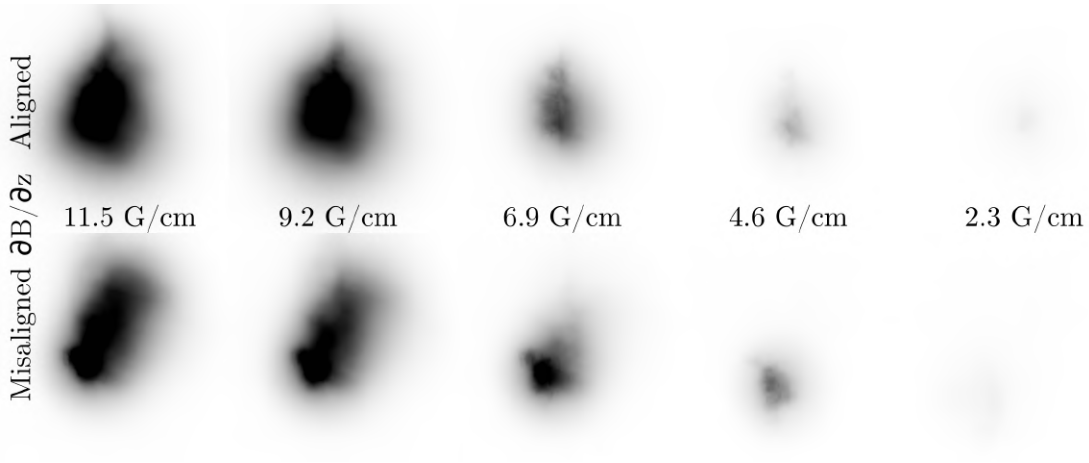

Figure 3.5: Fluorescence images of cesium atoms for different magnetic field gradients. The top row shows the evolution for a well-aligned MOT, while the bottom row corresponds to a misaligned configuration. As the magnetic field gradient decreases, the atomic cloud in the top row stays almost in its original position, whereas in the bottom row it drifts away from the field center.

stage). Subsequent loss terms are governed by two-body loss coefficients, which depend on the molecular interaction potentials. It makes them species-specific and generally fixed for a given experimental setup. However, these losses also depend on the density of the atoms in the sample. To maximize the total number of atoms, it is therefore advantageous to keep the cloud density low during the loading stage. The simplest way to achieve this is by reducing the magnetic field gradient, which results in a larger cloud volume and lower density, while a high loading rate may still be maintained.

This approach, however, leads to inefficient transfer into optical dipole traps, whose typical dimensions are below 0.3 mm. In such cases, the overlap between a diffuse and diluted MOT cloud and the tightly focused optical trap is poor, reducing transfer efficiency. A more effective strategy is thus to load a dilute MOT for an extended period and then rapidly compress the cloud—this is the so-called compressed MOT (CMOT) stage. This method allows maintaining a high number of atoms while temporarily increasing the density, which should allow for efficient transfer to further cooling stages.

Compression is typically realized by increasing the magnetic field gradient and detuning the MOT beams further to the red, sometimes accompanied by a reduction in the cooling beam intensity. The steeper magnetic field results in a stronger

confinement, reducing the cloud volume and increasing the density [70].

If the magnetic field gradient is increased instantaneously (here, below 1 ms) without simultaneous adjustment of the laser beams parameters, a significant fraction of atoms can be lost. The region of maximum light absorption shifts toward the trap center, reducing the effective MOT capture area. Additionally, atoms in low-field-seeking states, such as ^{39}K in the $^2S_{1/2}$ $F = 1$, $m_F = 1$ state, may experience a strong magnetic force pushing them out of the trap if they remain in the outer regions of the MOT during compression. Notably, for this state, the sign of the Zeeman shift reverses at $B \approx 100$ G, making it high-field-seeker beyond that point. With our system's maximum gradient of $\partial B/\partial z \approx 115.2$ G/cm, this transition occurs at a distance of approximately 0.87 cm from the field center, which is smaller than the MOT cloud size achievable at this stage (over 1.5 cm).

A more favorable approach is to ramp up the magnetic field slowly, allowing atoms to follow the changing potential toward the trap center. In our system, we find that a ramp duration of approximately 2 ms—with the gradient increasing from $\partial B/\partial z \approx 7$–15 G/cm to $\partial B/\partial z \approx 35$–115 G/cm, depending on the atomic species or mixture, yields optimal results (see Section 7). Although this ramp time may seem short, it is long compared to the excited-state lifetime ($\sim$30 ns), allowing for many absorption and spontaneous emission cycles to occur during the compression phase.

Knowing the optimal time for the magnetic field to rise, it leads us to the next important question: what is the optimal duration of the compressed stage? This stage must be short enough to avoid non-adiabatic losses. At the same time, it must be long enough to allow the atoms to reach the area near the center of the trap. The longer this stage is, the bigger the impact of density-dependent losses, particularly two- and three-body collisions. Finding a trade-off becomes especially relevant when working with mixtures, where one species significantly outnumbers the other.

As an example, in our analysis of the ^{39}K–^{40}K mixture cooling (see Section 6), the number of atoms of the bosonic isotope exceeds that of the fermionic one by two orders of magnitude. In such a case, it is crucial to assess whether the high density of the majority species leads to excessive losses in the minority component. In particular, from the perspective of subsequent cooling procedures, the loss of a significant fraction of the less abundant isotope may hinder efficient cooling or compromise the accuracy of cloud parameter measurements.

To illustrate this point, we refer to Fig. 3.6 (discussed also in section 6). The figure shows the evolution of the number of atoms and their density during the compression phase. Blue triangles represent ^{39}K atoms, while black squares and red circles correspond to ^{40}K atoms in the single-species and mixture configurations, respectively. The left panel displays the time evolution of the number of atoms, and

the right panel shows the corresponding evolution of the density.

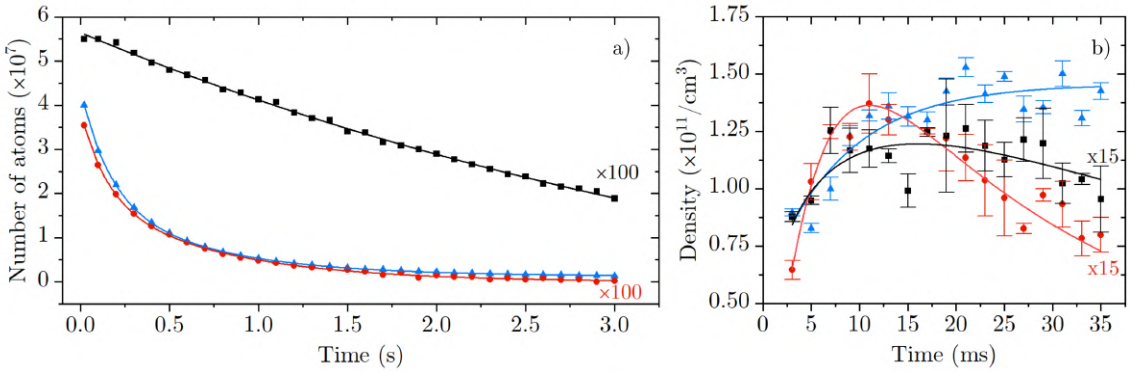

Figure 3.6: Time evolution of the number of atoms (left panel) and peak density (right panel) for ^{39}K (blue triangles) and ^{40}K in the single-species (black squares) and in the mixture with ^{39}K (red circles) configurations.

As shown, the initially dilute fermionic ^{40}K cloud starts to follow the loss profile of the more abundant bosonic ^{39}K cloud. The density of ^{40}K increases rapidly, reaching a peak after which two-body losses dominate, leading to a reduction in both the density and the number of atoms. This highlights the need for optimizing compression time, which in our experiments is found to be 10–20 ms, depending on the mixture.

The increase of the density leads to heating, a commonly discussed trade-off in cold atom experiments. Several mechanisms contribute to this effect:

- **Adiabatic Heating:** If the compression is fast, the work done on the gas increases its internal energy. In analogy to an ideal gas, the process follows the relation $TV^{\gamma-1} = const$, with γ denoting the adiabatic index.
- **Radiative Heating:** Increased density raises the likelihood that photons emitted via spontaneous emission are reabsorbed by nearby atoms, leading to excess heating [71].
- **Loss-induced Heating:** Two-body losses preferentially occur in the trap center where the density is the highest and atoms are the coldest. The loss of these coldest atoms increases the average temperature of the remaining sample [72].

All of these mechanisms contribute to heating during compression. Detailed quantitative results for all investigated species and mixtures are presented in Section 7. As

an example, for ^{39}K, the density increases from 2×10^{10} cm^{-3} to 1.2×10^{12} cm^{-3} in the optimized scenario, while the temperature rises from 2.5 mK to 11 mK. Importantly, the number of atoms after the optimal compression decreases by no more than 20% across all studied species and mixtures. The remaining number of atoms is still sufficiently high to allow for further efficient cooling; however, the elevated temperatures imply that any delay before the next cooling stage may lead to significant cloud dilution. This issue is species-dependent: in the case of cesium, the temperature reached after compression is still quite low and the subsequent gray optical molasses cooling stage requires only turning off the magnetic field (in approximately 300 μs) and switching an acousto-optic modulator (in less than 1 μs), which is negligible on the relevant timescales. Potassium becomes significantly hotter than cesium after compression. For further cooling, technical aspects of the potassium laser system require switching from the D2 to the D1 transition using mechanical shutters, which introduces a non-negligible 2.6 ms delay—comprising 1 ms of shutter closing/opening time and 1.6 ms of jitter. This gives the cloud quite a lot of time to expand and leads to the observable dilution of the sample.

To mitigate this, we modified a D2D1-CMOT method [31], [73] to adapt it to the specific features of our laser system. At the end of the compression, we open the D1 line shutter, thereby introducing light tuned to the D1 transition into the system. For the isotopes to which this method is applied (^{39}K and ^{41}K), 0.5 ms after triggering the D1 shutter, we initiate the closing of the D2 shutter. In this configuration, the D1 light intensity is ramped up in 1 ms and for 0.5 ms both D1 and D2 lights are simultaneously present in the system. For the next 1 ms, the D2 light is ramped down until it is completely turned off. The current laser system (more detailed discussion in chapter 6) does not allow for independent control of the intensity or frequency of the D2 and D1 line lights. Therefore, unlike in the methods described in the literature, we are unable to selectively address the cooling transition on the D1 line and the repumping transition on the D2 line. Consequently, our implementation cannot reach the same low temperatures reported in previous works, which benefit from the large D1 hyperfine splitting [31], [73]. Nevertheless, it allows us to preserve both the number of atoms and the density of the sample prior to initiating gray molasses cooling.

3.3 Gray molasses cooling

The compression stage could already end the sample preparation stage if our goals were, for example, to perform a homo-. or heteronuclear photoassociation, which can be efficiently implemented at this point [74]. Furthermore, with the cloud parameters

obtained for cesium, an optical dipole trap could already be loaded, enabling efficient atom transfer to a relatively deep trapping potential. Unfortunately, in the case of potassium atoms—especially bosonic isotopes—the temperatures achieved at this stage are too high for the efficient transfer. Therefore, we introduce an additional stage of optical molasses, whose goal is to reduce the temperature of both potassium and cesium atoms and facilitate efficient loading into the optical dipole trap.

Optical molasses cooling was first observed in the 1980s. However, the physical mechanism behind it was not fully understood at the time. As early as 1988, when optical molasses were applied to sodium atoms, the authors reported a temperature of $T = 43$ μK and noted: "Surprisingly, this strongly violates the generally accepted theory of Doppler cooling which predicts a limit of 240 μK," highlighting both their surprise and the lack of a theoretical explanation at the time [75]. The explanation followed a year later, when Claude Cohen-Tannoudji and Jean Dalibard introduced a theoretical model that ultimately contributed to Cohen-Tannoudji receiving the Nobel Prize in Physics [76]. Since then, sub-Doppler cooling techniques have been developed and successfully applied to a wide range of atomic species, including sodium, rubidium, potassium, and cesium [73], [77]–[79].

Here, we present the main mechanisms underlying various types of optical molasses and discuss their roles in the context of our experiment.

Cooling in gray molasses is based on the Sisyphus effect. The name is not accidental—the process is analogous to the mythological fate of Sisyphus, who was condemned to eternal torment: endlessly pushing a boulder uphill, only to have it roll back down each time he neared the top of the mountain.

The Sisyphus effect operates in an analogous manner. Consider a two-level atom with a ground state $|g\rangle$ and an excited state $|e\rangle$ illuminated by a pair of counter-propagating laser beams. If the energy of the ground state varies with position, one can choose beam parameters such that the probability of excitation is highest when the atom is near the peak of this spatial modulation. Upon spontaneous emission, the atom typically returns to the ground state at a lower potential energy. From the atom's perspective, its motion resembles that of Sisyphus pushing a rock uphill: each time it reaches an area near the top of the potential hill, it is returned to the valley. If excitation tends to occur when the atom is at higher potential energy and spontaneous decay is position-independent, then over many absorption–emission cycles, the atom loses kinetic energy, resulting in cooling. This process is schematically illustrated in Fig. 3.7.

But how can such spatial modulation of the ground-state light shift be achieved? We will start with a simplified one-dimensional model—the extension to three dimensions is straightforward because the cooling axes are almost decoupled.

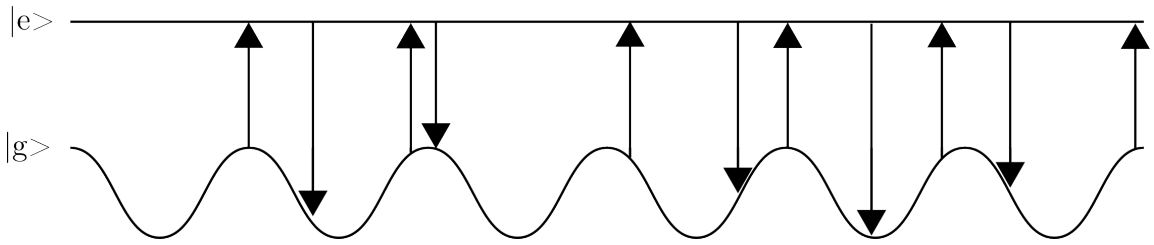

Figure 3.7: Schematic illustration of Sisyphus cooling. The energy of the ground state $|g\rangle$ is periodically modulated due to the presence of counterpropagating laser beams. The laser is blue-detuned from the transition in such a way that the highest probability of excitation occurs when the atom is near the top of the potential hill, i.e., when its energy is the highest. The atom is then excited to the state $|e\rangle$ via photon absorption. After a short time, it decays back to the ground state via spontaneous emission, losing kinetic energy in the process. Cooling occurs because excitation predominantly happens at points of maximum ground-state energy, while spontaneous emission is equally probable regardless of the position.

Consider two counter-propagating laser beams with orthogonal linear polarizations ($lin \perp lin$ configuration).Their superposition forms a standing wave whose polarization varies along z in the sequence circular σ^+- linear- circular σ^-- linear rotated by 90°, repeating every half-wavelength $\lambda/2$. As a result, the AC-Stark shifts of the magnetic sub-levels m_{F} oscillate in space, producing the periodic potential required for Sisyphus cooling as presented in Fig.3.8, taken from [76].

If instead the beams have opposite circular polarizations σ^+ and σ^- ($\sigma^+\sigma^-$ configuration), the field is linearly polarized everywhere, but its axis rotates smoothly along z, completing one full turn over the distance λ.This "corkscrew" polarization does not generate position-dependent light shifts of the m_{F} sub-levels as presented in Fig.3.8, from [76].

Spatial oscillations of polarization and intensity in such cases lead to position-dependent energy shifts of superpositions of m_{F} sub-levels within a single hyperfine manifold F through the AC-Stark interaction. In some cases, the different polarizability of individual sub-levels further enhances this effect, enabling efficient Sisyphus cooling [56], [77].

To further enhance the cooling efficiency, one can consider the presence of two ground-state sublevels: the so-called dark state $|g_1\rangle$, which does not interact with the light field, and the bright state $|g_2\rangle$, which is coupled to the excited state $|e\rangle$ and experiences spatially modulated energy shifts. The cooling process again relies on the Sisyphus mechanism: atoms in the bright state climb a potential hill, get excited

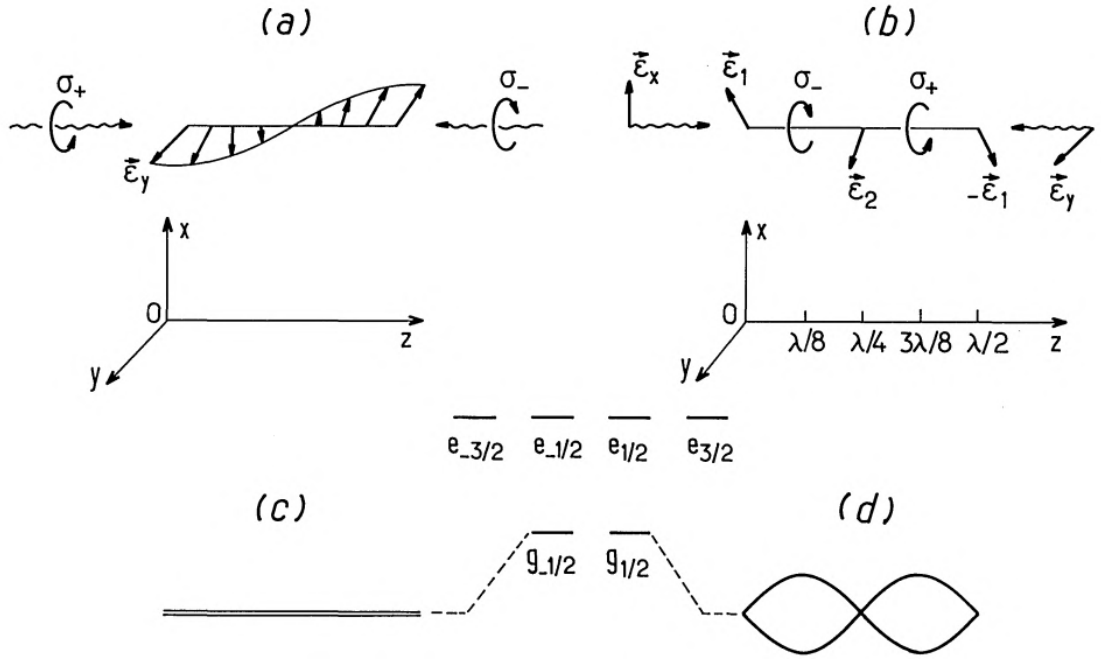

Figure 3.8: Schematic illustration of light field generated by two counterpropagating beams with orthogonal circular (a) and linear (b) polarizations, and respective shift of magnetic sublevels for emerging 'corkscrew'-like polarization (c), and oscillating linear-circular case (d). The figure taken from [76].

to the state $|e\rangle$, and subsequently decay.

In this configuration, however, spontaneous emission can move atoms not only back to the bright state $|g_2\rangle$ but also to the dark state $|g_1\rangle$. Since the dark state is decoupled from the light field, atoms remain trapped in it unless they are transferred back to $|g_2\rangle$. This repumping process is most efficient in regions where the bright and dark states are energetically close—that is, where the light shift of $|g_2\rangle$ is minimal [56].

As a result, atoms preferentially re-enter the bright state at the bottom of the potential hill, which further enhances the cooling effect. This configuration—relying on population redistribution between bright and dark ground states—is characteristic of gray optical molasses cooling (gray = superposition of bright and dark). This process is schematically presented in the Fig. 3.9.

In our system, gray optical molasses are used for cooling cesium atoms. The cooling beam is detuned by 6Γ from the ${}^2S_{1/2}, F = 4 \rightarrow {}^2P_{3/2}, F' = 4$ transition, creating position-dependent bright and dark m_F states. However, after excitation, there is a non-zero probability that the atom decays to the $F = 3$ ground state via

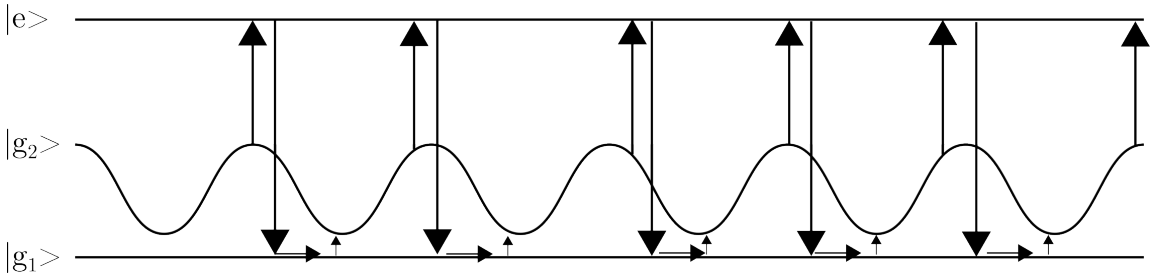

Figure 3.9: Schematic illustration of gray optical molasses cooling. The energy of the ground state $|g_2\rangle$ is periodically modulated, enabling Sisyphus cooling. A key difference arises during the spontaneous emission stage: the atom decays to a non-modulated ground state $|g_1\rangle$, from which it is coupled back to the modulated $|g_2\rangle$ state, repeating the cycle. As a result, the overall energy loss per cycle is greater than in standard Sisyphus cooling.

spontaneous emission. To prevent population accumulation in this hyperfine level, a resonant repumping beam addressing the ${}^2S_{1/2}, F = 3 \rightarrow {}^2P_{3/2}, F' = 3$ transition is employed to continuously return atoms to the cooling cycle.

This method is impressively efficient: it reduces the atomic temperature from 200 μK to 23 μK within 8 ms, while retaining approximately 75% of the initial number of atoms. The high effectiveness of this scheme results from the large excited state hyperfine splitting in cesium. For potassium atoms, a similar cooling approach using the D2 line is possible but significantly less efficient due to smaller excited-state splittings [80]. Therefore, in our setup, we implement gray molasses on the D1 line, where the separation of the excited-state hyperfine levels is larger than for the D2 line.

One can construct a laser cooling system such that the cooling and the repumping beams are phase coherent (as is the case in our potassium laser system) which could be utilized to create a coherent superposition of the ground states. This enables excitation of Raman transitions, giving rise to the so-called λ-enhanced gray molasses cooling mechanism [81]. In this configuration, two laser frequencies are used, with a frequency difference matching the ground-state hyperfine splitting of the atom. Both beams are globally detuned to the blue side of the optical transition, and this detuning can reach even up to 6Γ.

In our case, this method is applied to all naturally occurring potassium isotopes and the cooling takes place using the D1 line. Regardless of the initial temperature or isotope, we achieve final temperatures of $T = 8 - 15$ μK within 5–10 ms. This result is particularly notable in terms of efficiency, especially for the ^{41}K isotope,

which reaches this temperature starting from values much higher than $T = 10$ mK reached directly after the compression stage.

A natural question arises: what fundamentally limits the cooling efficiency of gray molasses, both in the standard configuration and in its Λ-enhanced variant? In our opinion, that is strongly supported by the existing literature, the principal limiting factor is the high density of the atoms at this stage. During the early development of optical molasses techniques for alkali atoms such as cesium, it was already observed that the limit for the achievable temperatures decreases with density [79].

Although Λ-enhanced configuration of the gray molasses strongly suppresses spontaneous-emission events through Raman transitions, residual excitations and subsequent spontaneous decays still occur. In the standard (not enhanced) scheme, such decays are even more frequent. In a dense cloud, a spontaneously emitted photon is therefore likely to be reabsorbed by a neighboring atom, which transfers recoil energy and ultimately heats the sample.

A second limitation is purely experimental. For gray molasses to operate efficiently, the cooling beams must be well overlapped to produce a spatially varying light shift, and their polarizations must be precisely controlled. Both conditions are challenging to fulfill in a real experimental setup, particularly because one has no direct access to the polarization state or overlap quality of the beams inside the vacuum chamber.

Moreover, to generate a corkscrew-like, or 'oscillating' polarization in the overlapping region, the incident and retro-reflected beams must ideally have equal power. Such balance is difficult to achieve in practice. In our setup, it is impossible due to the use of retro-reflected beams and uncoated surfaces of the main chamber glass cell. The incoming beam travels through the glass cell, lenses, waveplates, and mirrors, and the returning beam passes through the same elements again, suffering non-negligible optical losses that lead to power imbalance.

Another major factor that limits cooling efficiency in many experiments is the presence of stray magnetic fields. Gray molasses are highly sensitive to residual magnetic fields, which induce Zeeman shifts between m_F states and reduce cooling efficiency. In Ref. [82], we showed that the achievable temperature in gray molasses for ^{39}K atoms scales with the magnetic field as $T \sim 225(10)B^2$, where the temperature T is in given microkelvin and B is the magnetic field given in gauss. Therefore, in the presence of the Earth's magnetic field of approximately 0.505 G (as expected for the laboratory in Warsaw [83]), the minimum achievable temperature without magnetic field compensation is estimated to be around 56 μK.

A major advantage of gray optical molasses is the ease of implementation in the case of atomic mixtures. As described in the previous sections, gray molasses are

typically operated near the D1 or D2 transition of the cooled species. Consequently, the cooling light for one species has a negligible effect on other atoms in the mixture. For example, for potassium, the cooling light close to the D1 transition ($\lambda = 770$ nm) is detuned from the cesium D2 line transitions by more than 80 nm, so the probability of off-resonant excitation is extremely small. While off-resonant dipole interactions with other species are always possible, gray molasses typically employ large beams with low intensity, resulting in negligible dipole trapping/anti-trapping potentials for the atoms.

Moreover, as previously discussed, the efficiency of gray molasses cooling depends strongly on magnetic field compensation. However, this is a general requirement, regardless of the atomic species involved. Therefore, in multispecies experiments, the need to minimize residual magnetic fields benefits all species simultaneously. This is particularly important as many sub-Doppler cooling techniques—such as degenerate Raman sideband cooling (dRSC)—are difficult to implement in atomic mixtures. The dRSC requires the creation of an optical lattice and the magnetic field has to be applied to ensure degeneracy between successive vibrational states in the lattice and magnetic sub-levels of an atom [59], [60]. For different species, with different lattice potentials and magnetic moments, identifying common parameters that enable simultaneous cooling is significantly more complex than in the case of gray molasses.

Another possible cooling strategy involves initial loading into a magnetic trap, followed by evaporative cooling and subsequent transfer to an optical dipole trap—or in some cases, direct transfer without evaporation. However, in mixtures, this approach can be limited by enhanced three-body losses, especially if such losses occur with a high probability. For instance, potassium can be efficiently evaporated to quantum degeneracy in an optical dipole trap [61] but cesium does not evaporate efficiently due to its large three-body loss coefficient at zero magnetic field, being on the order of 10^{-24} cm^{-6}/s^{-1} (for $F = 3, m_F = 3$ state). This is five orders of magnitude higher than in potassium-41 (for $F = 1, m_F = 1$ state) [45], [61]. In mixtures of potassium-41 and cesium, the presence of the latter can hinder the evaporation of the former by introducing heteronuclear collisional losses, which are increasing with the density, therefore leading to anti-evaporation due to the selective removal of the coldest atoms from the trap.

Although many experimental groups address this challenge by preparing the two components of the mixture sequentially, using species-specific cooling stages [84], gray optical molasses greatly simplifies the process by enabling simultaneous and efficient cooling of both types of atoms in the mixture. In our case, we do not observe large differences at this stage if potassium and cesium are cooled in a single-species scenario

or simultaneously.

Cooling in gray molasses is highly efficient and allows one to reach temperatures significantly below the Doppler limit. This aligns well with the strategy outlined at the beginning of this chapter, namely to optimize one parameter at a time. Further cooling typically takes place in either an optical dipole trap or a magnetic trap, depending on the collisional properties of the cooled atom. In our case, it was quite obvious that efficient evaporative cooling would require tuning the interactions because of the very high three-body loss coefficient of cesium—thus motivating the use of an optical dipole trap.

Evaporation in an optical dipole trap is an extremely effective cooling technique; however, one major drawback is that typically only a small fraction of atoms can be transferred from the cloud cooled using methods discussed so far. Depending on the transfer method, as well as the parameters of the atomic cloud and the trap itself, the transfer efficiency usually ranges from 2% to 12%, with values more often found at the lower end of this range [55], [85].

Gray molasses are particularly well suited for transferring atoms into an optical dipole trap, as they are— by design— optical molasses. The term "molasses" refers to the viscous force they exert on atoms, which for an atom moving with velocity $\vec{v}$ takes the form $\vec{F} = -\alpha\vec{v}$, where α is the viscosity coefficient. This means that if an atom attempts to escape the trap region, e.g. due to gravitational potential, it will effectively decelerate and remain close to its original position. In our setup, with properly chosen trapping parameters (see Section 6, 7), the atomic cloud can be held in optical molassess for more than 1 s, which is promising in terms of more efficient transfer to the optical dipole trap. Of course, during the molasses stage, losses are still present; therefore, optimal transfer time is much lower than 1 s, as presented in section 7. At the same time, the cloud expands throughout the optical molasses region, significantly complicating the determination of its temperature and density. An example of the atomic cloud at the beginning of the cooling process and at several subsequent times during the molasses trapping stage is shown in Fig. 3.10.

Practical aspects of gray molassess cooling

At the end of this chapter, we would like to describe several practical aspects of preparing a system for cooling in gray optical molasses, including remarks on what we consider to be an effective procedure, based on authors' own experience. Naturally, this discussion assumes that the laser system has already been set up and the beams have been initially aligned and are ready for the cooling procedure.

A good first step is to minimize the residual magnetic field as much as possible. As

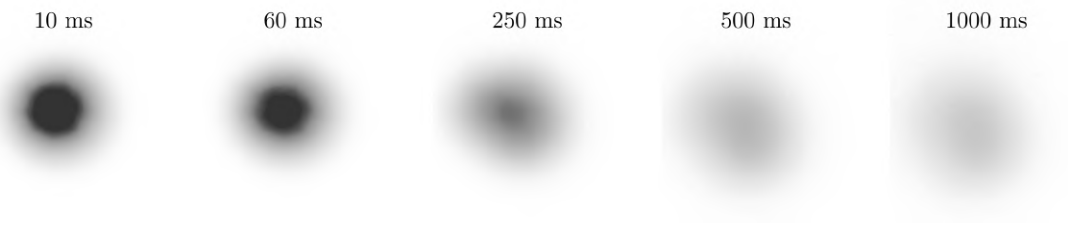

Figure 3.10: The cloud of ^{39}K atoms at various times during the gray optical molasses cooling.

discussed earlier in this chapter, the presence of a magnetic field significantly reduces the efficiency of sub-Doppler cooling. While this can be done using professional magnetic field meters, smartphone applications are often sufficiently accurate for this purpose if the device has a Hall sensor. Any reduction of the magnetic field is beneficial at this stage. The smartphone can be used to determine the direction of the field and amplitude, after which magnetic field coils should be adjusted to generate a compensating field of equal magnitude but opposite direction.

Once the magnetic field is minimized, the procedure for implementing gray molasses depends strongly on whether a Λ-enhanced configuration is used or not. In the case of standard (non-Λ-enhanced) configuration, a repumping beam is typically applied, tuned to one of the available transitions between the lower hyperfine ground state and an excited state. The appropriate frequency should already be known at this stage of the development of the experiment. If not, it is advisable to take fluorescence images and measure the brightness of the cloud as a function of the frequency of the repumping beam while keeping the frequency of the cooling beam fixed (e.g. at the value used for the MOT operation). This enables the identification of the frequencies at which the fluorescence signal is the strongest, thus facilitating the detection of the transition and the selection of the optimal repumper frequency.

Once the repumping beam frequency is determined, the next step is to identify the cooling beam frequency and the range over which it can be scanned. Using the maximum available power, scanning the cooling frequency should reveal a region where a (yet) 'suboptimal' optical molasses effect becomes visible.

To confirm whether gray molasses cooling operates, a helpful strategy is to first determine, during an earlier stage of the experiment (e.g., CMOT), the time t after which the atom cloud disappears due to free expansion. Then, set the duration of the gray molasses stage to t, omitting any subsequent free fall, and monitor at which cooling frequencies the atomic cloud remains visible. Optimizing the number of atoms in this regime allows one to identify frequencies where cooling occurs. If cooling

is effective, a viscous force should be present and prevent rapid cloud expansion, maintaining its localization.

If instead the cloud is dispersed during the molasses phase, the most likely cause is excessive power of the repumping beam. In this case, repeating the measurement with reduced repumping intensity is recommended. If trapping is still not observed, misalignment of the laser system may be responsible. Alignment should include both the propagation direction and the polarization of the beams.

Once trapping is observed, a logical next step is to optimize the intensities of both cooling and repumping beams by monitoring the final cloud temperature (or cloud size after a fixed time of expansion). This process is iterative: check intensities, detunings, and alignment repeatedly until the optimal parameters are found. If the temperature is already low but higher than expected, it can be helpful to check whether the cloud is still visible with longer gray molasses durations. When the cloud becomes barely visible, another minimization of the magnetic field can be beneficial, but this time using feedback from the atoms. If the compensation field is correctly selected, the cloud should diffuse symmetrically over time within the imaging area, or molasses beam area. As has been already mentioned, we are able to extend the gray molasses cooling phase for potassium atoms (effectively, the cloud's lifetimes) to over 1 s, but only with proper compensation of the magnetic field. In the case of cesium atoms, a spatial drift of the laser beam is observable due to thermal effects in acousto-optical modulators, and it limits the trapping time to about 100 ms.

For Λ-enhanced gray molasses, the optimization procedure is a bit simpler. Although the magnetic field optimization step remains essential, the frequency configuration is partially predetermined: optimal performance of gray molasses is expected when the two-photon resonance condition is fulfilled, that is, when the frequency difference between the cooling and repumping beams matches the hyperfine splitting of the ground state. Subsequently, it is a good approach to scan the 'global' frequency while keeping the two-photon detuning fixed. In this way, it is possible to identify the optimal cooling conditions and obtain a characteristic response similar to the one shown in chapter 6.

If cooling is less efficient than expected, one possible reason is the presence of a residual magnetic field. The performance can be evaluated in two ways: either by measuring the temperature after molasses cooling, or by analyzing the shape of the resonance that occurs when the two-photon condition is satisfied — that is, when the frequency difference between the cooling and repumping light matches the ground-state hyperfine splitting, enabling efficient Raman transitions between the hyperfine states. Based on our observations, the resonance curve obtained during a two-photon detuning scan typically shifts and broadens when the magnetic field is not properly

compensated. Both effects are illustrated in Fig. 3.11.

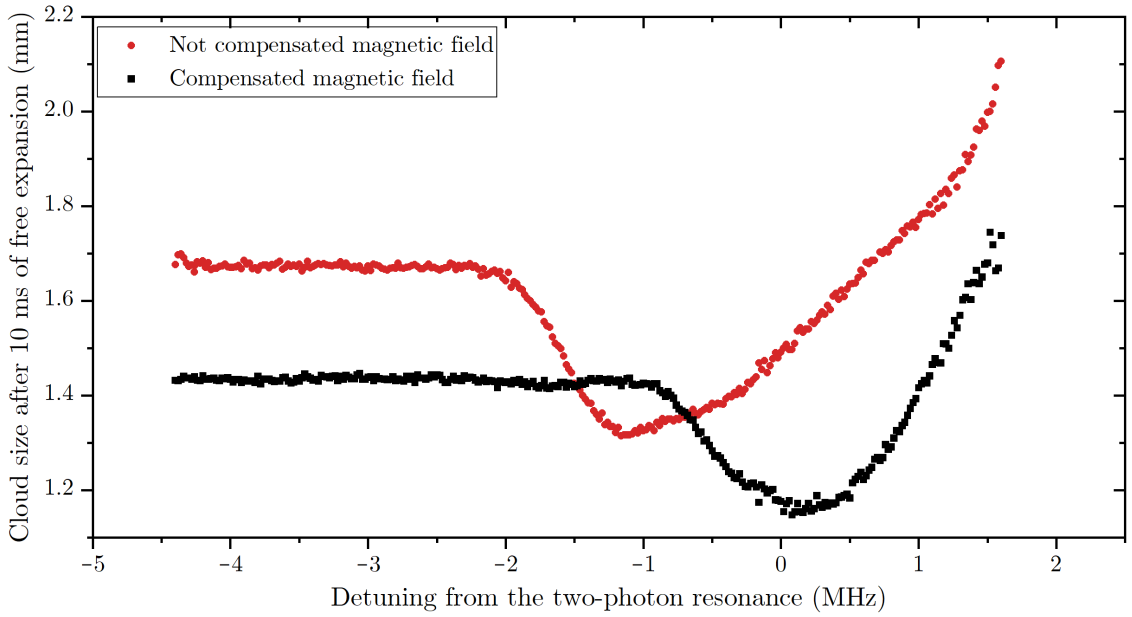

Figure 3.11: The size of the cloud as a function of the detuning from the two-photon transition for compensated (black), and not-compensated (red) stray magnetic field.

The final step—regardless of the specific implementation of gray molasses—is the optimization of the beam intensity and the intensity decrease trajectory, as in many cases high intensity of cooling beams increases transfer between the previous stage and optical molasses, but also leads to higher temperatures. Unfortunately, in this case, there is no alternative to repeated scanning and trial-and-error adjustments.

The application of these optimization methods allowed us to achieve efficient cooling in gray optical molasses, thereby completing the laser cooling strategy defined at the beginning of the chapter. However, this does not mark the end of the preparation stage for mixtures intended for spectroscopic studies. While some measurements could, in principle, be performed at the MOT or CMOT stage, these traps are somehow 'dynamic'. At neither stage do we have control over the internal atomic state, as it is continuously changing by ongoing absorption and emission processes. Moreover, Feshbach spectroscopy cannot be performed at this point because the position of the atomic cloud is determined by the minimum of the magnetic field gradient. As a result, applying a magnetic field for Feshbach spectroscopy would shift the trap center, making it difficult to distinguish whether observed losses arise from the trap displacement or from actual magnetoassociation processes. These challenges are re-

solved by transferring the atoms into an optical dipole trap, which will be described in the following section.

3.4 Optical dipole trap

One of the earliest applications of what is now known as an optical dipole trap can be traced back to 1986, when A. Ashkin, J. Dziedzic, J. Bjorkholm, and S. Chu used a tightly focused laser beam to trap dielectric particles—both Mie particles (larger in diameter than the wavelength of the light) and Rayleigh particles (smaller than the wavelength of the light) [86]. A particularly important sentence appears at the end of the article: "*Finally, we expect that these single-beam traps will work for trapping atoms as well as for macroscopic Rayleigh particles since atoms can be viewed as Rayleigh particles with a different polarizability.*" In a sense, this sentence marked the beginning of a new chapter in the field of ultracold matter, eventually announcing the successful trapping of atoms in optical dipole traps.

That same year, another groundbreaking article reported the transfer of laser-cooled sodium atoms from optical molasses into an optical dipole trap. The authors estimated that approximately 500 atoms were trapped and held for "several seconds" [87].

Since these initial demonstrations, optical dipole traps have played a crucial role in the realization of Bose-Einstein condensates and degenerate Fermi gases [88], [89], the formation of ultracold ground-state molecules [90], the observation of superfluidity and supersolidity in ultracold atomic systems [91], [92], and many more. Thanks to its wide range of applications and versatility, the optical dipole trap has become a standard tool in laboratories studying ultracold atoms. Its ubiquity and utility have inspired a wealth of literature, including several reviews explaining the fundamental principles of dipole trapping. However, for the sake of consistency within this dissertation, we will first outline the operating principles relevant to the present work, relying primarily on the information presented in [93].

One can consider a simplified model in which an atom is treated as a two-level system with a single valence electron. When a rapidly oscillating electric field $E_F(r,t) = \hat{e}\,\tilde{E}(r)\,exp(-i\omega_L t)$ of frequency ω_L and polarization vector $\hat{e}$ is applied to the atom, an oscillating atomic dipole moment $p(r,t) = \hat{e}\,\tilde{p}(r)\,exp(-i\omega_L t)$ is induced. The amplitude of the dipole moment $\tilde{p}(r)$ is related to the amplitude of the electric field $\tilde{E}(r)$ via complex atomic polarizability α, such that $\tilde{p}(r) = \alpha\,\tilde{E}(r)$. The time-averaged induced dipole potential U_{dip} can then be written as the time average

of the interaction energy between the atomic dipole and the oscillating field:

$$U_{\text{dip}} = -\frac{1}{2}\langle p(r,t)\, E(r,t)\rangle.$$

If the oscillating electric field is provided by a laser beam, we can relate the field amplitude to the beam intensity I via $|\tilde{E}|^2 = 2I/c\epsilon_0$ relation, where c is the speed of light in vacuum and ϵ_0 is the vacuum permittivity. Substituting into the dipole potential expression yields

$$U_{\text{dip}} = -\frac{1}{2}\langle p(r,t)\, E(r,t)\rangle = -\frac{1}{2c\epsilon_0} I\ \text{Re}(\alpha). \tag{3.5}$$

For the power absorbed by the dipole, an analogous analysis gives:

$$P_{\text{abs}} = \langle p(r,t)\, \dot{E}(r,t)\rangle = \frac{\omega}{c\epsilon_0} I\ \text{Im}(\alpha).$$

By treating the laser beam as a stream of photons, we use $P_{\text{abs}} = \hbar\omega_L \Gamma_{\text{sc}}$ to find the photon scattering rate:

$$\Gamma_{\text{sc}} = \frac{1}{\hbar c\epsilon_0} I\ \text{Im}(\alpha). \tag{3.6}$$

Already from Eqs. 3.5 and 3.6, it is evident that both the dipole trapping potential and the photon scattering rate depend solely on the light intensity and on the real (Re) and imaginary (Im) parts of the atomic polarizability, which can be expressed as [93]:

$$\alpha = 6\pi\varepsilon_0 c^3 \cdot \frac{\Gamma/\omega_0^2}{\omega_0^2 - \omega_L^2 - i\,(\omega_L^3/\omega_0^2)\,\Gamma},$$

for an atom with a natural linewidth Γ and resonance frequency ω_0. Inserting this expression into Eqs. 3.5 and 3.6, we obtain:

$$U_{\text{dip}}(\mathbf{r}) = -\frac{3\pi c^2}{2\omega_0^3}\left(\frac{\Gamma}{\omega_0 - \omega_L} + \frac{\Gamma}{\omega_0 + \omega_L}\right) I(\mathbf{r})$$

$$\Gamma_{\text{sc}}(\mathbf{r}) = \frac{3\pi c^2}{2\hbar\omega_0^3}\left(\frac{\omega_L}{\omega_0}\right)^3 \left(\frac{\Gamma}{\omega_0 - \omega_L} + \frac{\Gamma}{\omega_0 + \omega_L}\right)^2 I(\mathbf{r})$$

Assuming that the detuning $\Delta = \omega_L - \omega_0$ is small compared to the resonance frequency ($|\Delta| \ll \omega_0$), the rotating wave approximation (RWA) can be applied [93]. This allows the rapidly oscillating term involving $\omega_0 + \omega_L$ to be neglected. The

factor $(\omega_L/\omega_0)^3$ can be written as $(1+\Delta/\omega_0)^3$, which, for small Δ/ω_0, can be approximated to first order as unity. The expressions then simplify to:

$$\begin{aligned} U_{\mathrm{dip}}(\mathbf{r}) &= \frac{3\pi c^2}{2\omega_0^3}\cdot\frac{\Gamma}{\Delta}\cdot I(\mathbf{r}), \\ \Gamma_{\mathrm{sc}}(\mathbf{r}) &= \frac{3\pi c^2}{2\hbar\omega_0^3}\left(\frac{\Gamma}{\Delta}\right)^2 I(\mathbf{r}). \end{aligned} \tag{3.7}$$

Based on the two previously introduced formulas, the operating principle of the optical dipole trap becomes clear: the coupling between the electric field of the laser beam and the atomic dipole moment leads to the formation of a potential that is linearly proportional to the local intensity of the laser field. This implies that, for a laser beam with a Gaussian profile, the resulting trapping potential will spatially follow a Gaussian shape. As already mentioned at the end of the previous chapter, the true advantage of the dipole trap over other trapping methods lies in its low sensitivity to the magnetic sublevel of the atom. This allows for the preparation of a sample in a well-defined internal state and its conservation for relatively long durations. The only mechanism that could cause a change in the atomic state is the off-resonant scattering of photons from the trapping beam.

Scattering of photons from the dipole trap by the atomic sample is also important from the perspective of the temperature of ultracold atoms. When a photon with a frequency corresponding to the trapping light scatters from the atomic cloud, not only does it alter the internal atomic state, but also gives it a momentum kick. As a result, the temperature evolution $\dot{T}$ of atoms in the three-dimensional trap due to photon scattering can be described by the equation

$$\dot{T} = \frac{1}{3}T_{rec}\Gamma_{sc}, \tag{3.8}$$

where T_{rec} is the recoil temperature calculated from Eq. 3.1.

Analyzing Eq. 3.7, one may notice that the dipole potential is inversely proportional to the detuning from resonance, while the photon scattering rate scales with the inverse square of the detuning. This means that, for the purpose of dipole trapping, it is favorable to use a laser beam that is far-detuned and of high intensity. This raises the question: what precisely constitutes a "far-detuned" and "high-intensity" beam?

The answer is primarily technical: it depends on the availability of laser sources and amplifiers that can operate reliably over extended periods. In practice, lasers operating at a wavelength of 1064 nm are commonly used, as there exists a well-developed technology for high-power fiber amplifiers based on ytterbium-doped fibers.

Currently, these systems can produce single-mode beams with output power exceeding 130 W and a linewidth on the order of several kHz. Longitudinally multimode lasers can reach even higher powers, but are rarely suitable for experiments requiring long lifetimes of trapped samples.

For the purpose of this discussion, we consider a high-power laser with parameters representative of our experimental setup, namely up to 70 W of optical power and a beam waist of 250 μm. While a single widely tunable source covering the relevant spectral range is not available in practice, this assumption provides a convenient framework to estimate what range of wavelengths would allow for simultaneous trapping of cesium and potassium atoms pre-cooled in optical molasses. For this problem, we assume that both species have a temperature of approximately 15 μK, and that the trapping potential must be at least ten times deeper than the thermal energy of the atoms, i.e., $U_{\mathrm{dip}} = 150\ \mu\mathrm{K} \times k_B$, to enable confinement of atoms in the higher-energy tail of the Maxwell-Boltzmann distribution. Typically, dipole traps contain more than 10^6 atoms, and in a single-chamber setup, the lifetime is limited by collisions with the background gas, with a typical value of $\tau \approx 4$ s. To ensure that no more than about 1% of the atoms experience a change in their internal state due to photon scattering during this period, the maximum allowed scattering rate is $\Gamma = 2500$ photons/s. The 1% threshold is chosen as a practical criterion, since such a small variation in the internal state population would have no measurable impact on the outcome of a typical experiment and thus can be safely neglected. These constraints define the parameter range in which the dipole trap must operate reliably. A calculation of the trap depth and photon scattering rate under the above conditions as a function of the trapping wavelength is shown in Fig. 3.12. From this figure, it is evident that the requirements are fulfilled for wavelengths roughly in the range 900–1100 nm.

As shown in the figure, there is a significant increase in both scattering and trapping potential near the D2 and D1 transitions of potassium and cesium. The scattering rate quickly decreases away from resonance, in accordance with the relationship $\Gamma \propto 1/\Delta^2$. As one can notice in the bottom left panel of figure 3.12 in the case of potassium, the condition defined above ($\Gamma < 2500$) is satisfied for wavelengths detuned by more than 5 nm from the resonance. This implies that, in order for both atomic species to be trappable, the allowed wavelength range is above about 900 nm (about 5 nm above D1-line of cesium [41]).

A trapping laser with a wavelength near 900 nm would naturally generate the deepest potential and might therefore appear to be the most favorable option. However, commercial lasers operating in this range typically offer limited output power. However, as illustrated in the lower right part of the figure, a standard trapping

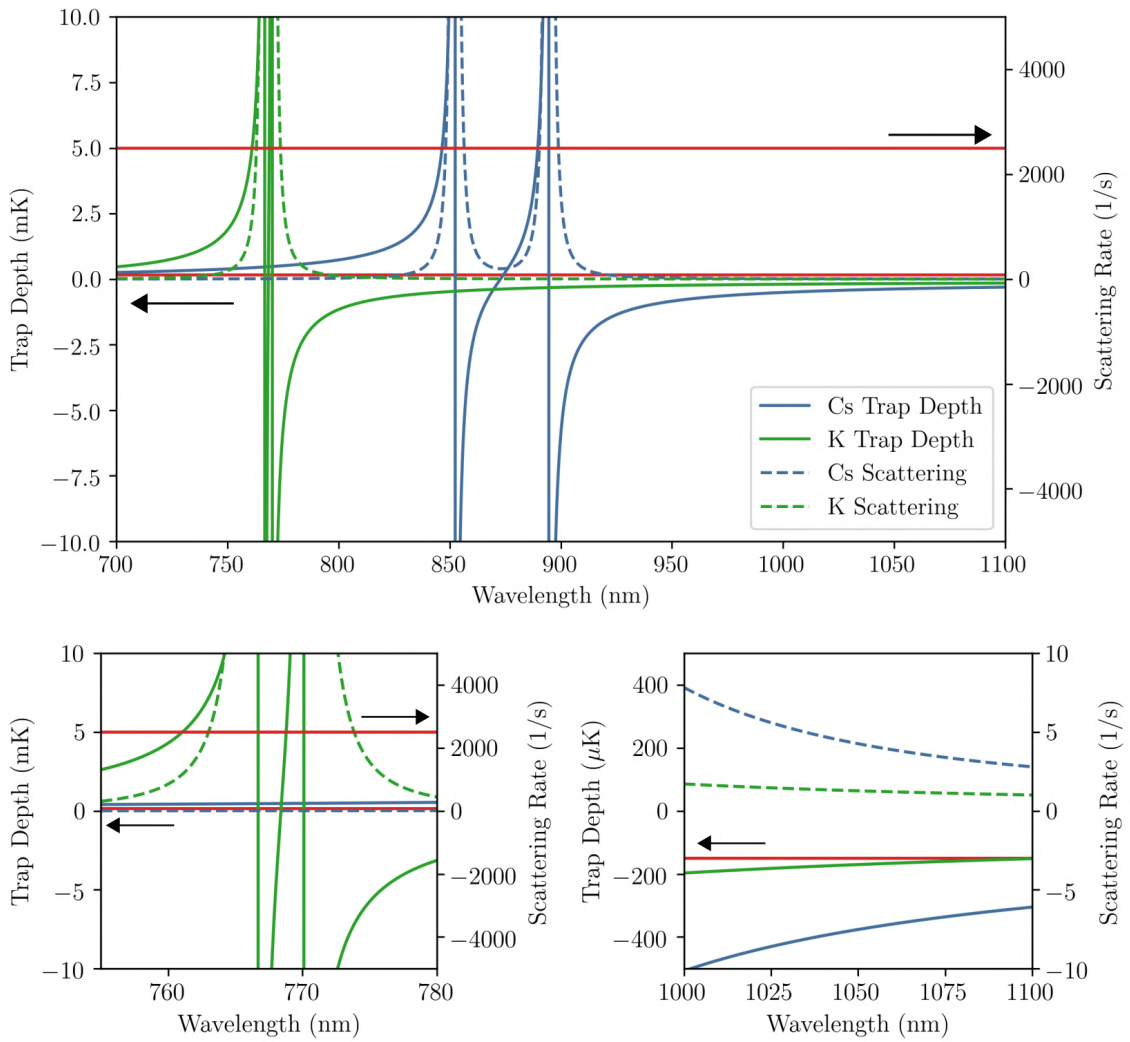

Figure 3.12: Trap depth, and scattering rate of the optical dipole trap as a function of wavelength (top) for potassium (green) and cesium (blue) atoms. In the bottom two magnifications of the figure are presented. On the left side the area around potassium D1, D2 line transitions, and in the right side area around typical trap wavelength 1064 nm. Red lines correspond to trap depth 150 μK, and scattering rate 2500 1/s.

laser with a wavelength of 1064 nm also satisfies these conditions. Moreover, at this wavelength, the scattering rate is negligible relative to the size of the atomic sample.

The advantage of a 1064 nm laser over a 900 nm laser becomes even more apparent

when analyzing not the scattering rate, but the thermal evolution of the atomic sample in the dipole trap. As shown in Figure 3.13, the heating rate of atoms in the optical trap strongly depends on the trapping laser wavelength. A scattering rate of around 2500 photons/s leads to substantial heating, which imposes a more strict requirement than simply minimizing photon scattering: it becomes necessary to limit the rate of temperature increase to prevent the atoms from being heated beyond the trap depth during their expected lifetime. To quantify this, we define a condition on the temperature evolution,

$$\dot{T} \leq \frac{|U_{\mathrm{dip}}|}{k_B}, \tag{3.9}$$

which sets an upper bound on the allowable heating rate. This inequality defines the heating-limited lifetime—the time over which atoms remain confined before their temperature exceeds the trap depth—for various laser wavelengths. This constraint is also illustrated in Figure 3.13. It should be emphasized that the lifetime criterion adopted here is in fact a rather soft criterion: in practice, any heating shortens the useful trapping time and can degrade experimental performance. The impact of heating strongly depends on the specific experimental objectives: in the present system, designed primarily for spectroscopy in cold atomic gases, moderate heating rates can be tolerated, whereas in setups aiming for quantum degeneracy, even minimal heating can critically impede evaporation to the required phase-space densities.

If heating is negligible, one can focus on the trapping potential presented in the Figure 3.12, as well as resulting from Eq. 3.7. Here, two additional important features can be identified. First, it is possible to generate a repulsive dipole potential if the trapping beam is blue-detuned relative to the atomic transitions. In such cases, to confine atoms a so-called hollow-core beam must be employed, i.e., a beam with a dark central region .

Second, of particular importance for mixtures of atomic species, there exist specific wavelengths (so-called tune-out wavelengths) at which contributions from multiple possible levels, usually mainly the D1 and D2 lines, cancel each other, leading to a net-zero dipole potential regardless of the beam intensity. This might be relevant in dual-species systems. The optical dipole potential is not the only force acting on the atoms — gravity is also present, acting differently depending on the atomic mass. In the case of a K-Cs mixture, with a mass ratio of $m_{\mathrm{Cs}}/m_{\mathrm{K}} \approx 3.33$, the gravitational potential is significantly different for the two species. This can lead to spatial separation within the trap, which might hinder molecule formation or evaporation effects. However, by introducing an additional laser beam at the tune-out wavelength — where the attractive and repulsive dipole contributions cancel for one

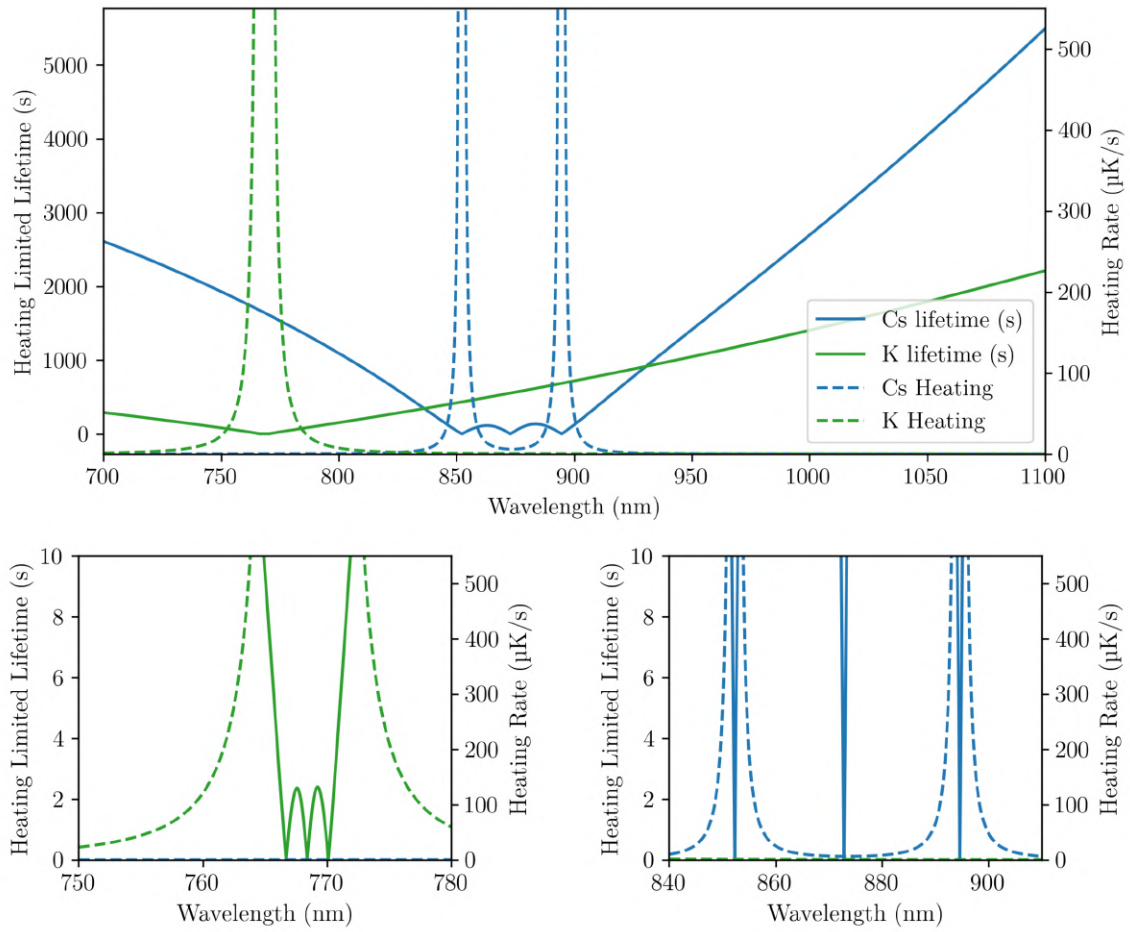

Figure 3.13: Absolute value of heating limited lifetime (line), and heating rate (dotted line) for the potassium (green), and cesium (blue) in the optical dipole trap as a function of wavelength (top). On the bottom two magnifications around potassium and cesium D1 and D2 lines are presented.

species — it becomes possible to independently tailor the effective trapping potentials experienced by cesium and potassium atoms.

With this, we have described the general characteristics and operating principles of the optical dipole trap, focusing primarily on how to achieve efficient confinement of atoms. The obvious question is: how do atoms move, or how are they trapped inside such a trap?

For a typical dipole trap formed by a red-detuned Gaussian beam, the potential

near its minimum can be well approximated by a parabolic shape. In this regime, the atomic motion is well described by a harmonic oscillator potential, which in one dimension is given by

$$U_{\text{dip}} \approx \frac{1}{2} m\omega_x^2 x^2,$$

where x is the spatial coordinate, m is the atomic mass, and ω_x is the characteristic trap frequency [94].

The trap frequency determined in this way is crucial for experiments involving cold atoms and their evolution within the trapping potential, as it determines the relevant time scales of the processes taking place and the parameters of the atomic cloud. For a trap characterized by resonance frequencies $\{\omega_x, \omega_y, \omega_z\}$, the spatial width σ of the atomic distribution in an optical dipole trap is given by

$$\sigma = \sqrt{\frac{k_B T}{m\omega_i^2}}, \tag{3.10}$$

which leads to a peak atomic density n_0 of

$$n_0 = \frac{N}{(2\pi)^{3/2}\sigma_x\sigma_y\sigma_z}. \tag{3.11}$$

The peak density directly affects the collision rate in the trap, thereby influencing the efficiency of evaporative cooling and the visibility of atom loss features in Feshbach spectroscopy.

In this work, the primary goal was to perform Feshbach spectroscopy and investigate the collisional properties of K-Cs mixtures. Therefore, maximizing the atomic density was one of the milestones. Due to limited trap lifetimes, the evaporative cooling stage was often omitted. Nevertheless, measurements of the trap frequencies were employed as a precise diagnostic of the trapping potential.

In practical experimental conditions, in order to achieve efficient trapping with limited optical power, the laser beams are focused onto the atomic cloud. This focusing increases the local light intensity and results in confinement also along the beam's propagation direction due to spatial variations in intensity—a mechanism absent in collimated beams. However, accurately determining the beam waist at the trapping area, or even the laser power after transmission through the border between the laboratory and the vacuum chamber, is subject to significant uncertainty. In such cases, the trap frequency serves as a reliable and precise diagnostic tool.

Returning to the analogy of an atom in an optical dipole trap being like a harmonic oscillator with a characteristic natural frequency, if the oscillator is driven at

its resonance frequency, its amplitude and velocity will grow. This implies that periodic modulation of the trapping potential (i.e. the light intensity) can lead to atom loss, particularly in the following scenarios: (i) when the modulation is slow enough for atoms to escape the trap (e.g., due to gravity), and (ii) when the modulation frequency matches the trap frequency. The latter case can be used to accurately determine the trap frequency and, in turn, the depth of the trapping potential [95]. The results of parametric heating measurements carried out in our experiment are presented in the section 4 describing the design of the optical dipole trap in our system.

The diagnostic method for the optical dipole trap concludes the overview of cooling techniques employed in our experiment. Following the sequence outlined in this chapter, the atoms were first captured in a magneto-optical trap (MOT), then compressed by increasing the magnetic field gradient (CMOT), further cooled in gray molasses (GMC), and finally transferred to an optical dipole trap (ODT). This cooling sequence was successfully applied to the preparation of both ^{39}K-Cs and ^{41}K-Cs mixtures. The resulting outcomes are presented in Sections 7, 8. To conclude this part with a real physical result, absorption images showing the evolution of the atomic cloud through successive stages of trapping are displayed in Fig. 3.14. These images were taken with the light resonant only with the potassium transition, resonant only with the cesium transition, and with two beams to image both clouds simultaneously.

In the above discussion, we have not addressed the ability of the optical dipole trap to preserve the electronic and magnetic states of the trapped atoms. This was deliberate, as the preparation of an atomic sample in a specific internal state has not yet been considered. The following section presents the methods developed for optical pumping of both potassium and cesium atoms.

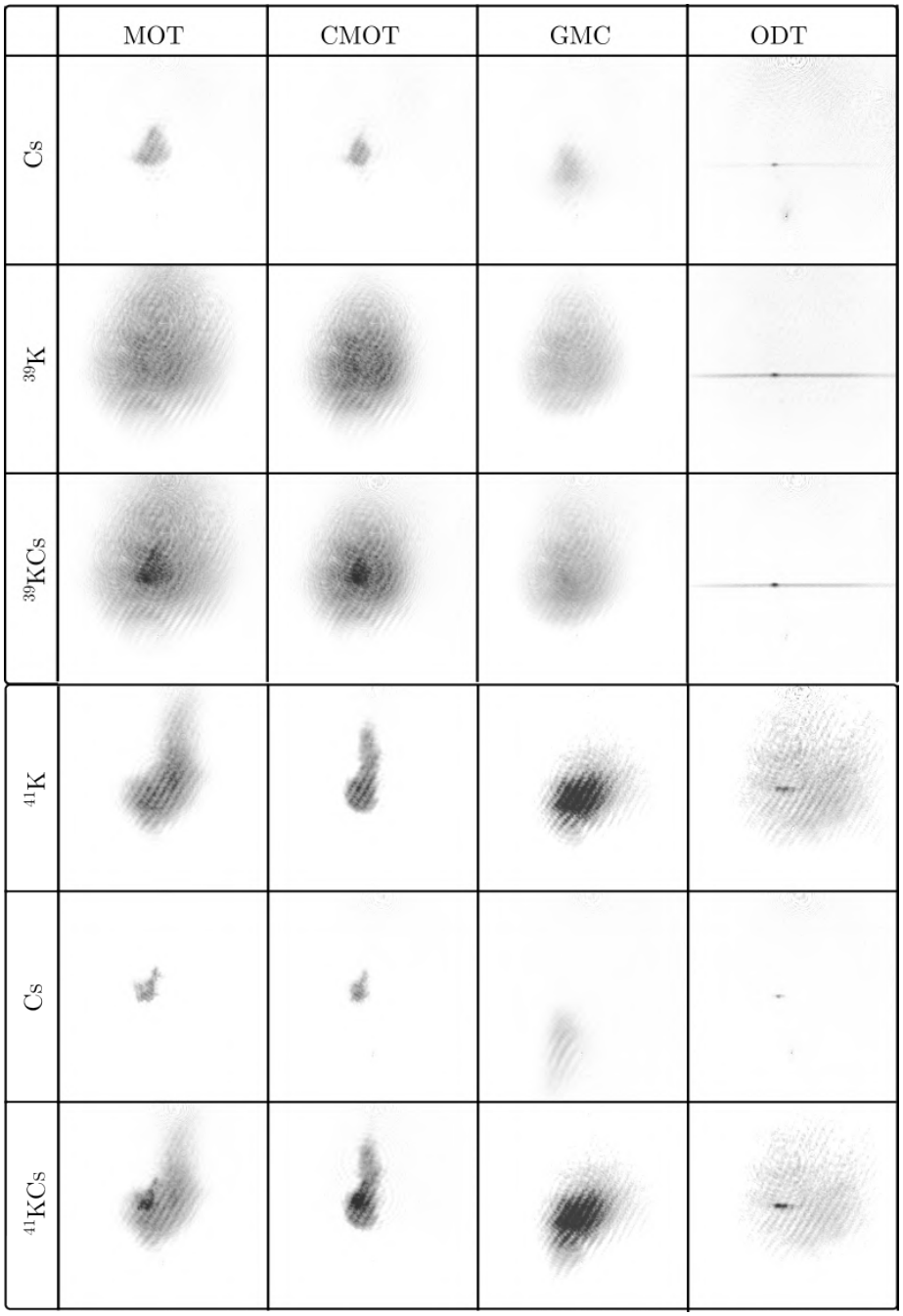

Figure 3.14: Absorption images of trapped ^{39}K, ^{41}K, and Cs atoms for single-species and mixture configurations (rows), shown at successive cooling stages (columns). The images of the mixtures in the first three rows and the images in the last three rows were taken approximately eight months apart. During that time the setup was re-aligned several times and also experienced long-term drifts, which caused the noticeably different shape of the cesium cloud and the dipole trap.

3.5 Optical pumping

As discussed in the chapter 2, the properties of an atom — even within a single species — can strongly depend on its Zeeman or hyperfine state. A simple yet illustrative example is the behavior of an atom in a magnetic field gradient: depending on its magnetic sublevel, it may be attracted to a region of low magnetic field (low-field seeker), remain unaffected by the field ($m_{\mathrm{F}} = 0$), or be repelled towards stronger fields (high-field seeker). Furthermore, even among low-field-seeking states, atoms with different magnetic moments will experience different trapping forces, and thus be more or less strongly confined.

In the case of the key result presented in this work—Feshbach spectroscopy—the collisional properties of the atoms are highly sensitive to their magnetic state. Consequently, a significant part of the research effort in this dissertation has been devoted to developing methods for controlling the distribution of atoms among various hyperfine and magnetic levels. These methods are presented in this section.

The first aspect that must be controlled early in the experiment—ideally during the magneto-optical trap (MOT) stage—is the population of the hyperfine F states. This is important for cesium atoms, but absolutely crucial for bosonic potassium.

It should be noted that during the MOT stage atoms are constantly pumped between different energy levels by the cooling beams. Once the trap is turned off, e.g., during free fall, atoms will populate both ground hyperfine states. In the case of cesium, due to the large excited-state hyperfine splitting, the approximation of a closed cycling transition is mostly valid, and most atoms at the end of cooling will populate the higher ground state $F = 4$. For potassium, as discussed earlier, this approximation breaks down due to the small excited-state splitting. As a result, atoms populate both F levels of the ground states in nearly equal proportions after the trap is turned off. In such a situation, if the number of atoms is measured using e.g. absorption imaging, which only addresses one transition, the measurement will be systematically inaccurate. Therefore, a method is required that transfers the entire population into the desired ground hyperfine state prior to imaging.

Fortunately, the required optical pumping technique is conceptually simple. For two ground hyperfine states F and $F + 1$, and an excited state F', if the selection rules allow both $F \to F'$ and $F + 1 \to F'$ transitions, then illuminating the atoms with only one of the two optical frequencies creates a bright and a dark state. As a result, the entire atomic population accumulates in the dark state.

This method was applied in our experiment to optically pump all three potassium isotopes as well as cesium atoms. As can be seen, optical pumping into a specific hyperfine state is straightforward, particularly because different alkali atoms possess

the same number of hyperfine F states forming the D1 and D2 lines, and the ground-state hyperfine structure is well-separated. This enables the creation of a dark state in a relatively simple and efficient way. However, the situation becomes significantly more complex when pumping into a specific magnetic sublevel-due to the varying number of states and their degeneracy or small energy splittings in the absence of—or under weak—magnetic fields.

In the case of cesium, optical pumping into stretched states (i.e. those with the highest absolute value of the magnetic quantum number) is relatively simple, thanks to the large excited-state hyperfine splitting. This makes it possible to form a dark state that also corresponds to a stretched state. To illustrate the procedure, let us assume that atoms have already been prepared in the $F = 3$ ground state using the method described earlier, and that the goal is to prepare the sample in the fully polarized $F = 3$, $m_{\mathrm{F}} = 3$ state. Such a configuration is favorable for heteronuclear molecule formation in the absolute ground state or for achieving a quantum-degenerate gas [47], [96].

The first step of the optical pumping is to circularly polarize the laser light and set the magnetic field direction so that only transitions with $\Delta m_{\mathrm{F}} = +1$ are driven. Under these conditions, addressing the $F = 3 \rightarrow F' = 2$ transition, the selection rules ensure that the $m_{\mathrm{F}} = 3$ state becomes a dark state. In this situation, the last possible excitation is the $F = 3$, $m_{\mathrm{F}} = 1 \rightarrow F' = 2$, $m'_{\mathrm{F}} = 2$ transition. This excited state can decay via three allowed channels—$\Delta m_{\mathrm{F}} = 0, \pm 1$—into $F = 3$, $m_{\mathrm{F}} = 1$ (which continues the pumping cycle) or into the dark states $F = 3$, $m_{\mathrm{F}} = 2$ or $m_{\mathrm{F}} = 3$, where the pumping ceases. As a result, atoms accumulate approximately equally in these two dark states.

In order to achieve a completely polarized sample, the pumping configuration must also allow for a less probable $\Delta m_{\mathrm{F}} = 0$ excitation. This can be realized either by changing the polarization of the light from circular to elliptical, or more reliably, by tilting the quantization axis through a small rotation of the magnetic field direction. In this case, the $F = 3$, $m_{\mathrm{F}} = 2$ state is no longer a perfectly dark state because there is a small probability of excitation on the $F = 3$, $m_{\mathrm{F}} = 2 \rightarrow F' = 2$, $m'_{\mathrm{F}} = 2$ transition. Consequently, atoms from all other m_{F} states can be efficiently pumped out and eventually accumulate in the desired $m_{\mathrm{F}} = 3$ state.

Naturally, there is always a finite probability of off-resonant excitations. Therefore, throughout the pumping process, the repumping beam addressing the $F = 4$ state must remain active. While this beam has previously been referred to as the cooling beam during the whole cooling procedure, here it serves as a repumper.

In our setup, with careful tuning of the magnetic field direction and magnitude, laser frequencies, and intensities, we achieve a polarized cesium sample in which

more than 90% of atoms populate the $F = 3$, $m_\mathrm{F} = 3$ state. An analogous procedure enables equally efficient polarization in the $F = 3$, $m_\mathrm{F} = -3$ state, if the quantization axis is reversed.

The situation becomes significantly more complex when attempting to pump atoms into non-stretched states, due to the lack of an obvious mechanism for forming dark states. Obtaining a properly polarized sample in such cases is nontrivial. To circumvent these technical limitations for the purpose of Feshbach spectroscopy, we employed an alternative method that allows selective removal of atoms from the $F = 3$, $m_\mathrm{F} = 3$ state.

This approach enables an unambiguous identification of the magnetic state associated with a given spectroscopic signal by performing three distinct measurements. In the first one, the sample is fully polarized in the $F = 3$, $m_\mathrm{F} = 3$ state. In the second one, the polarization is partially reduced so that atoms in both $F = 3$, $m_\mathrm{F} = 3$ and $F = 3$, $m_\mathrm{F} = 2$ states are present. In final measurement, all $F = 3$ magnetic sublevels are populated except for $F = 3$, $m_\mathrm{F} = 3$. If a signal appears only in the first configuration, it can be attributed to the $F = 3$, $m_\mathrm{F} = 3$ state. If it appears in both the second and third configurations, it originates from the $F = 3$, $m_\mathrm{F} = 2$ state. If it is present only in the third configuration, it must be associated with one of the lower m_F states ($m_\mathrm{F} < 2$).

To create the sample used in the third case, it is essential to selectively remove atoms only from the $F = 3$, $m_\mathrm{F} = 3$ state. This is accomplished by employing a linearly polarized laser beam driving a π-transition and performing the optical pumping in a strong ($B = 88$ G) magnetic field. The large Zeeman splitting under these conditions enables spectral resolution of individual magnetic sublevels, as illustrated in Fig. 2.4.

Polarizing potassium atoms into the desired magnetic state is considerably more challenging. While one could, in principle, use the same optical pumping method as for cesium, the creation of a true dark state is hindered by the small hyperfine splitting of the excited state. This makes it impossible to address the excited-state hyperfine levels independently. In such a case, it is advantageous to perform optical pumping on the D1 line, where the excited-state separation is significantly larger.

However, in this configuration, optical pumping on the $F \to F - 1$ transition cannot be used to produce a sample polarized in the lowest-energy magnetic sublevel, $F = 1$, $m_F = 1$. Therefore, atoms are pumped sequentially. First, a pair of σ^+ polarized beams resonant with the $F = 2 \to F' = 2$ and $F = 1 \to F' = 1$ transitions is used. Under these conditions, both $F = 2$, $m_F = 2$ and, in principle, $F = 1$, $m_F = 1$ are dark states. In practice, off-resonant excitation leads to a significant fraction of the population (about 80%) accumulating in the $F = 2$, $m_F = 2$ state.

To transfer this population into the lower hyperfine state, we address the $F = 2 \rightarrow F = 2$ transition using a linearly polarized beam, which redistributes atoms into the $F = 1$, $m_F = 1$ and $m_F = 0$ states. Subsequently, a circularly polarized beam is again used to excite the $F = 1 \rightarrow F' = 1$ transition. After two iterations of this sequence, the resulting sample is polarized with approximately 80% of atoms in the $F = 1$, $m_F = 1$ state, while the remaining 20% occupy the $F = 1$, $m_F = 0$ state. This result holds regardless of which bosonic potassium isotope is prepared. This method, with addressed transitions and pumping paths leading to polarization in $F = 2$ or $F = 1$ stretched states is presented in Fig. 3.15.

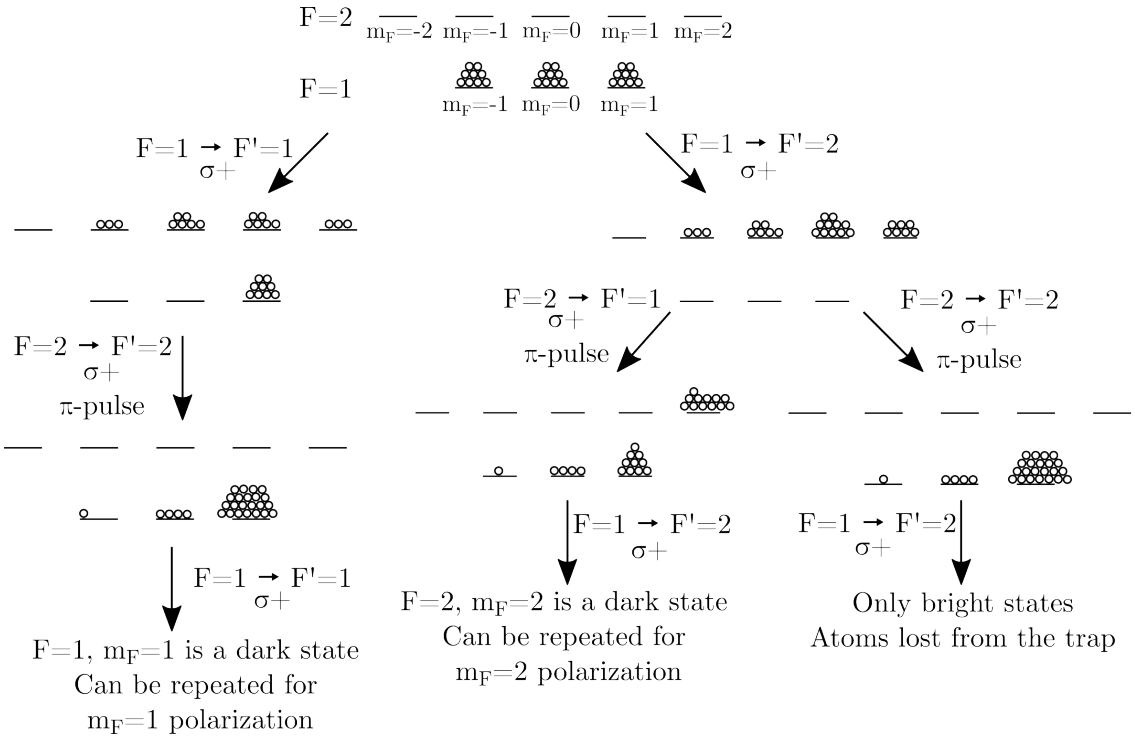

Figure 3.15: Experimental sequence for the spin polarization of potassium atoms. Each step is indicated by an arrow, with the transition that is addressed shown next to it. σ^+ denotes circularly polarized light driving the $\Delta m_{\mathrm{F}} = +1$ transition, while π refers to a pulse of a linearly polarized light, as explained in the main text.

Due to the low abundance the fermionic isotope in our setup, trapping in the optical dipole trap is not feasible. Therefore, using a method analogous to the one described above for $F = 2$, $m_F = 2$, we pump atoms into the $F = 9/2$, $m_F = 9/2$ state. This state is favorable for magnetic trapping due to its high magnetic moment.

The only additional requirement in this case is to employ a second optical beam resonant with the $F = 7/2 \rightarrow F' = 9/2$ transition to prevent the formation of a dark state in the lower hyperfine level.

3.6 Imaging

Throughout the description of the cooling procedures, we provided information on the achieved parameters of the atomic clouds such as the number of atoms, temperature, and density. However, apart from a few brief mentions, the methods used to extract these properties were largely omitted. Therefore, in this chapter, we would like to discuss them on the basis of existing literature. [22], [97], [98].

A key aspect of a reliable imaging is the calibration of both the camera and the optical system. In addition to describing the imaging layout based on the configuration of lenses, it is beneficial to test the system using the actual sample that will be imaged. Vertical cameras were calibrated relative to the horizontal camera because there exists one axis that can be 'seen' by all cameras.

For the horizontal camera, a convenient method of calibration is based on observing the free fall of the atomic cloud. After switching off the trapping and cooling beams, the center of mass of the cloud is expected to follow a free-fall trajectory under the influence of gravitational acceleration g, such that its vertical position z evolves over time t as

$$z(t) = z_0 + \frac{1}{2} g t^2. \tag{3.12}$$

If we introduce a conversion factor from pixels to meters, $A_{\mathrm{m/px}}$, we can fit the function $z_{\mathrm{px}} = z(t)/A_{\mathrm{m/px}} = a \cdot t^2 + b$ to the data describing the position of the cloud on the camera chip as a function of the fall time. This allows us to extract the conversion factor from pixels to meters as $A_{\mathrm{m/px}} = g/2a = 4.08 \times 10^{-6}$ m/px. An example of such calibration data is shown in Fig. 3.16.

This calibration enables reliable determination of key parameters such as the number of atoms, temperature, and density. For most of the experiments, absorption imaging was used to extract these quantities.

According to the Beer–Lambert law, if a laser beam of initial intensity I_0 passes through an absorbing medium with optical density OD, its transmitted intensity decays exponentially:

$$I = I_0 e^{-\mathrm{OD}}. \tag{3.13}$$

In the case of an atomic cloud, the optical density can be expressed as the product of the atomic absorption cross-section σ and the column density $n(x, y)$—the number

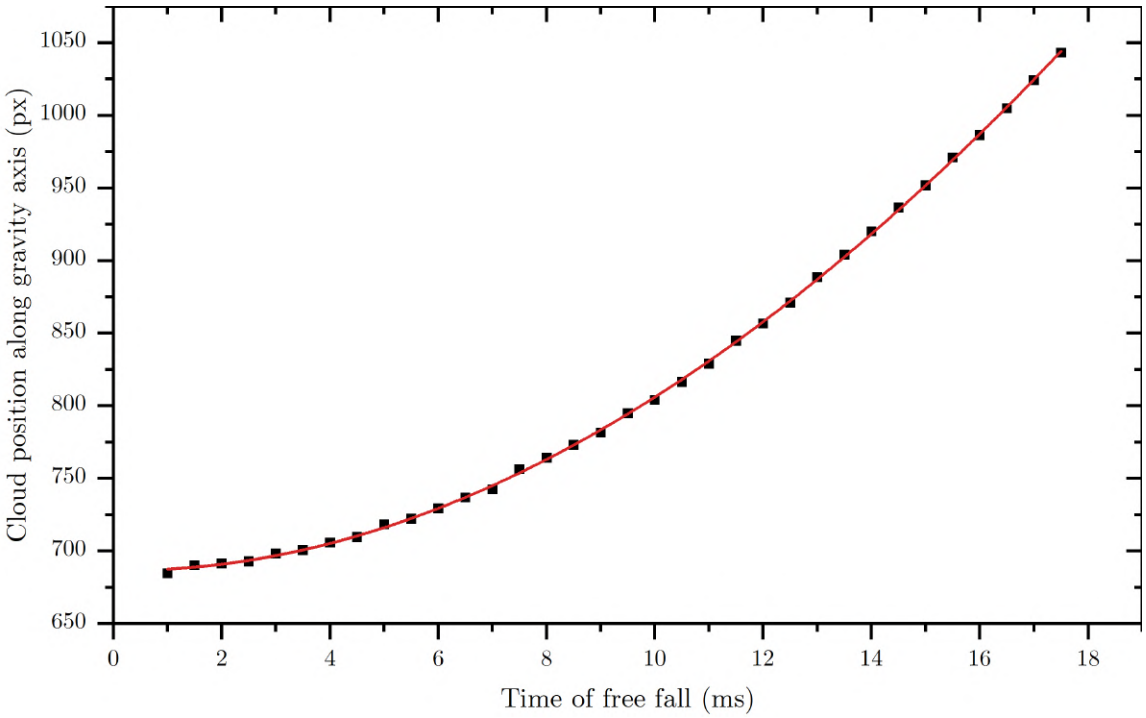

Figure 3.16: Cloud position along the axis of gravity as a function of the cloud's fall time (black squres), with fitted second-order polynomial (red line).

of atoms per unit area along the propagation direction of the imaging beam. Hence, the column density is given by

$$n(x,y) = -\frac{1}{\sigma} \ln\left(\frac{I}{I_0}\right). \tag{3.14}$$

This requires acquiring two images taken in succession: one reference image without atoms (I_0), and one with the atoms present (I). This approach compensates for imperfections in the imaging path, such as dust, scratches, or inhomogeneities. Additionally, to correct for background signals, a third image is taken without the absorption beam, yielding the background level I_{bg}. In that case, Eq. 3.14 becomes

$$n(x,y) = -\frac{1}{\sigma} \ln\left(\frac{I - I_{\mathrm{bg}}}{I_0 - I_{\mathrm{bg}}}\right). \tag{3.15}$$

An example of a typical set of absorption images is shown in Fig. 3.17

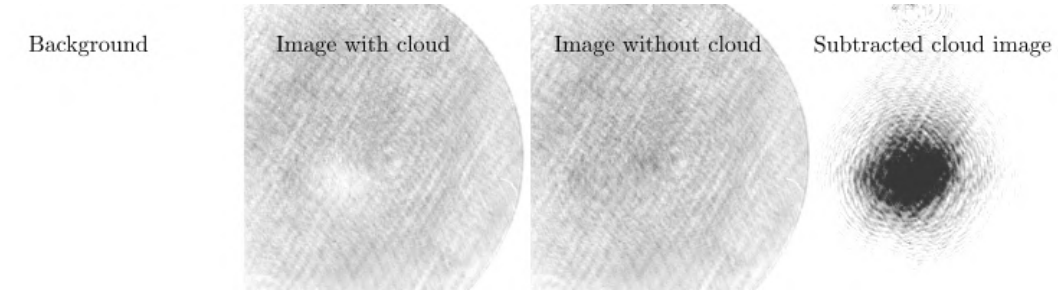

Figure 3.17: Typical set of images used to extract atomic cloud profile from absorption imaging. From left to right: first image shows the background, the second shows the cloud (visible as a brighter spot near the center), the third shows the probe beam without atoms, and the fourth is the result of subtraction according to equation 3.15.

Having determined the column density and knowing the real-space pixel area $(A_{\mathrm{m/px}})^2$ from calibration, the total number of atoms N is calculated as

$$N = \sum_{x,y} n(x,y) \times (A_{\mathrm{m/px}})^2. \tag{3.16}$$

To determine the cloud's peak density, additional steps are required. Absorption imaging is always performed after a short time-of-flight expansion, allowing the trap and the fields to switch off. Although this delay is usually short, it can introduce systematic errors in determining the initial cloud size. Therefore, we employ the time-of-flight (ToF) method, in which the trap is switched off and absorption images are taken at several different times after release of the sample. The evolution of the cloud size is then extrapolated to $t = 0$. Assuming a Gaussian spatial profile with initial width σ_0 and expansion governed by the thermal velocity $v = \sqrt{k_B T/m}$, the size of the cloud evolves as

$$\sigma(t)^2 = \sigma_0^2 + \frac{k_B T}{m} t^2. \tag{3.17}$$

Fitting a curve of the form $y = b + at^2$ yields both the initial size $\sigma_0 = b^{1/2}$ (at $t = 0$) and the temperature $T = m/k_B \times a$. Figure 3.18 shows an example of the free expansion of cesium atoms along with photos of the cloud at three different expansion times.

In all the results presented in this thesis, the absorption imaging was performed using the cycling transitions ${}^2S_{1/2}F = 2 \rightarrow {}^2P_{3/2}F = 3$ for ^{39}K and ^{41}K, ${}^2S_{1/2}F = 9/2 \rightarrow {}^2P_{3/2}F = 11/2$ for ^{40}K, and ${}^2S_{1/2}F = 4 \rightarrow {}^2P_{3/2}F = 5$ for ^{133}Cs. Absorption imaging was always preceded by optical pumping to the appropriate hyperfine state, as discussed in the previous section.

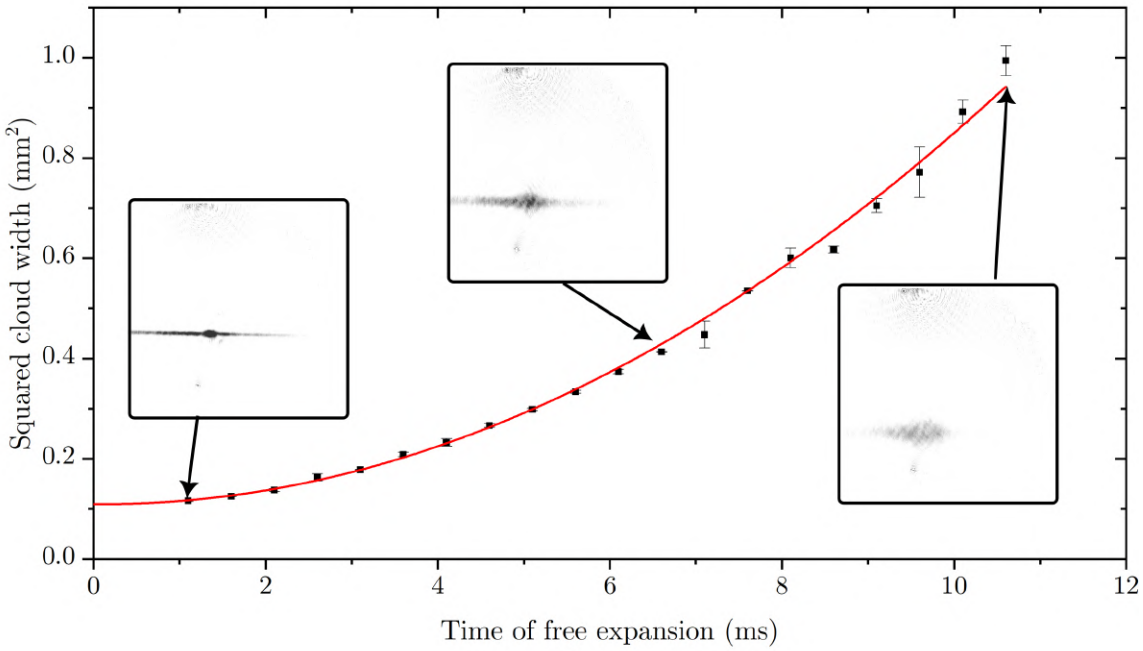

Figure 3.18: The width of the cloud along gravity, released from an optical dipole trap, as a function of free expansion time (black squares), with fitted theoretical curve (red line). Examples of absorption images at three stages of expansions are also presented.

These techniques are essential to determine the atom number, temperature, and density, thereby allowing the derivation of other essential parameters characterizing the cloud. However, absorption imaging has several limitations. First, it relies on rapid switching of the imaging beam, typically achieved using acousto-optic modulators. In practice, the finite response time of these devices introduces uncertainty and noise in the imaging signal. Perhaps most importantly, absorption imaging becomes inefficient for small or dilute samples. In such cases, detecting the difference in transmitted light becomes challenging and it might be hard to reliably measure properties of the cloud of atoms. In these regimes, fluorescence imaging offers a much more sensitive alternative, especially if the primary measure of interest is the atom number or the *change* in the number of atoms caused by some physical phenomena that is investigated. A comparison between an absorption and fluorescence image taken with the same but small number of cesium atoms ($< 10^6$) is shown in Figure 3.19.

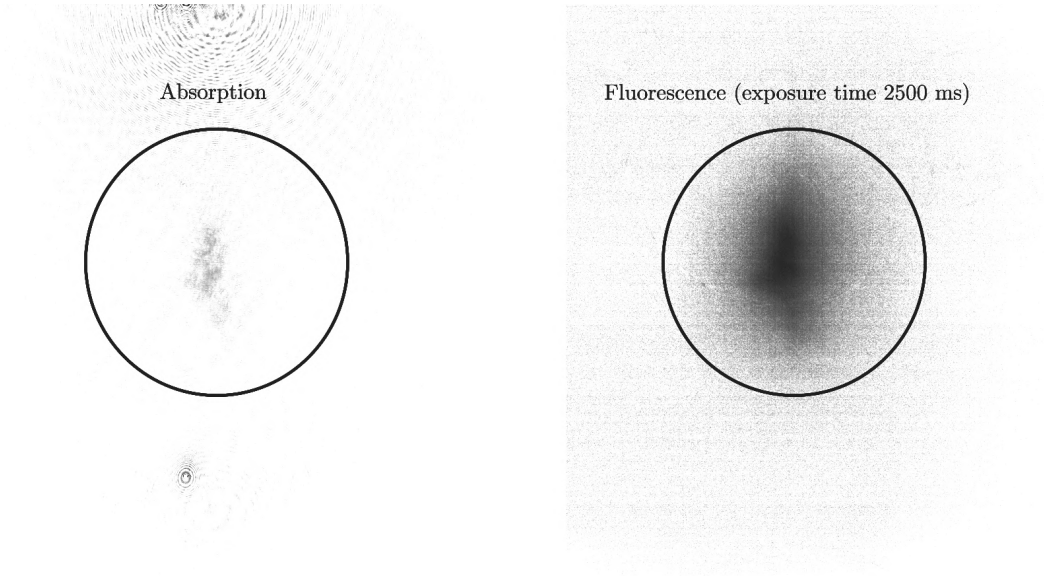

Figure 3.19: Images of cesium atoms obtained via absorption imaging (left), and fluorescence imaging with an exposure time of 2500 ms (right)

The fluorescence imaging relies on the detection of photons emitted during the spontaneous decay of an excited state. This allows the simultaneous excitation of two transitions in an optical molasses configuration and the collection of the resulting fluorescence signal over an extended period. In our experimental setup, the signal acquisition time (or exposure time), was restricted to a maximum of 20 ms. Prolonged imaging durations resulted in the distortion of the atomic cloud, affecting the precision of the atom number or temperature determination.

Extracting the number of atoms from fluorescence imaging is not straightforward, especially when the alignment of the MOT beams or the exposure time varies throughout the experimental sequence. In some cases, a magnetic trapping field gradient may be applied to extend the fluorescence collection time but this makes the quantitative analysis of fluorescence quite complicated. To address the challenging calculation of the number of atoms, we adopted a robust and frequently used approach: for most of the measurements, we computed the total pixel brightness after background subtraction.

This method involves acquiring two images—one with atoms and one without—and subtracting them to isolate the actual cloud image, free from background fluorescence caused by the imaging beams. Unfortunately, a 40 ms delay between the two exposures makes the measurements sensitive to fluctuations in the beam in-

tensity, polarization, or frequency, resulting in artifacts in the subtracted image. To suppress this effect, K. Dinçer proposed an additional background subtraction procedure tailored to our setup. For each fluorescence image, two regions are defined: one encompassing the atomic cloud and another without any atomic signal. In the first region, the number of pixels n and their total brightness s are calculated; in the second, the average pixel brightness m is determined to quantify residual background due to imperfect subtraction. The corrected brightness of the atomic sample, s_r, is then given by

$$s_r = s - m \times n \tag{3.18}$$

This technique is well-suited for detecting atom loss or optimizing trap alignment. However, precise determination of sample parameters, such as phase-space density, requires an accurate measurement of the number of atoms.

To calibrate the fluorescence signal such that it gives a trustworthy estimation of the number of atoms, we need to establish a relation between the brightness of the fluorescing cloud and the actual atom number. We obtain the latter using absorption imaging. To verify the relationship between these two methods, we recorded the MOT loading curve using both techniques and confirmed that the proportionality was maintained as the atom number increased. The results of this comparison are presented in Figure 3.20.

The presentation of the employed detection methods could end at this point, but it is worth briefly mentioning the software employed to analyze the parameters extracted from the images. A significant part of the experimental control system was developed by K. Dincer and P. Arciszewski, with the latter also creating software that enabled fast data processing. This allowed near real-time visualization of images following each imaging sequence, graphical selection of regions of interest, parameter extraction through a user-extensible set of analysis functions that can be defined by the user, and visualization of results via automatically generated plots [99].

However, the detection techniques described above suffer from one fundamental limitation: they are insensitive to the internal magnetic state of the atoms. As discussed in Section 2, the observation of Feshbach resonances requires precise knowledge of the input collision channels, which are determined by the magnetic states of the interacting atoms. This makes it necessary to develop methods for determining the population of individual magnetic sublevels.

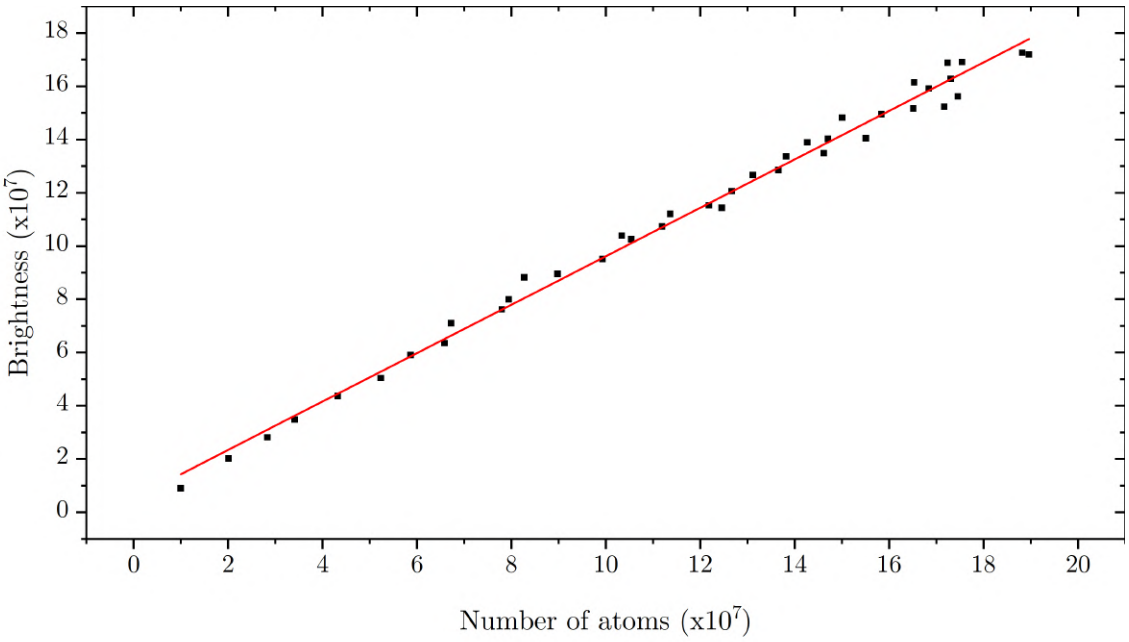

Figure 3.20: Brightness of the atomic cloud measured via fluorescence imaging as a function of the atom number determined from the absorption imaging. The red line is a linear fit, indicating a proportional relationship between the two quantities.

3.7 Spin-State selective imaging

The knowledge of a spin composition of a trapped atomic sample is crucial for assessing the expected collisional properties of atoms. It is also necessary to monitor the efficiency of optical pumping which we implement to enhance the signal in the Feshbach spectroscopy studies or in the transfer of atoms into the magnetic trap. In the latter, we would like to prepare atoms in a stretched Zeeman state that experiences the strongest confinement. In such a case, the cloud compression, collision rate, and therefore thermalization efficiency are all maximized.

In spectroscopic measurements, spin-state control is essential, as different states couple differently to the magnetic field. This alters the position and width of observed loss spectra. In the photoassociation spectroscopy, where a high density of molecular transitions originating from various spin configurations exists, the absence of spin-state control may result in missing important lines or misassigning them, potentially leading to incorrect determination of the molecular potential [100].

These examples underscore the importance of the ability to prepare a sample

in a selected magnetic state, as discussed in the previous section. The remaining question is how to experimentally determine the spin-state distribution of a given atomic sample. This section describes imaging methods developed for determining the spin state of potassium and cesium atoms.

The most common method for obtaining spin-resolved imaging relies on the Stern–Gerlach separation induced by the magnetic field gradient. Consider, for example, the $F = 3$ ground state of cesium, which contains magnetic sublevels $m_F = \{-3, -2, ..., 2, 3\}$. Due to the Zeeman effect, these sublevels experience different energy shifts in a magnetic field. In the linear Zeeman regime (see Eq. 2.1), the energy shift is proportional to m_F. The force acting on atoms in a magnetic field gradient is given by $F = -\mathrm{d}E/\mathrm{d}z$, so atoms in different m_F states will experience different forces, leading to different accelerations. After a period of free evolution, this causes a spatial separation of the spin components. An example of such Stern–Gerlach imaging for a spin mixture of cesium atoms belonging to the $F = 3$ manifold is shown in Fig. 3.21.

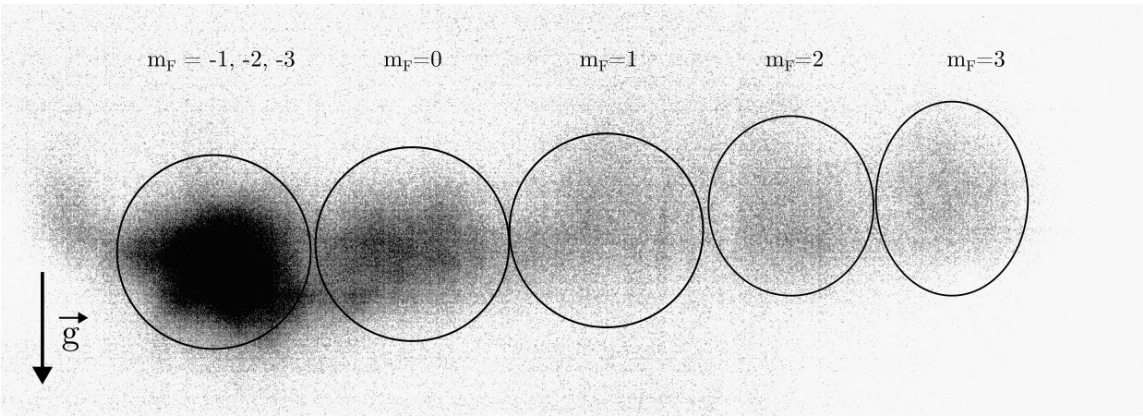

Figure 3.21: Stern–Gerlach separation of cesium atoms initially uniformly distributed between magnetic sublevels of the $F = 3$ manifold. The atoms were released from the optical dipole trap, and uniform horizontal magnetic field together with a magnetic field gradient was applied to obtain separation of the magnetic sublevels after 15 ms of time of flight. The majority of the population occupies the region of the magnetic trap, where low-field seekers are confined (leftmost image). High-field seekers, on the other hand, are repelled from the magnetic field minimum (remaining images). As a result, clouds corresponding to these states can be individually imaged. Significant drop in the density of the cloud can be observed.

The vertical Stern–Gerlach separation initially appeared infeasible in our setup.

It typically requires combining coils that produce a strong vertical homogeneous bias field (such as Feshbach coils) with additional coils that generate a magnetic field gradient (such as MOT coils). When the uniform magnetic field is sufficiently large, the local curvature of the magnetic field around the atomic cloud in the transverse directions becomes negligible. As a result, the field gradient is effectively flat in these directions and no distortion of the thermal distribution of the cloud is expected. However, in our setup both the gradient and the bias field coils are aligned horizontally. This has two significant consequences: first, it is difficult to shift the magnetic field minimum downward along the direction of gravity to achieve a homogeneous gradient along the vertical axis and to obtain magnetic levitation; second, the field gradient in the horizontal direction is inherently twice as strong, which enhances unwanted cloud dispersion. Despite these challenges, K. Dinçer managed to achieve vertical Stern–Gerlach separation in his doctoral work, although the resulting clouds were strongly dispersed, as shown in Fig. 3.22.

To avoid dilution of the cloud, which for small samples (e.g. ^{41}K) can make individual spin states undetectable, we extended this technique to allow spin separation along the horizontal axis. At low temperatures (< 30 μK), atomic clouds remain within the imaging region for about 20 ms of free fall. This makes it possible to apply a weak magnetic gradient—insufficient for levitation—that separates spin states horizontally without significantly spreading the cloud vertically. To illustrate the difference between vertical and horizontal separation under comparable conditions, Fig. 3.21 shows measurements performed with ^{133}Cs. Using the same atomic species in both horizontal and vertical separation cases ensures that the observed contrast is not affected by differences in the sample size or its temperature. In this configuration, excessive dilution is prevented and reliable spin-state resolution is achieved.

This method is fast and effective, but not without limitations. Suppose we image ^{41}K atoms in the $F = 1$ state after an optical dipole trap stage, where the atom number (on the order of 1×10^5) limits signal visibility regardless of the imaging technique. In such cases, applying a magnetic field and allowing sufficient free fall for Stern–Gerlach separation may dilute the clouds and reduce the visibility of individual m_F states below the detection threshold. Especially in a non-polarized sample, the number of atoms in each magnetic sub-level in such a case would reach 3×10^4. A more favorable solution in this case is a method that does not require free fall.

An alternative approach developed in this work is based on absorption imaging combined with a so-called RF pumping. After releasing the atoms from the trap, a small homogeneous magnetic field ($B < 1$ G) is applied to remove the degeneracy of the magnetic sublevels. Then, an RF field is used to transfer population between ground-state hyperfine levels. For example, the transition $^2S_{1/2}, F = 1, m_F =$

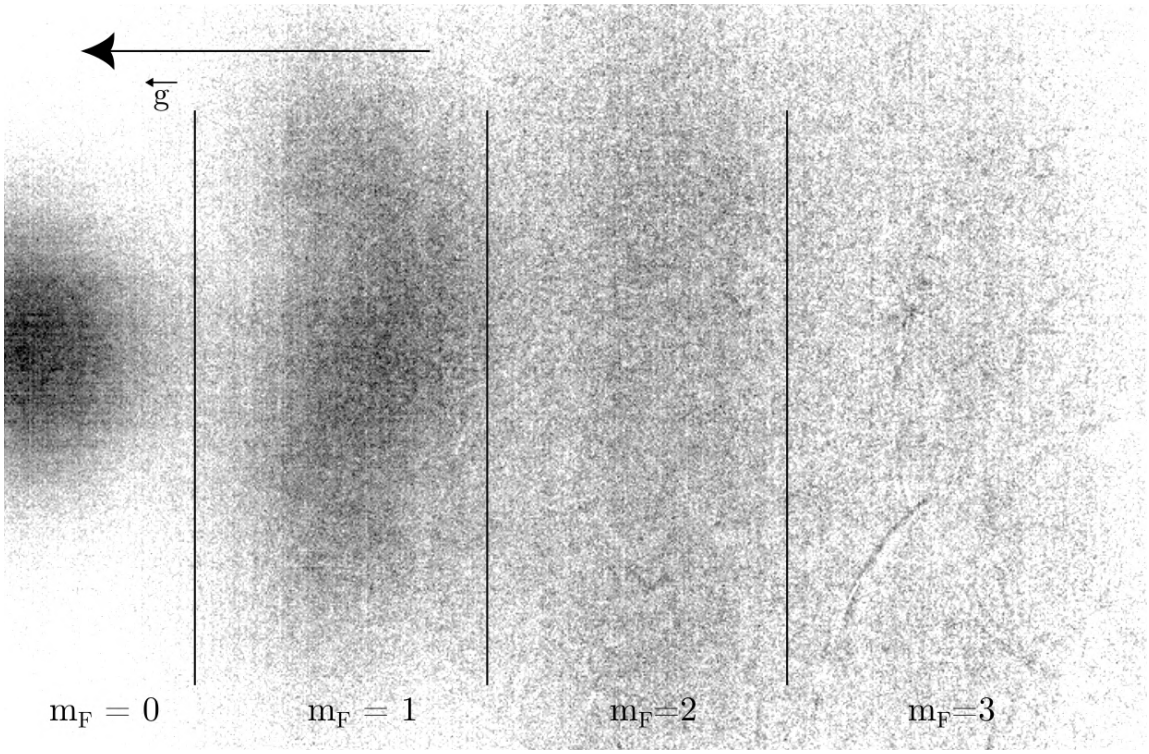

Figure 3.22: Vertical Stern–Gerlach separation of cesium atoms released from the optical dipole trap. To facilitate comparison with Fig. 3.21, atoms were also prepared in all magnetic sublevels of the $F = 3$ state, and released from the optical dipole trap. The image has been rotated by 90° such that the direction of separation agrees with Fig. 3.21. The direction of gravity is indicated by the arrow in the top-left corner.

$1 \rightarrow^2 S_{1/2}, F = 2, m_F = 1$ is forbidden for electric-dipole coupling but allowed as a magnetic-dipole transition. This mechanism allows atoms initially in a dark state (e.g., $F = 1$, $m_F = -1, 0, 1$) to be pumped into a bright state (e.g., $F = 2$, $m_F = -2, -1, ..., 2$) that can be detected via absorption imaging. This provides complete control over which spin states are made visible. An example measurement of the number of ^{41}K atoms as a function of the RF frequency—with and without pumping—is shown in Fig. 3.23. These measurements were performed when 0.37 G field was applied, but due to the residual magnetic field of 50 mG remaining after optical pumping, these transitions are visibly shifted.

Two conclusions can be drawn from the Fig. 3.23. First, the relative number of atoms observed for different transitions reflects the initial population distribution

among the spin states. Second, the measurements provide very high precision in determining the magnetic field. This aspect will be discussed in details in Chapter 4.

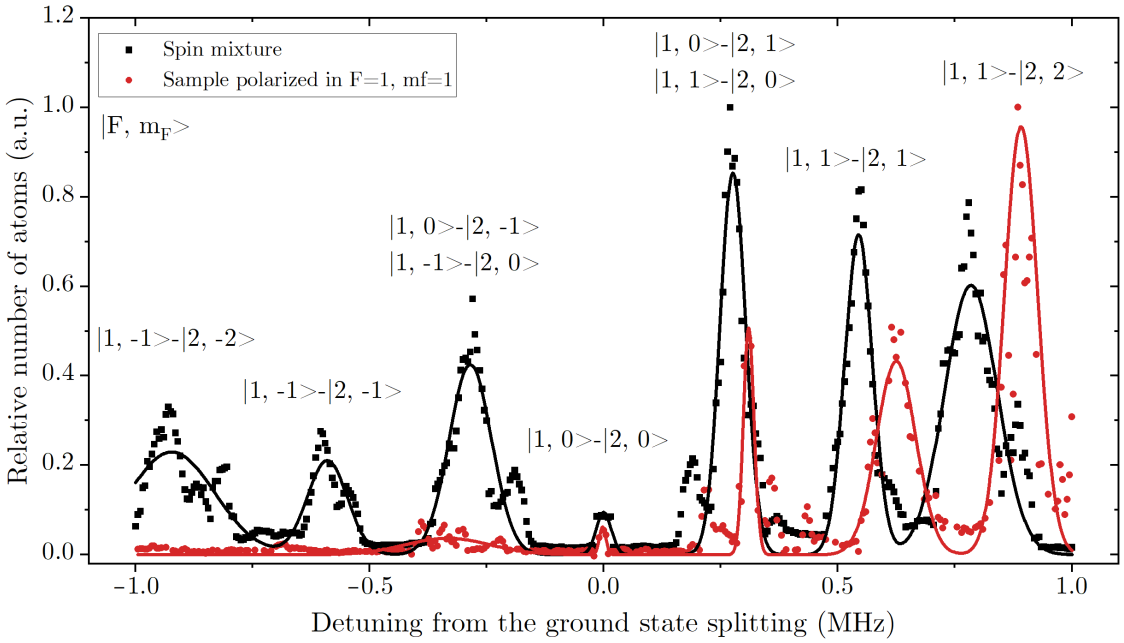

Figure 3.23: The number of detected atoms after RF spectroscopy in a low magnetic field. The black data points correspond to an atomic cloud initially prepared as a spin mixture, while the red data points are atoms optically pumped to the $|F = 1, m_F = 1\rangle$ state before the RF spectroscopy is performed. Transitions are labeled using $|F, m_F\rangle$ notation. Both datasets were independently normalized, as only relative amplitudes between different m_F states are important from the perspective of the presented method. The exact location of each transition has been determined from fits of gaussian functions (black and red lines, color coding like for data points).

This method is general and applicable to all atomic species that possesses a magnetic moment, but it has certain drawbacks. First, it is relatively slow — a reliable measurement requires several data points in order to resolve the transition in a way that allows fitting a Gaussian or a Lorentzian profile to estimate the amplitudes. More importantly, reliable spin-state determination requires precise control over the pumping duration. When a single transition between two states is driven and only one state is initially populated, the system exhibits long-lived Rabi oscillations with slow decoherence, appearing due to the long lifetime of both states and the absence of other nearby transitions. The population oscillates between the two states, and

the measured absorption signal reflects these oscillations. Only after an interrogation time longer than the decoherence time do the populations equilibrate between the two states. An example of Rabi oscillations between $F = 1, m_F = 1$ and $F = 2, m_F = 2$ states with the Rabi frequency $\Omega = 2\pi \times 1.67$ kHz is shown in Fig. 3.24. The pumping duration must be carefully chosen to reflect the real spin populations and not just the population at a given stage of Rabi oscillations. A precisely chosen time is important for the reliable determination of the amplitude of the signal, but it is also crucial to keep the same time between each data point for meaningful measurements. What if the sample is initially invisible to absorption imaging? In the case of fermionic potassium, ^{40}K, we were able to trap at most 5×10^5 atoms. If these are equally distributed among the $F = 9/2$, $m_F = \{-9/2, ..., +9/2\}$ states, each contains roughly 5×10^4 atoms. This number is the noise level of our detection system is insufficient for absorption imaging. In this case, we developed an alternative, though less accurate method. It works only for the stretched states, but is still useful to estimate the spin-state population.

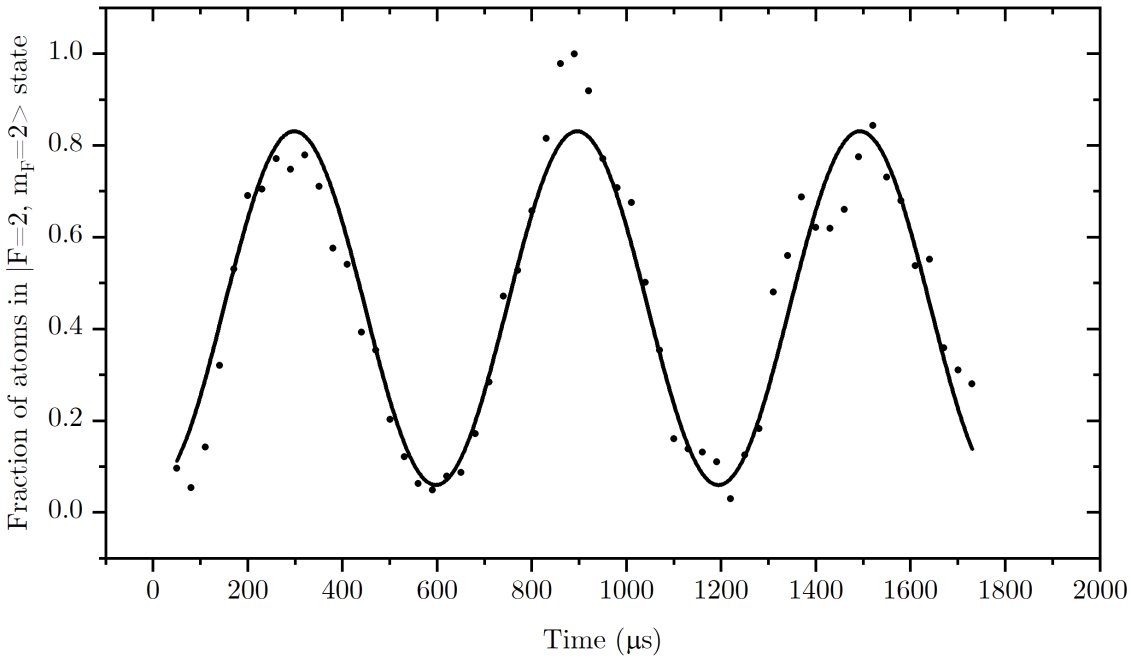

Figure 3.24: Rabi oscillations between the $F = 1, m_F = 1$ and the $F = 2, m_F = 2$ states. The fraction of atoms in $F = 2, m_F = 2$ is shown as a function of the pumping time t. A sine function (black line) is fitted to extract the Rabi frequency $\Omega = 2\pi \times 1.88(1)$ kHz.

The final method that we use to diagnose the spin composition of a sample is based on magnetic trapping. As emphasized previously, different spin states interact differently with a magnetic field gradient. A typical example is magnetic levitation, or trapping in a weak magnetic field gradient that merely compensates for the gravitational force acting on the atoms. Consider ^{39}K atoms as an example. Using the masses and magnetic moments given in Chapter 2, we can calculate the minimum gradient required for magnetic levitation. These values are shown in Figure 3.25. As can be seen, the minimum gradient required to levitate atoms in the $|F = 2, m_F = 2\rangle$ state is 6.85 G/cm, while for the $|F = 2, m_F = 1\rangle$ state it is 13.70 G/cm. In this case, determining the number of atoms in the stretched state ($m_F = 2$), or evaluating the optical pumping efficiency, becomes relatively straightforward. The protocol is as follows: in the first step, we magnetically trap (or levitate) a sample containing a mixture of spin states in a magnetic field gradient of approximately 13 G/cm. Under these conditions, a significant fraction of atoms in the $m_F = 2$ state will remain trapped, while atoms in the remaining spin states will fall out of the trapping region. Assuming that the initial population is equally distributed among all spin states and the total number of atoms is N, the magnetic trap will contain $N_{\mathrm{MT}} = n\eta N$ atoms, where the numerical factor $n = 0.2$ reflects the fractional occupation of the $m_F = 2$ state, and η denotes the trapping efficiency.

By measuring η and repeating the procedure for a spin-polarized sample, the number of trapped atoms N_{MT} can again be determined. The ratio $N_{\mathrm{MT}}/(\eta N)$ then provides a lower bound on the fraction of atoms occupying the $|F = 2, m_F = 2\rangle$ state. It should be noted, however, that optical pumping may lead to heating or expansion of the atomic cloud. Therefore, the method yields a lower limit on the population of the $|F = 2, m_F = 2\rangle$ state, i.e., that more than n of atoms occupy this state.

In this chapter, we discussed the methods used for cooling, trapping, and imaging atomic samples. Many of these techniques were applied for the first time to cool previously unexplored mixtures such as ^{41}K–Cs and ^{39}K–^{40}K. These methods enabled a broad range of experimental achievements: measuring three-body loss rates in ^{39}K–Cs and ^{41}K–Cs mixtures; observing Feshbach resonances in the ^{39}K–Cs system, including many previously unreported features (see Chapter 7); producing the world's first ^{41}K–Cs mixture and characterizing its collisional properties (see Chapter 8) and investigating interspecies interactions in the ^{39}K–^{40}K Bose–Fermi mixture (see Chapter 6). These results would likely not have been possible without the careful development of the methods described here, which largely justifies the length and technical depth of this chapter. The development and the first-time implementation of these techniques represent a significant part of the author's work and a unique contribution to modern atomic physics.

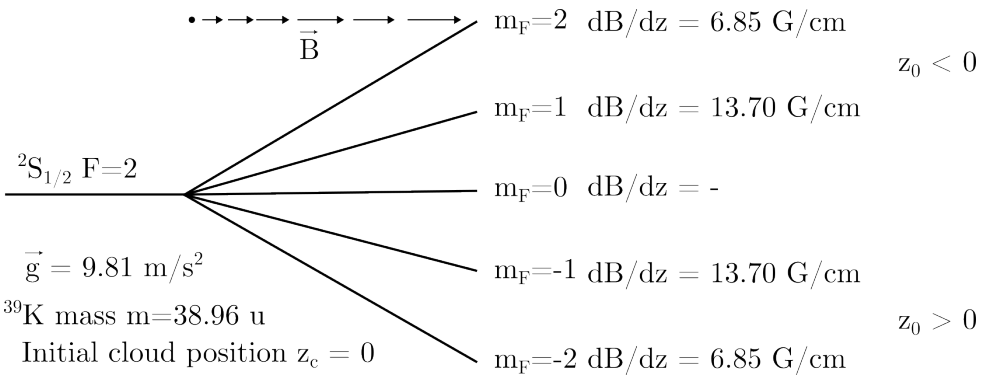

Figure 3.25: Magnetic structure of the $^2S_{1/2}, F = 2$ state of ^{39}K in a presence of magnetic field gradient. For each m_F sublevel, the minimal gradient required for magnetic levitation is shown. The cloud is initially at $z_c = 0$, with z increasing along the direction of gravity. The position z_0 marks the field center needed for levitation at the given gradient. For $m_F = 0$, levitation is impossible in the linear approximation of the Zeeman effect.

Naturally, applying such advanced cooling methods requires a substantial experimental infrastructure, much of which had to be designed and built from scratch. Fortunately, modern experimental physics is conducted within research teams, allowing different individuals to contribute to specific parts of the system. To properly acknowledge the contributions of all team members involved in constructing the apparatus—and to describe in detail the experimental platform that made these results possible—the next chapter is devoted to the technical aspects of the system.

Chapter 4

Ultracold atoms experiment at UW

In the preceding chapters, we presented the motivation behind our research, the properties of the atoms used, and the theoretical background of the investigated phenomena. We then introduced the theoretical and partially experimental framework underlying the cooling methods employed. However, for all of these elements to be meaningful and practically applicable, it is necessary to build and prepare an experimental apparatus in which the research can be carried out. In the context of cold atom physics, it is difficult to speak of "building an experimental setup" in the usual sense, as a complete system often occupies nearly the entire laboratory.

In cold atom experiments, many components must be developed and operate in harmony in order to reach even the first milestone—capturing atoms in a magneto-optical trap (MOT). The experimental apparatus includes laser systems (often consisting of several stages of beam preparation), the vacuum system, imaging system, sources of magnetic fields used for atom trapping or for defining the quantization axis, the experiment control system, and scripts or programs for data acquisition and analysis. Consequently—and this is admittedly a personal view—such systems cannot realistically be built by a single person. Instead, they are the result of collaborative work carried out by research groups, in which many people contribute to different aspects, often working in parallel on various components. Therefore, this chapter largely reflects the work not only of the researcher submitting this dissertation but also of other individuals who constitute the research team. While this may not be the appropriate place for formal acknowledgments, it seems important to clearly highlight the contributions of those most involved, especially:

- P. Arciszewski, who prepared the vacuum system, magnetic field coils, control system of the experiment, data analysis tools, and the first versions of the cesium laser setup;

- J. Dobosz, who contributed extensively to all of these components and additionally developed much of the essential electronics without which the experiment could not have reached its current level of functionality;
- K. Dincer, who developed the imaging system and refined many of the components, in particular the control infrastructure of the experiment;
- Dr. M. Semczuk, who guided the design of the majority of the experimental setup, consistently oversaw the construction and optimization process, ensuring that all parts were developed in the correct order, functioned together, and could be integrated into the aforementioned "harmony".

Over the course of several years, a fully functional laboratory was established from an almost empty room, resulting in a world-class experimental platform. A comparison between the state of the laboratory at the beginning of this PhD project, six years ago (2019), and its current state (2025) is shown in Fig. 4.1. This chapter is devoted to describing the key components of the experimental apparatus—beginning with a brief overview of the vacuum system and magnetic field sources, followed by the methods used for the laser frequency stabilization, and concluding with the implementation of the optical dipole trap. The stabilization methods are discussed here in detail, as they are rarely described in scientific articles despite being crucial for the reliable operation of the experiment. The design and the performance of the laser systems for cooling are presented in detail in chapters 6 and 7 and are therefore not discussed here. A comprehensive discussion of the experimental control and imaging systems can be found in the PhD thesis of Koray Dinçer [100].

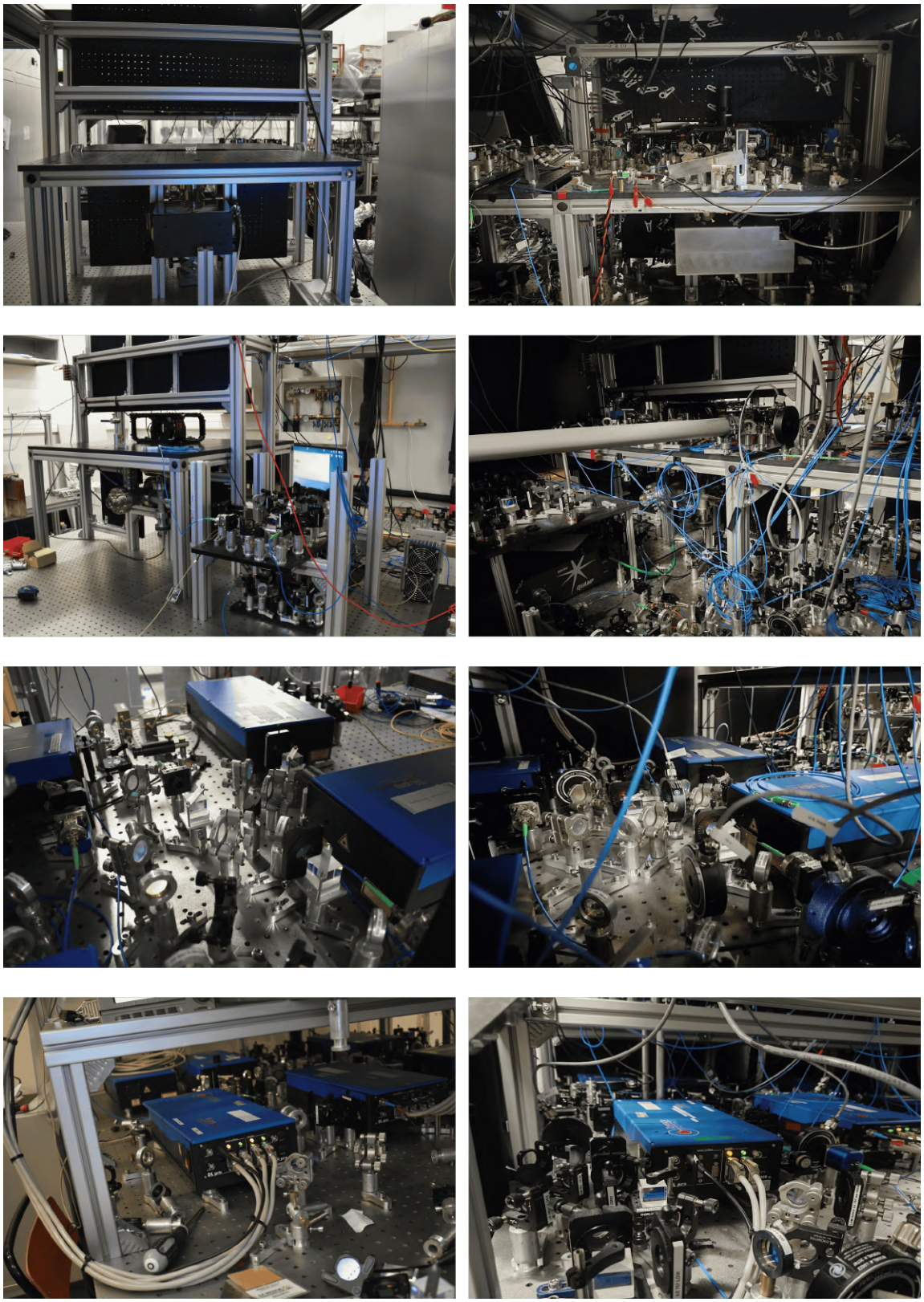

Figure 4.1: Photographs of the ultracold K-Cs experimental setup taken six years ago (left column) and its current configuration as of 2025 (right column). The top two rows show the main vacuum chamber surrounded by optics for the laser-beams distribution, while the bottom two rows depict the optical table with the main components of the laser system.

4.1 Vacuum system and magnetic field sources

The vacuum system used in this work, as well as the magnetic field coils, was constructed mostly by P. Arciszewski, whose master's thesis contains a detailed description of the preparation procedure and the motivation behind the chosen design. Therefore, in this section, we provide only a concise overview of the most relevant features of the apparatus as a more extensive discussion can be found in Ref. [101].

In cold-atom experiments, the performance of the vacuum system can strongly influence the achievable results, as each stage of the experimental sequence is sensitive to the residual gas pressure. This factor determines both the number of atoms that can be captured in the magneto-optical trap (MOT), limited by background gas collisions, and the attainable lifetimes in conservative traps, which in turn affect the efficiency of spectroscopy, evaporative cooling, and related procedures.

The apparatus employs a vacuum system in a single-chamber configuration, meaning that the atomic sources—two cesium dispensers and two potassium dispensers containing a natural isotopic mixture—are mounted directly inside the main experimental glass cell. Atoms released from the dispensers are captured in the MOT and are subsequently cooled in stages described in the previous chapter. This is one of the simplest possible configurations, as it lacks any additional sources of precooled atoms (such as a 2D-MOT) or devices for pre-cooling prior to capture, for instance, a Zeeman slower.

The simplicity of the design comes with trade-offs that cannot be fully assessed without measurements performed with cold atoms. For example, increasing the dispenser current to release more atoms, which could improve the signal-to-noise ratio at the final cooling stage, simultaneously raises the background gas density and thus enhances collisional losses, potentially reducing the lifetime in conservative traps to the point where no further measurements become possible. Consequently, in such systems, optimizing the balance between the number of atoms and the lifetime limited by the background gas collisions is crucial.

To determine the optimal balance between the number of atoms in the optical dipole trap and the background-limited lifetime, measurements were performed using ^{41}K atoms. For this purpose, the atoms were transferred into the optical dipole trap, where the $1/e$ lifetime (the time after which the number of atoms decayed to $1/e$ of its initial value) was measured. We typically observe a double-exponential decay, as illustrated in Fig. 4.2 for the dispenser current of 3.8 A, where it can be seen that during the first ~ 0.7 s the decay is very rapid, after which the characteristic decay time becomes significantly longer. We attribute the first decay to collisions within the atomic cloud and thermalization, while the second stage is already dominated by

collisions with the background gas. Based on these decay curves, we estimate that the second stage corresponds to the background-limited lifetime.

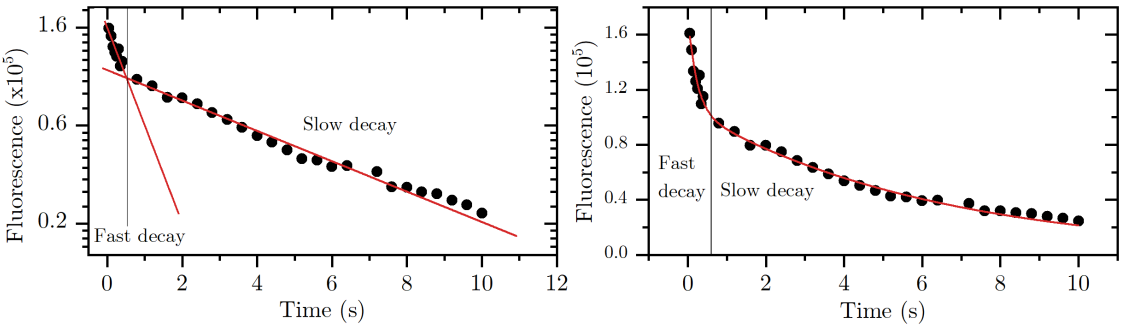

Figure 4.2: The decay curve of the fluorescence signal, proportional to the number of atoms in the optical dipole trap, plotted as a function of time on a logarithmic scale (left) and on a linear scale (right). The data were fitted with two independent exponential decays (left) and with a double-exponential fit (right). In each plot, the time range corresponding to the slow decay and the fast decay are indicated. Measurements were performed at a dispenser current of 3.8 A.

We characterized the number of trapped atoms and the lifetime in the optical dipole trap for dispenser currents ranging from $I = 3.0$ A to $I = 3.8$ A. The same experimental sequence was used for all measurements, leading to the curve shown in Fig. 4.3, which presents the trap lifetime and the initial number of atoms in the optical dipole trap as a function of the dispenser current.

From the graph, two important conclusions can be drawn. First, despite the simplicity of the vacuum system, it is still possible to achieve lifetimes reaching up to $\tau \approx 9$ s. Second, increasing the dispenser current above 3.8 A no longer improves the number of atoms, while it continues to reduce the lifetime in the optical dipole trap. Naturally, the situation presented here refers to the single-species scenario; in experiments with potassium–cesium mixtures, both dispensers must operate simultaneously.

For the spectroscopy experiments wit ^{41}K–Cs and ^{39}K–Cs mixtures described in this thesis, we identified suitable dispenser currents (3.2 A for both cesium and potassium) that yielded the number of atoms in the optical dipole traps exceeding $N > 10^6$ for each atomic species, while maintaining a background gas collision limited lifetime of $\tau_{\mathrm{BG}} \approx 4$ s. For reference, in the ^{41}K–Cs mixture the three-body recombination losses, which scale with density, limit the $1/e$ trap lifetime to $\tau_{3\mathrm{B}} \approx 1.7$ s, indicating that the measurement efficiency is constrained more by the three-body losses than

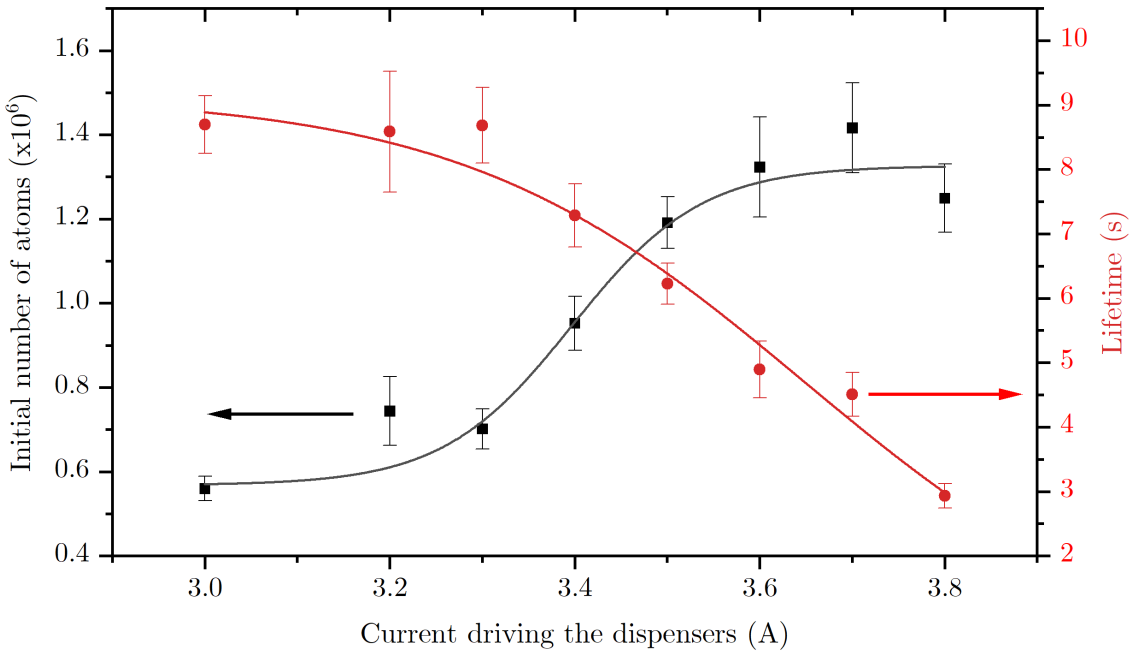

Figure 4.3: The plot shows the number of atoms in the optical dipole trap (left vertical axis, black squares) and their $1/e$ lifetime (right vertical axis, red circles) as a function of the dispenser current.The fits serve as a guide to the eye.

by the design of the vacuum system. Therefore, increasing the complexity of the vacuum setup would not have significantly improved the results.

The vacuum is maintained by titanium sublimation filaments (Agilent Technologies) connected to a sublimation pump, which is activated intermittently whenever a noticeable reduction in the lifetime is observed. Day-to-day pumping is provided by a 75 liters/second ion pump (Agilent Technologies VacIon Plus 75). This combination enables rapid recovery of the vacuum. For example, when working with the fermionic potassium isotope, the dispensers operate at relatively high currents (4 A) to compensate for the low abundance of the isotope [42]. This reduces the lifetime to $\tau \approx 0.6$ s. Under such conditions, Bose–Bose K–Cs spectroscopy would be impossible. However, after running the sublimation pump, while keeping the ion pump active, the lifetime solely due to the background collisions typically recovers to $\tau \geq 4$ s within a day.

The heart of the vacuum system is the glass science cell where the trapping region for all measurements is located. Three retroreflected, mutually orthogonal laser beams pass through the cell and are used at different stages of cesium and potassium

laser cooling. While the frequencies and configurations of the beams vary between experimental stages, the same optical paths are shared. Consequently, all optical elements along these paths are achromatic, ensuring high reflectivity ($R \geq 97\%$) and precise control of polarization for both potassium and cesium light.

The cooling beams are relatively large, with $1/e^2$ diameters of approximately $w = 30$ mm, to provide a large spatial capture range. The final mirrors directing the beams onto the atomic cloud must therefore have diameters of at least 50 mm to accommodate 45° reflections. To provide optical access to the cell, the vacuum system is raised above the surface of the optical table and is supported by a frame made from aluminum profiles. This way we can set up several optical paths directly on the table and thus limit the number of optical components on the platform near the cell. In the vertical plane, additional optical breadboards are mounted that host two-inch optics dedicated to the preparation of the cooling beams, allowing efficient use of available optical access to the science cell (see top photos in Fig. 4.1). A rendering of the vacuum system, prepared by P. Arciszewski is shown in Fig. 4.4.

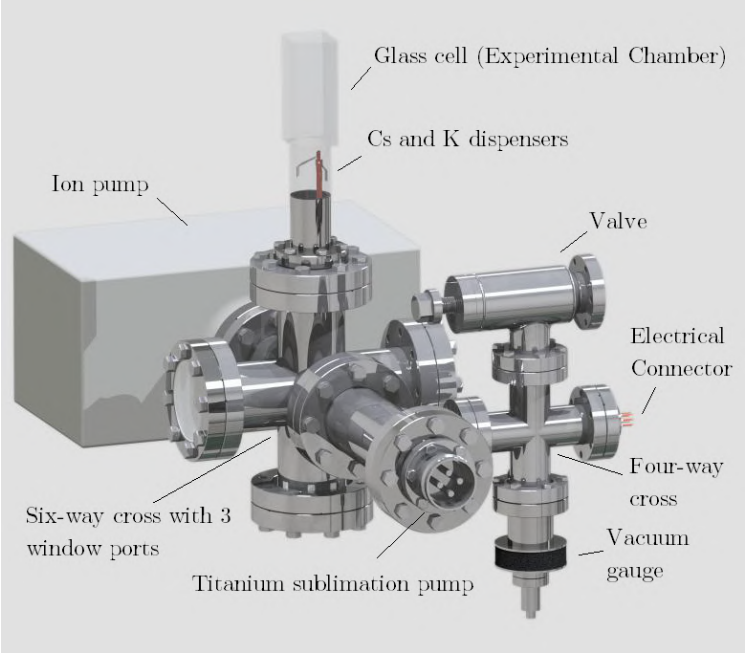

Figure 4.4: Rendering of the vacuum chamber prepared by P. Arciszewki.

To enable accurate density determination and reliable imaging of the atomic cloud from three orthogonal directions, the setup incorporates two objectives, which image the beam onto three cameras. Along the horizontal axis, a single camera is shared

between potassium and cesium atoms; in this case, the cloud image on the camera is not magnified.

Along the vertical axis, two cameras are used, separated by a dichroic mirror, which allows for simultaneous and independent imaging of potassium and cesium atoms. The imaging system has a magnification of four and was constructed in such a way as to enable both fluorescence and absorption imaging. A more detailed discussion can be found in the doctoral dissertation of K. Dinçer [100].

As mentioned in the previous chapter, many aspects of cooling, and even the feasibility of performing spectroscopy, are strongly dependent on the sources of magnetic fields. In our setup, the glass cell is enclosed in a cage of coils used both for precise compensation of external magnetic fields (e.g., during the gray optical molasses stage) and for defining the quantization axis during optical pumping. The precise current control and fast switching of the current flowing through the coils are provided by electronics that formed the basis of our publication [82], where the details of the design and specifications are discussed.

In addition to the compensation coils, the system includes additional two pairs of coils: producing fields in the Helmholtz configuration (e.g., for Feshbach spectroscopy - called here the Feshbach coils) and in the anti-Helmholtz configuration (for trapping in a MOT or a magnetic trap - called here the MOT coils). The coils are powered by two 'Delta Elektronika' power supplies, delivering up to 45 A (anti-Helmholtz) and 70 A (Helmholtz) of current. These current values, with the utilized design of the coils, provide a maximal gradient of the magnetic field of 57.6 G/cm along the direction of gravity (115.2 G/cm along the coil axis) and a uniform magnetic field of about 510 G. In the standard configuration, the magnetic field decay is relatively slow, and can reach even 50-100 ms, which can cause issues during various experimental stages. For example, after compression in the magneto-optical trap, where the 45 A current flows through the coils, the next stage is gray molasses cooling, for which even small residual magnetic fields can significantly affect the achievable number of atoms and the final temperature. To reduce the field turn-off time, a MOSFET-based circuit was implemented, allowing the maximum field to be switched off in less than 200 μs. A more detailed discussion of the magnetic field switching system can be found in the doctoral dissertation of J. Dobosz [69], while the design and initial characterization of the coils using a Hall effect sensor are presented in the thesis of P. Arciszewski [101].

The ability to precisely determine the magnetic field is crucial for spectroscopy of Feshbach resonances. Therefore, a calibration was performed using a single-loop antenna (see Fig. 4.5) constructed by P. Arciszewski that was used to drive transitions between the Zeeman sublevels $^2S_{1/2}\, F = 1, m_{\mathrm{F}} \rightarrow {}^2S_{1/2}\, F = 2, m'_{\mathrm{F}}$ of ^{41}K atoms. For

Figure 4.5: Photo of the single-loop wire in the 3D-printed housing used as an antenna for the calibration of the magnetic field.

this purpose, the atoms were loaded into an optical dipole trap and optically pumped entirely into the ${}^2S_{1/2}\,F = 1$ state (without selective pumping between magnetic sublevels). Then, a magnetic field B_{tot} was turned on using Feshbach or compensation coils. After 100 ms of settling time for the field to stabilize at its setpoint, an RF signal of frequency ν was applied via the antenna and held on for 500 ms, longer than it is needed to reach a full decoherence of Rabi oscillations between the magnetic sublevels. This resulted in an even distribution of population between the m_F and m'_F states, limiting the sensitivity of the process to the pumping time. Subsequently, the field was switched off within another 100 ms, which is a sufficiently long time even in the absence of a dedicated fast-switching circuit, and the sample was imaged using absorption imaging on the ${}^2S_{1/2}\,F = 2 \rightarrow {}^2P_{3/2}\,F = 3$ transition. Thus, atoms could only be detected if a magnetic dipole transition occurred between Zeeman levels belonging to different hyperfine states. Knowing the transition frequency as a function of the magnetic field from the Breit–Rabi formula (see Eq. 2.2), this procedure allows for an accurate determination of the applied magnetic field B_{tot}. This relation can then be converted to the coil current, and in our system, it is even more advantageous to express it as a relation between the control voltage applied to the coils' power supply and the magnetic field.

By controlling the magnetic field along a given axis, for example B_x, the total field in the system can be written as

$$B_{tot}^2 = (B_x + B_{xs})^2 + B_{yz}^2, \tag{4.1}$$

where B_{xs} and B_{yz} denote the stray magnetic field along the x axis and in the perpendicular y and z axes, respectively. Consequently, when the magnetic field is controlled in our system through a voltage V applied to the power supply, the above

relation takes the form

$$B_{tot}^2 = (\alpha V + B_{xs})^2 + B_{yz}^2, \tag{4.2}$$

where α is the calibration coefficient that quantifies the dependence of the magnetic field on the applied voltage. By varying the voltage and monitoring the corresponding shift of a selected transition frequency we were able to use the Breit–Rabi formula to determine the magnetic field associated with that frequency. This way it was possible to calibrate all coils generating homogeneous magnetic fields used in the apparatus. A representative calibration curve for the Feshbach coils is shown in Fig. 4.6.

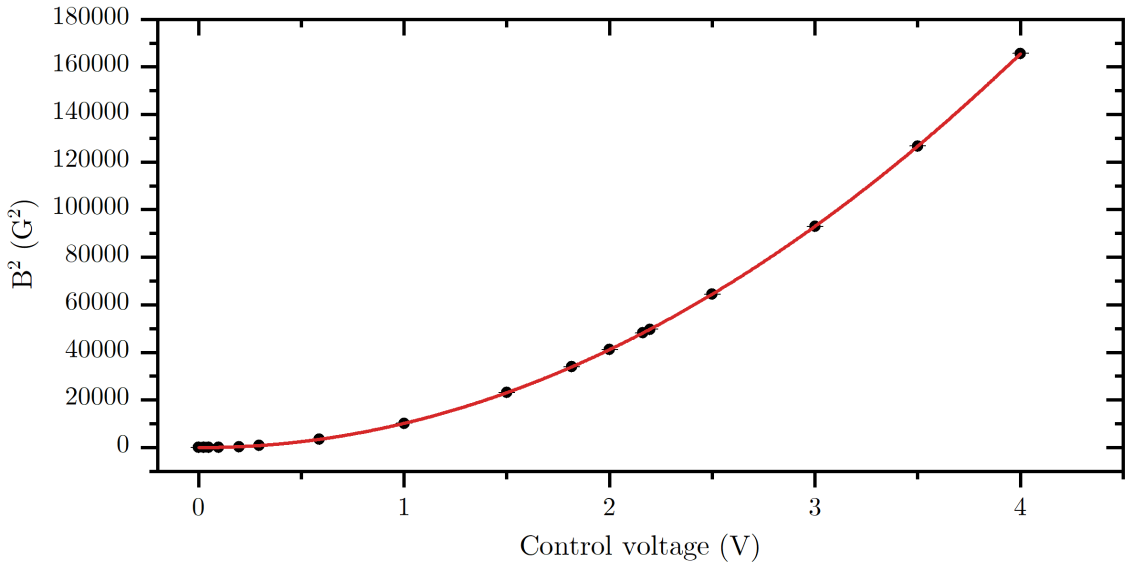

Figure 4.6: Calibration curve of the magnetic field generated by the Helmholtz coils. Each data point corresponds to a measured transition between magnetic sublevels of ^{41}K, from which the square of the applied magnetic field B^2 was calculated for a given control voltage V applied to the coil power supply. The red line shows the fitted curve corresponding to Eq. 4.2.

The calibration obtained in this manner, thanks to the very narrow linewidths of the transitions and the well-known analytical formula, enables the determination of the magnetic field with high precision. The calibration results for the three compensation coils and the coils used for Feshbach spectroscopy are presented in Table 4.1, which also includes results obtained independently by P. Arciszewski using a Hall sensor [101]. As can be seen, the results obtained using RF-spectroscopy and a Hall probe differ significantly. It should be emphasized that the Hall probe measurements

	Comp $\vec{x}$ (G/V)	Comp $\vec{y}$ (G/V)	Comp $\vec{z}$ (G/V)	Feshbach (G/V)
Hall effect sensor	5.964(24)	8.051(31)	2.561(26)	106.26(1.12)
RF spectroscopy	6.029(5)	7.759(14)	2.515(1)	101.996(33)

Table 4.1: Calibration coefficients α obtained for three compensation coils (Comp) oriented along the orthogonal directions ($\vec{x}$, $\vec{y}$, $\vec{z}$) and for the coils used in Feshbach spectroscopy (Feshbach). The results were determined with a Hall sensor and by using RF spectroscopy, with the latter used for interpreting all the data presented in the thesis.

were carried out six years ago, using a coil assembly that was not yet permanently mounted around the vacuum system but only placed in a temporary holder in the intended configuration. It is therefore possible that the holder experienced a slight misalignment during mounting in its final destination. Moreover, we cannot state with absolute certainty that the atomic cloud inside the optical dipole trap is located exactly at the geometric center of the coils.

The vacuum system, the imaging paths and objectives, and finally the magnetic field coils and their calibration are essential components of the setup that were discussed above. Without these elements, laser cooling of atoms would not be possible. However, working with cold atoms also requires advanced laser systems. Such systems are presented in the publications that form part of this thesis (see chapters 6 and 7). Unfortunately, scientific articles are usually concise in form and do not allow for a detailed description of certain crucial aspects of the apparatus. Therefore, the next two sections of this thesis are devoted to the methods of laser frequency stabilization and to the construction of the optical dipole trap setup.

4.2 Laser frequency stabilization

Laser frequency stabilization is essential in cold-atom experiments. Its quality affects not only the achievable temperatures and atom numbers but also the stability of these parameters between experimental runs. In some cases, the construction of the laser cavity and the electronics that control the current and the temperature of the laser diode provide sufficient passive stability for the active frequency stabilization to be unnecessary in some applications. For example, with our cesium lasers it is possible to load a magneto-optical trap and maintain a visible cold-atom signal for about 15 minutes without any active frequency stabilization methods. However,

for spectroscopic measurements in the optical dipole trap (such as the presented observation of the Feshbach resonances), measurements can span over 12–24 hours. If the sample parameters were to vary significantly between runs, the observation of the atom loss would not be possible. Thus, methods must be employed to ensure laser frequency stability over both short and long timescales.

In our experiment, specifically in the four MOPA (Master Oscillator Power Amplifier) systems used for cooling cesium atoms (two lasers: cooler and repumper) and potassium atoms (two lasers, one tuned to the D2 line and the other tuned to the D1 line), we rely on frequency stabilization electronics provided by the manufacturer of the laser. Each MOPA system (Toptica TA Pro) is equipped with a dedicated temperature and current controller (Toptica Digilock110), which, together with the software, allows for frequency stabilization using two PID controllers. However, such systems require a frequency reference that makes it possible to generate an error signal which enables unambiguous distinction if the frequency of the laser drifted above or below the frequency of the reference.

In our case, the reference signal is obtained by lock-in detection using Doppler-free saturated absorption spectroscopy of selected atomic transitions. For this purpose, we use Toptica CoSy (Compact Spectroscopy) modules equipped with a glass cell containing vapors of cesium or potassium. The operating principle of the module is straightforward. The incoming laser beam is split into two paths. In the first path, the light is split again, and each of the resulting probe beams passes through a glass vapor cell and is detected by separate photodiodes. In the second path, the light is directed to generate a counter-propagating pump beam, which overlaps with one of the aforementioned probe beams, producing a sub-Doppler (saturated absorption) signal. The other probe beam passes directly through the cell, yielding a Doppler-broadened Voigt profile. The two signals are then subtracted, resulting in a Doppler-free spectrum without the Voigt background. A schematic of this setup, together with exemplary spectra, is shown in Fig. 4.7.

Unfortunately, the employed modules allowed heating the cesium vapor cell only up to about 30–35°C and the potassium cell up to 40–45°C. While the cesium cell temperature was sufficient for the spectroscopy, in the case of potassium — especially for the D1 line, which has an oscillator strength about two times weaker than the D2 line — such a temperature did not provide adequate vapor pressure (see chapter 2) to obtain a signal with a signal-to-noise ratio high enough for a reliable frequency stabilization [103]. Therefore, a modification of the spectroscopy module was required, namely the addition of an extra heating source. For this purpose, the spectroscopy cell was removed from the module, and the original heating method was first identified. A set of resistors was glued in series along the lateral walls of

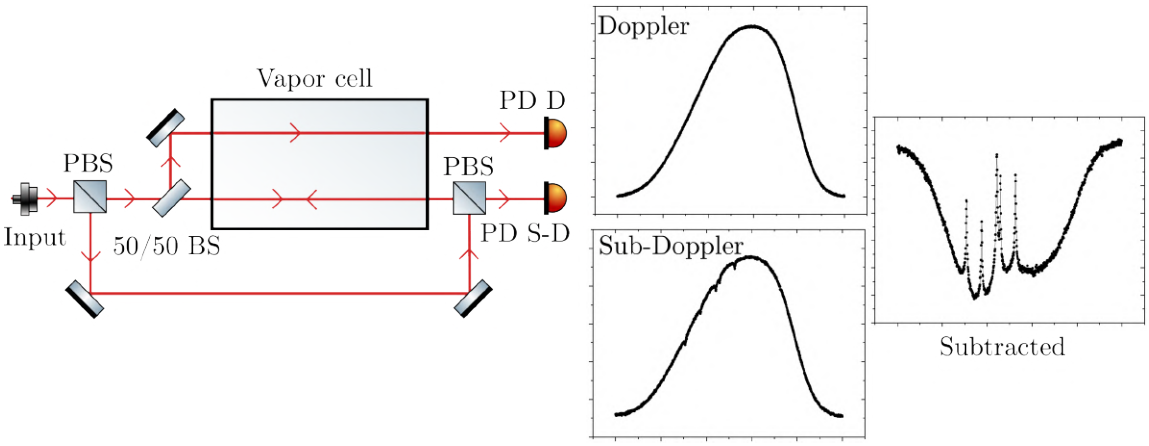

Figure 4.7: Typical setup for Doppler-free saturation spectroscopy. The beam entering the system from the fiber input (Input) is split into two paths at a polarizing beam splitter (PBS). In one path, the beam is further divided into two equal parts by a 50/50 beam splitter (BS), after which both beams propagate through a vapor cell and are detected on two separate photodiodes (PD). On the second path, the beam is retroreflected and overlapped with one of the previously described beams. In this way, the photodiodes record both the Doppler-broadened spectrum (PD D) and the sub-Doppler signal (PD S-D). Next to the photodiodes, three exemplary spectra obtained for cesium are shown: the Doppler-broadened spectrum, the sub-Doppler spectrum, and their differential signal. The concept of the figure was adapted from the CoSy module's manual. All schemes of optical systems throughout this thesis were prepared using the Optical Component library [102].

the cell, so that heating occurred mainly through two of its sides. A photograph of the Cosy system and spectroscopy cell with a visible set of the resistor arrangement is presented in Fig. 4.8.

This made it straightforward to raise the cell temperature by adding an independent power supply. Two additional holes were drilled on the side of the module, allowing the connection of an auxiliary power source and a PT100 temperature sensor. The PT100 sensor was glued directly onto the cell surface and used to monitor the temperature, which, with the applied current of 150 mA (and 19 V voltage), now reaches 65°C.

With this modification the transitions of interest became clearly visible. In order to avoid issues with the frequency dependence on the laser power common in the side-of-fringe locking technique, we stabilize the laser to the peak of the absorption profile by modulating the laser frequency by approximately the linewidth of the

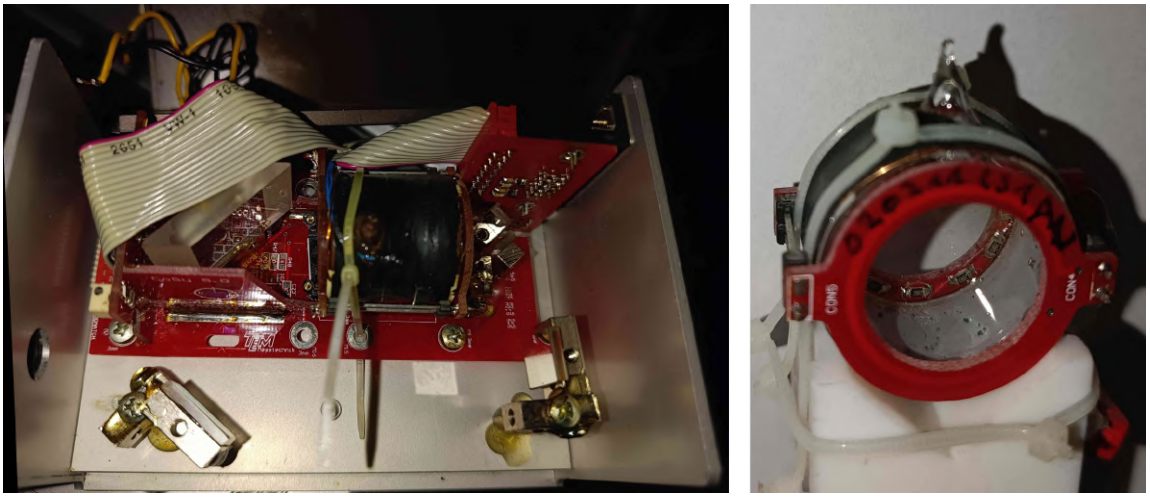

Figure 4.8: Picture of the interior of the CoSy system (left panel). The figure shows the fiber input (opening in the housing at the lower left side) and the glass cell (wrapped in black tape at the center of the system). Yellow and black cables (top left) connected as an additional heating source are also visible. The right panel shows a photograph of the spectroscopy cell removed from the CoSy module. Inside the cell, on the far wall, part of the resistor assembly can be seen.

atomic transition Γ with a modulation frequency of 20–60 kHz. The spectroscopy signal is then demodulated in the Digilock110 controller to obtain a lock-in detection signal. This approach makes the stabilization much more sensitive to frequency fluctuations while suppressing sensitivity to laser intensity noise, enabling reliable long-term frequency locking. This method is used in our setup for the stabilization of both cesium cooler and repumper lasers. Examples of saturation spectroscopy signals and lock-in detected signals for cesium cooler and repumper lasers are presented in Fig. 4.9.

Unfortunately, in order to maintain frequency stabilization, continuous modulation of the laser frequency is required. From the perspective of the atoms, this means that the effective spectral width of the laser is on the order of Γ, i.e., about 6 MHz. In the case of cesium, the large hyperfine splitting ensures that cooling still operates efficiently under these conditions. However, for potassium atoms, the small hyperfine splitting combined with the spectrally broadened cooling light significantly reduces the stability of the number of trapped atoms, lowering it by about 40% for ^{39}K. For this reason, it was necessary to extend the setup with an additional stabilization part.

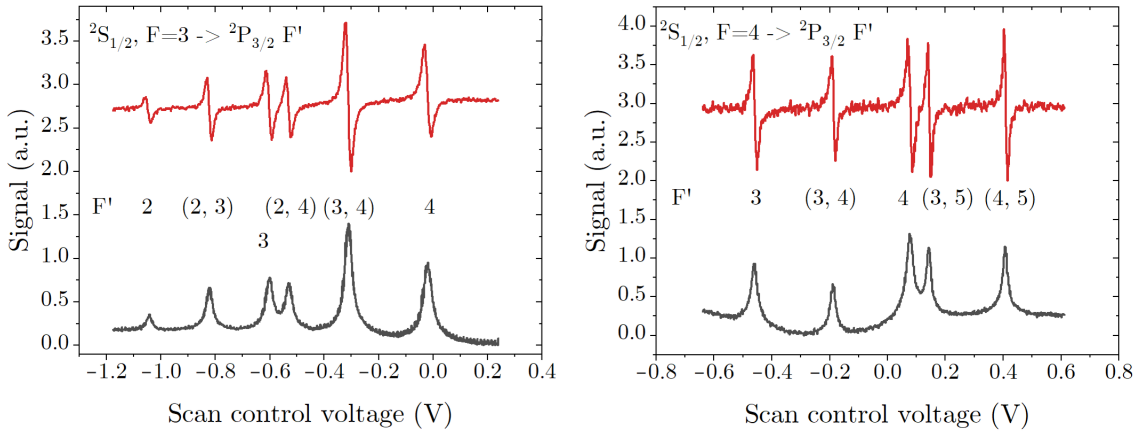

Figure 4.9: Saturated absorption spectroscopy signal for cesium, used for stabilizing the lasers used in laser cooling. The plots show the spectroscopy signal (black curve) together with the corresponding lock-in detection signal (red curve). The observed transitions are indicated, with the hyperfine ground and excited states labeled at the top. Between the curves, the labels mark which signal corresponds to a given hyperfine excited state F'. Values in parentheses denote crossover resonances between the indicated hyperfine levels.

To enable stabilization without broadening the spectral width of the cooling light, an optical setup was constructed in which an acousto-optic modulator (AOM) in a double-pass configuration is used to modulate the beams employed for spectroscopy. A fraction of the light from the optical amplifier (part of the MOPA system) is directed into an additional optical path containing the double-pass AOM with a central frequency of 110 MHz. After the second pass, the light is coupled into an optical fiber and delivered to the CoSy module. A schematic of this optical setup is shown in Fig. 4.10a).

To allow the AOM to operate at its central frequency while being simultaneously modulated, we used a voltage-controlled oscillator (VCO, Gooch & Housego 1080AF-AENO-2.0) connected to a homemade bias-tee, the schematic of which is shown in Fig. 4.10b). In this configuration, a DC power supply and the modulation signal from the Digilock110 are combined, producing a modulated voltage with a constant offset. This voltage drives the VCO, which converts it into a frequency-modulated RF signal for the AOM. The stabilization procedure is then carried out in the exact same manner as in the case of cesium. The main difference is that only the light sent to the spectroscopy module is frequency modulated and this very weakly translates int frequency fluctuations of the main beam used for cooling.

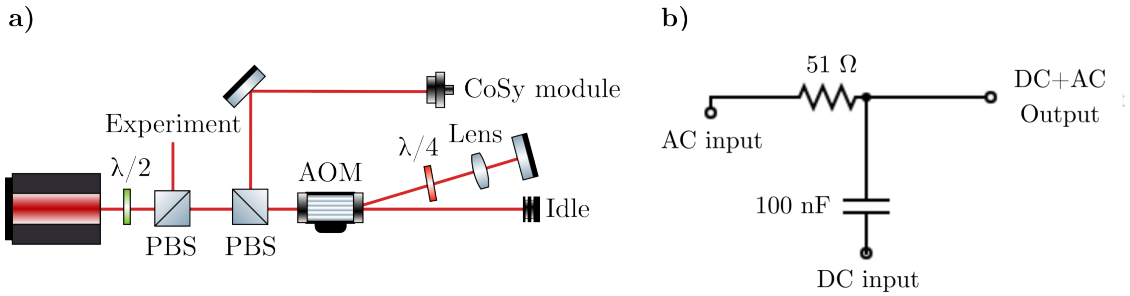

Figure 4.10: a) Optical setup used to obtain the spectroscopy signal. The beam exiting the laser passes through a half-wave plate ($\lambda/2$) and is then split by a polarizing beam splitter (PBS) into the experimental path and the stabilization path. In the latter, an acousto-optic modulator (AOM) is placed in a double-pass configuration using a quarter-wave plate ($\lambda/4$) and a lens. After the double diffraction, the beam is sent to the CoSy spectroscopy module. Panel b) shows the electronic schematic of the bias-tee circuit.

A drawback of this method is that the frequency modulation via the AOM also introduces amplitude modulation of the light, which leads to a considerably noisier sub-Doppler spectroscopy signal. Nevertheless, the generated error signal is sufficiently robust to allow reliable frequency stabilization. This method was applied to the lasers operating on the D1 and D2 lines of potassium, and an example of the obtained spectroscopic signal is shown in Fig. 4.11.

Spectroscopy signals presented in Fig. 4.9 are used to stabilize the cesium cooling and repumping lasers to the ${}^2S_{1/2}$, $F = 3 \rightarrow {}^2P_{3/2}$, $F' = 3$ and ${}^2S_{1/2}$, $F = 4 \rightarrow {}^2P_{3/2}$, $F' = 4 + 69$ MHz transitions, respectively. Prior to stabilization, the cooling beam is frequency-shifted by 69 MHz using a single-pass acousto-optic modulator. This shift ensures that the subsequent frequency tuning systems can operate in an optimal range of acousto-optic modulators during the different stages of the cooling sequence (see chapter 7).

For potassium lasers, the chosen transitions for stabilization are ${}^2S_{1/2}$, $F = 2 \rightarrow {}^2P_{3/2}$, F' and ${}^2S_{1/2}$, $F = 2 \rightarrow {}^2P_{1/2}$, $F' = 2$. Because of the small excited-state hyperfine splitting on the D2 line, the relevant F' states cannot be individually resolved. Therefore, the transition is typically denoted as generally addressing the excited state F'. It should also be noted that, prior to spectroscopy, the lasers are frequency-shifted due to the presence of double-pass acousto-optic modulators by 202 MHz and 250 MHz for the D1- and D2-line lasers, respectively.

As can be seen from this discussion, most stabilization methods initially relied

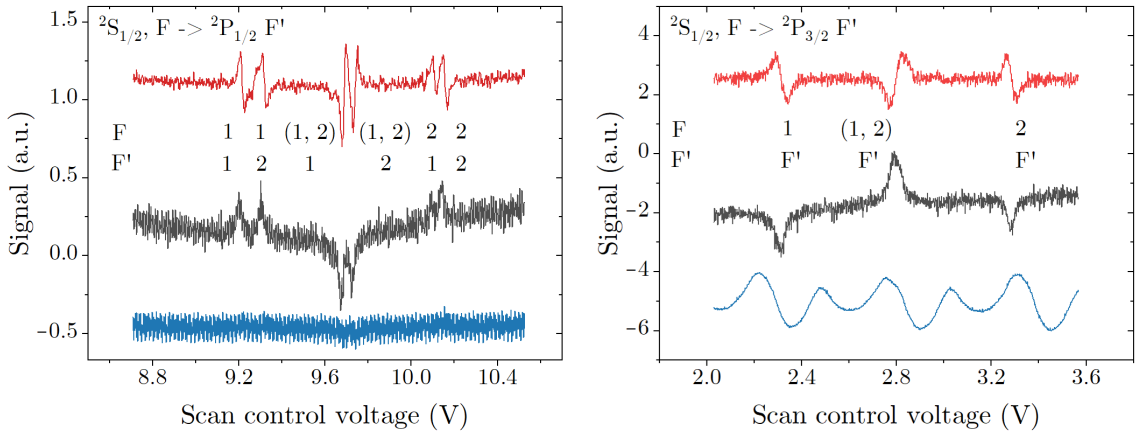

Figure 4.11: Saturated absorption spectroscopy signal of potassium, used for stabilizing the lasers applied in laser cooling. In both panels, the saturated absorption spectrum (black curve), the noisy spectrum with applied modulation (blue curve), and the lock-in detection signal (red curve) are shown. In the top-left corner of each plot, the fine-structure levels involved in the transition are indicated. Between the curves, the labels mark which transition corresponds to the ground- and excited-state hyperfine levels F and F'. Due to the small splitting of the excited-state hyperfine structure of the D2 line, only the F' label corresponding to all allowed sublevels of the $^2P_{3/2}$ state is shown. Values in parentheses denote crossover resonances between the indicated hyperfine levels.

on the procedures recommended by the equipment manufacturer, but these turned out to be insufficient. In experimental physics, it is common that systems which in theory appear straightforward to implement prove to be significantly more complex in practice. Nevertheless, through a series of modifications, lasers were stabilized with adequate precision to enable the complex cooling sequence. In the next chapter, we describe the optical dipole trap—the final stage of the experiment—which, despite its seemingly simple operating principle and nearly trivial construction, turned out to be even more challenging and required substantially greater effort than the stabilization methods presented here.

4.3 Optical dipole trap

The operation principle of optical dipole traps was discussed in the previous chapter 3. From an experimental perspective, the concept can be summarized by noting

that successful trapping requires a high-power laser beam, far detuned from any atomic resonance, which is tightly focused onto the cloud of ultracold atoms.

In our experiment we use "Azurelight 50 W" low noise fiber amplifier seeded by a fiber laser ("The Rock", NP Photonics RFLM-25-1-1064.46-1) producing approximately 15 mW of light at a wavelength of $\lambda_{\text{vac}} = 1064.40$ nm, with a manufacturer specified linewidth <5 kHz. The output of the amplifier is a single-mode Gaussian beam ($M^2 < 1.1$) with a power of about 42 W. It is divided into two paths, each passing through an acousto-optic modulator (AOM) with a central frequency of 110 MHz (Gooch & Housego 3110-197). One of the beams is coupled into an optical fiber, while the other is transmitted free-space toward the upper optical platform at the level of the glass science cell. The fiber-coupled beam, with power limited to P_D=4–12 W due to the damage threshold of the fiber, is later used to generate a tightly focused "dimple" trap. The free-space beam, carrying the remaining power, forms a large-volume optical dipole trap, hereafter referred to as the "reservoir trap".

The AOMs serve both as fast beam switches ($t < 100$ μs) and as reliable elements for intensity control. The optical layout on the optical table is shown schematically in Fig. 4.12.

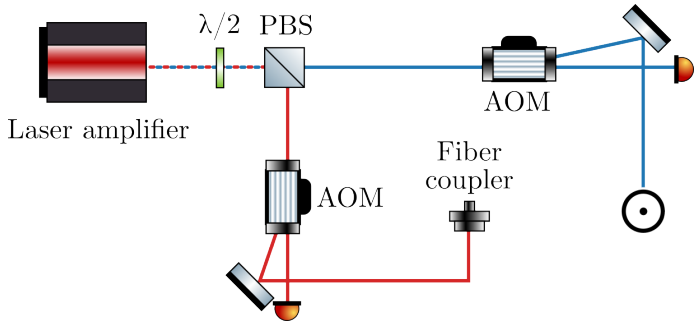

Figure 4.12: Laser system generating the beams used for optical trapping of atoms. The output beam from the laser is split into two paths by a half-wave plate ($\lambda/2$) and a polarizing beam splitter (PBS). Each path contains an acousto-optic modulator serving as a fast switch. The beam used as the dimple (red) is coupled into an optical fiber and delivered to the experimental chamber, while the reservoir beam (blue) is sent to the experiment in free space. The circle-with-dot symbol indicates that the beam is sent upwards towards the science cell located on an elevated platform.

On the upper platform surrounding the glass cell, a lens system ensures the focusing of the laser beams onto the atomic cloud. The reservoir beam is reduced in diameter by lenses $f = 250$ mm and $f = 500$ mm, and directed via a polarizing beam splitter onto a lens with a focal length $f = 250$ mm, which focuses it onto the atoms.

After passing through the cell, the beam is collimated, its polarization is rotated by 90° and with a help of two mirros the beam is sent again into the cell such that after a second focusing, it passes through the atomic cloud and crosses with the previous beam at an angle of 140°, thereby forming a crossed-beam dipole trap. Since both beams have the same frequency, the rotation of the polarization plane prevents an optical lattice from forming. This configuration is illustrated in Fig. 4.13.

The fiber-coupled beam is expanded by a telescope and overlapped with the reservoir path on the same polarizing beam splitter. The lenses are chosen so that, when focused on the atoms, the waist of the reservoir beam is $w_R \approx 220\ \mu$m, while that of the dimple beam is $w_D \approx 45\ \mu$m. The resulting laser system, including both beams, is shown in Fig. 4.13. The selected beam sizes, together with the available laser power, allow for the formation of an optical dipole trap with a maximum depth of $U = 170\ \mu\text{K} \times k_\text{B}$ ($U = 110.7\ \mu\text{K} \times k_\text{B}$) for the reservoir and $U = 1.17\ \text{mK} \times k_\text{B}$ ($U = 0.73\ \text{mK} \times k_\text{B}$) for the dimple trap in the case of cesium (potassium) atoms.

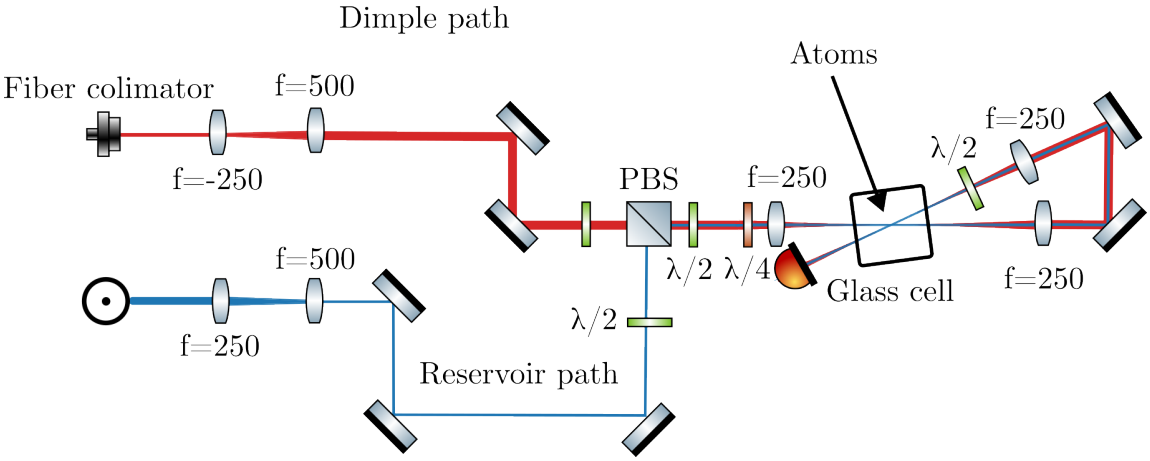

Figure 4.13: Laser system generating the optical dipole traps. The dimple beam (red) exits the optical fiber and is expanded using a telescope. Its polarization is then rotated with a half-wave plate ($\lambda/2$), after which it is overlapped with the reservoir beam at a polarizing beam splitter. Both beams are subsequently guided through a set of mirrors and lenses and are focused twice onto the atomic cloud. The reservoir beam propagates in free space and is reduced in size by a two-lens system before being combined with the dimple beam. In the figure, each lens is labeled with f, and its focal length is given in millimeters.

In this arrangement, we were able to trap $N_\text{Cs} \approx 3 \times 10^5$ cesium atoms and $N_{^{39}\text{K}} \approx 2 \times 10^5$ potassium atoms in single-species dimple traps with $P_D = 4$ W.

Depending on alignment, up to $N \approx 10^7$ atoms of both potassium and cesium could be captured in the reservoir trap operated at 32 W (the maximum power available after accounting for AOM losses). However, in this configuration, the atomic lifetime was severely limited to $t < 1$ s. In addition, for potassium, we observed the formation of a "hole" in the trap, at the crossing point of the beams, as illustrated in Fig. 4.14.

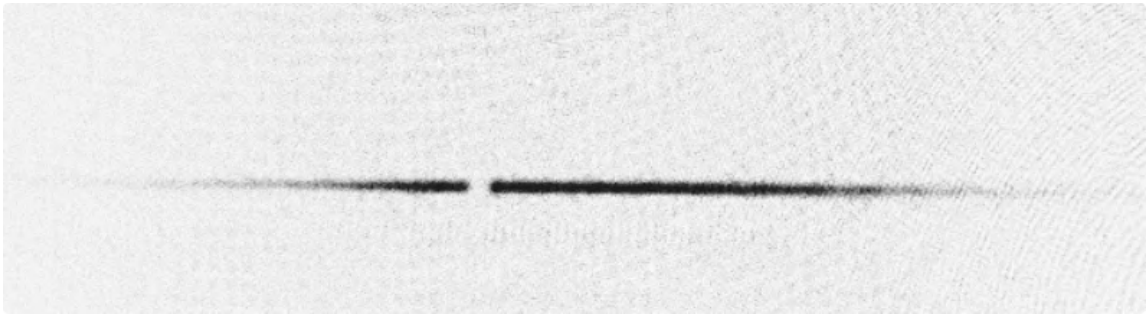

Figure 4.14: Potassium atoms trapped in the intersecting dimple beams. At the crossing point, the atoms are lost, creating an appearance of a "hole" in the spatial distribution of atoms.

Initially, the origin of this effect was unclear. Since the hole appeared precisely where the highest atomic density was expected, together with the short lifetimes of the atoms (initially incorrectly attributed to the background gas collisions), further evaporation or spectroscopy experiments would not have been possible. After a long investigation, we identified the cause in the design of the optical dipole trap; in the initial layout, there were no waveplates after the PBS overlapping the dimple and the reservoir beams (see Fig. 4.13). Therefore, the returning beam after their first pass through the cell had the same polarization as the incident beams. As a result, at the crossing point, an optical lattice was formed, which was sensitive to mechanical vibrations of the setup.Introducing an additional half-wave plate into the retroreflected path corrected this problem, and the trap began to function as intended. Nevertheless, lifetimes remained limited to 1–2 s, shorter than expected based on the measurements in the magnetic trap.

Ultimately, the main limitation was traced back to imperfect polarization. The beams exiting the initial polarizing beam splitter (used for overlapping dimple and reservoir beams) contained a small part of orthogonal linear polarization. Unexpectedly, the trap performance proved highly sensitive to this imperfection. To quantify it, we performed two independent measurements: one using a commercial polarimeter (PAX100, Thorlabs), and another based on a polarizing beam splitter combined with an optical power meter. These showed that the unwanted polarization compo-

nent amounted to only 0.43% of the total power, i.e., about 140 mW out of 32 W in the reservoir beam. By inserting an additional pair of half- and quarter-wave plates immediately after the polarizing beam splitter, this fraction was reduced to 0.017% (about 6 mW). Surprisingly, after adjustment, the measured lifetime of ^{39}K atoms increased from $\tau \approx 0.3$ s to $\tau \approx 4$ s.

Despite this improvement, a major limitation of our configuration remains: it is not possible to operate the reservoir and dimple traps simultaneously. If both beams are turned on, their polarizations are always orthogonal, and the resulting interference produces an optical lattice between the incoming reservoir beam and the returning dimple beam. This effect prevents efficient transfer of atoms from the reservoir to the dimple after initial cooling and evaporation. However, this limitation could in principle be avoided by using acousto-optic modulators to deflect the beams into opposite diffraction orders, introducing a frequency offset of 200–250 MHz between the reservoir and dimple beams, thereby suppressing the formation of an optical lattice. In the present configuration, however, the beams are overlapped using a polarizing beam splitter (PBS). Based on our experience, even a slight imperfection in the PBS alignment results in residual polarization impurities. Consequently, either the reservoir or the dimple beam always acquires an unwanted polarization component, which could in principle be corrected with a combination of half- and quarter-wave plates. Yet, such a compensation scheme would inevitably act on both beams in the same way, purifying the polarization of one while deteriorating it for the other. Therefore, all measurements presented in this thesis were carried out in the reservoir trap only, while the setup remains extendable by adding a separate path for the dimple trap.

Clearly, the calculated parameters of the employed optical dipole trap cannot be regarded as fully reliable or as an exact estimate of its properties. The beam waist at the focus was estimated from camera measurements and gaussian fitting of the transverse intensity profile. However, this does not guarantee that the camera was placed exactly at the focal plane. Moreover, the optical power was evaluated using a power meter. The dipole beam passes several times through the glass cell, and multiple reflections may reduce the power actually reaching the atomic sample; therefore, a precise estimate of the exact power (or, in fact, intensity) that is 'seen' by atoms is only approximate. Furthermore, it is not possible to determine whether the incoming and returning beams overlap precisely at their focus. For these reasons, the exact trap depth was determined experimentally using the parametric heating method [95].

In this measurement, cesium atoms were first loaded into the optical dipole trap (reservoir). The trap power was then periodically modulated for 500 ms by an

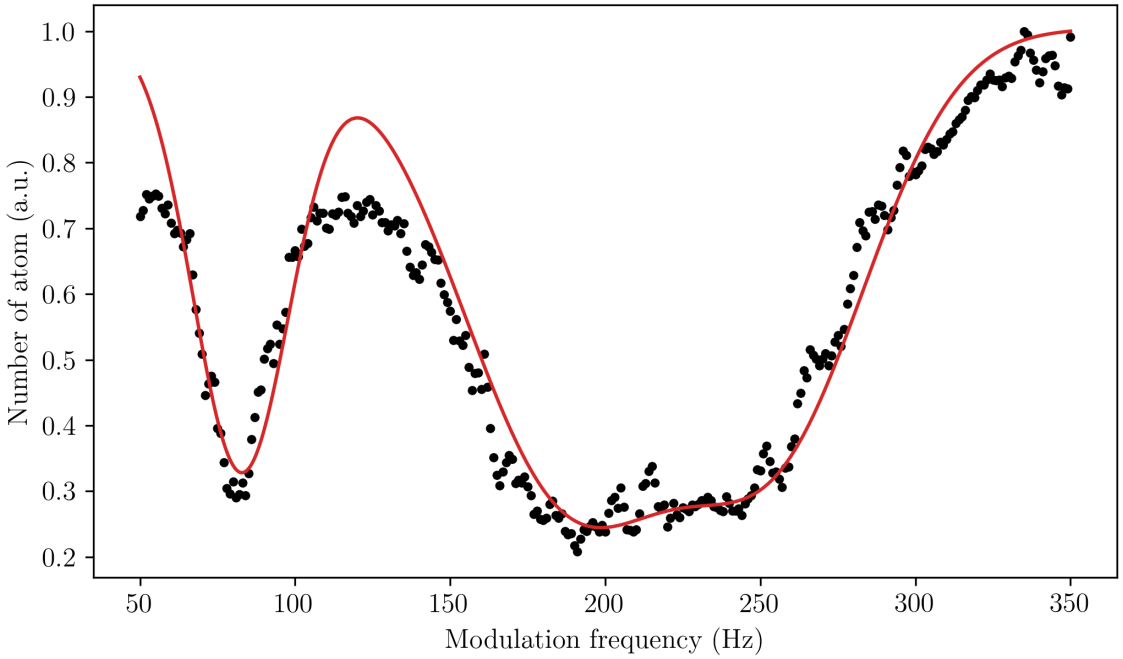

Figure 4.15: Measurement of the number of cesium atoms as a function of the modulation frequency of the dipole trap intensity (black points). The red line indicates the sum of Gaussian profiles, each centered at the calculated trap frequencies.

acousto-optic modulator between 80 and 100% of the maximum available power. After this modulation period, the trap was switched off, and a fluorescence image was taken to estimate the remaining number of atoms. This procedure was repeated for modulation frequencies in the range of 50–350 Hz, allowing us to observe atom loss due to parametric heating. The measured loss features were compared to the calculated trap frequencies. Each of the three observed loss resonances (corresponding to oscillator frequency in three spatial directions) was modeled by a Gaussian profile, and the parameters were fitted to match the experimental data. Once the trap parameters had been extracted for cesium, the procedure was repeated with potassium atoms. It was confirmed that the fine-tuned parameters obtained from measurements with the cesium sample accurately reproduced the loss profile for potassium. An example of the atom loss spectrum for cesium, together with the theoretical curve, is shown in Fig. 4.15. From this measurement, we determined the mean trap depth $U = 165.55\ \mu\text{K} \times k_b$ ($U = 102.3\ \mu\text{K} \times k_b$) and the trap frequencies $\omega = 2\pi \times (41, 94, 103)$ Hz ($\omega = 2\pi \times (60, 137, 150)$ Hz) for cesium (potassium).

The characterization of the optical dipole trap used in the experiment summarizes features of the apparatus, since the trap itself represents the final stage of our experimental sequence. This smoothly leads to the presentation of the obtained results, described in the following chapters. The next three chapters (chapter 5-chapter 7) correspond to papers that have either been published or will be submitted for publication. Chapter 8 presents the most recent results, which also motivated the construction of the experiment and the preparation of the current setup: the Feshbach spectroscopy of the ^{41}K–Cs mixture. We will begin, however, by describing the cooling procedure for ^{40}K atoms.

Chapter 5

Sub-Doppler laser cooling and magnetic trapping of natural-abundance fermionic potassium.

The article presented in this chapter constitutes the first description of laser cooling of atoms in our apparatus and was prepared by only two authors: the doctoral candidate submitting this thesis and the Dr. Mariusz Semczuk.

The history of this work partly explains the novelty of the reported results. Based on the available literature, we expected that observing a cloud of the fermionic potassium isotope would not be feasible. Even in more advanced setups equipped with an additional 2D MOT source, the number of captured fermionic atoms was limited to about $N = 5 \times 10^5$ in the case of unenriched dispensers [104]. Therefore, in a single-chamber system without an auxiliary source, we anticipated a much smaller number of atoms, insufficient for observation at the magneto-optical trap stage. To our surprise, by loading the MOT and subsequently compressing it, the signal from the fermionic atoms was clearly visible, even without any isotope-specific optimization. This unexpected observation raised a new question: if we can detect these atoms, what else can we achieve with the sample?

This question motivated us to optimize the trapping, compression, and gray molasses cooling parameters, and subsequently to load the atoms into a magnetic trap. Although we did not succeed in trapping the atoms in an optical dipole trap (even though we believe it should be possible with more careful optimization), the procedure demonstrated, for the first time to our knowledge, sub-Doppler cooling of

fermionic potassium atoms in a single-chamber setup without enriched dispensers, as well as the production of a magnetically trapped sample of these atoms.

Naturally, if the obtained results only served to satisfy our curiosity, the publication would not be particularly relevant for future experiments or for other researchers. However, the results demonstrate something more: when planning experiments with ultracold fermionic potassium, it is often assumed that enriched dispensers—currently very costly—are necessary. Our measurements show that careful optimization of all experimental parameters can be achieved with cheaper dispensers of natural isotopic abundance, thereby saving expensive enriched dispensers and delaying their depletion. This is particularly important since the developing and refining of cooling procedures can be very time-consuming.

For the sake of completeness, we note the following: the doctoral candidate developed the cooling procedures, performed all measurements, and carried out the data analysis. He also prepared the first draft of the manuscript, which, due to his limited publishing experience at that time, required multiple revisions by the supervisor.

Dr. Semczuk, thanks to his extensive experience, designed the sequence of steps necessary to turn the work into a publishable article and defined what measurements needed to be performed for a reliable evaluation of the results. He assisted with the data analysis and refining the experimental sequence. Furthermore, he repeatedly revised the text, ensured a logical flow of the presentation, prepared all elements necessary for submission, and carefully handled the responses to the referees' comments.

Results presented in this chapter are published in [105]: Mateusz Bocheński and Mariusz Semczuk 2024 J. Phys. B: At. Mol. Opt. Phys. 57 (2024) 035301

5.1 Abstract

We demonstrate the largest number of ^{40}K atoms that has ever been cooled to deeply sub-Doppler temperatures in a single-chamber apparatus without using an enriched source of potassium. With gray molasses cooling on the D_1-line following a standard D_2-line magneto-optical trap, we obtain 3×10^5 atoms at 10(2) µK. We reach densities high enough to measure the temperature via absorption imaging using the time-of-flight method. We magnetically trap a mixture of $m_F = -3/2, -5/2$ and $-7/2$ Zeeman states of the $F = 7/2$ hyperfine ground state confining 5×10^4 atoms with a lifetime of 0.6 s or $\sim10^3$ atoms with a lifetime of 2.8 s – depending on whether the temperature of the potassium dispensers was chosen to maximize the atom number or the lifetime. The background pressure-limited lifetime of 0.6 s is a reasonable starting point for proof-of-principle experiments with atoms and/or molecules in optical tweezers as well as for sympathetic cooling with another species if transport to a secondary chamber is implemented.

Our results show that unenriched potassium can be used to optimize experimental setups containing ^{40}K in the initial stages of their construction, which can effectively extend the lifetime of enriched sources. Moreover, the demonstration of sub-Doppler cooling and magnetic trapping of a relatively small number of potassium atoms might influence experiments with laser-cooled radioactive isotopes of potassium.

5.2 Introduction

Observation of the first degenerate Fermi gas in 1999 [23], only four years after the successful creation of a Bose-Einstein condensate [2], expanded the scope of experimental platforms where phenomena are predominantly governed by quantum statistics [106]. The choice of fermions for laser cooling is rather limited if compared to the number of available bosonic species. Among alkali atoms, only lithium and potassium have long-lived isotopes obeying Fermi statistics, ^{6}Li and ^{40}K. Laser cooling of the latter benefits from the availability of high-power CW lasers, nowadays primarily based on telecom technology [107] or tapered amplifiers [108]. However, working with ^{40}K has a major drawback: natural potassium contains only 0.012% of this isotope. Pioneering works that demonstrated laser cooling and trapping of several thousands ^{40}K atoms used single-chamber setups (like in this work) with a natural source of potassium [53], [109]. These early results made it abundantly clear that an isotopically enriched source would be needed to provide a sufficiently large number of atoms to implement evaporative cooling. Since then, almost all experiments using fermionic potassium have relied on sources enriched to 3%–6% [110], [111]. The

main issue with enriched potassium is its high price and limited availability – since the late 1990s, the price has gone up by more than an order of magnitude. As a result, experiments with enriched fermionic potassium do not use Zeeman slowers and almost exclusively rely on 2D MOTs [112] or double-stage MOTs [23] as a source of pre-cooled atoms. As opposed to other alkali species, single-chamber apparatuses are rarely used with ^{40}K, even though a single-chamber design with a source located near the trapping region has enabled studies of the BEC-BCS crossover regime with ^{6}Li [113]. In recent years, some efforts have been made to bypass the need for potassium enrichment. Both a Zeeman slower [114] and a 2D MOT [115] have been demonstrated, but they have not been widely adopted by the community.

In this work we demonstrate the largest number of ^{40}K atoms that has ever been cooled to deeply sub-Doppler temperatures in a single-chamber apparatus without using an enriched source of potassium. We achieve state-of-the-art final temperatures and phase-space densities, comparable with experiments that use 2D MOTs [112] or double-stage MOTs [23] as a source of pre-cooled atoms. Even though the final number of atoms is rather small, we are near the limit of what can be obtained in a single-chamber apparatus using a natural abundance potassium. As a proof-of-principle measurement, we trap 5×10^4 atoms in a magnetic trap, sufficiently many to enable sympathetic cooling by another species [114] if the magnetically trapped clouds are transferred to a second chamber with a much better vacuum. Our results also show that during the construction of a new experimental setup for experiments with ^{40}K, cheap natural potassium sources can be used for optimization, thus effectively prolonging the useful lifetime of the enriched source.

5.3 Experimental setup

The experimental chamber is based on a fused silica glass cell without any antireflection coatings. Ultra-high vacuum is maintained by a 55 l/s ion pump (VacIon Plus 55 Noble Diode) supported by a titanium sublimation pump (fired no more than twice per year). The vacuum chamber is designed for laser cooling of cesium and potassium atoms; therefore, we use two dispensers per species as atomic sources (SAES Getters Cs/NF/5.5/17 FT10 for Cs and K/NF/3.1/17 FT10 for K). We use potassium with a natural abundance of isotopes, that is, the content of ^{40}K is only $\sim$0.012%. All dispensers are located about 7 cm from the center of the magneto-optical trap (MOT). We use an LED emitting at the central wavelength of 370 nm (FWHM $\sim$10 nm) to increase the MOT loading rate due to the light-induced atomic desorption (LIAD) process [116]. This method of increasing the additional free-atom load in the trapping region allows us to release less atoms from the dispensers into

the setup, thus minimizing the deterioration of the vacuum quality. The base pressure (i.e., when the dispensers have not been turned on for several days) reaches 10^{-11} mbar.

The quadrupole field for the magneto-optical and the magnetic trap is created by a pair of coils in a nearly anti-Helmholtz configuration. The coils are arranged such that the axis of the strongest gradient B'_{axial} is in the horizontal plane. Throughout the paper, we report the radial gradient B'_{r} because it sets the effective trapping potential in the vertical direction.

The laser system is designed to maximize the available power by limiting double passes through acousto-optic modulators (AOMs) after the final amplification stage. In general, the design allows us to switch between potassium isotopes (^{39}K, ^{40}K or ^{41}K) on a sub-millisecond time scale and to implement sub-Doppler cooling on the D_1 line for all isotopes. Here, we discuss only the core elements of the laser system relevant to the current work on ^{40}K. The details of the entire laser system will be the subject of further publication.

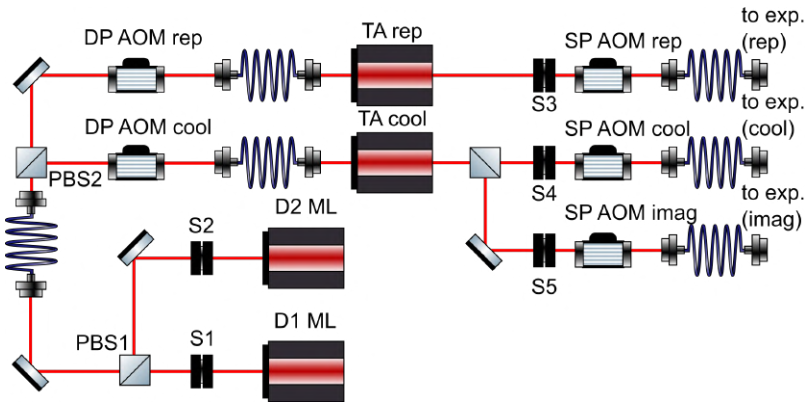

Figure 5.1: Simplified scheme of the ^{40}K laser cooling system. D1 ML and D2 ML: master lasers (Toptica TA pro) stabilized to crossover transitions of the D_1 and the D_2 line in ^{39}K, respectively; DP AOM$_{\mathrm{cool}}$ and DP AOM$_{\mathrm{rep}}$: double pass acousto-optic modulators providing total frequency shifts +(700–850) MHz and −(700–800 MHz), respectively, TA$_{\mathrm{cool}}$ and TA$_{\mathrm{rep}}$: tapered amplifiers (Toptica), SP AOM$_{\mathrm{cool}}$ and SP AOM$_{\mathrm{rep}}$: single pass acousto-optic modulators operating at fixed frequencies of +80 MHz and −80 MHz, respectively, which work as fast optical shutters, S1–S5: mechanical shutters.

Figure 5.1 shows a simplified layout of the laser system. We use two master oscillator tapered amplifiers (Toptica TA pro) stabilized to crossover transitions in ^{39}K, one on the D_1 line and the other on the D_2 line. The beams from both master

lasers are combined on a polarizing beam splitting cube (PBS1) and are coupled into the same single mode, polarization maintaining fiber with perpendicular polarizations. The PBS2 splits each of the D_1 and D_2 beams into two paths, called cooling and repumping paths, where two double pass acousto-optic modulators $\mathrm{DPAOM_{cool}}$ and $\mathrm{DPAOM_{rep}}$ provide frequency tuning around optimized values of +350 MHz and −370 MHz, respectively, before seeding dedicated tapered amplifiers $\mathrm{TA_{cool}}$ and $\mathrm{TA_{rep}}$ (both are Toptica TA pro models, but we only use tapered amplifiers from these systems). Mechanical shutters S1 and S2 (Uniblitz LS6Z2) are used to choose whether the D_1 or D_2 line light is amplified. Single-pass acousto-optic modulators $\mathrm{SPAOM_{cool}}$ and $\mathrm{SPAOM_{rep}}$ provide final frequency shifts of +80 MHz and −80 MHz, respectively, and work as fast optical shutters. To eliminate light leakage caused by the finite extinction of the AOMs, mechanical shutters S3-S5 (Uniblitz LS6Z2) are used. Our design allows us to reach all frequencies required for efficient cooling on both ^{40}K lines. In fermionic potassium, the splitting of the $\mathrm{P_{3/2}}$ state is sufficiently large to allow efficient (compared to bosonic potassium isotopes) cooling and compression using the D_2 line, therefore we do not need to implement a D_1&D_2-line compressed MOT as used in experiments with ^{39}K and ^{41}K [31], [73]. The design of our laser system provides an additional feature, namely the phase coherence of the cooling and the repumping beams, which might be useful for driving Raman transitions between hyperfine states. Phase coherence has been shown to increase the cooling efficiency on the D_2 line for some species [78], but it is not clear whether it provides any benefit in our setting since the role of phase coherence for gray molasses on the D_1 line has not been studied in the literature.

The single-chamber design of our vacuum system and the use of unenriched dispensers as a source of ^{40}K heavily restrict the possibility of optimizing the MOT. In particular, we are forced to choose between maximizing the atom number and maximizing the lifetime. These two are strongly coupled unlike in setups where a 2D MOT or a Zeeman slower is used, even if these sources rely on natural abundance potassium [114], [115]. We use three retro-reflected MOT beams, each collimated with a standard 30 mm diameter lens to a $1/e$ diameter of about 25 mm. This size guarantees that there is no noticeable distortion of the beams caused by the glass cell walls, which are separated by 30 mm. After passing through the glass cell, the diameter of the beams is decreased to ≈9 mm with a telescope to fit through 0.5″ wave plates. This choice is made to avoid purchasing custom-made, 30 mm diameter waveplates which are rather costly if they have to be achromatic (our setup is also used for laser cooling of cesium). The retro-reflected beams are slightly focused to partially compensate for reflection losses on the uncoated glass cell walls.

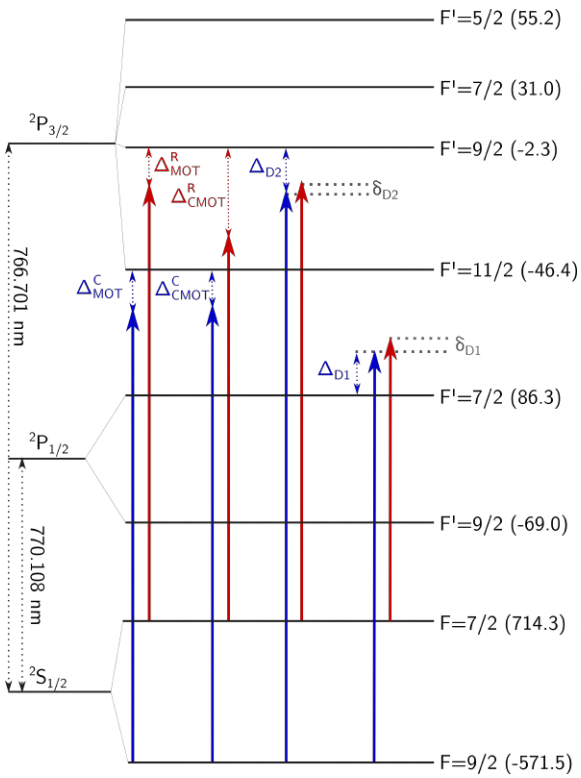

Figure 5.2: Atomic level scheme showing the D_1 and the D_2 lines of ^{40}K. The vertical arrows mark the beams dedicated to the cooling methods investigated in this work. For the D_2 line the figure shows detunings of MOT beams from the cooling transition $\Delta^{\mathrm{C}}_{\mathrm{MOT}}$ and from the repumping transition $\Delta^{\mathrm{R}}_{\mathrm{MOT}}$, detuning of the compressed MOT beams ($\Delta^{\mathrm{C}}_{\mathrm{CMOT}}$ and $\Delta^{\mathrm{R}}_{\mathrm{CMOT}}$), single-photon detuning of gray molasses beams Δ_{D2} and the detuning from the two-photon resonance δ_{D2}. For the D_1 line we use, by analogy, single-photon detuning of gray molasses beams Δ_{D1} and the detuning from the two-photon resonance δ_{D1}. The colors blue and red refer to the cooling and to the repumping beam, respectively. The hyperfine shifts are in units of MHz and are based on [42].

5.4 Magneto-optical trap

For magneto-optical trapping we use well-established laser cooling methods where we close the $^2S_{1/2}, F = 9/2 \rightarrow {}^2P_{3/2}, F' = 11/2$ cooling transition by providing repumping light on the $^2S_{1/2}, F = 7/2 \rightarrow {}^2P_{3/2}, F' = 9/2$ transition to depopulate the ground hyperfine state with lower total angular momentum F. It should be

noted that this level has a higher energy than the $F = 9/2$ level, unlike other alkali atoms. In figure 5.2 we present the relevant energy levels and schematically show various detunings of the laser beams used at different stages of laser cooling on both the D_1 and the D_2 line.

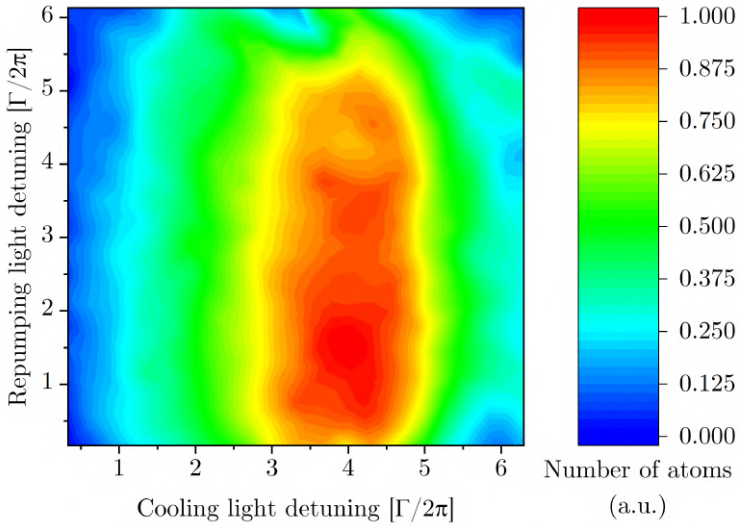

Figure 5.3: Normalized number of atoms as a function of red-detuning from the cooling and the repumping transitions. Here, $\Gamma \approx 2\pi \times 6.035$ MHz is the natural linewidth of the D_2-line.

During MOT loading we use maximum available laser power with total intensities of cooling (repumping) beams equal to $29I_s$ ($18I_s$), where $I_s = 1.75\ \mathrm{mW\,cm^{-2}}$ is the saturation intensity of the D_2 line (used also for the D_1 line). We have found that we can obtain the highest atom number in the MOT for the magnetic field gradient of 11 $\mathrm{G\,cm^{-1}}$, the cooling light red-detuned by -3.5Γ to -4.5Γ and the repumper red-detuned by -0.5Γ to -4Γ (see figure 5.3). Here, $\Gamma \approx 6.035$ MHz is the natural linewidth of the D_2 line transitions. Throughout the article we also use this value for the D_1 line. All measurements reported in the following paragraphs are obtained for the cooler (repumper) detunings equal to -4Γ (-1.5Γ).

With optimized parameters, we have compared MOT loading curves for two cases relevant to this investigation (see figure 5.4). In the first case, the number of atoms is maximized by increasing the dispenser current to 4 A, thus heating it beyond typical temperatures we use while working with nearly 8,000 times more abundant ^{39}K. The MOT loading rate is further enhanced with LIAD. Increased temperature of the dispenser reduces the quality of vacuum (see section 5.6) as it releases significant

amounts of other, more abundant, potassium isotopes that collide with trapped ^{40}K. Additionally, due to the nearby location of cesium dispensers, we also observe an increase in the partial pressure of cesium, enhanced even more by the use of LIAD. For regular operation, when working with ^{39}K or Cs or their mixture, this crosstalk is minimized by choosing the temperature of the dispenser (corresponding to 3.6 A current) that provides a satisfactory compromise between the number of atoms and the lifetime of the atoms trapped in an optical dipole trap ($\sim$5 s). For the study of sub-Doppler cooling, which takes on the order of 15 ms, this reduced lifetime is irrelevant, thus the efficiency of the cooling process is investigated under these conditions.

The second case considers loading the MOT using only LIAD, with atomic sources having been turned off for more than a day resulting in a much improved background pressure. As expected, the trapped atom number is significantly smaller but the lifetime of trapped atoms is longer (see section 5.6). However, the overall performance of sub-Doppler cooling is essentially the same as in the first case considered.

Under conditions optimized for the maximum atom number we achieve a loading rate of 5×10^5 atoms s^{-1}, trapping about 5.5×10^5 atoms, nearly two orders of magnitude more than in the first reported MOTs of fermionic potassium [53], [109]. When the dispensers have been off for at least a day and only LIAD is used, the MOT loading rate drops to 1×10^4 atoms s^{-1} and we can trap at best 8.5×10^4 atoms. The steady-state temperature of the MOT is 250 µK, well above the Doppler limit of $T_{\mathrm{D}} = 145$ µK [42] indicating that sub-Doppler cooling mechanisms that are typically present in MOTs of ^{40}K [23], [53], [117], [118] do not seem to work in our setup. We have determined that this discrepancy is caused by the waveplates we use to set the polarization of the MOT (and gray molasses): their settings are optimized for D_1 line cooling which deteriorates the quality of polarization for cooling on the D_2 line. By fine-tuning the polarization of the MOT beams we can reach 170 µK, somewhat lower than reported for example in [117] and [112]. However, this leads to inefficient cooling on the D_1 line. The figure of merit for us has been the combined efficiency of all cooling stages, not of each individual stage, and, as we show next, 250 µK is a sufficiently good starting point to proceed with further cooling.

5.5 Sub-Doppler cooling

We compress the cloud to cool it down and increase its density using a D_2-line compressed MOT stage. This is obtained by changing the cooling (repumping) beam detuning to -1Γ (-5Γ) and increasing the magnetic field gradient to 18 G cm^{-1} in $<$0.6 ms (set by the response time of the coil current driver). Once the magnetic

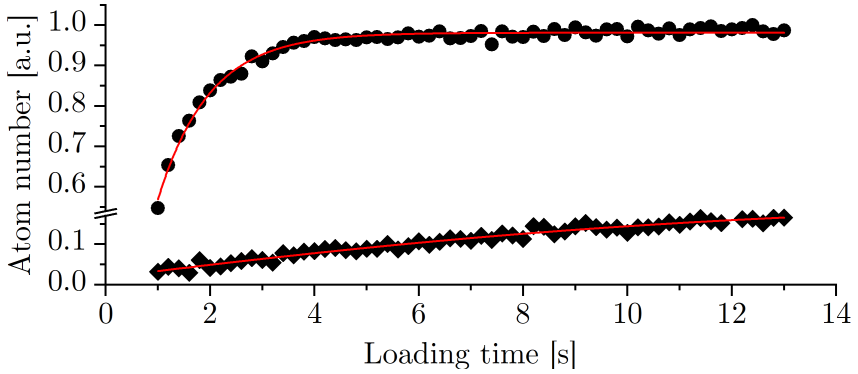

Figure 5.4: Magneto-optical trap loading curves normalized to the maximum trappable atom number. With dispensers and LIAD *turned on* (dots) the maximum number of atoms is $N_{\max} = 5.5 \times 10^5$. With dispensers *turned off* and LIAD *turned on* (diamonds) this number drops to $N_{\max} = 8.5 \times 10^4$.

gradient has reached the new value we ramp down the power of the cooling and the repumping beam in 10 ms to $6I_s$ and $1.4I_s$, respectively. We are not able to simultaneously ramp the frequency and the power due to the limitation of the RF source driving AOMs. This might be the reason that we do not observe a significant temperature drop, ending up with a cloud at 160 µK. However, during this process there is no significant loss of atoms and we reach a phase space density (PSD) of $\rho = 1.6 \times 10^{-7}$.

We first investigate to what extent our setup allows sub-Doppler cooling on the D_2 line. Previous works using the D_2 line reached temperatures below 50 µK in optical molasses with the cooling beam red-detuned by more than -4Γ [111], [112] from the $F' = 11/2$ level or by using coherent superposition of ground hyperfine states with red-detuned gray molasses [56]. We essentially follow the work of Bruce *et al* [56] where D_2-line gray molasses for ^{40}K have been implemented for the first time. After the magnetic field of the compressed MOT has been switched off, we set the compensation coil currents to nullify the background magnetic field [82] and detune the repumping and the cooling light to produce a coherent superposition of ground-state hyperfine levels via the excited state $F' = 9/2$. We investigate the dependence of the final atom number and the final temperature on both the single-photon detuning from the $F' = 9/2$ level, Δ_{D2}, and on the two-photon detuning δ_{D2} between the cooling and the repumping light. Here, we have used the cloud size after a fixed expansion time as a proxy for temperature to generate the plots shown in figures 5.5(a) and (b). We find that the maximum atom number and the minimum temperature can be ob-

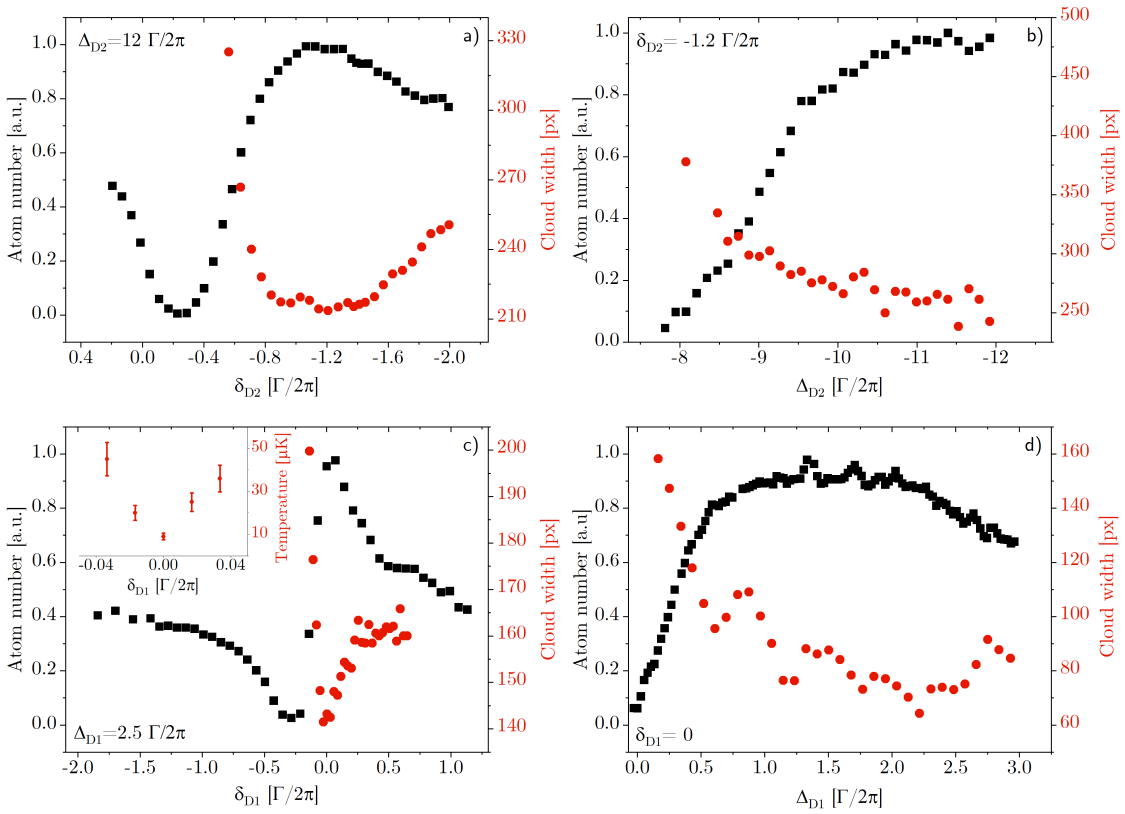

Figure 5.5: Plots of the cloud width (red dots) and the number of atoms (black squares) as a function of (a) detuning from the Raman (two-photon) transition and (b) red-detuning (single–photon detuning) from the $^2P_{3/2}$, $F = 9/2$ level obtained after 8 ms of cooling. Analogous measurements for the D_1 line gray-optical molasses cooling lasting 10 ms as a function of (c) detuning from the Raman (two-photon) transition and (d) blue-detuning from the $^2P_{1/2}$, $F = 7/2$ level. For each plot, we show the value of the detuning that is fixed. Inset in 5.5(c): the temperature measured for five two-photon detunings in close proximity to the two-photon transition on the D_1 line, obtained with optimized single-photon detuning and optimized cooling powers.

tained after 8 ms of cooling for the two-photon detuning of approximately $\delta_{D2} = -1\Gamma$ and the single-photon detuning of approximately $\Delta_{D2} = -12\Gamma$, very similar to values reported by Bruce *et al* [56]. Unfortunately, we observe a nearly 80% loss of atoms with a negligible temperature drop to 140 μK, as determined with a time-of-flight

method. We have determined that this is primarily caused by optimization of the cooling paths for the 770 nm light, i.e. D_1-line light. MOT beams and gray molasses beams are coupled into the same optical fiber and share the same paths when the light leaves the fiber to form a MOT. We control the polarization of the overlapped beams with half- and quarter-waveplates with the design wavelength of 767 nm (D_2 line). We optimize the polarization of the 770 nm light, which slightly degrades the target polarization of the MOT beams and D_2 line molasses, leading to observed inefficiencies. It is not surprising that under such conditions the sub-Doppler cooling mechanisms on the D_2 line do not perform as well as reported by other groups [56], [111], [112]. When waveplates are optimized for gray molasses of the D_2 line, we can cool atoms to 70(4) µK, slightly colder than 80(1) µK reported in [56]. At the same time, the cooling on the D_1 line becomes very inefficient: the coldest cloud reaches ∼80 µK. Most of the sub-Doppler cooling techniques rely on simultaneous ramping of the laser frequency and power. This feature cannot be implemented with our current RF sources driving AOMs and this is the most likely reason why we could not match 48 µK achieved by Bruce *et al* [56]. The issue of the poor performance of the D_2 line gray molasses is inconsequential for our measurements – when constructing the laser system, we had expected to use sub-Doppler cooling on the D_1 line all along while treating the MOT as a source of pre-cooled atoms. As such, the experimental setup has been optimized to maximize the atom number in the MOT and minimize the final temperature of the cloud after D_1-line cooling. Potential improvements could be achieved if achromatic waveplates were used.

Now we focus our attention on the gray molasses cooling on the D_1 line. It has been shown by several authors [31], [73], [81], [117] that this cooling method assures highly efficient and fast cooling with negligible atom loss. In fact, it has been implemented already for all alkali atoms where sub-Doppler cooling mechanisms on the D_2 line do not work efficiently due to the small hyperfine structure energy splitting of the $P_{3/2}$ state. Gray molasses require good control over the background magnetic field, and it is necessary to cancel all external stray magnetic fields for the best performance. We have nullified stray fields using a method we have developed and illustrated with ^{39}K [82] which has enabled us to cool that isotope to ∼8 µK. Gray molasses cooling starts immediately after the D_2-line compressed MOT. The magnetic field and the D_2 light are turned off, and the compensation of the stray magnetic fields is engaged. We block the light from the master laser (D2 ML) with the shutter S2, simultaneously opening the shutter S1 that sends the D_1 light to the tapered amplifiers. Due to the opening and closing times of shutters, and their jitter, the D_1 gray molasses stage cannot start sooner than 0.8 ms after turning off the magnetic field. During that time, the cloud drops freely and becomes diluted due

to its rather high temperature, but we are able to achieve a transfer of almost 100% of atoms to gray molasses with light intensities of $8.7I_s$ and $2.2I_s$ for the cooling and the repumping beam, respectively. We proceed with optimization of single- and two-photon detuning (see figures 5.5(c) and(d)) and the cooling time. We have found that during the 10 ms cooling stage when we simultaneously ramp down the cooling (repumping) beam intensity from $8.7I_s$ to $2.9I_s$ ($2.2I_s$ to $0.8I_s$) we are able to decrease the temperature to (10±2) µK, on par with temperatures reported by other groups [117], [118] while losing less than 20% of atoms. With nearly 3×10^5 atoms in a mixture of states we obtain a free-space phase-space density $\rho = 3.5\times10^{-5}$. For the determination of the final temperature we have used a time-of-flight method using both fluorescence and absorption images (examples of both types of images taken at different expansion times are shown in figure 5.6). Both methods have shown very good agreement, giving essentially the same temperature of (10±2) µK. Here, the shortest expansion time after release from gray molasses is 4.3 ms, limited by the 14 ms repetition time of mechanical shutters S1 and S2 (see figure 5.1), whereas the longest expansion is 9 ms, limited by our ability to reliably image diluted samples.

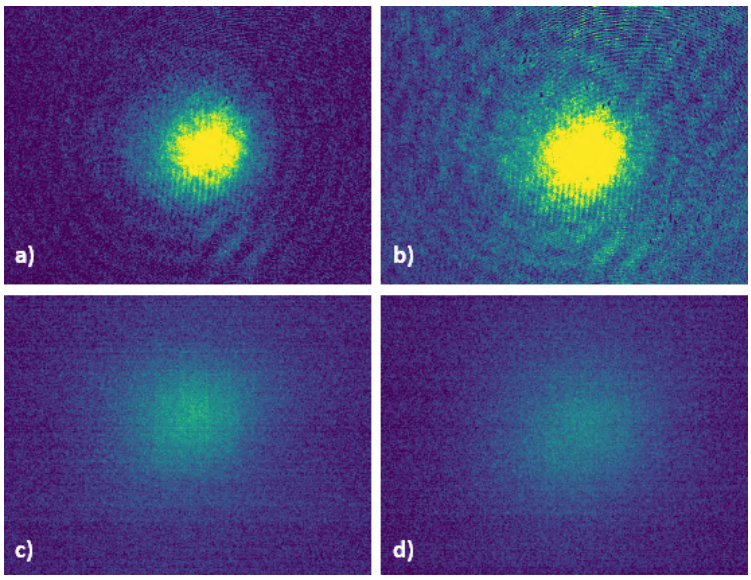

Figure 5.6: Examples of absorption (a),(b) and fluorescence (c),(d) images taken 4.6 ms (a),(c) and 7.6 ms (b),(d) after turning off the D_1-line gray molasses. Due to the timing of the shutters used in the laser systems, the expansion time could not be shorter than 4.3 ms. The upper limit on expansion time is only slightly larger than 7.6 ms due to the loss of optical density resulting from the small atom number.

5.6 Magnetic trapping

The high laser cooling efficiency of the sample allows us to transfer atoms to a conservative magnetic potential. A magnetic trap has a large capture volume and could facilitate sympathetic cooling of ^{40}K with ^{23}Na, ^{41}K or ^{87}Rb [114], [119], [120]. In such a cooling scheme, the final temperature of fermions is set by the ability to evaporate the coolant (e.g. ^{23}Na, ^{41}K or ^{87}Rb), and one can enter the degenerate regime without notable loss of ^{40}K atoms.

To transfer atoms from gray molasses to the magnetic trap we perform hyperfine pumping of the atomic population to the $^2S_{1/2}, F = 7/2$ hyperfine state by switching off the repumping light, then after 500 µs switching off the cooling light and turning on the quadrupole field. We use the highest gradient we can safely sustain in our setup, $B'_{\mathrm{r}} = 57.6\ \mathrm{G\,cm^{-1}}$ (note that the horizontal gradient is nearly $B'_{\mathrm{axial}} = 115\ \mathrm{G\,cm^{-1}}$) which is sufficiently high to capture atoms distributed between $m_{\mathrm{F}} = -3/2, -5/2, -7/2$ states. If after hyperfine pumping the population was equally distributed between Zeeman sublevels we would expect a 37.5% transfer efficiency – we obtain 16%.

We have investigated the same two cases that we have considered for MOT loading: dispensers turned on to maximize the trapped atom number and dispensers turned off for a day and loading enhancement with LIAD. For the atom-number maximized case we are able to magnetically trap about 5×10^4 atoms, with a lifetime of 0.6 s. This lifetime can be extended to over 2.8 s after keeping the dispensers off for a day and enhancing the loading rate with LIAD. However, this results in a much lower number of trapped atoms, just above 3,000. The lifetime measurements are shown in figure 5.7. We have not implemented spin polarization as we have focused on a proof-of-principle demonstration of magnetic trapping but there is nothing fundamental nor technical that would prevent us from trapping a little over 10^5 spin polarized atoms in our current setup under the condition of a reduced lifetime. It is worth emphasizing that the reported lifetime is a lower bound on what can be achieved in our setup as both the sample's spin polarization and/or trapping atoms in the $F = 9/2$ hyperfine state would lead to the increase of the storage time.

We have not been able to reliably measure the temperature of the magnetically trapped cloud as it becomes diluted after a short expansion time. This might indicate that the transfer from gray molasses introduces some heating, which would not be surprising given the nature of optical pumping and the fact that the gray molasses is slightly offset from the minimum of the magnetic potential. However, we believe that it is primarily due to the small number of atoms that approaches the detection sensitivity of our imaging system. For the lifetime measurement in the magnetic

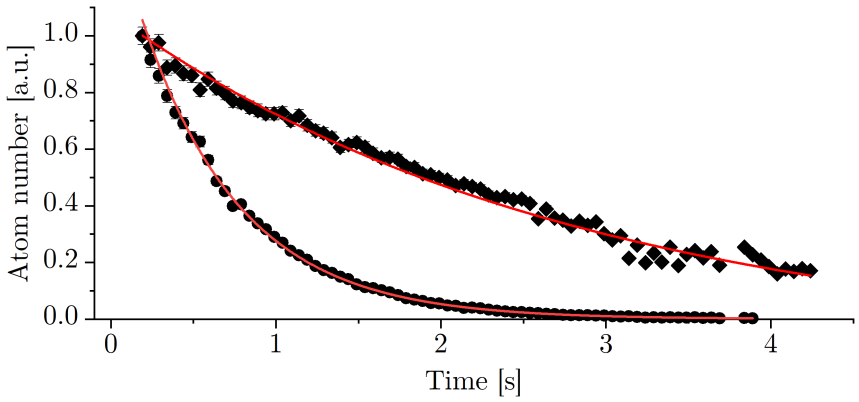

Figure 5.7: Lifetime of $F = 7/2$ potassium in a magnetic trap. Circles (diamonds) represent data normalized to the initial trapped atom number with (without) dispensers turned on. The decay is fitted with exponential functions with time constants $\tau_1 = 0.61$ s (circles) and $\tau_2 = 2.82$ s (diamonds).

trap, the small atom number is less of an issue. We release atoms after a given hold time and recapture them in the MOT, where the fluorescence signal is collected for 20 ms. The imaging time has been chosen such that loading of the MOT from the background gas during imaging is negligible.

5.7 Summary

We have presented sub-Doppler cooling of ^{40}K using a source with natural composition of potassium isotopes and a single chamber apparatus. With 3×10^5 atoms at a temperature of (10±2) µK after D_1 gray molasses cooling stage we demonstrate that even without isotopically enriched sources it is possible to achieve state-of-the-art cloud parameters in a single-chamber setup. Our results open doors to using unenriched fermionic potassium in modern experiments including quantum computing with atoms in optical tweezers and creation of ground-state molecules containing ^{40}K if magnetically trapped atoms are sympathetically coolled with another species. For the proof-of-principle work in optical tweezers, including the formation of ground-state ^{40}KCs molecules that we are pursuing, the vacuum quality might be a secondary issue. However, the observed deterioration of the vacuum quality when atomic sources are operational can be a serious problem in many experiments involving evaporation. As a remedy, optical or magnetic transport can be used to move the sample to another chamber with much better vacuum as has been demonstrated

both for atoms [121], [122] and for molecules [123], where the cloud has been moved by 46 cm in just 50 ms.

Our work might encourage precision spectroscopic measurements of stable potassium isotopes [124] in simplified experimental setups (no enriched sources, no Zeeman slowers, no 2D MOTs etc) while still providing samples at ∼10 µK thus significantly reducing the Doppler effect. Our results on sub-Doppler cooling of small numbers of atoms might be useful to β-decay experiments, where similarly sized samples of laser-cooled ^{37}K and ^{38m}K isotopes have been used [125]. Here, it is not only a matter of the reduction of the Doppler effect but, we believe, of the demonstrated gain in phase-space density that might improve the quality of measurements.

In the same setup as used in this work we routinely cool 5×10^7 ^{41}K to ∼10 µK, achieving lifetimes of magnetically trapped samples of several seconds. The content of ^{41}K in natural potassium is 6.7%, therefore if we were to use a source with ^{40}K enriched to 5% (e.g. dispensers from AlfaVakuo e.U.) we could expect more than 10^7 fermionic atoms at ∼10 µK after gray molasses. After implementing spin polarization we could reasonably expect to magnetically trap $> 10^6$ ^{40}K atoms with a lifetime of > 5 s while still using a very simple single-chamber design.

In a related work performed using the same experimental setup we have achieved nearly 90% transfer efficiency of ^{40}K from the D_1-line gray molasses to the magnetic trap operating at 57.6 G cm^{-1}. The transferred sample has been spin-polarized in the $F = 9/2$, $m_\mathrm{F} = 9/2$ state, with the lifetime reaching 1.5(1) s.

Chapter 6

Magnetic trapping of an ultracold ^{39}K-^{40}K mixture with a versatile potassium laser system

As can be seen in the previous chapter, methods for cooling potassium were presented, but the description of the laser system itself was limited only to the aspects relevant to the cooling of the fermionic isotope. This, however, did not do justice to the actual laser system that was constructed and which incorporates many new elements of interest in contemporary AMO physics.

The laser system was designed in a modular way. Using two MOPA systems, two optical amplifiers, and several acousto-optic modulators. It enables sub-Doppler cooling of three potassium isotopes, with performance matching, if not exceeding, values reported by other authors. The modular architecture and the efficiency of the applied techniques make the system particularly relevant in the context of ongoing miniaturization of experimental platforms, such as those used in atomic interferometry. Moreover, the setup can be straightforwardly adapted to cool metastable potassium isotopes, which could represent a step toward studies at the interface of atomic and nuclear physics.

The engineering achievements described in this article were not the only factors justifying its publication. The most important result of these studies was the first production of heteronuclear ^{39}K–^{40}K mixture confined in a magnetic trap, and the demonstration that interactions within this mixture lead to an effective reduction of the sample lifetime. The realization of this mixture is of interest both for the observation of new phenomena such as p-wave superfluidity [126], and for investigations of three-body loss coefficients and the scaling laws for mixtures with a small mass

difference [127].

The creation of potassium isotope mixtures also highlights the versatility of the laser system. The ability to cool different isotopes simultaneously is attractive in view of producing a quantum-degenerate fermionic sample. In particular, the temperature reached for bosonic potassium in the magnetic trap lies below the Ramsauer–Townsend minimum for these atoms (the minimum of the elastic collision cross section that for potassium-39 occurs at the temperature of 400 μK [22]). This suggests that the RF-knife evaporation of ^{39}K in the magnetic trap could be used for sympathetic cooling of ^{40}K atoms - at least until reaching the limit imposed by the negative scattering rate of ^{39}K at zero magnetic field. This constitutes the natural next step in our research, which will require additional dedicated work in the future.

The article presented in this chapter has three authors. The first author, who is also the doctoral candidate submitting this thesis, constructed the laser system, carried out all cooling procedures and measurements reported in the article, performed the data analysis, and prepared the first version of the manuscript.

The second author performed part of the beat-note measurement and its analysis. He also contributed to discussions on the overall structure of the publication and provided valuable feedback that helped shape the first version of the manuscript.

Dr. Semczuk designed the laser system and guided its construction, defined the research objectives, advised on the cooling procedures, and was supervising the creation of the draft of the manuscript. He ensured the quality of the obtained results, participated in planning all measurements, prepared the final version of the manuscript and handled the submission process and the preparation of the responses to the reviewers.

Results presented in this chapter are published in [128]: Mateusz Bocheński, Jakub Dobosz, and Mariusz Semczuk, "Magnetic trapping of an ultracold ^{39}K-^{40}K mixture with a versatile potassium laser system," Opt. Express 32, 48463-48478 (2024)

6.1 Abstract

We present a dual isotope magneto-optical trap (MOT), simultaneous sub-Doppler laser cooling, and magnetic trapping of a spin-polarized ^{39}K-^{40}K Bose-Fermi mixture realized in a single-chamber setup with an unenriched potassium dispenser as the source of atoms. We are able to magnetically confine more than 2.2×10^5 fermions ($F = 9/2\,, m_F = 9/2$) and 1.4×10^7 bosons ($F = 2\,, m_F = 2$) with a lifetime exceeding 1.2 s. For this work, we have developed a versatile laser tailored for sub-Doppler cooling of all naturally occurring potassium isotopes and their mixtures. This laser system incorporates innovative features, such as the capability to select an isotope by activating or deactivating specific acousto-optic modulators that control the light seeding tapered amplifiers. Switching between isotopes takes ∼1µs without any mechanical adjustment of the components. As a final step in characterizing the laser system, we demonstrate sub-Doppler cooling of ^{41}K.

6.2 Introduction

The research of ultracold isotopic mixtures is of significant importance for diverse scientific investigations. Although some rationales for delving into this domain are somewhat technical in nature, such as refining the production techniques for fermionic ^{3}He* [129], ^{6}Li [130], ^{40}K [114], and bosonic ^{39}K [104] and ^{85}Rb [131] quantum gases through sympathetic cooling, the implications extend far beyond mere technical advancements. Isotopic mixtures are advantageous from an experimental standpoint for at least three reasons: the almost identical mass of constituents limits their gravity-induced separations in shallow traps used in the quantum degenerate regime, they experience nearly identical confining optical potential, and the laser systems can operate at nearly the same wavelength avoiding the use of achromatic or broadband-coated optics. Ultracold mass-imbalanced mixtures would separate due to gravity, which needs to be compensated by magnetic levitation [132] or by adding a confining optical potential at a suitable wavelength [133]. These are largely the reasons why isotopic mixtures were used in the first successful demonstrations of the simultaneous superfluidity of fermionic and bosonic systems [134] and the miscibility of quantum liquids [131]. Photoassociation studies of homo and heteronuclear mixtures of nearly identical mass [135] can also provide valuable information about the mass scaling of molecular potential models or the Born-Oppenheimer approximation.

The availability of three stable isotopes, bosonic ^{39}K and ^{41}K, and fermionic ^{40}K, makes potassium a versatile tool in modern ultracold experiments [136], [137]. All isotopes have already been brought to the quantum degenerate regime both by direct

evaporation [23], [61], [138] and by sympathetic cooling by other atomic species [120], [139], [140]. With isotopic mixtures, off-resonance excitation of transistions in one isotope while cooling the other one (and vice versa) could limit the efficiency of sub-Doppler cooling. However, with the proper adjustment of the experimental parameters, it was possible to simultaneously cool ^{3}He* and ^{4}He* [129], ^{6}Li and ^{7}Li as well as ^{39}K with ^{41}K [104], and ^{40}K with ^{41}K [114]. In the latter two cases, ^{41} K was used as a coolant to bring the mixture to quantum degeneracy.

This work provides the first demonstration of the so far experimentally unexplored ultracold mixture of ^{39}K and ^{40}K which we cool to sub-Doppler temperatures (below 30 µK), spin polarize and magnetically trap. Some applications of this mixture, such as investigating models of controlled chemical reactivity via ultracold isotope-exchange reactions between heteronuclear dimers, would require formation of ground state ^{39}K^{40}K [141]. In other applications, the availability of six possible combinations of isotopes makes potassium an interesting tool for the cross-verification of quantum chemistry models beyond the Born-Oppenheimer approximation by precision Feshbach spectroscopy [142] or by spectroscopy of weakly bound ground state molecules [143], [144]. Our work could be considered as the first step towards realizing a proposal of Bazak and Petrov [126], where they showed that ^{39}K-^{40}K, as composite fermionic molecule with a boson lighter than a fermion, is a unique candidate to obtain a strongly p-wave-attractive Fermi gas in quasi-2D thus providing a platform for studies of p-wave superfluidity. Sub-Doppler cooled mixture, as demonstrated here, could be used in optical tweezer experiments for the production of ultracold heteronuclear molecules [145], for the creation of mixed-species atom arrays [146] or, upon excitation to Rydberg states, as a medium for exploring strongly interacting multi-component fluids of light [147]. A fascinating research avenue opened up by the laser system design that can be explored in our experimental setup is the formation of triatomic heteronuclear fermionic molecules ^{39}K^{40}K^{41}K trapped in atomic arrays.

The experimental setup uses unenriched alkali dispensers located 7 cm away from the trapping region. This choice requires heating the dispensers to maximize the number of ^{40}K atoms, which also increases the number of ^{39}K atoms in the background gas. As a result, when ^{39}K or ^{40}K isotopes are magnetically trapped, their lifetime is on the order of 1.5 s. We have found that the lifetime of ^{40}K atoms when magnetically co-trapped with ^{39}K decreases to 1.20(4) s, which we attribute to the occurrence of heteronuclear collisions. The proven capability to achieve sub-Doppler temperatures using *unenriched* dispensers instead of costly *enriched* ones is indeed a beneficial feature for experiments with relevant timescales in the tens of milliseconds range, such as studies on quantum memories [148]. With enrichment reaching 3%, the dispensers could be operated at a much lower temperature, comparable to

what we typically use when working only with ^{39}K or ^{41}K, which would extend the background-limited lifetime to nearly 10 s. The reported lifetimes are too short for rf evaporation in a magnetic trap, but they might be sufficient to enable transfer to a second chamber with much better vacuum. Thus, our approach could be an alternative to using 2D MOTs or Zeeman slowers. It is worth noting that for many experiments performed in optical tweezers or for photoassocation spectroscopy such a short lifetime might be sufficient.

An important aspect of this work is the demonstration of a novel approach to constructing laser systems for laser cooling of multiple isotopes. Our design is modular, allows for a 1 µs-scale switching between isotopes, has built-in coherence between the cooling and the repumping beam, and, most importantly, can be used for simultaneous sub-Doppler cooling of isotopic mixtures. The fast switching between isotopes might be particularly useful in high data-rate light-pulse atom interferometers [149], [150], quantum tests of the weak equivalence principle [151], fluorescence imaging of individual components of the mixture or selective removal of one (or both) isotopes following the creation of ground state ^{39}K^{40}K molecules. The two shutters that are used to select whether D_1 or D_2 line cooling takes place are the only movable mechanical components that are required for the operation of the laser system. However, these could be replaced with acousto-optic modulators if one is willing to accept an additional 10%-20% loss of power. An extension to other potassium isotopes such as ^{37}K and ^{38}K^m requires the addition of only a pair of acousto-optic modulators per isotope in the frequency tuning module. We have presented the state-of-the-art capabilities of the laser system by sub-Doppler cooling of ^{39}K [82], ^{40}K [105] and ^{41}K (Supplement 1). We complete the characterization of the setup by demonstrating a simultaneous sub-Doppler cooling of an isotopic mixture of ^{39}K and ^{40}K.

6.3 Laser system design

Each laser cooling experiment depends on the capability to adjust the laser beam frequency to optimize the mechanisms suitable for a specific cooling phase. Although electro-optic modulators are sometimes used for this purpose, the most common method is the utilization of acousto-optic modulators (AOMs) in a double-pass setup [152]. The latter method avoids introducing undesired frequency components into the experiment and can also serve as a fast shutter, crucial for promptly turning off the laser light. Nevertheless, there is a fundamental limitation to this approach: achieving close to 90% diffraction efficiency into the desired order is rare, resulting in a more than 20% loss of laser power in a double-pass configuration, with actual experimental losses often closer to 40%. Beam-shape distortions are frequently ob-

served, which may lead to problems with coupling efficiency when transmitting light through fibers. Consequently, the design of a laser system must satisfy numerous, sometimes conflicting, requirements. Increasing the laser power to compensate for losses is not always feasible, as typical high-power sources utilize tapered amplifiers that exhibit output powers closely tied to the wavelengths employed. Although cooling cesium or potassium does not present significant power-related challenges if the cost of the laser system is a secondary issue, experiments with lithium or sodium face more noticeable technical limitations in terms of the laser power that can be utilized.

In tapered amplifiers, several tens of milliwatts of seed power can be amplified up to several watts within a broad wavelength range, often spanning 10-20 nm around the specified central wavelength. As a result, multiple frequency components, even separated by several THz, can be amplified simultaneously [153]. Unfortunately, not all that power is useful, because the spatial quality of the output beam is usually low, with $M^2 \sim 1.5 - 2$. This results in a low efficiency of coupling this light into a single-mode fiber for distribution within the experimental setup.

We have developed a modular design for the laser system, where modules are interconnected through single-mode, polarization-maintaining fibers. This approach facilitates the optimization of each module's performance independently without causing misalignment in the overall system. The use of optical fibers shortens the free-space beam propagation enhancing the overall stability of the system. The laser system comprises three modules, which are detailed in the subsequent sections: the stabilization module (SM) which generates frequency-stabilized light on the D_1 and D_2 lines, the frequency tuning module (FM) where fine-tuning of frequency and selection of the cooled isotope is carried out using acousto-optic modulators, and the amplification module where the final beam preparations take place, power is amplified using tapered amplifiers, and the output is directed to the experimental setup through fibers. Such a functional separation can be very useful for space saving because individual modules can be located at different places in the laboratory and even stacked on top of each other, as is done in our case.

The structure of the energy levels in potassium exhibits certain peculiarities, such as a small splitting of the excited $P_{3/2}$ state and the inverted hyperfine structure of the ground state of ^{40}K. These features make the convention of naming transitions as 'cooling' or'repumping' somewhat superficial. In order to maintain consistency with the existing literature, we have opted to adhere to the conventional terminology in the article. For bosonic and fermionic isotopes, the transitions on the D_2 (D_1) line identified as 'cooling transitions' are $^2S_{1/2}\, F = 2 \rightarrow {}^2P_{3/2}, F' = 3$ ($^2S_{1/2}\, F = 2 \rightarrow {}^2P_{1/2}, F' = 2$) and $^2S_{1/2}\, F = 9/2 \rightarrow {}^2P_{3/2}\, F' = 11/2$ ($^2S_{1/2}\, F = 9/2 \rightarrow {}^2P_{1/2}\, F' =$

9/2), while the term 'repumping transitions' refers to ${}^2S_{1/2}\,F = 1 \rightarrow {}^2P_{3/2}\,F' = 2$ (${}^2S_{1/2}\,F = 1 \rightarrow {}^2P_{1/2}\,F' = 1$) and ${}^2S_{1/2}\,F = 7/2 \rightarrow {}^2P_{3/2}\,F' = 9/2$ (${}^2S_{1/2}\,F = 7/2 \rightarrow {}^2P_{1/2}\,F' = 7/2$). In this context, transitions with fractional total angular momentum F correspond to ^{40}K. The transitions relevant to the current work can be seen in Figure 6.1. The structure for ^{41}K is shown for completness and is relevant for sub-Doppler cooling of this isotope discussed in Supplemental material.

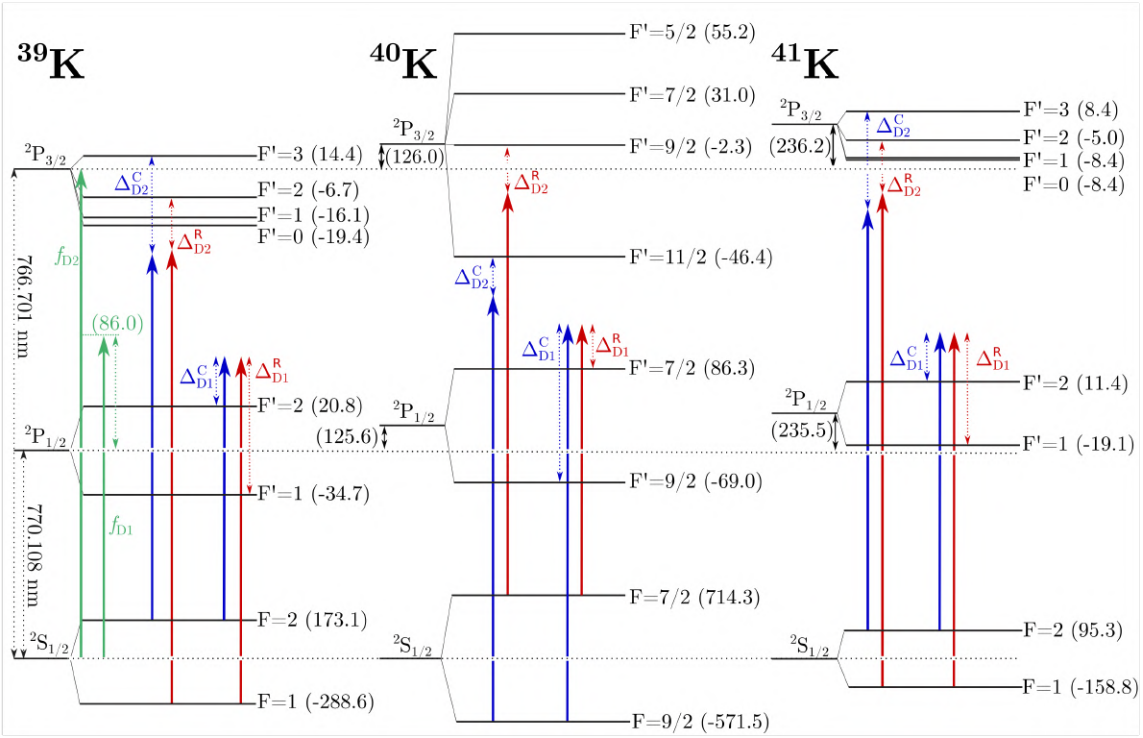

Figure 6.1: Diagram of the atomic levels in three stable potassium isotopes relevant to the current work. The frequencies delivered by the stabilization module are marked in green and labeled f_{D1}, f_{D2}, corresponding to the D_1 and the D_2-line stabilized lasers. The detuning 86 MHz of the f_{D1} frequency from the D_1-line frequency is shown. Detunings Δ are labeled with superscripts 'C' and 'R', standing for 'cooling' and 'repumping', while subscripts 'D1' and 'D2' indicate which D line they refer to. Blue and red colors refer to laser frequencies corresponding to cooling and repumping transitions, respectively. The hyperfine shifts are in units of MHz and are based on [42].

6.3.1 Stabilization module (SM)

The main function of this module (see Figure 6.2) is to provide a sufficiently high power of frequency-stabilized light to seed tapered amplifiers in the amplification module after frequency shifting in the frequency tuning module. In our implementation of the laser system, the module generates light at frequencies $f_{\mathrm{D1}} = 389.286144$ THz for the D_1 line cooling and $f_{\mathrm{D2}} = 391.016170$ for the D_2 line cooling. The setup comprises two MOPA systems that contain an ECDL and a tapered amplifier (Toptica Photonics TA Pro). One of the MOPAs is optimized by the manufacturer for potassium cooling at 767 nm, whereas the other was originally purchased for rubidium (optimized for 780 nm) but is currently being used for the potassium D_1 line at 770 nm, although with a minor decrease in output power. For frequency stabilization, about 10 mW of laser light is split from the main path, is frequency shifted by an acousto-optic modulator in a double-pass configuration, fiber-coupled and sent to a commercial Doppler-free saturated absorption spectroscopy module (CoSy, TEM Messtechnik GmbH). We use $^2S_{1/2}, F = 2 \rightarrow^2 P_{1/2}, F' = 2$ and $^2S_{1/2}, F = 2 \rightarrow^2 P_{3/2}, F'$ transitions for stabilizing the lasers operating on the D_1 and the D_2 line of ^{39}K, respectively. The hyperfine structure of $^2P_{3/2}$ is not resolved; therefore, we assign the excited state a generalized total angular momentum F' [154]. With an external VCO we could drive the AOM at 125 MHz (101 MHz) and modulate it by ± 3 MHz at 7 kHz (15 kHz) for the $D_2(D_1)$-line stabilization using a home-built bias tee. This way the lock-in detection could be implemented with the laser controller while minimizing the fluctuation of the frequency of the cooling light that otherwise would be present if the current of the laser was modulated.

The MOPA systems generate $\sim$1 W of light each. The beams are then overlapped on a polarizing beam splitting cube and coupled into a single, single-mode polarization-maintaining fiber with an efficiency of $\sim$60%. Care has been taken to ensure that the beams are coupled into perpendicular axes of the fiber to minimize polarization drifts. Although the maximum total power we send into the fiber can reach $\sim$2 W for several miliseconds during the experimental sequence, we do not observe any long-term effects arising from the use of relatively high power light with a standard fiber. Each beam path can be independently blocked with a mechanical shutter (Uniblitz LS6Z2) which allows us to choose whether the D_1-line light or the D_2-line light is sent to the next module (see Fig. 6.2). Switching between D lines takes about 1 ms, with a 1.6 ms delay after applying the trigger signal. With the current shutter driver it takes $\sim$12 ms before a shutter that has been closed could be opened again. This imposes some limitations if one would like to turn on the D_2-line light immediately after D_1 line cooling, but in most applications we do not find it to be a serious constraint. Moreover, it can be easily overcome with a faster

mechanical shutter [155] or by adding an acousto-optic modulator to each tapered amplifier. However, this would decrease the available power by 10%-20%.

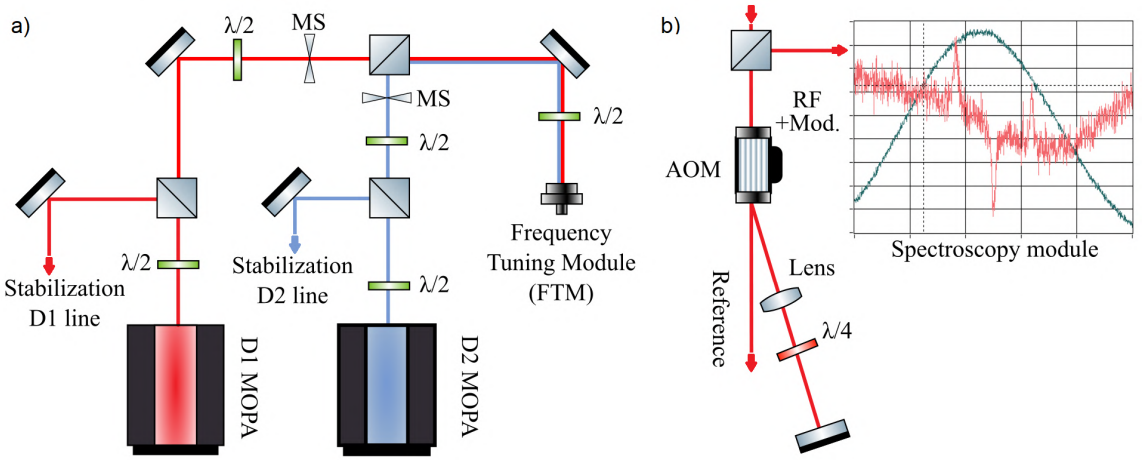

Figure 6.2: a) Layout of the stabilization module. Beams from two MOPAs (Master Oscillator Power Amplifier)) stabilized on the D_2 or D_1 transitions in ^{39}K are overlapped on a polarizing beam splitting cube (PBS) and sent to the frequency tuning module. The D line that is used at any given cooling stage is selected by opening or closing an appropriate mechanical shutter (MS); b) the section responsible for frequency stabilization. The layouts for both D lines are nearly identical. The light from the tapered amplifier passes through the acousto-optic modulator (AOM) in a double-pass configuration and is sent to the potassium vapor cell in the spectroscopy module. The central frequency of the AOM is modulated to derive an error signal from Doppler-free saturated absorption spectroscopy (shown for the D_2 line in the inset). The 0th-order beam can be used as a frequency reference or for diagnostics.

6.3.2 Frequency tuning module (FTM)

The entire module is built on an aluminum plate ($90 \times 60 \times 2$ cm). Most aluminum pedestals that we use to mount optical components are attached to the plate using epoxy. Standard laboratory clamps are utilized to secure supports for lenses, acousto-optic modulators, and irises, with M6 holes being drilled and threaded at designated positions. The light is transmitted from the SM using a single-mode, polarization-maintaining fiber, where the D_1 and D_2 light propagate along two primary orthogonal axes of the fiber. By employing a half-wave plate and a polarizing beam splitting

cube we ensure that the power from each axis of the fiber is equally distributed into two distinct paths.

In each path, there are three acousto-optic modulators set up in a double-pass configuration, positioned consecutively so that the 0th order beam of one AOM serves as the input beam for the next (refer to Figure 6.3a). The diffracted beams (either 1st or -1st order, depending on the AOM) undergo two passes through the AOMs and are coupled into a shared single-mode, polarization-maintaining fiber that transmits light to the amplification module. We have chosen to use AOMs that operate at central frequencies of 80 MHz, 110 MHz, and 350 MHz, as these are readily available from various manufacturers and can achieve a diffraction efficiency of more than 85% in a single pass. The selected operating frequencies of the modulators consider the inclusion of single-pass 80 MHz AOMs at the output of the amplification module (see 6.3.3 for a discussion), which are used to control the intensity of the cooling beams and serve as fast shutters. Consequently, the frequency difference between the light produced by the cooling and repumping paths does not correspond to the hyperfine splittings of potassium isotopes.

After the frequency shift with the AOMs is performed, the light from each path is coupled to a dedicated fiber and is sent to the amplification module. Under normal circumstances, it is impossible to ensure optimal diffraction efficiency of each AOM and efficient coupling into a fiber because the laser beam travels a distance of up to 2 m (for the last AOM in the chain) and diffraction becomes non-negligible, making it nearly impossible to assure satisfactory performance for all AOMs in the chain but the first one. We have developed a systematic approach that mitigates the issue of diffraction and technical requirements imposed by modulators (like the optimal beam size). We optimize the diffraction efficiency of the first modulator configured in the double-pass configuration, then we optimize the coupling efficiency into the fiber by appropriately shaping the beam with lenses. We add another modulator and shape the 0th order beam from the previous AOM with a set of lenses to optimize its diffraction efficiency. It results in a very poor fiber-coupling efficiency on its own. To improve that, we exploit a key feature of modulators which are set up in a double-pass configuration: the frequency-shifted beam has a perpendicular polarization to the incoming beam due to the use of a quarter-wave plate. In our approach (see Figure 6.3b) the beam enters an AOM after passing through a polarizing beam-splitting cube, then passes the AOM twice, and on its way back it reflects off the PBS because its polarization is now perpendicular to the polarization of the incoming beam. It is then rerouted to the opposite wall of the PBS with the help of four mirrors. The space between the mirrors is used to shape the beam, and each subsequent beam-shaping stage must consider the presence of the beam-shaping optics in all previous

stages. This is somewhat tedious to set up for the first time, but allows us to obtain >50% fiber coupling efficiency for the last modulator in the chain (here, for ^{41}K), while for the first one (for ^{40}K) it approaches 75%. The difference is primarily the result of the beam distortion caused by the crystals in the AOMs.

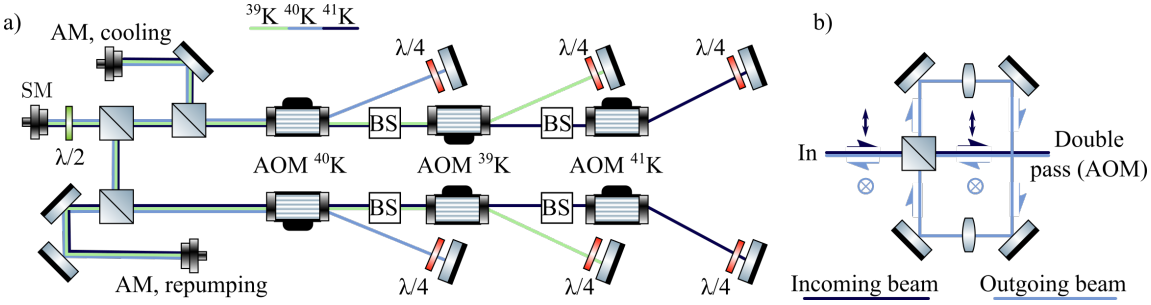

Figure 6.3: a) Layout of the frequency tuning module. Light originating from the stabilization module (SM) is split into two separate paths to address the cooling and repumping transitions. Three modulators in a double-pass configuration are utilized in each path to produce the necessary frequencies for the three stable potassium isotopes. Subsequently, the light from each path is guided into a single-mode, polarization-maintaining fiber and then sent to the amplification module, identified as 'AM, cooling' and 'AM, repumping'. The abbreviation 'BS' refers to the beam shaping section illustrated in b), where the incoming beam could be adjusted using lenses to improve the diffraction efficiency of the acousto-optic modulator (AOM); we have not taken advantage of this option. After the beam undergoes a double-pass and polarization rotation, it is reflected by the polarizing beam splitting cube (PBS). Subsequently, its shape is fine-tuned using lenses to improve coupling into the optical fiber before being redirected to the opposite side of the PBS. Mirrors are used to fine-tune fiber coupling. This method enables the individual beam shaping of light for each isotope. To improve clarity, the incoming and outgoing beams are maintained apart.

The effective frequency tuning range of the entire laser system is related to the bandwidth of AOMs, but in a somewhat indirect manner: the frequency can be changed as long as the power delivered to the amplification module is sufficiently high for the tapered amplifiers to operate without noticeable amplified spontaneous emission. This minimum power level, 20 mW for the repumping amplifier and 10 mW for the cooling amplifier, has been determined by observing the emission spectra of the amplifiers using an Ocean Optics USB4000 spectrometer. The spontaneous emission around 767 nm and 770 nm has been kept below 1% of the peak value at the

frequency of interest, corresponding to the spontaneous emission reaching the level of the noise floor of the device. For the 780 nm amplifier, here used for repumping light, the spontaneous emission around 780 nm never reaches the noise floor level, but even then no frequency component exceeds 5% of the repumping light frequency. Moreover, spontaneous emission around 780 nm does not propagate well throug our laser system due to spatial filtering by AOMs and optical fibers and as a result does not seem to cause any issues.

The modular design of the laser system enables its extension to other potassium isotopes by using the 0th order of the last acousto-optic modulator in each path of the FTM. Based on the hyperfine structure values of radioactive potassium isotopes reported in [156], we have calculated that detunings of -545 MHz and -476 MHz (-756 MHz and 449 MHz) from the cooling and repumping transitions are required, respectively, to address transitions in ^{37}K (^{38}K^m). Such detunings can be easily obtained by commonly available AOMs set up in double-pass configurations, with central frequencies of 250 MHz and 350 MHz.

6.3.3 Amplification module (AM)

The amplification module, illustrated in Figure 6.4, comprises two tapered amplifiers: one generates cooling light ('cooler') and the other repumping light ('repumper'). Both amplifiers are seeded with light from the frequency tuning module. The amplification module is divided into distinct sections for repumping and cooling light. The key difference between these segments lies in the absence of an absorption imaging path in the repumping section and the use of AOMs with different diffraction orders (-1st and +1st for the cooling and repumping sections, respectively). The light emitted from the 'cooler' ('repumper') is subjected to a frequency change of -80 MHz (+80 MHz) after passing through an Acousto-Optic Modulator (AOM) before being coupled into a dedicated single-mode polarization-maintaining fiber. This fiber then transmits the light to another optical table where the vacuum chamber is located. Acting as fast switches, the modulators also facilitate the selection of the fiber to which the light is directed: by changing the frequency of the rf signal driving the modulator, we can select if the light is used for cooling/repumping or optical pumping/spin polarization. This approach works well because the power needed for optical pumping is relatively low and as a result we drive the AOM 25 MHz below the central frequency. Even then more than 50 mW can be deliverd to the vacuum chamber. Driving the AOM 25 MHz *above* the central frequency is used for the idle mode when we want to turn off and turn on the light in quick succession and there is not enough time for the mechanical shutter to close and then reopen. This assures

that there is no resonant light present for example during the time of flight measurement following sub-Doppler cooling. In situations where more time is available (generally more than 20 ms), we transition to the idle frequency solely for the duration required for the shutters to open or close. Immediately following this period, the main AOM frequency is utilized to reduce RF reflections and mitigate long-term thermal effects in the modulator. The frequency shift that has been introduced is offset by the FTM. The absorption imaging beam is controlled with a separate AOM.

The amplification module employs two MOPA systems (Toptica TA PRO) identical to those utilized in the stabilization module. By eliminating the mirrors between the ECDL laser diodes and the amplifiers, we were able to introduce external light from the frequency tuning module to seed the amplifiers.

Finally, mechanical shutters (Uniblitz LS6Z2) are used to prevent light leakage into the system. It has been observed that even when the acousto-optic modulators are switched off, there is a light leakage at the microwatt level that can negatively impact the lifetime of atoms held in either a magnetic or optical dipole trap.

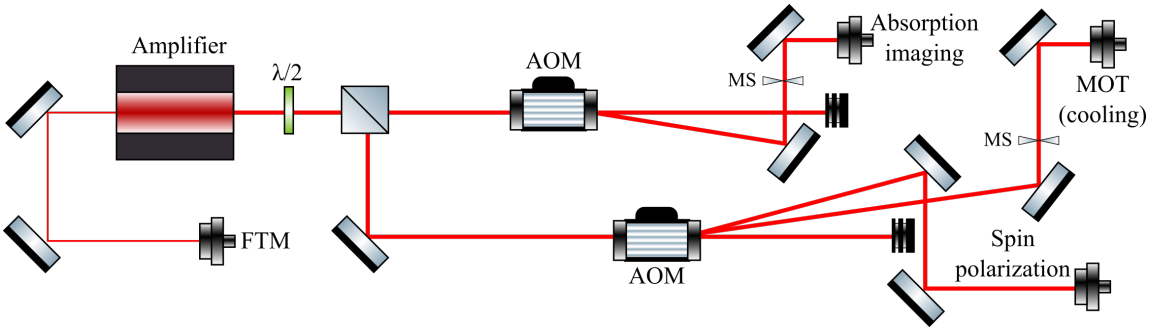

Figure 6.4: Layout of the the cooling section of the amplification module. Light from the frequency tuning module (FTM) seeds the optical amplifier which output is then split into two paths. In the first path, an acousto-optic modulator controls the absorption imaging. The modulator in the second path is used to select between the cooling path for the magneto-optical trap and the spin polarization path.

The system is designed to obtain the highest power for cooling and repumping light, limited only by the maximum power of the amplifiers and the efficiency of the AOM in the amplification module. The nominal output power of the new tapered amplifiers (after the optical isolator) was 1.3 W but in nearly 10 years since the purchase it dropped to slightly above 1 W, presumably due to aging of the amplifier chip. The powers available close to the vacuum chamber are within the range of 300-500 mW (200-400 mW) for the cooling (repumping) light. This apparent loss of power comes partially from the 90% efficiency of the AOM in the amplification

module and the 50% coupling efficiency into optical fibers connecting the AM and the vacuum chamber. Such losses are anticipated when utilizing tapered amplifiers, as they typically produce light with relatively low spatial quality, characterized by an M^2 value of approximately 1.5 to 2. However, the main decrease in power comes from the limited availability of the seeding power: the losses in the FTM (see Section 6.3.2) depend on the isotope and for the last AOM in the chain are higher than for the first, and unfortunately, for ^{41} K we are never able to reach the maximum allowed seeding power.

6.3.4 Switching between isotopes - timing

The major advantage of the laser system that distinguishes it from known designs is its ability to remotely and quickly switch between isotopes without the need for any mechanical adjustments. This would be very useful for experiments that require a fast repetition rate [157]. On a practical note, the ability to switch to ^{39}K when working primarily with other potassium isotopes has proven to be extremely useful when debugging or optimizing the performance of the experimental setup.

To determine the switching time between isotopes, we have used an oscilloscope to record the beatnote between the reference light from the cooling amplifier and the light from the repumping amplifier seeded with the ^{41}K repumper (*Beatnote 220 MHz* region in Figure 6.5 and the associated inset). Then we turn off the ^{41}K AOM and turn on the AOM responsible for the ^{39}K repumper (*Beatnote 254 MHz* region in Figure 6.5 and the associated inset) using the same experimental sequence that we would use in the actual experiment. Figure 6.5 shows four distinct regions that appear in such a measurement. The first and last regions correspond to repumping amplifiers seeded with ^{41} K and ^{39} K light, respectively. We have confirmed the expected beatnote frequencies by fitting sinusoidal functions to both beatnote regions. After the ^{41} K is turned off there is a time (*TA relaxation*) in which the intensity of light decreases, but the repumping amplifier operates at the initial frequency. The next region shows spontaneous emission of the amplifier where no beatnote is observed, and the intensity of the photodiode signal drops. The turn-off time of the AOMs in the frequency tuning module is below 200 ns therefore the relaxation of the amplifier does not seem to be related to the presence of the seeding light. On the basis of multiple measurements, we have estimated the switching time to be on the order of 1.5 µs. This coincides with the timing resolution of our experimental control system and at this point in time we are unable to confirm if it is possible to have a significantly shorter switching time and if the relaxation of the amplifier plays an important role on a shorter time scale.

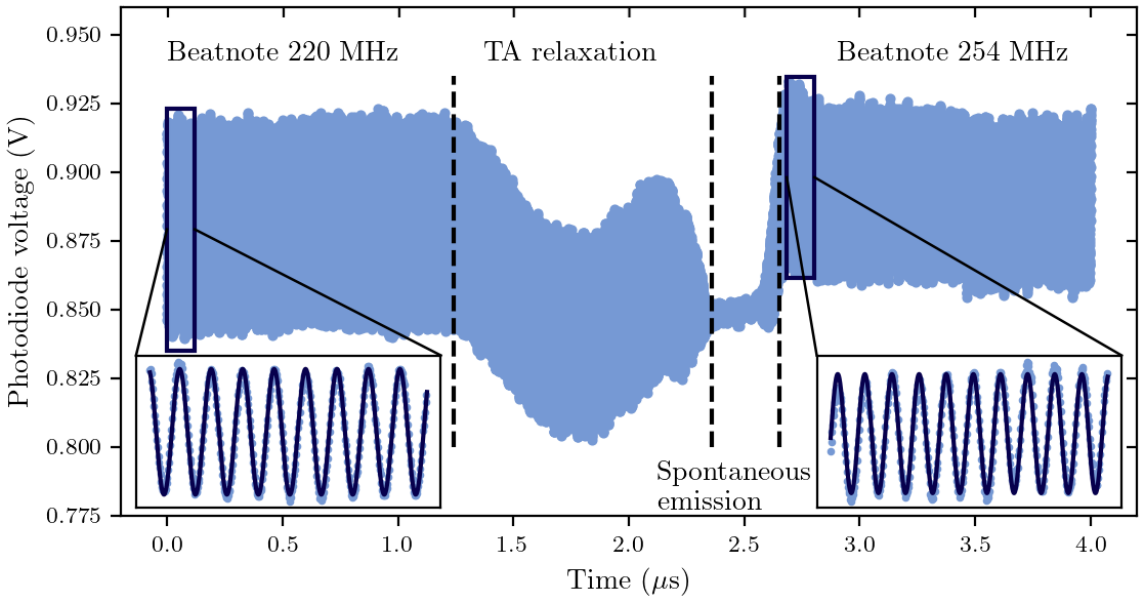

Figure 6.5: The beatnote signal indicating switching time between frequencies for laser cooling different isotopes successively. The figure displays four distinct regions delineated by dashed vertical lines, representing the beatnote between the stabilized laser and the repumping beam for cooling ^{39}K, TA relaxation, TA spontaneous emission (without a discernible beatnote), and the beatnote following the activation of the repumping beam for the ^{41}K isotope. In the inset, an amplified beat signal (light blue) is depicted, with the fitting of a sine function (navy blue).

6.4 Sub-Doppler cooling and magnetic trapping of the ^{39}K-^{40}K mixture

The preceding section has provided a detailed discussion of the laser system. References [82] and [105], combined with sub-Doppler cooling of ^{41}K described in the Supplement 1, have established that the reported design can be used for state-of-the-art sub-Doppler cooling of all stable potassium isotopes. We now introduce an essential functionality of the laser system: the ability to simultaneously cool a *mixture* of potassium isotopes, which we demonstrate by sub-Doppler cooling and magnetic trapping of a doubly spin-polarized mixture of ^{39}K-^{40}K.

Among the isotopic mixtures of potassium, Bose-Bose (^{39}K-^{41}K) and Bose-Fermi (^{41}K-^{40}K) mixtures have been already brought to quantum degeneracy [104], [114]. To the best of our knowledge, simultaneous laser cooling of ^{39}K and ^{40}K has not been

described in the literature so far. Here, we go beyond showing just that and demonstrate that the mixture can be cooled to sub-Doppler temperatures and confined in a magnetic quadrupole potential with high efficiency. One notable aspect of our finding is the use of a dispenser source that contains naturally occurring potassium (93.3% of ^{39}K and 0.012% of ^{40}K) [42] and is placed 7 cm from the center of the magneto-optical trap. To enhance the number of fermions that can be loaded into the magneto-optical trap, it is necessary to increase the temperature of the dispenser beyond its usual operational parameters. The number of atoms that can be trapped is constrained by the single-chamber design of the vacuum system and the use of an unenriched atom source. Any increase in atom flux leads to a rise in the background pressure. This approach limits the lifetime of magnetically trapped atoms to $\sim$1.5 s but removes the need to use expensive enriched sources. The output power of the amplifiers utilized in the spectroscopy and amplification modules is another limiting factor. The power of the seeding light must be shared between two isotopes, resulting in a lower power available for each isotope compared to working with a single isotope. These constraints are related to hardware and can be addressed by employing enriched dispensers and more powerful optical amplifiers that are already available commercially.

Each tapered amplifier in the amplification module is seeded with a minimum of two adjacent frequencies required for two isotopes, therefore it becomes difficult to determine the light intensity for a specific frequency component. In this section of the manuscript, all intensities are estimated based on the power of seeding light and the assumption that for frequencies in close proximity (less than 2 GHz apart), the amplification of each frequency component should be similar. Multifrequency amplification in a tapered amplifier may produce sidebands that could affect the number of atoms or the temperature [158]. The influence of this phenomenon is negligible as we have not detected any significant variations when comparing the cooling efficiency of an individual isotope with that of a mixture. In addition, we have also investigated the presence of additional frequency components by monitoring the beatnote between the cooling light and repumping light for frequencies differing by up to 500 MHz. The power present in the sidebands observed in the spectrum, which are more than 200 MHz away from the closest transition, has been found to be below 4%. It should be noted that the existence of sidebands may have a more profound effect on the cooling of the ^{39}K-^{41}K mixture, where light frequencies used for cooling (or repumping) of two isotopes are much closer to each other.

We employ the same single-chamber apparatus in which cooling of other potassium isotopes has been performed. The main chamber is a fused silica glass cell, which mitigates the issue of eddy currents interfering with magnetic field switching.

The axis of symmetry of the magnetic coils is horizontal and as a result the vertical gradient of the magnetic field (here 6.9 G/cm) is one half of what is achieved when the coils are arranged with the symmetry axis oriented vertically. For details of the apparatus see [101]. Throughout the article, we quote the magnetic field gradient in the direction of gravity (vertical direction). The cooling performance is characterized when the dispenser current is 3.8 A to improve the SNR. On a daily basis, when working only with ^{39}K or ^{41}K the dispenser is turned off or heated resistively with a current of 3.6 A.

We start by loading a double isotope magneto-optical trap, which saturates at the $N_{40\mathrm{K}} = 3 \times 10^5$ and $N_{39\mathrm{K}} = 4 \times 10^7$ atoms, with temperatures of $T_{40\mathrm{K}} = 200$ µK and $T_{39\mathrm{K}} = 1.1$ mK, where subscripts indicate the isotope. The optimized parameters for both isotopes can be seen in Table 6.1.

Stage	B' [G/cm]	Isotope	I_c [I_s]	I_r [I_s]	δ_c [Γ]	δ_r [Γ]	N	T [µK]	ρ
MOT	6.9	^{39}K	7.6	3.6	-8	-5	4×10^7	1100	7×10^{-10}
(12 s)		^{40}K	16.5	8	-3.8	-1.7	3×10^5	200	2×10^{-10}
CMOT	40	^{39}K	1.6	1.2	-9	-7	4×10^7	2000	8.4×10^{-10}
(20 ms)		^{40}K	19	15	-3.5	-3.5	3×10^5	260	2×10^{-9}
D1-D2 CMOT	$40 \to 0$	^{39}K	$1.2 \to 0$	$1.2 \to 0$	-8	-4	-	-	-
(3 ms)		^{39}K$_{\mathrm{D1}}$	$0 \to 0.4$	$0 \to 0.5$	-1	+8	-	-	-
		^{40}K	$19 \to 0$	$5 \to 0$	-3.5	-3.5	-	-	-
GMC	0	^{39}K$_{\mathrm{D1}}$	8.8	2.5	+4	+13.2	2×10^7	28	1.6×10^{-7}
(12 ms)		^{40}K$_{\mathrm{D1}}$	11.4	2.2	+28.2	+2.5	2.5×10^5	13	1.2×10^{-7}

Table 6.1: Main cooling stages used in simultaneous sub-Doppler cooling of the ^{39}K-^{40}K mixture and their respective durations. For each stage, we quote the magnetic field gradient B', intensities $I_{\mathrm{r(c)}}$ and detunings $\delta_{\mathrm{r(c)}}$ (for definitions see Figure 6.1) of the cooling and repumping light, the atom number, the temperature and the phase-space density. The intensities are expressed relative to the saturation intensity of the D_2 line ($I_\mathrm{s} = 1.75$ mW/cm^2), while the detunings from the cooling and repumping transitions are specified relative to the natural width of the D_2 line (Γ= 6.035 MHz). The index "D1" in the third column refers to the light on the D_1 line. The cloud parameters are not included in the D1-D2 CMOT stage because it is impossible to switch the shutters back to the D_2 line for absorption imaging. During the D1-D1 CMOT stage, shutters are switching and D_1 and D_2 lines are present simultaneously for about 0.6 ms (for ^{39}K), as explained in the main text.

We have adjusted the intensities and alignment of the cooling beams to enhance the efficiency of sub-Doppler cooling and magnetic trapping. This does not guarantee that the clouds in a magneto-optical trap would overlap well, but ultimately ^{40}K is

centered within a larger cloud of ^{39}K. The ratio of the number of fermions (N_{40}) to bosons (N_{39}) in the MOT is on the order of 1% and as a result only the fermionic MOT is influenced by the presence of the other isotope. This appears as a decrease in the initial loading rate by 20% (from 3×10^5 s^{-1} to 2.4×10^5 s^{-1}) and doubling the losses from 0.16 s^{-1} (only ^{40}K present) to 0.30 s^{-1} (^{40}K with ^{39}K present). This could be explained if we assume that the hotter bosonic atoms surrounding the fermionic cloud effectively act like the background gas. Due to the limitations of our imaging system and the small number of fermions involved, we have not been able to perform an analysis that would allow us to quantify the interspecies light induced collisions. Even with increased losses, we observe impressive performance in the following cooling phases, which is comparable to the cooling efficiency of ^{40}K alone [105].

Following the magneto-optical trapping stage, we compress the mixture by increasing the magnetic field gradient and red-detuning the D_2 line cooling light (see Table 6.1 for detailed parameters). We need to find a balance between reaching the highest density of both isotopes and minimizing the loss of atoms due to interspecies and intraspecies collisions. As can be seen in Figure 6.6a, losses of both species in the mixture are rapid. For ^{39}K, the light-induced losses seem to be exclusively homonuclear, which is expected since there are almost 100 times more bosons than fermions. The observed increase in the loss rate for ^{40}K when ^{39}K is present strongly suggests that heteronuclear collisions are the cause. We believe that the similarity in the loss rates of ^{39}K, whether compressed with or without ^{40}K, compared to the loss rate of ^{40}K compressed with ^{39}K, is merely coincidental and is primarily due to the significantly smaller number of fermions compared to bosons. We verified that there was no difference in the time evolution of the atom number when we compressed only one isotope with and without the cooling light for the other isotope present. We ensure that all experimental scenarios are conducted under nearly identical conditions: the experimental sequence and the cooling light powers remain constant, regardless of whether a single isotope or a mixture is being studied. When we study only one isotope, we prevent the other isotope from loading into the magneto-optical trap by detuning the repumping beam to the blue side of its respective transition. This adjustment does not alter the available power and only slightly changes the frequency, which is insufficient to affect the light-induced collisions in the other isotope. The observed lifetime of ^{40}K atoms in the compressed MOT (Figure 6.6a) appears to exceed the expected vacuum-limited lifetime of 1.5 s. This can be explained by the fact that atoms are still continuously loaded from the background gas while light-assisted collisional losses in the relatively dilute cloud of ^{40}K do not play a major role in the compressed MOT dynamics. Substantial light-assisted collisional losses are observed

for ^{39}K alone or for ^{40}K when ^{39}K is present (owing to heteronuclear collisions), and in these cases the additional loading of the trap does not play a role in the evolution of the atom number over more extended periods, as shown in Figure 6.6. In general, for the duration of typical compressed MOT stages, additional loading can be safely neglected.

We choose 20 ms as an optimal compression time to ensure consistent daily operation, minimizing the slight dependence of the efficiency of this cooling stage on the alignment of the cooling beams, their powers and the initial atom number. However, after the chosen compression time, the density of ^{40}K is typically several percent below its maximum, as can be seen in Figure 6.6b, where the maximum density of $n_{40\mathrm{K}} = 9 \times 10^9$ atoms/cm^3 ($n_{39\mathrm{K}} = 1.4 \times 10^{11}$ atoms/cm^3) for ^{40}K (^{39}K) can be reached after 13 ms (20 ms) of compression. This step increases the density and the phase-space density of both isotopes, with a greater increase of the latter for ^{40}K (see Table 6.1).

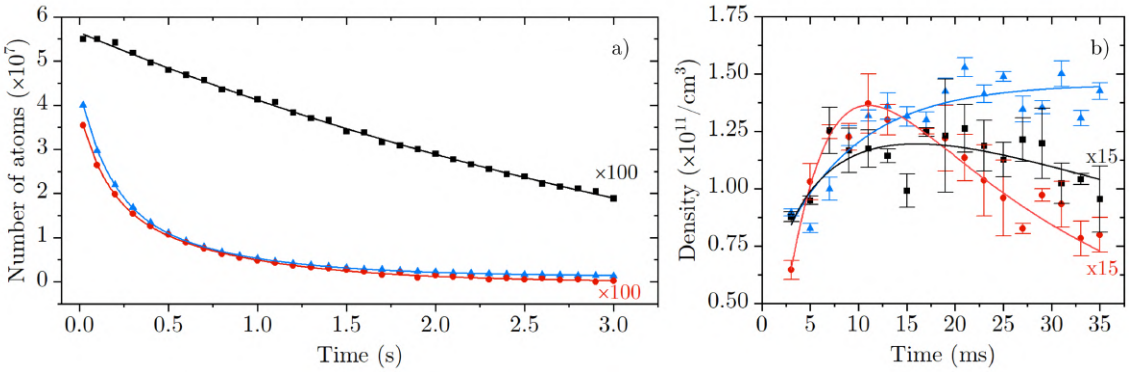

Figure 6.6: a) The evolution of the atom number in a compressed magneto-optical trap (CMOT) over time. The data points for ^{40}K are multiplied by a factor of 100 for better visual comparison with the behaviour of ^{39}K atoms. b) Changes in density within the CMOT during a time interval relevant to sub-Doppler cooling. In both figures, the data points represented by red circles and black squares are for ^{40}K with and without ^{39}K present while blue triangles represent ^{39}K atoms with ^{40}K atoms present. We have not observed any difference in the time evolution of the ^{39}K atom number regardless of whether ^{40}K is present or not, therefore the latter scenario is omitted for clarity. The lines are guides to the eye.

A standard compressed MOT (CMOT) is followed by a modified D1-D2 CMOT only for ^{39}K, similar to the approach chosen with ^{41}K (see Supplement 1). For ^{40}K, whenever cooling is optimized for one of the D lines, the presence of light from the

other D line immediately heats the atoms, inducing a large loss. This is purely a consequence of the design of the laser system. Hence, when we transition from the D_2 and to the D_1 line for ^{40}K, we ensure that the amplification module does not output light for cooling of the fermionic isotope, as discussed in [105]. As a result, there is a 1.2 ms window when the cloud of ^{40}K expands freely. At the end of this stage the quadrupole field is turned off and we engage the compensation of the stray fields.

In the final step, we begin simultaneous sub-Doppler cooling in gray optical molasses on the D_1 line of each isotope (see Table 6.1 for experimental details). After 12 ms of cooling we reach the temperature of 28 µK (13 µK) with 2×10^7 (2.5×10^5) atoms at the phase-space density of 1.6×10^{-7} (1.2×10^{-7}) for ^{39}K (^{40}K). At this point, we have lost 50% bosons and only 15% fermions. These results may not be as good as those reported in the literature for single-isotope cooling [73], [82], [105], but a similar reduction (with respect to single-isotope operation) has also been observed in a recent study of simultaneous sub-Doppler cooling of ^{6}Li and ^{7}Li [159]. Relatively large losses, especially for ^{39}K, occur during transfer to gray optical molasses. This seems to stem from the limited cooling power in a dual isotope operation, because with the same experimental sequence, but with the laser system set to emit only the ^{39}K cooling light, the overall performance is nearly identical to what we observe in a single isotope case [82]. Choosing not to include a molasses ramping step, commonly used in such experiments, could explain the higher temperatures observed compared to the temperature of the experiments with a single isotope. The choice to exclude this step has been driven by constraints in laser power, as its inclusion would lead to a significant reduction in the number of atoms. However, we have successfully transferred the mixture to a magnetic trap.

We initiate the spin polarization of both isotopes right after the gray molasses stage. First, we apply a 2.5 G magnetic field within 1 ms to establish the quantization axis, followed by switching off the residual light travelling along the MOT paths. Circularly polarized light is utilized for optical pumping on the D_1 line, addressing four transitions (two for each isotope): $2S_{1/2}\,F = 1,\, F = 2 \rightarrow {}^2P_{1/2}\,F = 2$ and ${}^2S_{1/2}\,F = 7/2,\, F = 9/2 \rightarrow {}^2P_{1/2}\,F = 9/2$. The light at each frequency component has an intensity of $0.6I_\mathrm{s}$. It is delivered to the setup via a single polarization-maintaining fiber and enters the vacuum chamber along a dedicated optical path. After 500 µs, beams addressing states with higher F are turned off while the remaining beams are extinguished 200 µs later. This procedure transfers atoms to weak-field seeking states; nearly 90% of fermions to $F = 9/2$, m_F=9/2 without introducing measurable heating, and nearly 80% of bosons to $F = 2$, m_F=2 with a temperature increase by a factor of two. A 57.6 G/cm magnetic field gradient (along

the weaker vertical axis) is turned on in 1 ms, trapping 1.4×10^7 of ^{39}K and 2.2×10^5 of ^{40}K. After 25 ms hold time in the magnetic trap, the average temperatures of the clouds are 61(4) μK for ^{39}K and 85(5) μK for ^{40}K, with corresponding phase-space densities of $5{\times}10^{-8}$ and $2{\times}10^{-9}$.

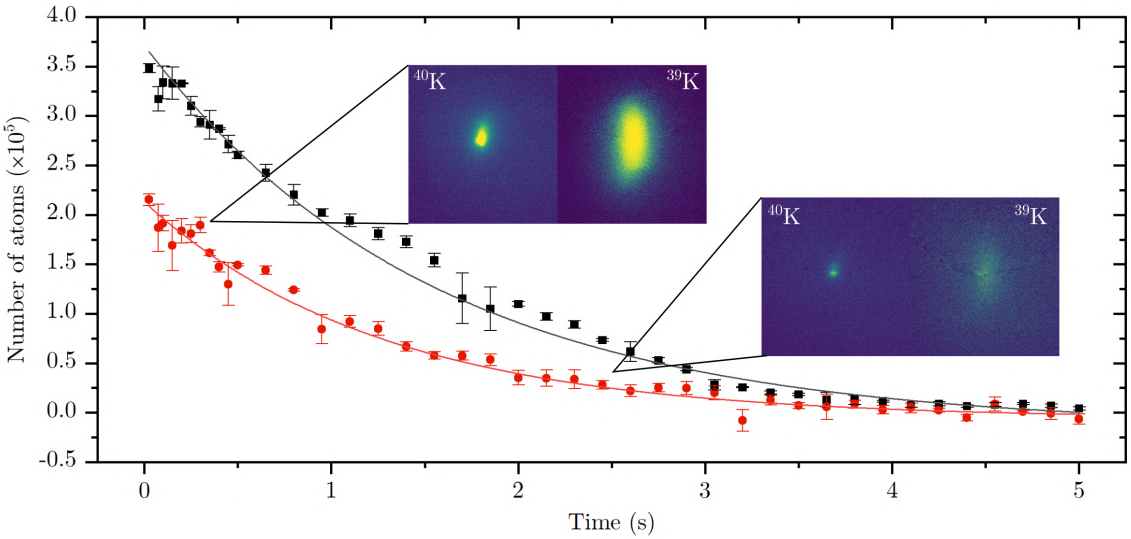

Figure 6.7: The lifetime of ^{40}K atoms in a magnetic trap with a gradient of 57.6 G/cm (aligned with gravity) is examined in two scenarios: a trap containing only a single species (black squares, with a lifetime of $\tau = 1.48(6)$ s) and a trap with the presence of the ^{39}K isotope (red dots, with a lifetime of $\tau = 1.20(4)$ s). The fitted curves are exponential decays. The insets show fluorescence images of both isotopes taken after two different trapping times.

The measured lifetime of the spin-polarized magnetically trapped atoms (Figure 6.7) is limited by the increased background gas pressure, primarily as a result of the operation of the dispensers at an elevated temperature. The $1/e$ lifetime of the fermionic potassium in the single isotope case is $\tau = 1.48(6)$ s, essentially the same as 1.45(5) s we observe when we trap only ^{39}K. The population of ^{40}K, when the ^{39}K-^{40}K mixture is trapped, decays with a time constant $\tau = 1.20(4)$ s. Within our experimental uncertainty, the lifetime of the bosonic isotope in the mixture is the same as when it is trapped alone. These lifetime measurements indicate the appearance of heteronuclear collisions, but a more quantitative analysis would most likely require using an enriched potassium source to increase the number of fermions. It would also allow us to increase the background gas-limited lifetime by running the dispenser at a much lower current. When the system is optimized to work only

with ^{39}K or ^{41}K, the individual isotopes can be trapped magnetically with a lifetime approaching 10 s.

6.5 Conclusion

We have successfully created the first, to the best of our knowledge, heteronuclear mixture of ^{39}K and ^{40}K trapped in a conservative potential. We have characterized the operation of a dual-isotope magneto-optical trap and the following cooling stages, including spin polarization of both isotopes. The results are particularly notable because of the simplicity of the experimental setup that uses a single-chamber vacuum system and an unenriched potassium source, which might make it a good platform for example for studies of quantum memories, where all the interesting physics happens on a milisecond time-scale [148]. The limitations imposed by the lifetime of trapped samples could be overcome if the atoms were magnetically transported to a separate chamber with a much better vacuum. It needs to be noted that in this particular mixture, evaporative cooling in the magnetic trap is not feasible due to the negative scattering length of ^{39}K. However, implementation of degenerate Raman sideband cooling following the gray molasses phase for ^{40}K, and possibly also for ^{39}K, [160], [161], should allow for efficient transfer of the mixture into an optical dipole trap which would increase the phase-space density of the sample, making it suitable for example for photoassociation studies. Under such conditions, fast optical transport to a separate chamber could be implemented [162], where the vacuum-limited lifetime would not be an issue. One could then envision using ^{39}K $[(F, m_F) = (1, 1)]$ around a 402.4 G Feshbach resonance [139] as a coolant for ^{40}K $[(F, m_F) = (9/2, 9/2)]$. Levitating ^{40}K in this state with magnetic field gradient of 6.4 G/cm and using a 1064 nm crossed optical dipole trap with a waist of 240 µm would make the trap depth for ^{39}K ≈25 µK shallower than for ^{40}K, possibly enabling selective evaporation. Our simulations show that the separation of the clouds would not exceed 20 µm for ^{39}K trap depths down to 15 µK. The demonstrated mixture could be immediately useful for optical tweezer experiments and photoassociation studies of heteroisotopic potassium molecules. The latter could be used to investigate the limits of the Born-Oppenheimer approximation [163], [164] by comparison with the spectroscopic data acquired for other homo- and heteronuclear potassium mixtures.

We have demonstrated an innovative laser system design that allows for sub-Doppler cooling of all stable potassium isotopes and their combinations, which has played a crucial role in achieving the results presented in this study. A modular design of the frequency tuning module of the laser system makes it easy to adapt it to cooling radioactive potassium isotopes, for example to study β -decay with laser-

cooled ^{37}K and ^{38}K^m isotopes [125]. A microsecond-scale switching time and an effectively maintenance-free approach to choosing which isotope is cooled make the laser system very useful for experiments in which bosonic and fermionic mixtures [46] or heteronuclear ground-state polar molecules are studied [59], [60]. In our group, the laser system is currently utilized to investigate properties of ultracold ^{39}K-Cs and ^{41}K-Cs mixtures.

The current design of the laser system is relatively expensive, because it utilizes four commercial MOPA systems. One could consider building the spectroscopy module around external cavity diode lasers instead of tapered amplifiers. It would not provide sufficient power (>10 mW) for seeding amplifiers in the amplification module, but this could be overcome by using a double-pass of seeding light through the gain medium of the amplifier. This solution has been shown to work for seeding powers as low as 200 µW [165] and has been demonstrated for simultaneous trapping of ^{85}Rb and ^{87}Rb [153].

6.6 Supplemental material: Sub-Doppler cooling of ^{41}K

The discussed laser system has been used to demonstrate state-of-the-art sub-Doppler cooling of ^{39}K [82] and ^{40}K [105]. For completeness, here we present sub-Doppler cooling of the remaining stable isotope, ^{41}K. We employ the same single-chamber apparatus in which cooling of other isotopes has been performed. Three retroreflected trapping beams with a diameter of about 25 mm and intensities of $23I_\mathrm{s}$ and $17.5I_\mathrm{s}$ for the cooling and the repumping beam, respectively, create a magneto-optical trap (MOT). With a magnetic field gradient of 7 G/cm, a 6.2 Γ detuning of the cooling and repumping beams from their respective transitions, and a 6 s loading time the number of atoms in the MOT saturates at $N = 5{\times}10^7$ with a temperature of ∼10 mK. This corresponds to the phase-space density of $\rho \approx 10^{-11}$. Here, $\Gamma = 6.035$ MHz is the natural linewidth of the D_2 line, and $I_s = 1.75$ mW/cm^2 is the saturation intensity [42]. The axis of symmetry of the magnetic coils is horizontal and as a result the vertical gradient of the magnetic field is one half of what is achieved when the coils are arranged with the symmetry axis oriented vertically. For details of the coils system see [101]. Here, we quote the magnetic field gradient in the direction of gravity (vertical direction). Atoms are released from a dispenser containing a natural isotope mixture (approximately 6.73 % of ^{41}K), placed 7 cm from the center of the trap. The cooling performance is characterized when the dispenser current is 4 A to improve the SNR. On a daily basis, the dispenser is turned off or heated resistively

with a current of 3.6 A.

Mechanical shutters in the spectroscopy module limit the switching time from the D_2 line to the D_1 line to approximately 1.8 ms, with a jitter of around 0.8 ms. During this time, the cloud falls freely and expands, decreasing its density. This is a critical issue because, at this stage, the atoms are relatively hot compared to the MOTs of other species. The conventional D1-D2 compressed MOT (D1-D2 CMOT) method [31] cannot be applied when compressing the cloud as it requires addressing the repumping transition on the D_2 line and the cooling transition on the D_1 line which is impossible with the design of our laser system. However, it is possible to perform cloud compression and cooling in a modified D1-D2 CMOT by amplifying the light for both D lines simultaneously in the amplification module.

Compression in the modified D1-D2 CMOT begins immediately after the MOT has reached its steady-state atom number. We raise the magnetic field to 35 G/cm and set the D_2 cooling (repumping) light detuning at -3Γ (-3.5Γ) and intensity at $11.5I_s$ ($9I_s$). Simultaneously, we open the shutter located in the spectroscopy module sending the D_1 line light to the amplification module. This results in a detuning of +4.5Γ (+7.5Γ) and an intensity of $7.3I_s$ ($7.3I_s$) for the cooling (repumping) D_1 light. The temperature decreases to 1 mK and the phase-space density increases to $\rho \approx 10^{-9}$, without significant loss of atoms. The D1-D2 CMOT is crucial for enhancing the cloud's density and facilitating its cooling. Furthermore, it plays a critical role in allowing the shutters a sufficient time (2.6 ms) to transition between the D_2 and D_1 lines.

Gray optical molasses cooling begins when only D_1 light is present (the shutter of the D_2 line is completely closed) and the magnetic fields are turned off. At this stage, we detune the D_1 line cooling and repumping light by +5Γ from the transition to the excited state $2P_{1/2}$ $F' = 2$ (Fig. 6.8a) so that a two-photon condition in the Λ configuration is satisfied. Figures 6.8b and 6.8c show the efficiency of gray optical molasses in terms of the remaining atom number and the final temperature (expressed here as a size after a fixed expansion time) as a function of the single- and two-photon detuning from the excited $F' = 2$ level.

At the beginning of gray molasess cooling we use the maximum available intensity of the cooling light, $14.6I_s$, while the intensity of the repumping light ($13.6I_s$) has been the result of optimization of the transfer of atoms from the D1-D2 CMOT to gray optical molasses. Using AOMs in the amplification module, we linearly reduce the intensity of cooling (repumping) light to $4.6I_s$ ($4.2I$s) in 6 ms (Figure 6.8d). This procedure decreases the temperature with no apparent loss in sample density, while retaining about 80% of the initial population. Finally, we obtain a cloud of 4.5×10^7 atoms, with a temperature of 11 μK (measured using the time-of-flight

method) and a phase-space density $\rho = 1.7 \times 10^{-5}$. Such a low temperature is on par with 16 µK reported recently by Cherfan et *al.* [107] and nearly 4× lower than some of the reference results for ^{41}K [31], [80].

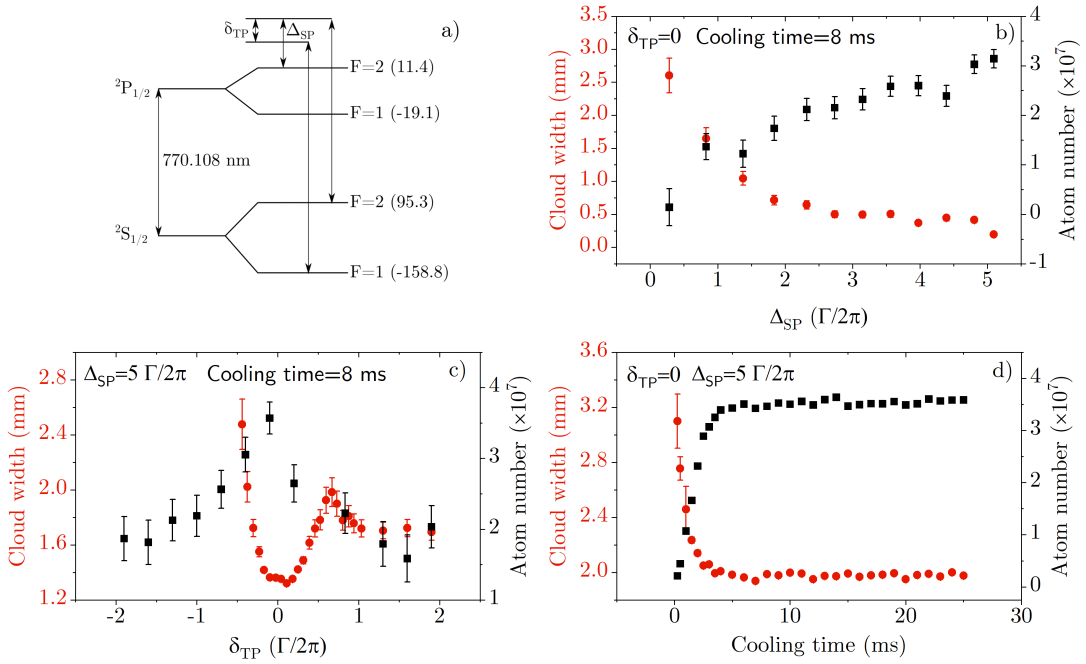

Figure 6.8: a) Hyperfine structure of the D_1 line of ^{41}K with frequencies of the cooling and repuming light used in gray-molasses cooling. Two-photon, and single-photon detunings are labeled as δ_{TP} and Δ_{SP}, respectively. The hyperfine shifts are in units of MHz. b)-d) Number of atoms and the width of the cloud after 10 ms expansion following the release from gray molasses, as a function of b) single photon detuning, c) detuning from the two-photon resonance, and d) cooling time in gray molasses. The initial increase in the number of atoms and the greater uncertainty in the width of the cloud in subplot d) can be attributed to the elevated initial temperature of the atoms: as the cloud expands over 10 ms, a portion of it moves beyond the imaging system's field of view.

Chapter 7

Sub-Doppler cooling of K-Cs mixtures: Feshbach spectroscopy, and loss analysis

The article presented in this chapter has not been published prior to the submission of this thesis, but it has been prepared for submission to *Physical Review A*.

This work represents, in many ways, the culmination of several years of effort by the entire research group, as it describes the most essential components of the apparatus: the vacuum system, the magnetic field coils, and the laser system for cooling cesium atoms.

In the article, we report on the cooling of bosonic potassium isotopes and cesium atoms, present the applied procedures, and discuss the method of efficient transfer to an optical dipole trap. We report the observation of several new Feshbach resonances in the ^{39}K–Cs mixture as well as reproduce results of earlier measurements by Gröbner et al. [84]. In our setup, the higher temperature of the mixture allows us to detect additional features associated with p-wave collisions as well as Feshbach resonances where cesium was prepared in the $F = 3, m_{\mathrm{F}} = 2$ state. These findings represent a significant contribution toward a more accurate determination of the molecular potentials for mixtures of all potassium isotopes with cesium atoms.

The observation of Feshbach resonances was performed using a new method, although based on a well-known effect. Specifically, spin mixtures of ^{39}K together with a spin-polarized cesium sample were loaded into an optical dipole trap. The standard Feshbach spectroscopy procedure was then applied, followed by Stern–Gerlach separation of the spin states. It turned out that the atom losses were not transferred between different magnetic levels, which enabled us to assign collision channels un-

ambiguously without the need to spin-polarize potassium, which accelerated the measurement process.

For the ^{41}K–Cs mixture, Feshbach resonances are not reported in this article. At an early stage of the study, their observation appeared to be impossible due to the reduced lifetime of this mixture. Since the ^{39}K–Cs mixture exhibits a longer lifetime compared to ^{41}K–Cs, we attribute this effect to interspecies interactions. To address this issue, the present article reports, for the first time, the three-body loss coefficients for both mixtures, which were calculated on the basis of the lifetime measurements.

Because this article covers a wide range of experimental techniques, all of the collaborators listed at the beginning of Chapter 4 are included as co-authors, reflecting their significant contributions to the construction of the apparatus. Each of the authors was also involved in the preparation of the final version of the manuscript.

The doctoral candidate submitting this thesis carried out all the measurements reported in the article, performed the data analysis, refined the experimental setup, and developed all cooling procedures presented here. He also prepared the first draft of the manuscript. The measurements, their sequence, and their significance for the field were discussed with and frequently proposed by Dr. Semczuk, who is also the last author of the article.

7.1 Abstract

We demonstrate simultaneous sub-Doppler cooling of ^{39}K-^{133}Cs, and ^{41}K-^{133}Cs mixtures to temperatures ∼10 µK, achieving performance comparable to that obtained with each species individually. The measurements were performed in a single-chamber setup, with atoms loaded directly from the background gas. For potassium isotopes, we implement sub-Doppler cooling with $D1$-line gray molasses, whereas cesium is cooled using the $D2$-line only. We spin polarize the atoms and confine Bose-Bose mixtures in a 1064 nm optical dipole trap.

The initial atom number and the density of optically trapped atoms are high enough to enable the observation of heteronuclear Feshbach resonances in the ^{39}K–Cs mixture, thus corroborating the results of Beulenkamp et al. [96], and presenting eight previously unobserved features, resulting from p-wave collisions, and different magnetic states of atoms. We have not yet observed resonances in the ^{41}K–Cs mixture because of the shorter lifetime of the mixture in the optical dipole trap. To provide a numerical value for the lifetime shortening, we estimate an upper bound of the three-body collision coefficient for both bosonic mixtures, through the analysis of the lifetime in the optical dipole trap.

The results presented are an important step towards Feshbach resonance spectroscopy of ^{41}K–Cs and photoassociation spectroscopy, being prerequisites for the eventual creation of ultracold ground-state molecules of KCs.

7.2 Introduction

Cooling mixtures of distinct atomic species unlocks a broad range of applications, governed by their collisional and interaction properties. To reach quantum degeneracy, mixtures with favorable collisional properties that allow for efficient cooling and thermalization like ^{41}K–^{87}Rb, ^{40}K–^{87}Rb, and ^{6}Li–^{23}Na [120], [140], [166], [167], have proven particularly advantageous. To observe new quantum phases, it is essential to employ systems in which interactions can be precisely tuned, e.g. using magnetic Feshbach resonances, as in the realization of quantum liquid droplets [168]–[170] or molecular Bose–Einstein condensates [171], [172]. For applications in quantum computation, quantum simulation, and ultracold chemistry, control over intraspecies interactions can be used to form heteronuclear molecules, which provide favorable anisotropic, long-range dipolar interactions [173]–[176].

Although recent experiments have demonstrated direct laser cooling of molecules [16], [177], the most common route to ultracold ground-state molecules still relies on laser cooling of atomic mixtures, followed by magnetoassociation and stimulated Raman

transfer [178], [179]. For this approach, it is crucial to know the positions of the Feshbach resonances and collisional properties of the mixture. These aspects have already been studied in detail for several species, including ^{23}Na–^{39}K, ^{87}Rb–^{133}Cs, ^{39}K–^{87}Rb, and ^{41}K–^{87}Rb, as well as for the mixture studied also in this work, ^{39}K–Cs [46], [96], [180]–[182]. The efficiency of this strategy has even enabled the first Bose–Einstein condensate of ultracold dipolar NaCs molecules [183].

In this context, potassium–cesium mixtures are particularly appealing due to the availability of three stable isotopes of potassium, which allow for the formation of both bosonic and fermionic KCs molecules. Realizing such systems, however, requires an efficient strategy for the laser cooling and a detailed understanding of their intra- and interspecies collisional properties, which are essential not only for molecules formation but also for achieving stable dual-species degenerate gases. A milestone in this direction was the Feshbach spectroscopy of the ^{39}K–Cs mixture [84], which paved the way for the recent production of ground-state ^{39}KCs molecules [96].

Here, we present an experimental setup that enables sub-Doppler cooling and optical trapping of both ^{39}K–Cs and ^{41}K–Cs mixtures. We develop and implement a cooling strategy, which allows us to obtain both mixtures with atom numbers exceeding $N = 2 \times 10^6$ for each species and sub-Doppler temperatures below $T < 15$ µK. These properties make the samples well-suited for Feshbach spectroscopy and studies of three-body interactions.

For the ^{39}K–Cs mixture, we implement a spin-resolved detection method based on the Stern–Gerlach effect and employ it for the Feshbach spectroscopy. This approach reduces the measurement time by a factor of three, since all collision channels in the potassium ground state can be probed in a single shot. Together with operating at higher temperatures than in the previous work (see Ref. [84]), this method enables us to confirm previously reported resonance positions and to identify eight additional loss features associated with different magnetic sublevels or higher partial waves.

Finally, we report preliminary investigations of the ^{41}K–Cs mixture. Although simultaneous cooling is achieved, the system exhibits reduced lifetime, which currently limits further spectroscopic studies. We attribute this limitation to enhanced heteronuclear three-body losses and provide initial estimates of the corresponding loss coefficients, along with a comparative analysis of lifetimes for both ^{39}K–Cs and ^{41}K–Cs mixtures.

7.3 Experimental setup and single species cooling

The vacuum system is based on a single-chamber design, with atomic dispensers (SAES getters) located 7 cm from the center of the magneto-optical trap, serving

as a source of atoms (see Fig. 7.1). In the system, two dispensers per species are available. During experiments with cold potassium and cesium mixtures, we typically run one dispenser per species at 3.2-3.6 A to maintain a satisfactory balance between the vacuum lifetime and the maximum number of trapped atoms. The potassium dispensers contain natural isotopic composition, consisting of 93.3% of ^{39}K, 0.012% of ^{40}K and 6.73% of ^{41}K [42]. The uncoated glass cell is vertically oriented and pumped with an ion pump and a titanium sublimation pump. The base pressure, when the dispensers have been off for 1-2 days, reaches 2-4$\times 10^{-11}$ mbar. During measurements, both types of dispensers are continuously running. The magnetic field generated by the dispensers at the location of the trap is negligible, as verified by RF spectroscopy of ^{41}K atoms.

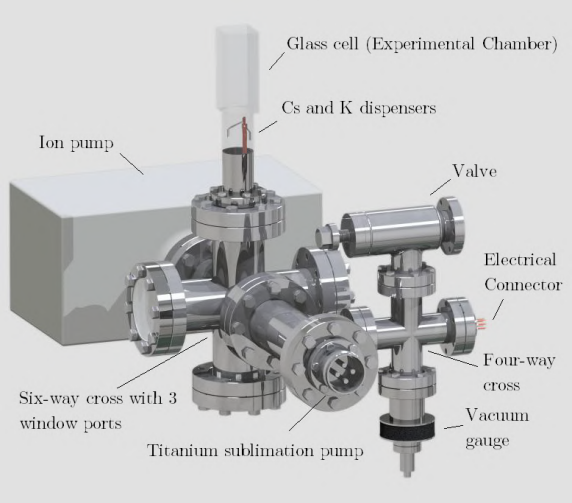

Figure 7.1: Rendering of the experimental chamber.

The magnetic fields in our system are generated by five pairs of coils. Three of them are arranged symmetrically around a glass cell to form a cage. These coils are used to compensate for residual ambient magnetic fields as well as to define a quantization axis during such stages of the experiment as optical pumping between Zeeman sublevels. A detailed description of the compensation coil system and its driving current source is provided in Ref. [82].

The remaining two pairs of coils are mounted radially in a single holder with a slit to suppress eddy currents that may arise during fast field switching. The holder is positioned horizontally, perpendicular to gravity, and is located near the glass cell, approximately 12 cm from the sample of cold atoms. The inner coil operates in a Helmholtz configuration, generating a uniform magnetic field for Feshbach

spectroscopy and magnetoassociation. The outer coil functions in an anti-Helmholtz configuration and is used during all stages that require a magnetic field gradient(such as magneto-optical trap loading or magnetic trapping).

The coils are powered by "Delta Elektronika SM45-70D" and "SM70-45D" power supplies, which can deliver up to 45 A and 70 A to the anti-Helmholtz and Helmholtz coils, respectively. These values limit the available gradient to about 115.2 G/cm along the coil axis and 57.6 G/cm in transverse directions. These values are sufficient for all of the experimental procedures and cooling methods introduced. The uniform bias field generated by the Helmholtz coils is limited to about 510 G, which is sufficient to reach many Feshbach resonances in both ^{39}K-Cs and ^{41}K-Cs mixtures [84].

For clarity of the manuscript, we first outline the cooling procedures for each individual species before presenting the results for the combined K–Cs mixtures. Finally, we discuss Feshbach spectroscopy of the ^{39}K–Cs mixture and estimate the upper bounds for the three-body loss coefficients in ^{39}K–Cs and ^{41}K–Cs systems.

Unless stated otherwise, all detunings are expressed in the units of natural linewidth of cesium $\Gamma_{\mathrm{Cs}} = 2\pi \times 5.223$ MHz, and potassium $\Gamma_{\mathrm{K}} = 2\pi \times 6.035$ MHz D2-lines. Laser intensities are reported in units of saturation intensity for the D2 line of cesium $I_{\mathrm{s}}^{\mathrm{Cs}} = 1.10$ mW/cm^2, and potassium $I_{\mathrm{s}}^{\mathrm{K}} = 1.75$ mW/cm^2 [41], [42].

7.3.1 Laser cooling of potassium atoms

The cooling procedures for the three potassium isotopes and the laser system used have been discussed in detail in our previous work [128]. Therefore, for the sake of the clarity of the manuscript, we only briefly outline the general cooling procedures, common for all potassium isotopes. The duration of each cooling step, the magnetic fields, the beam detunings, their intensities, the number of atoms, temperatures, and cloud densities in the case of single-species operation are summarized in Table 7.1.

The first cooling step involves trapping of atoms in a magneto-optical trap (MOT) utilizing lasers stabilized close to the D2-line frequency. The number of atoms in the magneto-optical trap typically saturates after 10–60 s, depending on the dispenser current and the abundance of the isotope in the source. Although a higher dispenser current shortens the MOT loading time, it significantly reduces the lifetime of the conservative traps due to the increased background pressure in the experimental chamber. These effects were discussed in detail in our previous work [105].

Stage	Atom	$\partial B/\partial z$ (G/cm)	δ_{C} (Γ)	δ_{R} (Γ)	I_{C} (I_s)	I_{R} (I_s)	N ($\times 10^6$)	T (μK)	ρ
MOT (10-60 s)	^{39}K	6	-8	-5	24.3	10.1	250	2500	8.5×10^{-10}
	^{41}K	6	-6.2	-6.2	23	17.5	43	10000	10^{-11}
	^{133}Cs	5.2	-3	-2.5	13.1	2.2	120	155	4.6×10^{-8}
CMOT (10-15 ms)	^{39}K	55	-9	-7	21	6.2	240	11000	9.7×10^{-10}
	^{41}K	35	-7	-7	23	17.5	42	-	-
	^{133}Cs	23	-3.5	-3.5	12.8	1.8	100	200	5.2×10^{-8}
D2D1-CMOT (2.6 ms)	^{39}K$_{\mathrm{D2}}$	55	-8	-4	12.2	6	210	140	3.6×10^{-7}
	^{39}K$_{\mathrm{D1}}$		-1	+8	15.6	12.8			
	^{41}K$_{\mathrm{D2}}$	35	-3	-3.5	11.5	9	40	1000	9.7×10^{-9}
	^{41}K$_{\mathrm{D1}}$		+4.5	+7.5	7.3	7.3			
	^{133}Cs	-	-	-	-	-	-	-	-
GMC (8-14 ms)	^{39}K$_{\mathrm{D1}}$	-	+4 (TP)	+13.2 (TP)	15.6 $\rightarrow$ 2.2	11.7 $\rightarrow$ 3	200	13	1.2×10^{-5}
	^{41}K$_{\mathrm{D1}}$	-	+5 (TP)	+10 (TP)	14.6 $\rightarrow$ 4.6	13.6 $\rightarrow$ 4.2	38	11	1.7×10^{-5}
	^{133}Cs	-	-42.3	-38.6	4.5	1.5	75	23	2.5×10^{-5}
TO-GMC 20-60 ms	^{39}K$_{\mathrm{D1}}$	-	+4 (TP)	+13.2 (TP)	1.4	0.3	150	16	8×10^{-6}
	^{41}K$_{\mathrm{D1}}$	-	+5 (TP)	+10 (TP)	2.2	0.7	35	-	-
	^{133}Cs	-	-42.3	-38.6	3.3	0.35	36	24	5.5×10^{-8}
Dipole trap	^{39}K	-	-	-	-	-	3.6	7.5	1.0×10^{-4}
	^{41}K	-	-	-	-	-	2	12	3.2×10^{-5}
	^{133}Cs	-	-	-	-	-	5.1	14	3.0×10^{-5}

Table 7.1: Main cooling stages in the single-species experimental procedure. In the table the first column represents a cooling stage and its duration range for different atomic species (in bracket). Following columns represents magnetic field gradient $\partial B/\partial z$ in the direction of gravity, detuning from cooling δ_{C} and repumping δ_{R} transitions, intensity of cooling I_{C} and repumping I_{R} beam, obtained number of atoms N, averaged typical temperature T and phase space density ρ. For the stages, where fulfilling two-photon condition is crucial, we emphasize it by (TP) in the bracket, next to the frequency. In the table, the cooling and repumping transitions, natural linewidth Γ and saturation intensity I_{s} depend on the species, as explained in the main body of the manuscript. Temperature and density for ^{41}K were omitted in stages at which the measurements were unreliable due to high temperature or distortion of the cloud shape.

When the number of atoms in the magneto-optical trap saturates, a compression stage is initiated to increase the cloud density, achieved by raising the magnetic field gradient and red-detuning the cooling and repumping beams. In accordance with the literature, we refer to this stage as a Compressed Magneto-Optical Trap (CMOT). At the end of the compression stage, we use mechanical shutters to block D2-line light, and to introduce the D1-line cooling and repumping beams. This activation takes 2.6 ms, where 1.5 ms is a timing jitter and 1.1 ms is a switching time. At this point, the frequencies of the cooling and repumping beams are tuned so that cooling is possible using both the D2 and D1 lines at the same time, utilizing the D2D1-CMOT method, similar to that described in the literature [31], [73]. We block the D2-line light using a mechanical shutter, so that after the compression stage only the D1-line light remains in the system.

In the next step, the magnetic field is turned off in 0.3 ms, and the output acousto-optic modulators in 0.1 ms are set to idle frequency for which the beam is not propagating to the experiment, but the modulator is still operating. This frequency reduces thermal effects that could appear due to the time of inactivity. When the magnetic field reaches zero, we introduce cooling in the λ-enhanced gray optical molasses. The stage of switching lines and turning off the magnetic field negatively affects the density of the sample, since the temperature at this stage is relatively high (2–10 mK), so the 0.4 ms of free expansion leads to observable dilution of the sample.

The cooling stage in gray optical molasses lasts 6–12 ms and allows for almost lossless temperature reduction to 8–13 µK, depending on the isotope and technical aspects, such as the alignment of the beams, or drifts in power and polarization. During this stage, we switch on the optical dipole trap, formed by a single beam generated by a 1064 laser, that passes twice through a cloud of atoms, so that a crossed dipole trap with an intersection angle of 22.5° is formed. To prevent the formation of a lattice, we rotate the polarization of the beam by 90° before its second pass through the cloud. The beams in the focus have a waist of 220×230 µm and a power of 32 W per beam. Considering the power losses from the beam passing through the uncoated glass cell, we employed a parametric heating method for more accurate trap diagnostics [184]. Using this method for potassium atoms, we obtained trap frequencies of $\omega_x, \omega_y, \omega_z = 2\pi \times [60,\ 137,\ 150]$ Hz, which correspond to a mean trap depth of $U = k_\mathrm{b} \times 102.3\ \mu$K, $U = k_\mathrm{b} \times 165\ \mu$K for potassium and cesium atoms, respectively.

Cooling in gray optical molasses, despite the obtained parameters of density, temperature, and number of atoms, yielded a transfer efficiency no higher than 0.3% for both bosonic isotopes. Therefore, another step was introduced, which for the sake

of clarity in the following part of the manuscript will be called Transfer-Optimized Gray Optical Molasses (TO-GMC). In this method, we perform gray molasses cooling optimized exclusively for transfer efficiency into the optical dipole trap.

The TO-GMC process starts immediately after the optical gray molasses stage. We keep the same frequency of the beams and start the optimization by finding beam intensities that yield the optimal transfer to the optical dipole trap. Our earlier work showed that properly optimized GMC in our system can hold the cloud for more than 1 s, but we choose to limit the holding time to 100 ms to mitigate losses from collisions with background gas [82]. The number of atoms transferred as a function of the beam intensities is shown in Fig. 7.2.

In the next step, we perform an optimization of the transfer time. With the previously selected beam parameters, we vary the time in a range of 10-100 ms, and we find that the maximum transfer efficiency occurs after $t = 50 - 60$ ms. The results of this optimization for ^{41}K atoms are shown in Fig. 7.2. In the end, for both bosonic isotopes we obtain a transfer efficiency into the optical dipole trap of ∼5.3% (^{41}K), or ∼1.8% (^{39}K) relative to the number of atoms at the end of the gray-optical molasses cooling, a significant improvement over the previous value of 0.3%.

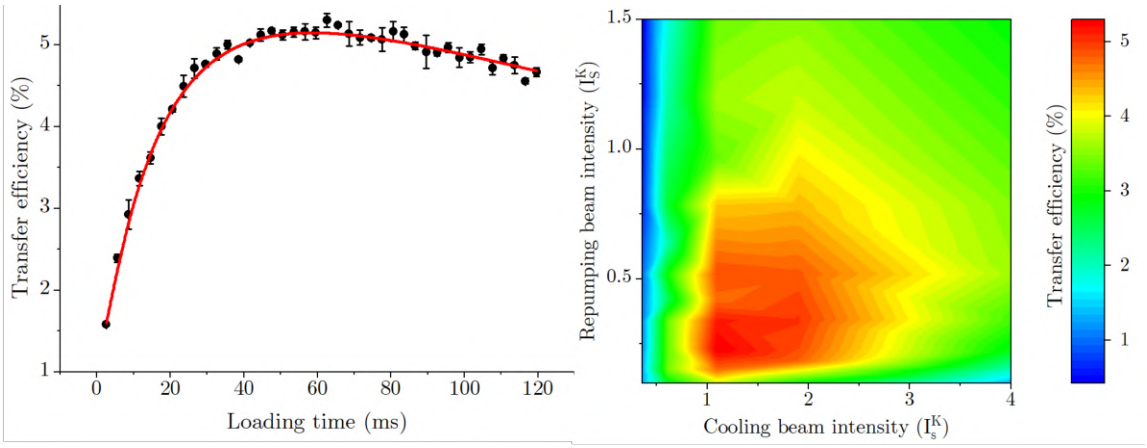

Figure 7.2: Transfer efficiency between gray optical molasses, and the dipole trap for potassium-41 atoms. Efficiency is presented as a function of loading time (left), and gray molasses beam intensities (right). Red curve on the left plot is presented as a guide to the eye.

The achieved transfer efficiency is promising for future experiments and represents a significant simplification compared to that obtained with well-established methods. For the ^{39}K isotope, cooling in gray optical molasses and subsequent magnetic trapping enabled the transfer of 2.7-8% of atoms to the optical dipole trap, but

at the expense of a high initial temperature in the range of 48 μK to almost 1 mK in the case of only trapping or trapping and magnetic transport [55], [138]. In the presented method, the initial temperature is lower than 15 μK.

Other methods, such as degenerate Raman sideband cooling, allowed for the transfer of 12% in the case of the fermionic isotope. However, it requires additional optical elements and optical paths, which may overcomplicate the experiment in the case of multi-species cooling [59]. In the case of our method, optical elements and paths are shared with MOT beams.

The transfer between gray optical molasses and an optical dipole trap as shown here is promising from the perspective of multi-species experiments because of its universality. Magnetic trapping, evaporation, and transfer to the optical dipole trap could not be efficient in the case of ^{40}K due to Pauli blocking of collisions, and for the ^{39}K atoms due to the Ramsauer-Townsend minimum at relatively high temperatures of 400 μK [138]. On the other hand, this method is the most efficient path toward the Bose-Einstein condensation of ^{41}K [31]. Other methods like Degenerate Raman Sideband Cooling might be promising from the perspective of the transfer of ^{39}K and ^{40}K, but to the best of our knowledge, have not been introduced yet, and could be hindered in the case of ^{41}K because of the small splitting of hyperfine levels [59], [60].

In multi-species experiments, the TO-GMC method introduced for one species does not interfere with the cooling of the other. This method only requires a relatively low-intensity light that is far detuned from the other species' main absorption lines, and its only additional requirement is turning off all magnetic fields, which is typical for optical molasses cooling procedures. The optimization of the transfer seems promising for all atomic species in which this cooling method was introduced, e.g. ^{6}Li, ^{7}Li, ^{87}Rb, ^{23}Na [77], [78], [81], [185].

The last stage of the sample preparation is spin polarization in the selected magnetic sub-level. In the case of bosonic potassium, we turn on the uniform magnetic field $B = 2.5$ G, and switch on two circularly polarized beams resonant with $^2S_{1/2}F = 1 \rightarrow {}^2P_{1/2}F = 1$, $^2S_{1/2}F = 2 \rightarrow {}^2P_{1/2}F = 2$ transitions. The polarization of beams and the direction of the magnetic field are set in such a way as to drive only $\sigma+$, or $\sigma-$ transitions. After 0.5 ms, we obtain a sample polarized in the $^2S_{1/2}F = 2,\ m_f = 2$ and $^2S_{1/2}F = 1,\ m_f = 1$ states. We turn off these two laser beams and introduce one that propagates in the opposite direction. This beam is tuned to the $^2S_{1/2}F = 2 \rightarrow {}^2P_{1/2}F = 2$ transition and has a linear polarization, exciting only the π transition. Finally, depending on the direction of the quantization axis, we obtain a sample containing 80% of atoms in the $^2S_{1/2}F = 1,\ m_f = 1$, or $m_f = -1$ state, with 20% of atoms occupying the $^2S_{1/2}F = 1,\ m_f = 0$ state.

7.3.2 Laser system and procedures for cooling of Cs atoms

The intensities of the cooling beams, detunings from the transition, number of atoms, temperature, and the phase-space density for laser cooling of cesium are presented in Table 7.1. In the procedure described here, only the D2 line is used; therefore, for the clarity of the following manuscript, we will omit a fine structure index, using only the total angular momentum F and the magnetic moment m_{F}.

The cesium laser system was designed to allow cooling atoms in a procedure similar to that used for potassium atoms. The system consists of two Toptica TA-Pro MOPA systems, stabilized with a CoSy (compact spectroscopy) module and Digilock 110. The laser used in the experiment as a repumper was stabilized to the $F = 3 \rightarrow F' = 3$ transition, while the cooling laser has an acousto-optic modulator in the stabilization path, allowing for stabilization 69 MHz above the $F = 4 \rightarrow F' = 4$ transition frequency. The lasers, unlike in the case of potassium (see Ref. [128]), are stabilized to the lock-in detected transitions obtained by modulation of the diode current at 41.12 kHz and 45.96 kHz for the repumping and cooling lasers, respectively. These modulations result in a broadening of the effective laser linewidth to about 4 MHz. A more detailed discussion of this effect can be found in the work [100].

The light from the optical amplifiers passes through dedicated mechanical shutters, followed by single-mode polarization-maintaining fibers used to propagate light to a second optical table, where fine-tuning of the frequency and free-space propagation to the experimental system takes place. Repumping beam, upon entering the system, is split into two paths, as presented in Fig.7.3b). In both paths, there is an acousto-optic modulator (AOM) in a double-pass configuration. One of the modulators operates at 80–100 MHz, and its main purpose is to tune repumping light for various stages of the experiment. This modulator is also used as a fast (sub-μs) switch.

In the second path, there is an AOM operating at –72 MHz, so that the beam is blue-detuned by the value of Γ_{Cs} from the $F = 3 \rightarrow F' = 2$ transition. After the double pass, this beam overlaps with one of the beams dedicated to potassium experiments and is sent to the vacuum system via an optical fiber. A linear polarizer and an achromatic quarter-wave plate are placed at the output of the fiber, in such a way as to create an optical path whose purpose is to optically pump atoms between magnetic sublevels. A schematic of this part of the laser system is shown in Figure 7.3b).

The path dedicated to fine-tuning the frequency of the light which is stabilized 69 MHz above $F = 4 \rightarrow F = 4$ transition involves more components, as it must accommodate both cooling and probing purposes. The scheme of this part of the system is presented in the Fig.7.3a). The beam from the optical fiber is deflected by

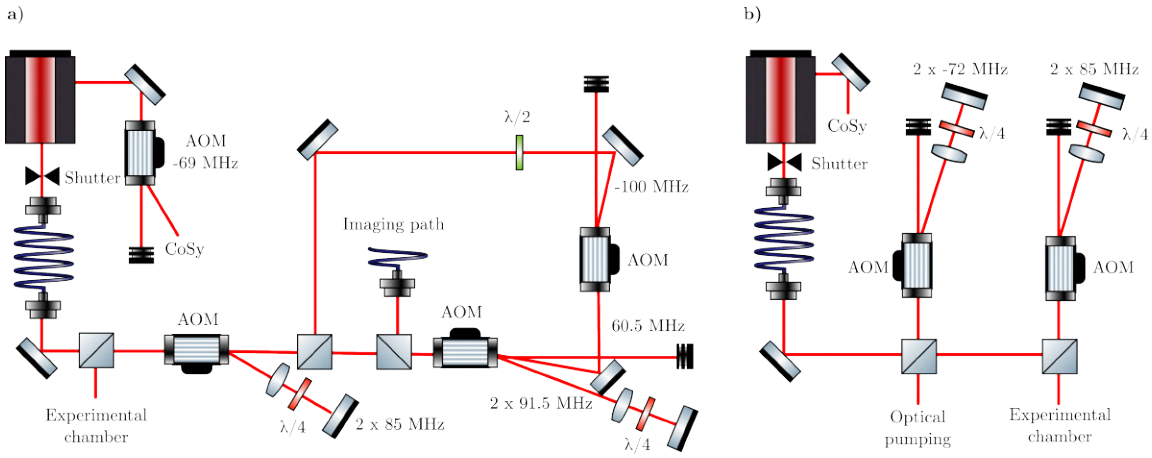

Figure 7.3: Laser system for cooling cesium atoms, presented in two parts. a) Distribution of light stabilized 69 MHz above $F = 4 \rightarrow F' = 4$ transition in Compact Spectroscopy (CoSy) module. Light is distributed and frequency tuned using acousto-optic modulators, where default deflection frequency is marked in the figure, with multiplier indicating double-pass configuration. b) Distribution of light stabilized to $F = 3 \rightarrow F' = 3$ transition.

an AOM operating at 85 MHz in a double-pass configuration. In this way, the light is tuned $2.5\Gamma_{\mathrm{Cs}}$ below the cooling transition $F = 4 \rightarrow F' = 5$. With the modulator turned off, the beam passes to a second AOM set to +91.5 MHz in a double-pass configuration. In this configuration, the beam is resonant with the $F = 4 \rightarrow F' = 5$ transition and is coupled into an independent optical fiber, enabling absorption imaging of the atoms.

If the modulator instead operates at +60.5 MHz, the beam is deflected in the single-pass configuration. The deflected beam then passes through another AOM operating at –100 MHz, becoming blue-detuned by $6\Gamma_{\mathrm{Cs}}$ relative to the $F = 4 \rightarrow F' = 4$ transition. The beam is then superimposed with the MOT cooling beam and distributed in the system. This beam is used only during the optical molasses cooling stage.

The cooling of cesium atoms begins by trapping the atoms in a magneto-optical trap, produced by a magnetic field gradient of 5.2 G/cm, and the cooling and repumping beams red-detuned by $3\Gamma_{\mathrm{Cs}}$, $2.5\Gamma_{\mathrm{Cs}}$ red-detuned relative to the dedicated transitions, respectively. This allows us to trap $N = 1.2 \times 10^8$ atoms at temperature $T = 155\ \mu$K with a phase-space density of $\rho = 4.6 \times 10^{-8}$.

To increase the density of the sample, we use the CMOT method, for which

both beams are red-detuned by $3.5\Gamma_{\mathrm{Cs}}$, relative to dedicated cooling and repumping transitions, while the magnetic gradient is increased to 23 G/cm in 2 ms. Then, when the field reaches the desired value, the compression process takes 8 ms. In this way, we increase the density of the cloud with slight loss in the number of atoms. Compression also leads to an increase of temperature to $T = 200$ μK. At the end of this stage, the phase space density of $\rho = 5.1 \times 10^{-8}$ is reached.

The increased temperature does not allow for efficient transfer of atoms to the optical dipole trap, and hence cooling in the optical molasses is introduced. The cooling beam is blue-detuned by $6\Gamma_{\mathrm{Cs}}$ from $F = 4 \rightarrow F' = 4$ transition. At the beginning, we use all the available light power, obtaining an intensity of 4.5 $I_{\mathrm{s}}^{\mathrm{Cs}}$, while the intensity of the repumping beam is reduced to 1.5 $I_{\mathrm{s}}^{\mathrm{Cs}}$, and its frequency is chosen so that the beam is resonant with the $F = 3 \rightarrow F' = 3$ transition. This cooling method, after 8 ms, allows the cloud temperature to be reduced to 23 µK, reaching a number of atoms $N = 7.5 \times 10^7$, and phase space density of $\rho = 2.5 \times 10^{-6}$.

For the cesium atoms, we also introduce the TO-GMC method at the end of the cooling. Here, the main limitation is introduced by the technical aspects of the experiment. The cooling beam propagates through paths longer than 2 m before reaching a vacuum chamber. This leads to a noticeable drift of the laser beam position during prolonged cooling, due to thermal effects appearing in the crystal of the acousto-optical modulator. We found that because of these effects, if the cooling takes longer than 60 ms, the GMC path becomes misaligned and the transfer efficiency decreases. That sets an upper limit for the cooling time. We also performed optimization similar to the one previously described for the potassium case. The results are presented in Fig. 7.4. Finally, with a transfer time of $t = 40$ ms performed with the cooling and repumping beam intensities of $0.35 I_{\mathrm{S}}^{\mathrm{Cs}}$, and $3.3 I_{\mathrm{S}}^{\mathrm{Cs}}$, respectively, we obtain $N_{\mathrm{ODT}} = 5.1 \times 10^6$ atoms in the optical dipole trap.

Finally, in the last stage, we polarize the cesium atoms in the energetically lowest magnetic sublevel. Firstly, we apply a magnetic field of 2.5 G and introduce a laser beam blue-detuned by $1.5\Gamma_{\mathrm{Cs}}$ from the $F = 3 \rightarrow F' = 2$ transition, with circular polarization. The direction of the magnetic field is set so as to introduce mostly $\sigma+$ transitions, with a non-negligible probability that the π transitions occur. During the pumping time, a beam resonant with the $F = 4 \rightarrow F' = 5$ transition is constantly turned on to excite atoms that could decay to the $F = 4$ state from the off-resonant excitations. Finally, we obtain samples polarized in the $F = 3, m_{\mathrm{F}} = 3$ state, with about 10% of atoms occupying other states, mostly $F = 3, m_{\mathrm{F}} = 2$.

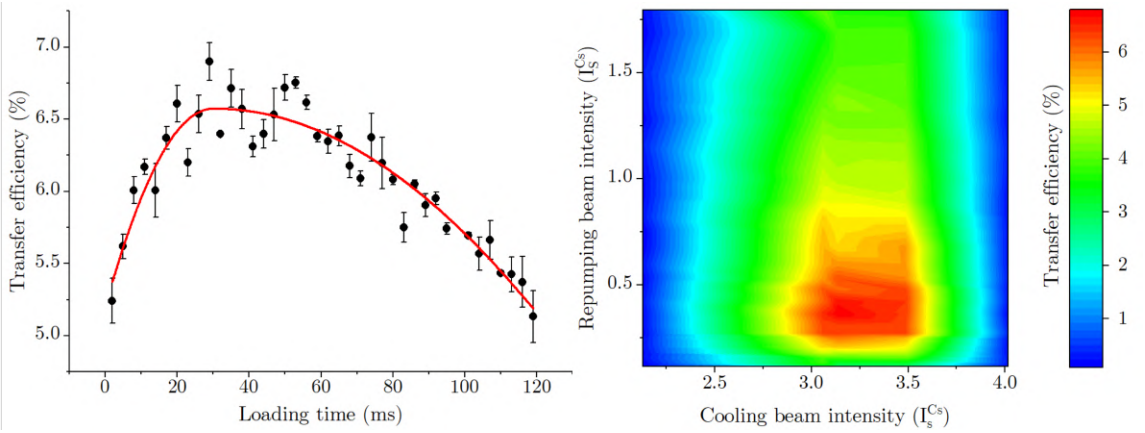

Figure 7.4: Transfer efficiency between gray optical molasses, and the dipole trap for cesium atoms. Efficiency is presented as a function of loading time (left), and gray molasses beam intensities (right). Red curve on the left plot is presented as a guide to the eye.

7.4 Laser cooling of K-Cs mixtures

In our multispecies experimental system, the optimal cooling strategy for the potassium-cesium mixtures is strongly dependent on the abundance of the potassium isotopes in the utilized source. For the less abundant isotope (^{41}K) the procedures have to be specifically optimized to obtain the highest number of these atoms in the optical dipole trap, even at the cost of a slightly lower number of cesium atoms. In contrast, in the ^{39}K–Cs mixture, both species are captured in comparable numbers in the magneto-optical trap, allowing for a balanced optimization that yields similar atom numbers in the dipole trap.

Obtaining a ^{39}K-Cs, ^{41}K-Cs mixture in our system is done using the same methods as for single-species operation, but with fine-tuned parameters for multi-species operation. We observe a slight reduction in the number of trapped atoms when both species are present, which we attribute to heteronuclear collisions between atoms. Also, as noted in the previous sections of the manuscript, the optimal compression for potassium and cesium atoms occurs at different magnetic field gradients. Hence, at this stage, we optimize the density of a more diluted (at the MOT stage) cloud, namely potassium atoms.

Finally, we obtain K-Cs mixtures in the optical dipole trap, with a temperature comparable to that of single-species operations, but with a reduced number of atoms to $N_{39K} = 3.1 \times 10^6$ and $N_{Cs} = 3.8 \times 10^6$ for ^{39}K-Cs mixture, and $N_{41K} = 1.1 \times 10^6$,

$N_{Cs} = 4.3 \times 10^6$ for ^{41}K-Cs mixture.

7.4.1 Feshbach spectroscopy in ^{39}K-Cs mixture

For clarity, in the following part of this manuscript, the magnetic sublevels of the hyperfine ground states are labeled alphabetically in order of increasing energy. Specifically, for ^{39}K, and ^{41}K atoms we use $|a, b, c\rangle$ to denote the states $^2S_{1/2}, F = 1, m_{\mathrm{F}} = \{1, 0, -1\}$, and similarly for ^{133}Cs atoms, $|a, b, \ldots\rangle$ corresponds to $^2S_{1/2}, F = 3, m_{\mathrm{F}} = \{3, 2, \ldots\}$

Feshbach spectroscopy is performed using two different approaches. Firstly, we perform measurements with the standard method, where a mixture of spin polarized samples of ^{39}K$|a\rangle$-Cs$|a\rangle$ (or ^{39}K$|c\rangle$-Cs$|a\rangle$) is trapped in the optical dipole trap. Then in 100 ms, a magnetic field is turned on and held for 500 ms. After that time, we switch off the magnetic field in 100 ms, and fluorescent imaging is performed, providing information about the number of remaining atoms. We perform fluorescence imaging for both species, but observable losses occur only for potassium atoms. We attribute this to the lower atomic mass of potassium and the shallower trap depth, which together result in more pronounced loss mechanisms in this case.

The presented standard method has certain limitations that cannot be easily overcome. In particular, standard optical pumping does not allow for obtaining a pure polarized sample. In our case, we observed approximately 10% of atoms occupying an energetically higher spin state (channel $|b\rangle$) for cesium atoms, leading to the observation of additional weak loss features. Better pumping of atoms often requires the use of additional methods, such as spin state purification through a magnetic trap, or RF-pulse pumping [84], [104].

Therefore, to confirm the assigned collision channels, we decided to depopulate the $|a\rangle$ channel and to repeat measurements. To do so, first, the atoms are polarized into the $F = 3$, $m_F = 3$ state. Then, a magnetic field of $B = 88$ G is applied. In this field, we introduce a 1 ms pulse of light driving only π transitions with an intensity of $0.6 I_s^{\mathrm{Cs}}$. The light is blue-detuned by $9\Gamma_{\mathrm{Cs}}$ from the zero-field $F = 3 \rightarrow F' = 3$ transition. At this detuning, the beam becomes resonant with the high-field transition $F = 3,\ m_F = 3 \rightarrow F' = 3,\ m'_F = 3$, while the closest allowed transition, $F = 3,\ m_F = 2 \rightarrow F' = 3,\ m'_F = 2$, remains detuned by approximately $3\Gamma_{\mathrm{Cs}}$.

To prevent the population from accumulating in the $F = 4$ state during the pumping process, a MOT cooling beam is applied simultaneously. Finally, atoms remaining in the $F = 3, m_F = 3$ state are removed, resulting in a sample predominantly occupying the $F = 3,\ m_F = 2$ state. With this method, we can assign Feshbach resonances to the cesium $|a\rangle$ or $|b\rangle$ channels.

For the potassium atoms, instead of optical pumping into the $F = 1,\ m_F = 0$ state, we implement a novel detection method. A mixture of magnetic states of potassium atoms, together with a spin-polarized cesium sample, is loaded into an optical dipole trap. The potassium population is initially equally distributed among the $F = 1,\ m_F = \{1,\ 0,\ -1\}$ states.

The resonance measurement procedure then follows the same sequence as previously described. However, before imaging, we perform spin-state separation using the Stern–Gerlach method. A homogeneous magnetic field is applied along with a magnetic field gradient, allowing the spatial separation of different spin states 8 ms after atoms are released from the dipole trap. The number of atoms in each spin component is then measured independently. An example of spatially separated atomic clouds in the vicinity of a Feshbach resonance and far from resonance is shown in Fig. 7.5.

Using measurements performed with spin-polarized samples, we confirmed that collisions occurring within one spin channel are not transferred to other channels. Despite its simplicity, this method allows for a three-fold increase in data acquisition speed and eliminates the need to pump potassium atoms into the $F = 1,\ m_F = 0$ state.

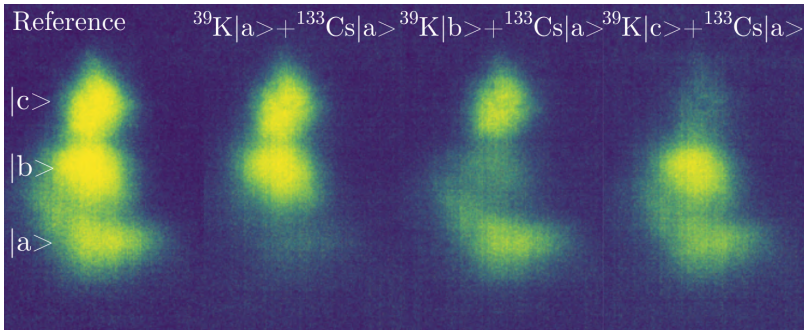

Figure 7.5: Fluorescence images of magnetically separated potassium samples after heteronuclear Feshbach spectroscopy. Each image shows three spatially separated potassium clouds corresponding to the magnetic sublevels of the $F = 1$ state with $m_F = \{1, 0, -1\}$, denoted as $|a\rangle$, $|b\rangle$, and $|c\rangle$, respectively. From left to right: reference image (no loss feature), and three cases showing atom loss due to Feshbach resonances between ^{39}K and ^{133}Cs in the channels indicated at the top of each panel.

With the methods described above, we observe 14 Feshbach resonances. Their thresholds, positions, widths, and theoretical locations based on the potentials from Ref. [84] are summarized in Table 7.2. The table also indicates resonances whose

positions have been previously reported in the literature. A comprehensive plot showing all resonances observed in the present work is presented in Fig. 7.6.

		Theory G2017	Experiment This work		Experiment Ref. [84], [96]		
K	Cs	B_{res} (G)	B_{res} (G)	Δ (G)	B_{res} (G)	Δ (G)	L
$\|a\rangle$	$\|a\rangle$	360.74	360.95(13)	2.67(38)	361.1(1)	3.2(4)	0
		442.43	443.28(2)	0.38(6)	442.59(1)	0.28(3)	0
		333.55	333.32(4)	1.55(40)	-	-	1
$\|a\rangle$	$\|b\rangle$	348.54	347.83(14)	3.96(42)	-	-	0
		318.12	315.95(11)	1.60(31)	315.551(2)	-	1
$\|b\rangle$	$\|a\rangle$	419.73	419.70(07)	2.43(16)	419.3(1)	3.0(5)	0
		391.02	394.42(11)	3.94(25)	-	-	1
$\|b\rangle$	$\|b\rangle$	408.73	408.40(12)	3.70(43)	-	-	0
		377.65	376.36(10)	2.39(34)	-	-	1
$\|c\rangle$	$\|a\rangle$	492.24	491.94(07)	2.06(32)	491.5(1)	2.1(4)	0
		465.56	463.99(05)	1.82(30)	463.251(5)	-	1
$\|c\rangle$	$\|b\rangle$	317.0	322.32(37)	8.07(1.68)	-	-	0
		482.0	482.27(12)	2.16(45)	-	-	0
		452.38	453.99(26)	8.84(1.16)	-	-	1

Table 7.2: Heteronuclear Feshbach resonances observed in the ^{39}K–Cs mixture. The table lists the collision channels, theoretical resonance positions calculated using the G2017 interaction potentials [84], and experimental positions (B_{res}) and widths (Δ) extracted from Lorentzian profiles fitted to the loss features presented in the Fig.7.6. Previously reported resonances from Ref. [84], [96] are also included for comparison. The final column indicates the orbital angular momentum L associated with each resonance.

7.4.2 ^{41}K-Cs mixture

The cooling procedure for the ^{41}K-Cs mixture is similar to the single species case. The main difference occurs in the CMOT stage, where similarly to ^{39}K-Cs we utilize the magnetic field of 35 G/cm, favorable for the density of ^{41}K atoms, but leading to observable losses in the cesium sample. Finally, we are capable of trapping both

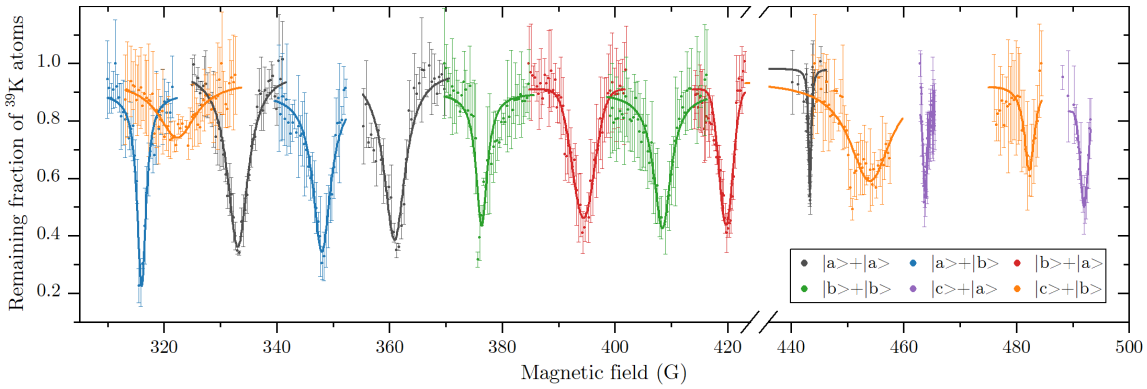

Figure 7.6: Overview of losses in ^{39}K atoms present due to the heteronuclear ^{39}K-Cs Feshbach resonances. A Lorentzian function is fitted to each feature to extract the position and the experimental width of the Feshbach resonance. Different colors correspond to different collision channels, as presented in the legend. Homonuclear losses are omitted for clarity.

atoms in an optical dipole trap, with temperatures and densities similar to those for the single-species scenario, but with a reduced number of atoms, as presented in the beginning of this section.

We observed a significant shortening of the lifetime of ^{41}K atoms in the optical dipole trap, when cesium is present. To make a comparison for both K-Cs mixtures, we reduced the number of atoms in the optical dipole trap reaching the same number of potassium-41 and cesium atoms, namely $N_{41K}, N_{Cs} = 1.0(1) \times 10^6$, and slightly larger sample of potassium-39 $N_{39K} = 1.2(1) \times 10^6$, reaching densities of $d_{41\mathrm{K}} = 6.14 \times 10^{11}$ atoms/cm^2, $d_{39\mathrm{K}} = 7.36 \times 10^{11}$ atoms/cm^2, $d_{\mathrm{Cs}} = 1.38 \times 10^{11}$ atoms/cm^2. With these samples, we observed a reduction in the $1/e$ lifetime of ^{41}K atoms from $\tau = 3.88(15)$ s to $\tau = 1.75(10)$ s due to the presence of cesium atoms in the optical dipole trap. In the mixture of the ^{39}K-Cs, we observed that the lifetime of ^{39}K decreases from 5.85(17) s to 2.46(05) s. We explain this as an effect of the heteronuclear collisions with cesium atoms. This assumption is supported by theoretically calculated heteronuclear scattering lengths, where singlet scattering lengths are $a_{\mathrm{s}}^{39\mathrm{K-Cs}} = -18.37\ a_0$, $a_{\mathrm{s}}^{41\mathrm{K-Cs}} = -72.79\ a_0$, and triplet $a_{\mathrm{t}}^{39\mathrm{K-Cs}} = 74.88\ a_0$, $a_{\mathrm{t}}^{41\mathrm{K-Cs}} = 179.06\ a_0$ [84].

We perform an initial three-body loss analysis for both mixtures. Firstly, spin-polarized atoms in the energetically lowest magnetic sublevels are trapped in the optical dipole trap. Then the $B = 5$ G field is applied to overcome spin flipping, and a lifetime is measured for each case. To address losses, we fit coupled differential

equations to the obtained curves:

$$\dot{N}_a = -\frac{2}{3}L_{aab}\int n_a^2 n_b d^3r - \frac{1}{3}L_{abb}\int n_a n_b^2 d^3r - L_{aaa}\int n_a^3 d^3r - N_a/\tau_{bg}. \qquad (7.1)$$

Here, the subscript a, b indicates atomic species, L are subsequent loss coefficients with bottom with bottom index indicating atoms participating in the collision, n is a position dependent temporal density of the sample, assuming Gaussian distribution of the cloud, and τ_{bg} is a lifetime resulting from the collisions with background gas. In this analysis, we introduce two simplifications. Firstly, the evolution of sample size and temperature is omitted, hence the fitting result represents an upper bound for the loss coefficient as most of the collisions take place in the center of the trap, occupied by the coldest atoms. Therefore, anti-evaporation might occur, leading to an artificial increase of the loss coefficient [45]. Second, we fix a known three-body coefficient, so calculations can be computationally simpler, namely $L_{\mathrm{KKK}} = 1 \times 10^{-29}$ cm^6 s^{-1}, $L_{\mathrm{KKK}} = 4 \times 10^{-29}$ cm^6 s^{-1}, $L_{\mathrm{CsCsCs}} = 3 \times 10^{-24}$ cm^6 s^{-1} for ^{39}K, ^{41}K, and ^{133}Cs, respectively [45], [46]. The curves resulting from these calculations are presented in Fig. 7.7.

Based on the loss analysis, we estimate that the upper bounds for the three-body loss coefficients are $L_{\mathrm{KCsCs}} < 1.50(51) \times 10^{-24}$ cm^6 s^{-1} and $L_{\mathrm{KKCs}} < 3.58(42) \times 10^{-24}$ cm^6 s^{-1} for the ^{39}K–Cs mixture, and $L_{\mathrm{KCsCs}} < 1.94(27) \times 10^{-23}$ cm^6 s^{-1}, $L_{\mathrm{KKCs}} < 7.19(28) \times 10^{-23}$ cm^6 s^{-1} for the ^{41}K–Cs system.

The extracted values of L_{KKCs} , and L_{KCsCs} are in a range consistent with those reported for other heteronuclear systems such as ^{39}K-^{87}Rb, ^{41}K-^{87}Rb, ^{23}Na-^{39}K, and ^{6}Li–Cs [46], [180], [186]. Moreover, higher loss coefficients for the ^{41}K-Cs mixture are confirmed by a shorter lifetime of the mixture in the optical dipole trap in comparison with ^{39}K-Cs.

7.5 Conclusions

In this work, we have presented a new experimental setup enabling the simultaneous sub-Doppler cooling and optical trapping of potassium–cesium mixtures. The developed procedures are efficient and adaptable, making them promising for application to other heteronuclear alkali systems.

The performance of the system was validated by Feshbach spectroscopy of the ^{39}K–Cs mixture, where we confirmed previously reported resonances and identified additional features relevant for the production of ground-state ^{39}K-Cs molecules.

We also report on the creation of an ultracold ^{41}K–Cs mixture in an optical dipole trap, to our knowledge for the first time. Feshbach spectroscopy of this sys-

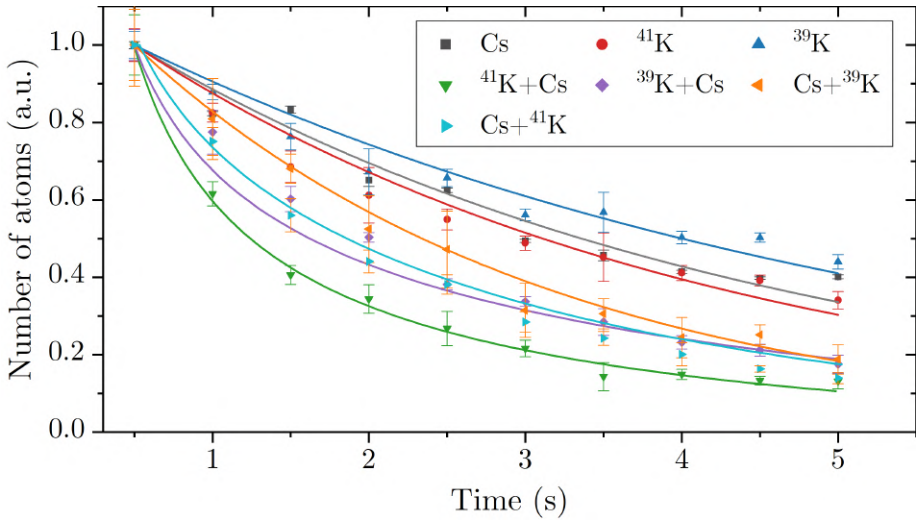

Figure 7.7: Normalized number of atoms, as a function of trapping time in the optical dipole trap. The data points represent decay of number of atoms in single-species and heteronuclear mixtures, with fitted curves based on Eq. 7.1 for the mixtures and exponential fits for the single-species cases. Colors and markers correspond to the specific decay curves shown in the legend. The labels (e.g., Cs+K, K+Cs) indicate the measured species (first) and the background species present (second). Range of the data was limited for the clarity.

tem remains challenging because of increased heteronuclear losses. As a first step, we provide preliminary estimates of the three-body loss coefficients, with precision limited by the developed methods, which, however, will form the basis for more detailed future studies.

Based on our current results, we expect that the same cooling approach can be extended to the ^{40}K–Cs system. However, this is not explored here due to the low natural abundance of ^{40}K in our source, leading to a number of atoms in the range of $1 - 5 \times 10^5$ at the MOT stage.

In general, the results presented in this work mark a significant step toward the realization of ultracold K–Cs bosonic mixtures and the formation of ground state ^{41}K-Cs molecules.

Chapter 8

Feshbach spectroscopy of ^{41}K-Cs mixtures

Obtaining a stable ^{41}K-Cs mixture and measuring Feshbach resonances has been for many years seen as an important milestones in our laboratory. Achieving this goal, however, required a number of intermediate steps. One of them was performing Feshbach spectroscopy in the ^{39}K-Cs mixture. Our reasoning was the following: if we could detect atom losses in the well-studied ^{39}K-Cs system, which involves the most abundant potassium isotope, then we had a reasonable chance of success in the ^{41}K-Cs case as well. If no losses could be observed in the former mixture, it would likely become necessary to develop additional cooling procedures or upgrade the experimental system to reach colder mixtures with higher densities.

The attempt to observe losses in ^{39}K-Cs was successful, as described in the previous chapter, therefore we became confident that substituting ^{39}K for ^{41}K woudl be succesful. It should be stressed that over the years we had made many attempts to observe resonances in ^{41}K-Cs, but almost all of them failed. For the past three years, at least one month every year has been dedicated exclusively to these measurements; unfortunately, without success.

We anticipated that the main challenges would arise from the shorter lifetime of the ^{41}K-Cs mixture, which limited the possibility of plain or forced evaporation in the trap. The second important limitation came from the reduced abundance of ^{41}K in dispensers containing potassium of natural isotopic composition. In the final year of the PhD studies of the author of this work, with the deadline for the submission of the thesis approaching, we decided to concentrate solely on this spectroscopy, abandoning all intermediate projects.

The first obstacle was that the literature reported only resonances observable in

the $|a\rangle + |a\rangle$ collision channel, where subsequent letters denote different magnetic states of potassium and cesium, following the notation introduced in the previous chapter [84]. As described earlier, we had developed methods of optical pumping and detection of the number of atoms in different spin states, so there was no fundamental reason to restrict ourselves exclusively to this collision channel. This limitation was quickly overcome thanks to the support of M. Frye and M. Tomza, who, based on interaction potentials presented in ref. [84], provided us with predicted positions of resonances in multiple channels. Calculated positions and widths of the resonances in cesium $|a\rangle$, and potassium $|a, b, c\rangle$ channels are presented in Table 8.1. Knowing the expected locations of the loss features enabled us to initiate our first measurements.

^{41}K	^{133}Cs	Position (G)	Theoretical width (G)
$\|a\rangle$	$\|a\rangle$	146.5	0.15
		236.1	2.20
$\|b\rangle$	$\|a\rangle$	175.7	0.13
		253.9	1.88
		305.1	0.07
$\|c\rangle$	$\|a\rangle$	273.55	0.43
		275.71	1.10
		323.5	0.07

Table 8.1: Positions of Feshbach resonances calculated by M. Frye and M. Tomza based on the interaction potential presented in [84]. The table lists the potassium and cesium collisions channels, the resonance positions, and their theoretical widths.

In the initial attempts, optical pumping of potassium atoms into a single spin state was absent. Their number, $N_{41K} \approx 5 \times 10^5$, was about five times lower than that of cesium atoms, $N_{133Cs} \approx 2.5 \times 10^6$. Consequently, their $1/e$ lifetime in the mixture was short, about $\tau \approx 200$ ms. This situation was highly unfavorable for observing losses, since we expected them to be more visible in the potassium sample. Our reasoning was threefold: first, the mass of ^{41}K is more than three times smaller than that of ^{133}Cs, so potassium atoms are more likely to be lost during collisions. Secondly, as discussed in Chapter 4, ^{41}K experiences an almost two times shallower optical dipole potential generated by the 1064 nm laser than cesium. Finally, in analogy to ^{39}K-Cs, losses had previously been observed exclusively in the potassium sample, both in our system and in the first report of Feshbach resonances in this mixture [84].

In the first experimental sequence, atoms were transferred into the optical dipole

trap, with cesium and potassium optically pumped into the lowest spin state $^2S_{1/2}$, $F = 3, m_F = 3$ (in the case of cesium), or lowest hyperfine state $^2S_{1/2}$, $F = 1$ (for potassium). Optical pumping of cesium atoms into this spin state required a magnetic field provided by the compensation coils oriented opposite to the field generated by the Feshbach coils. To prevent depolarization, the magnetic field of the compensation coils was therefore adiabatically rotated over 20 ms to align with the field generated by the Feshbach coils. Subsequently, the Feshbach field was ramped up to about 50 G in 50 ms, and the compensation coils were switched off within 20 ms. This procedure ensured that the cesium spin state was preserved, since a sudden reversal of the field vector would have led to mixing of spin states.

The magnetic field was then swept across the theoretically predicted resonance positions. Upon reaching values in the 260–300 G range, the atoms were held in the trap for 500 ms, after which the field was switched off in 100 ms, and both potassium and cesium clouds were imaged. Each point was measured three times, and the resulting average of the number of atoms is presented in Fig. 8.1 as a function of the applied magnetic field. As can be seen, the expected loss features did not coincide precisely with the positions predicted theoretically. However, reasonably close features were observed, for example in the plot for cesium atoms, 271 G versus the predicted 273.55 G, and 235 G or 240 versus 236.1 G. Such shifts could plausibly arise from the relatively high temperature of the atoms, which contributes to the total collisional energy.

A surprising observation was that the apparent losses were more pronounced for cesium atoms, contrary to the earlier intuition. Moreover, the observed losses were very small, in some cases barely detectable. Nevertheless, we decided to attempt an optimization by searching for a holding time (in the presence of a magnetic field) that would maximize the signal. For this purpose, the mixture was loaded into the dipole trap and the number of cesium atoms was recorded for different holding times, both at the suspected resonance (271 G) and in the off-resonance case (266 G). The results, shown in Fig. 8.2, indicate that the lifetime remained essentially unchanged, or even slightly longer, at the resonance location. This raised doubts about our initial interpretation. After many repeated measurements, it became clear that no genuine loss feature was truly present and what had been seen were just instabilities in the atom number.

Although this part of the thesis could be omitted, we include it here to illustrate how experimental noise can easily be mistaken for a resonance signal under unfavorable conditions. The search for such features and the characterization of the atomic samples took more than two months of continuous, almost automated measurements, carried out nearly around the clock. It is likely that, if we had not known

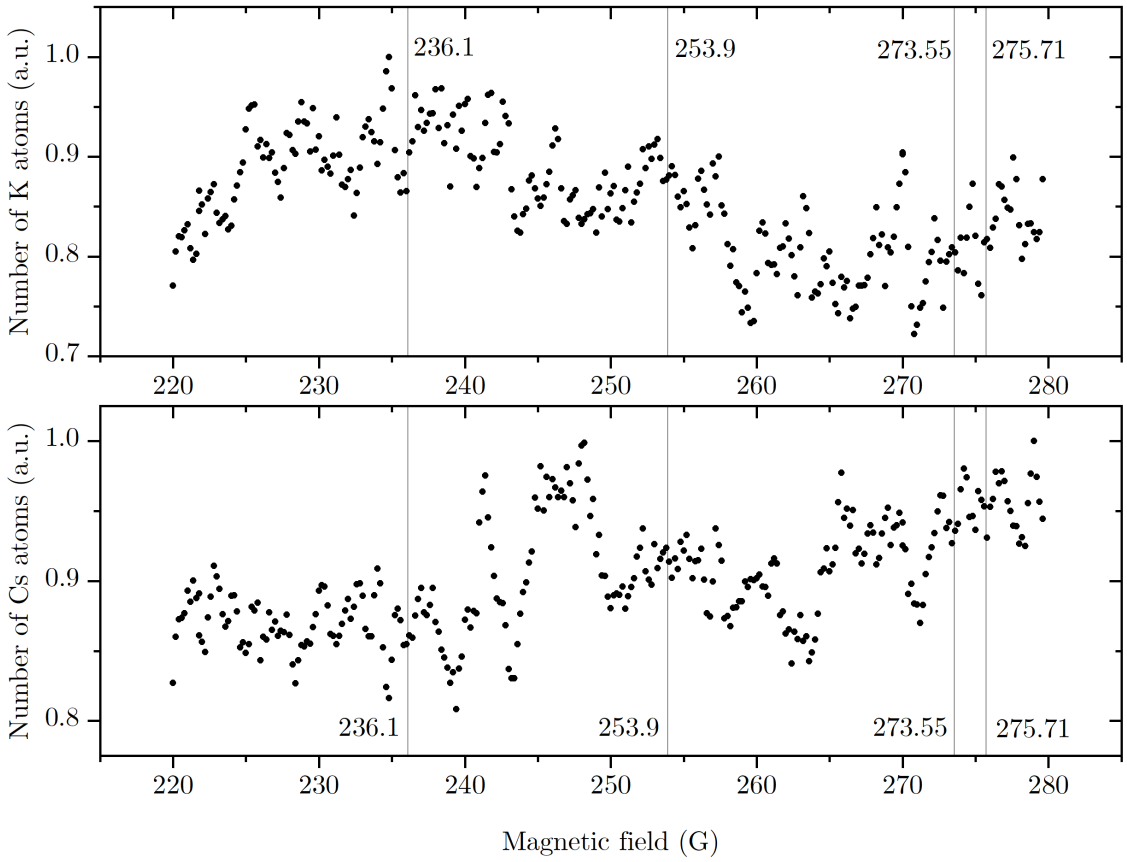

Figure 8.1: Number of potassium atoms (top panel) and cesium atoms (bottom panel) in the optical dipole trap as a function of applied magnetic field during Feshbach resonances measurement. Vertical lines mark theoretically predicted positions of Feshbach resonances.

the expected resonance positions and if we had not expected losses in this region, we would never have interpreted this noise as an expected loss signal.

After many unsuccessful attempts, including the addition of optical pumping and evaporation steps, we were ready to abandon the project. In a final act of experimental desperation, however, we decided to check resonance positions predicted in an earlier work [187]. While we knew that the interaction potential used there had later been improved [84], and thus the chance of success was small, checking these positions required no changes to the apparatus—only a shift of the measurement range to the vicinity of two resonances at 168.2 G and 171.2 G. In the early morning

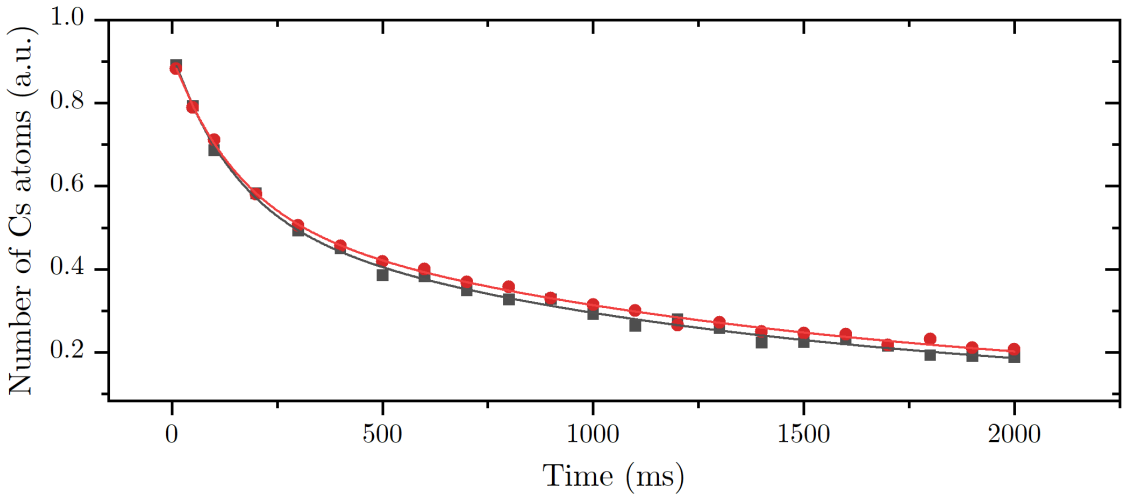

Figure 8.2: Lifetime of cesium atoms in the optical dipole trap in the ^{41}K-Cs mixture. The two curves correspond to the number of atoms as a function of the hold time at the suspected resonance field (red points) and off-resonance (black points). Solid lines represent double-exponential fits.

of October 16, 2024, at around 2:20 a.m., we observed the first clear loss of potassium atoms, significantly stronger than any one previously recorded. The signal was absent when cesium atoms were not present in the trap. These first results are shown in Fig. 8.3.

As can be seen, the signal is much more pronounced and corresponds to a loss of more than 20% of the atoms, compared with the previous profile where the losses amounted to about 5–10%, estimated from the number of atoms at the minimum and just outside the loss feature. Moreover, the results are in much better agreement with the reasoning presented earlier, where we expected the losses to occur predominantly for potassium atoms.

To ensure that these results were not once again observed due to the noise in the system, the measurements were repeated multiple times, and control experiments with single-species samples confirmed that no losses occurred in the absence of cesium. Lifetimes were then re-measured for the on and off resonance case, producing results consistent with expectations, as shown in Fig. 8.4.

The observed losses follow the anticipated behavior, as one would expect three distinct regimes in the lifetime curve. In the first regime, for very short times, the number of atoms on and off resonance should be identical, since this time period is too short for a significant number of collisions to occur. In the third regime, for

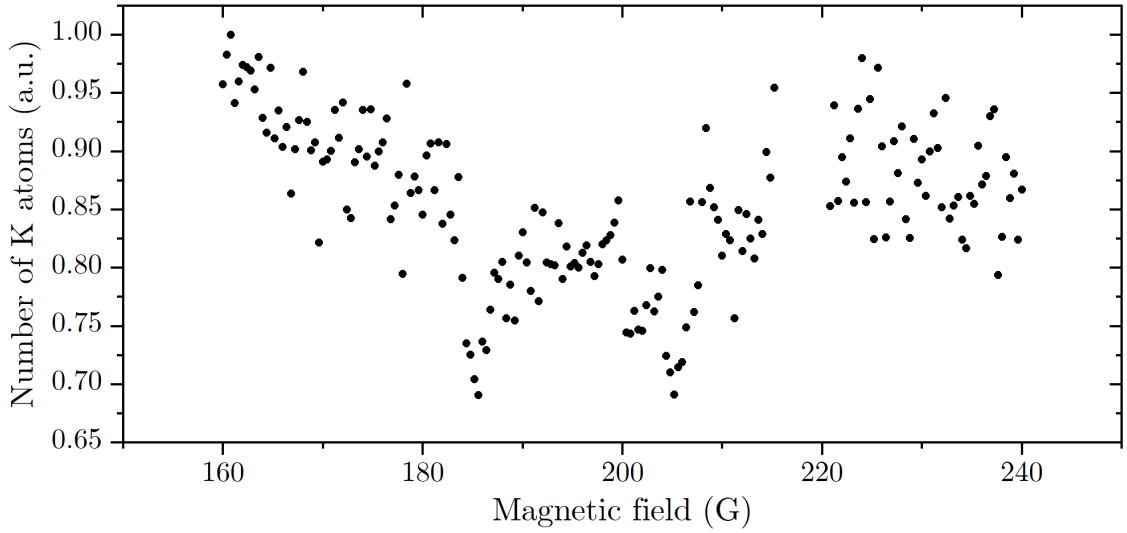

Figure 8.3: First clear observation of Feshbach resonances in the ^{41}K-Cs mixture. The plot shows the number of potassium atoms as a function of the magnetic field. Pronounced losses are visible around 185 G and 205 G.

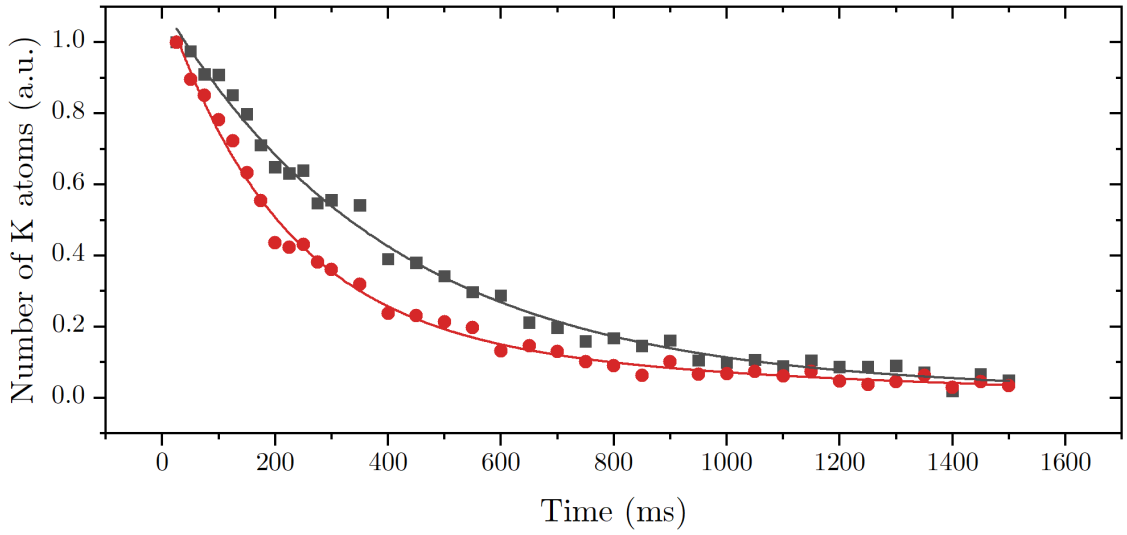

Figure 8.4: Lifetime of potassium atoms in the optical dipole trap in the presence of a heteronuclear Feshbach resonance (red points) and off resonance (black points). Solid lines are double-exponential fits.

very long times, the observed effects cease to be dominated by three-body losses and instead become limited by collisions with the background gas. This situation can be illustrated by taking it to the extreme: after a sufficiently long time, no atoms remain in the trap, and the outcome is identical both on and off resonance. This implies that there must exist an intermediate (second) regime between these two timescales, in which the losses induced by Feshbach resonances are most clearly visible.

This analysis reveals another important feature: if we assume that the decay can be described by an exponential function with the same offset and amplitude, as discussed earlier, then the lifetime determines the visibility of atom losses. More precisely, the larger the difference between the cloud lifetime on and off resonance, the clearer the loss profiles become. This naturally raises the question of how the lifetime depends on the sample parameters.

We therefore investigated how the lifetime varies with the relative number of potassium and cesium atoms, both on and off resonance. To this end, the cesium MOT loading time was varied, thereby adjusting the final number of atoms in the dipole trap, while the potassium loading time was kept constant. For each configuration, potassium atom loss curves were measured, and exponential fits provided the corresponding $1/e$ lifetimes. The results are shown in Fig. 8.5.

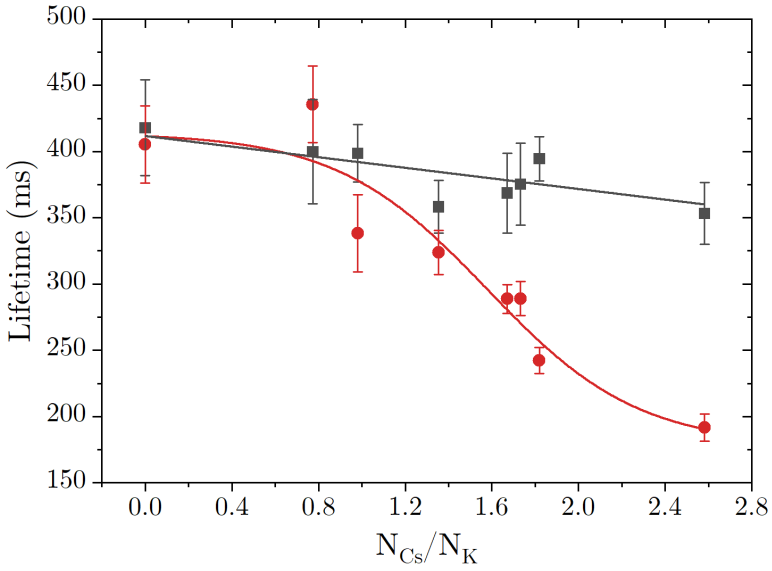

Figure 8.5: Lifetime of potassium atoms as a function of the ratio of number of potassium to cesium atoms in the dipole trap. Red points correspond to resonance, black points to off-resonance conditions. Solid lines are guides to the eye.

As can be seen, the lifetime difference, which determines the visibility of atom losses, increases with the ratio between the number of cesium and potassium atoms. Consequently, despite the shorter lifetime, the losses should be most visible in the case of the maximum number of cesium atoms. It is, of course, possible that the visibility would be even higher if the number of potassium atoms were further reduced. However, two important considerations must be emphasized. First, since the losses are observed in the potassium cloud, reducing the number of atoms decreases the signal-to-noise ratio during imaging. Second, the above analysis neglects one crucial fact: the greater the number of cesium or potassium atoms present in the trap, the higher the sample density, the smaller the average interatomic distance, and thus the higher the probability of collisions. These two reasons clearly indicate that, in the case of a reduced number of potassium atoms, the losses could in fact become less visible.

Independently of the previous discussion, the above measurements were aimed at optimizing the visibility of the loss signal and indeed provided the expected benefits. Figure 8.6 presents the results of the optimized Feshbach resonance measurement for the same data range as in Fig. 8.5. As can be seen, the visibility of atom losses has nearly doubled.

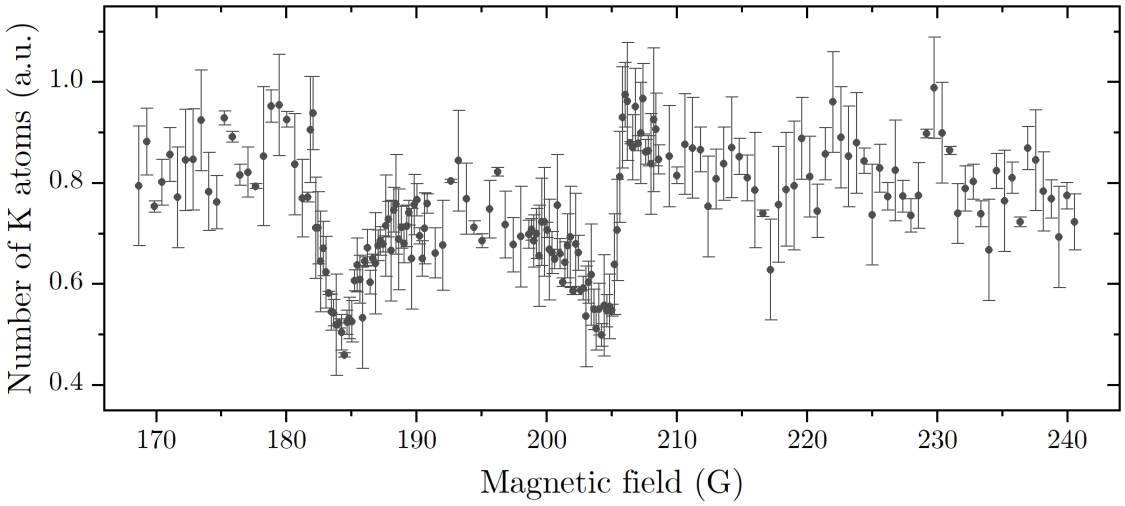

Figure 8.6: Optimized Feshbach spectroscopy measurement in the same range as in Fig. 8.3.

In such a way, we also confirmed that the observed loss features were indeed present due to the Feshbach resonances. However, none of the measured loss profiles coincided with theoretical predictions—neither with the earlier ones [187], nor with

those obtained using the refined potentials [84]. The first observation was therefore more a matter of luck than a theory-guided experiment. This also meant that the number and location of observable resonances remained unknown. Continued collaboration with M. Frye and M. Tomza allowed us to refine the interaction potentials and to search for additional resonances.

Finally, by employing the methods of pumping cesium into non-stretched states described in previous chapters, together with the spin-separation technique, we were able to observe nineteen resonances belonging to the first two partial waves (s-wave and p-wave) and to different collision channels. The observed resonances were then used to iteratively refine the interaction potentials: experimental findings guided successive improvements of the model, until the point was reached where theoretical predictions could accurately anticipate new resonances before they were experimentally observed. The measurement results are summarized in a single plot presented in Fig. 8.7, where all observed Feshbach resonances are displayed. Different colors mark different collision channels. A comprehensive overview of the observed losses and their experimentally determined widths is presented in Table 8.2.

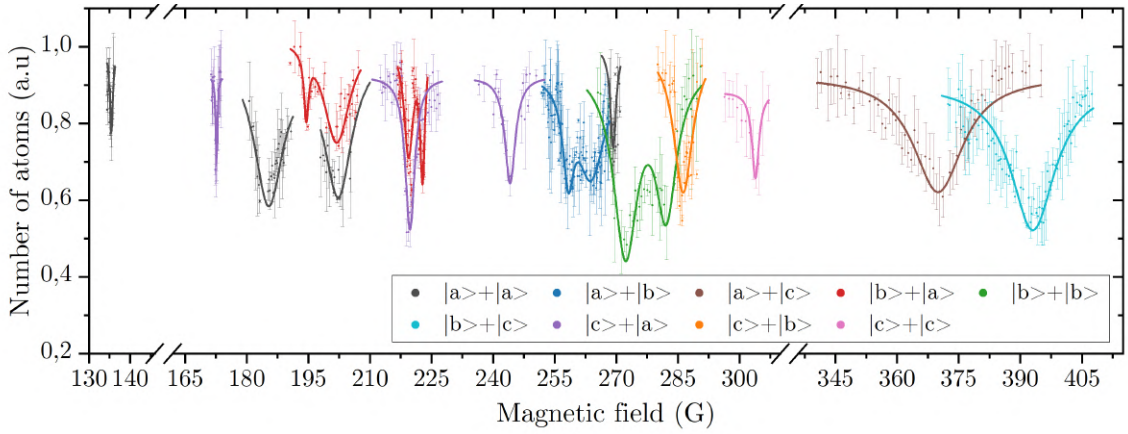

Figure 8.7: Overview of losses in the heteronuclear ^{41}K-Cs mixture due to Feshbach resonances. A Lorentzian function is fitted to each feature to extract the position and experimental width of the Feshbach resonance, resulting from the presence of Feshbach resonances. Different colors correspond to different collision channels, as presented in the legend.

The observed loss profiles, particularly their number, came as a considerable surprise. This is especially true given that no magnetic-field stabilization technique was applied in the setup, which implies an estimated minimum resonance width of 0.01 G. Therefore, as shown in Table 8.1, we expected to observe no more than six

Channel	Position (G)	Width (G)
^{41}K$\|a\rangle$+Cs$\|a\rangle$	135.43(30)	0.31(6)
	184.84(18)	4.29(63)
	203.04(19)	3.81(64)
	269.29(10)	0.63(32)
^{41}K$\|a\rangle$+Cs$\|b\rangle$	258.44(17)	3.73(65)
	264.04(27)	7.16(1.17)
^{41}K$\|a\rangle$+Cs$\|c\rangle$	369.16(34)	17.55(1.33)
^{41}K$\|b\rangle$+Cs$\|a\rangle$	194.70(21)	0.50(26)
	201.78(34)	5.56(74)
	219.46(09)	2.39(32)
	222.77(05)	1.04(16)
^{41}K$\|b\rangle$+Cs$\|b\rangle$	271.28(22)	4.35(77)
	282.41(40)	10.83(1.67)
^{41}K$\|b\rangle$+Cs$\|c\rangle$	392.64(31)	8.94(1.54)
^{41}K$\|c\rangle$+Cs$\|a\rangle$	172.70(06)	0.24(21)
	219.73(08)	3.16(25)
	243.25(31)	2.86(56)
^{41}K$\|c\rangle$+Cs$\|b\rangle$	285.74(21)	1.78(0.64)
^{41}K$\|c\rangle$+Cs$\|c\rangle$	302.86(4)	6.02(1.31)

Table 8.2: List of theobserved Feshbach resonances in the ^{41}K-Cs mixture. The table presents the collision channel, resonance position, and experimentally measured width of the loss feature.

resonances.

The measured number of resonances and their diverse characteristics—most notably the widths ranging from 0.2 to 17.55 G—appear very promising for further studies of this mixture. As demonstrated in recent work, ground-state molecules have been produced in a ^{39}KCs mixture using a Feshbach resonance at $B = 361.1$ G with a width of $\Delta = 3.2$ G [84], [96]. In the mixture studied here, we observed several broader resonances that would enable more precise tuning of interactions. Furthermore, the loss profiles appeared at magnetic fields that were nearly twice as low, which may reduce the need for the often-demanding cooling of the coil system.

In addition, in recent years it has become possible to cool cesium atoms to quantum degeneracy in the $^2S_{1/2}$, $F = 3, m_F = 2$ state ($|b\rangle$ channel) [32]. This means that, apart from the narrow magnetic-field region around 23 G for the lowest spin state, where evaporative cooling was previously efficient and atom losses were minimized [47], a similar favorable region has now been identified for another spin state at around 148 G. This makes the presented mixture and the performed measurements particularly promising for the realization of ultracold mixtures. In particular, a favorable loss profile was observed in the ^{41}K$|b\rangle$–^{133}Cs$|b\rangle$ mixture, where a broad resonance with $\Delta = 10.8$ G is available at $B = 282.4$ G. Naturally, the possibility of creating such molecules remains only a prediction at this stage, and substantial further work and many additional measurements will be required in this direction.

Chapter 9

Conclusions and outlook

The presentation of Feshbach resonances in ^{39}K–Cs and ^{41}K–Cs mixtures naturally summarizes this dissertation. These results represent the main objective of the doctoral work and provide a noticeable achievement in the experimental physics of cold atoms. The significance of these results is proven, and further underlined by the bibliography, which contains numerous works from the last decade reporting similar milestones. This clearly indicates that analogous studies remain at the forefront of current research.

Summarizing not only the final results but also the entire course of this work, numerous experimental systems and procedures were developed that enabled efficient sub-Doppler laser cooling of ^{39}K, ^{40}K, ^{41}K, and ^{133}Cs atoms. Among these, the bosonic isotopes were ultimately trapped in an optical dipole trap, while the fermionic atoms were confined in a magnetic trap. These procedures can, and most likely will, be used in the near future to achieve quantum degeneracy of these species, thereby opening a new chapter of research in our laboratory. Although this goal was not reached within the scope of the present dissertation, primarily due to time limitations, the experimental apparatus and the characterization of the prepared samples constitute a strong foundation for further progress. Importantly, while the cooling strategies for the investigated atoms had already been described in the literature, many of the experiments presented here were carried out for the first time in a relatively simple single-chamber vacuum system. This feature may be particularly relevant in the context of ongoing efforts to miniaturize experimental setups for industrial applications such as atom interferometry or frequency standards.

Beyond the cooling of single-species gases, mixtures were also investigated. In this case, the procedures are far less established, and it is difficult to predict the behavior of the atoms without experimental data. This is especially true for mixtures

cooled for the first time in this work—^{39}K–^{40}K and ^{41}K–^{133}Cs—where interaction and loss coefficients cannot be determined before experimental measurements. For this reason, it seemed particularly important to describe experiments on the cooling of these mixtures and to attempt to quantify heteronuclear losses. In the ^{39}K–^{40}K mixture, a phenomenological description was provided by analyzing the reduced lifetime in a magnetic trap. For the ^{39}K–^{133}Cs and ^{41}K–^{133}Cs mixtures, a more analytical approach was taken, using lifetime measurements in an optical dipole trap to extract upper bounds on loss coefficients. This constitutes an important theoretical contribution that may facilitate the production of quantum-degenerate mixtures in the future.

Efficient evaporative cooling, however, requires tunability of interactions. This is precisely where the main results of this dissertation lie: the measurement of heteronuclear Feshbach resonances in ^{39}K–Cs and ^{41}K–Cs mixtures. These findings not only confirm known properties but also expand our general understanding of interspecies interactions. Furthermore, as emphasized at the beginning of this chapter, the observation of Feshbach resonances provides constraints on interatomic potentials and may enable the formation of heteronuclear molecules with relatively high electric dipole moments. While the present results represent an essential step in this direction, the timescale between characterizing a new mixture and producing such molecules is often four to eight years, as shown in the literature [84], [96]. This makes the task a promising avenue for future researchers in the laboratory.

The studies presented here form the core of this dissertation, yet they do not mention all the research conducted during the doctoral project. Some topics were omitted because the measurements were still in very early stages, as in the case of optical levitation of atomic clouds and mixtures. In that context, a laser system was constructed and it was demonstrated that single-species samples can be levitated efficiently. Nevertheless, it has been decided to resume these investigations only after achieving efficient evaporative cooling of mixtures, particularly once higher optical trap powers become available, where gravitational sag plays an increasing role in separating the clouds. Time constraints did not allow to pursue this direction further within this work, but it remains a promising subject for future studies.

Another line of research, not included in this dissertation, was the measurement of Feshbach resonances in single-species samples of ^{39}K and ^{133}Cs. These studies were intentionally omitted, as they have been performed multiple times in the past, and including them here would have considerably lengthened the thesis without adding essential information for the main focus: heteronuclear mixtures.

Finally, some experiments were prepared but not fully completed. This was the case for cooling atoms in 1064 nm optical lattices, where trapping was successfully

demonstrated but the project has been discontinued due to other priorities. Another example was degenerate Raman sideband cooling (dRSC) in near-resonant optical lattices, where trapped samples were obtained but efficient cooling could not be achieved. In both cases, the necessary infrastructure was built and initial results were obtained. However, based on prior experience, it was clear that optimizing such cooling processes would require substantial effort and time investment. Once again, the decision was made to leave these developments as a foundation for future students and researchers in the group.

All these elements represent steps toward further progress. In this sense, while this chapter concludes the dissertation, it also opens the path to many exciting directions of research to be pursued in the coming years.

It is up to future researchers to decide which direction to pursue next. From the perspective of the newly obtained ^{39}K–^{40}K mixtures, a natural step would be to develop methods enabling the achievement of quantum degeneracy. However, this will require time and most likely the construction of a new vacuum system, where different approaches can be tested in order to identify the optimal path. In such an apparatus, two separate vacuum chambers (e.g. in the 2D-3D MOT configuration) should allow for reaching lower background pressure, enabling RF-knife evaporation of the bosonic isotope in a magnetic trap and sympathetic cooling of the fermionic isotope, if the collisional properties allow for efficient thermalization.

It would also be worth exploring the influence of an enriched source of the fermionic isotope in the new apparatus. In that case, larger number of atoms in the MOT might allow for transferring samples directly into an optical dipole trap, where performing evaporation might prove more efficient. Unfortunately, as emphasized repeatedly throughout this thesis, the optimal path cannot be determined without careful experimental testing. In any case, achieving a doubly degenerate mixture would constitute an important step toward the observation of p-wave superfluidity, which may become a relevant step for a better understanding of high-temperature superconductivity [126]. Naturally, preparing such a sample and observing superfluid behavior will also require additional experimental infrastructure, and all these steps will take considerable time in the future.

The cooling of the ^{39}K–^{40}K mixture was, to some extent, a side project within this thesis, while the main objective was the creation and characterization of the heteronuclear ^{41}K–^{133}Cs mixture. In this case, many of the intended goals have been successfully achieved, but the path toward ultracold ground-state molecules and quantum simulators has only just begun. Here, however, based on existing literature, further steps can be outlined. An initial approach would be the creation of molecules and the measurement of their binding energy, which would allow one to

determine the interaction potential with high accuracy. This raises a fundamental question: why do the existing potentials reproduce the results in the ^{39}K–^{133}Cs mixture so well, yet fail to predict the correct resonance positions in ^{41}K–^{133}Cs? And will the potential that matches the resonances of ^{41}K–^{133}Cs also predict the correct transitions in the other mixture? Answering these questions will require close collaboration between theoretical and experimental groups. Perhaps in the future, the fermionic ^{40}K–^{133}Cs mixture might provide further insights, but its preparation and study will require additional years of experimental work. However, this time could potentially be rewarded with the creation of fermionic molecules, which would open the door to a wealth of new laboratory research based on these properties.

For the ^{41}K–^{133}Cs mixture presented in this work, it would be highly beneficial to adapt the existing setup to perform photoassociation in a cold sample. Identifying the precise location of molecular states would be a really helpful step toward finding an optimal STIRAP pathway for producing ground-state molecules efficiently [188]. Naturally, even with all the necessary tools in place, a complete optimization will again be required. In such systems, lack of experimental realization always leads to the same questions: is it better to evaporate the sample—thereby losing atoms but increasing association efficiency—or rather to perform the procedure in a larger but hotter and more dilute sample, where many atoms are available despite the lower efficiency?

The production of molecules is only one step; it must be followed by the implementation of additional procedures to minimize losses [183], [189]. All these steps require considerable time and effort, but they also offer a promising direction for the work of future PhD students and researchers. Thus, as can be seen, the presented doctoral thesis may be a big step, but still only one step on the journey toward the development of ultracold potassium-cesium molecules in their rovibrational ground state.

Bibliography

[1] E. L. Raab, M. Prentiss, A. Cable, S. Chu, and D. E. Pritchard, "Trapping of neutral sodium atoms with radiation pressure", *Physical Review Letters*, vol. 59, no. 23, p. 2631, 1987.

[2] M. H. Anderson, J. R. Ensher, M. R. Matthews, C. E. Wieman, and E. A. Cornell, "Observation of Bose-Einstein condensation in a dilute atomic vapor", *Science*, vol. 269, no. 5221, pp. 198–201, 1995.

[3] C. Monroe, W. Swann, H. Robinson, and C. Wieman, "Very cold trapped atoms in a vapor cell", *Physical Review Letters*, vol. 65, no. 13, p. 1571, 1990.

[4] R. Williamson III and T. Walker, "Magneto-optical trapping and ultracold collisions of potassium atoms", *Journal of the Optical Society of America B*, vol. 12, no. 8, pp. 1393–1397, 1995.

[5] U. Schünemann, H. Engler, M. Zielonkowski, M. Weidemüller, and R. Grimm, "Magneto-optic trapping of lithium using semiconductor lasers", *Optics Communications*, vol. 158, no. 1-6, pp. 263–272, 1998.

[6] S. Atutov, R. Calabrese, V. Guidi, *et al.*, "Cooling and trapping of radioactive atoms: The Legnaro francium magneto-optical trap", *Journal of the Optical Society of America B*, vol. 20, no. 5, pp. 953–959, 2003.

[7] H. Katori, T. Ido, Y. Isoya, and M. Kuwata-Gonokami, "Magneto-optical trapping and cooling of strontium atoms down to the photon recoil temperature", *Physical Review Letters*, vol. 82, no. 6, p. 1116, 1999.

[8] T. Kuwamoto, K. Honda, Y. Takahashi, and T. Yabuzaki, "Magneto-optical trapping of Yb atoms using an intercombination transition", *Physical Review A*, vol. 60, no. 2, R745, 1999.

[9] A. J. Berglund, J. L. Hanssen, and J. J. McClelland, "Narrow-line magneto-optical cooling and trapping of strongly magnetic atoms", *Physical Review Letters*, vol. 100, no. 11, p. 113 002, 2008.

[10] R. Onofrio, C. Raman, J. Vogels, J. Abo-Shaeer, A. Chikkatur, and W. Ketterle, "Observation of superfluid flow in a Bose-Einstein condensed gas", *Physical Review Letters*, vol. 85, no. 11, p. 2228, 2000.

[11] M. Greiner, O. Mandel, T. Esslinger, T. W. Hänsch, and I. Bloch, "Quantum phase transition from a superfluid to a Mott insulator in a gas of ultracold atoms", *Nature*, vol. 415, no. 6867, pp. 39–44, 2002.

[12] M. Kasevich and S. Chu, "Atomic interferometry using stimulated Raman transitions", *Physical Review Letters*, vol. 67, no. 2, p. 181, 1991.

[13] S. Bize, P. Laurent, M. Abgrall, *et al.*, "Advances in atomic fountains", *Comptes Rendus Physique*, vol. 5, no. 8, pp. 829–843, 2004.

[14] C. Gross and I. Bloch, "Quantum simulations with ultracold atoms in optical lattices", *Science*, vol. 357, no. 6355, pp. 995–1001, 2017.

[15] L. Duca, T. Li, M. Reitter, I. Bloch, M. Schleier-Smith, and U. Schneider, "An Aharonov-Bohm interferometer for determining Bloch band topology", *Science*, vol. 347, no. 6219, pp. 288–292, 2015.

[16] L. Anderegg, B. L. Augenbraun, Y. Bao, *et al.*, "Laser cooling of optically trapped molecules", *Nature Physics*, vol. 14, no. 9, pp. 890–893, 2018.

[17] L. Caldwell, J. Devlin, H. Williams, *et al.*, "Deep laser cooling and efficient magnetic compression of molecules", *Physical Review Letters*, vol. 123, no. 3, p. 033 202, 2019.

[18] J. Chang, S. Lee, Y. Kim, Y. Lim, and J. W. Park, "Dual-species Bose-Einstein condensates of ^{23}Na and ^{41}K with tunable interactions", *Physical Review Research*, vol. 6, no. 1, p. 013 183, 2024.

[19] M. Harris, P. Tierney, and S. Cornish, "Magnetic trapping of a cold Rb-Cs atomic mixture", *Journal of Physics B*, vol. 41, no. 3, p. 035 303, 2008.

[20] A. Mosk, S. Kraft, M. Mudrich, *et al.*, "Mixture of ultracold lithium and cesium atoms in an optical dipole trap", *Applied Physics B*, vol. 73, no. 8, pp. 791–799, 2001.

[21] C. Myatt, E. Burt, R. Ghrist, E. A. Cornell, and C. Wieman, "Production of two overlapping Bose-Einstein condensates by sympathetic cooling", *Physical Review Letters*, vol. 78, no. 4, p. 586, 1997.

[22] M. Gröbner, "A quantum gas apparatus for ultracold mixtures of K and Cs", PhD. Thesis, University of Innsbruck, Innsbruck, Austria, 2017. [Online]. Available: `https://ulb-dok.uibk.ac.at/ulbtirolhs/content/titleinfo/2202711`.

[23] B. DeMarco and D. S. Jin, "Onset of Fermi Degeneracy in a Trapped Atomic Gas", *Science*, vol. 285, no. 5434, pp. 1703–1706, 1999.

[24] M. Bartenstein, A. Altmeyer, S. Riedl, *et al.*, "Exploring the BEC-BCS crossover with an ultracold gas of ^{6}Li atoms", in *AIP Conference Proceedings*, American Institute of Physics, vol. 770, 2005, pp. 278–288.

[25] R. Jannin, Y. van der Werf, K. Steinebach, H. L. Bethlem, and K. S. Eikema, "Pauli blocking of stimulated emission in a degenerate Fermi gas", *Nature Communications*, vol. 13, no. 1, p. 6479, 2022.

[26] Y. Margalit, Y.-K. Lu, F. Ç. Top, and W. Ketterle, "Pauli blocking of light scattering in degenerate fermions", *Science*, vol. 374, no. 6570, pp. 976–979, 2021.

[27] C. Regal, M. Greiner, and D. S. Jin, "Observation of resonance condensation of fermionic atom pairs", *Physical Review Letters*, vol. 92, no. 4, p. 040 403, 2004.

[28] F. Schreck, G. Ferrari, K. Corwin, *et al.*, "Sympathetic cooling of bosonic and fermionic lithium gases towards quantum degeneracy", *Physical Review A*, vol. 64, no. 1, p. 011 402, 2001.

[29] C. Presilla and R. Onofrio, "Cooling dynamics of ultracold two-species Fermi-Bose mixtures", *Physical Review Letters*, vol. 90, no. 3, p. 030 404, 2003.

[30] K. Van der Stam, E. Van Ooijen, R. Meppelink, J. Vogels, and P. Van der Straten, "Large atom number Bose-Einstein condensate of sodium", *Review of Scientific Instruments*, vol. 78, no. 1, 2007.

[31] H.-Z. Chen, X.-C. Yao, Y.-P. Wu, *et al.*, "Production of large ^{41}K Bose-Einstein condensates using D1 gray molasses", *Physical Review A*, vol. 94, no. 3, p. 033 408, 2016.

[32] M. Horvath, S. Dhar, A. Das, *et al.*, "Bose-Einstein condensation of non-ground-state caesium atoms", *Nature Communications*, vol. 15, no. 1, p. 3739, 2024.

[33] G. Salomon, L. Fouché, S. Lepoutre, A. Aspect, and T. Bourdel, "All-optical cooling of ^{39}K to Bose-Einstein condensation", *Physical Review A*, vol. 90, no. 3, p. 033 405, 2014.

[34] T. Sowiński, O. Dutta, P. Hauke, L. Tagliacozzo, and M. Lewenstein, "Dipolar molecules in optical lattices", *Physical Review Letters*, vol. 108, no. 11, p. 115 301, 2012.

[35] K. R. Hazzard, B. Gadway, M. Foss-Feig, *et al.*, "Many-body dynamics of dipolar molecules in an optical lattice", *Physical Review Letters*, vol. 113, no. 19, p. 195 302, 2014.

[36] T. Lahaye, C. Menotti, L. Santos, M. Lewenstein, and T. Pfau, "The physics of dipolar bosonic quantum gases", *Reports on Progress in Physics*, vol. 72, no. 12, p. 126 401, 2009.

[37] C. Politi, A. Trautmann, P. Ilzhöfer, *et al.*, "Interspecies interactions in an ultracold dipolar mixture", *Physical Review A*, vol. 105, no. 2, p. 023 304, 2022.

[38] D. Grün, S. White, A. Ortu, *et al.*, "Optical tweezer arrays of erbium atoms", *Physical Review Letters*, vol. 133, no. 22, p. 223 402, 2024.

[39] B. Gadway and B. Yan, "Strongly interacting ultracold polar molecules", *Journal of Physics B*, vol. 49, no. 15, p. 152 002, 2016.

[40] M. Śmiałkowski and M. Tomza, "Highly polar molecules consisting of a copper or silver atom interacting with an alkali-metal or alkaline-earth-metal atom", *Physical Review A*, vol. 103, no. 2, p. 022 802, 2021.

[41] D. A. Steck, *Cesium D-line data*, Available online at http://steck.us/alkalidata (revision 2.3.3, 28 May 2024).

[42] T. Tiecke, "Properties of potassium", *University of Amsterdam, The Netherlands, Thesis*, pp. 12–14, 2010.

[43] C. Kittel and H. Kroemer, *Thermal Physics*, 2nd ed. San Francisco: W. H. Freeman and Company, 1980, ISBN: 978-0-7167-1088-2.

[44] A. Gallagher and D. E. Pritchard, "Exoergic collisions of cold Na*-Na", *Physical Review Letters*, vol. 63, no. 9, p. 957, 1989.

[45] T. Weber, J. Herbig, M. Mark, H.-C. Nägerl, and R. Grimm, "Three-body recombination at large scattering lengths in an ultracold atomic gas", *Physical Review Letters*, vol. 91, no. 12, p. 123 201, 2003.

[46] L. Wacker, N. Jørgensen, D. Birkmose, *et al.*, "Universal three-body physics in ultracold KRb mixtures", *Physical Review Letters*, vol. 117, no. 16, p. 163 201, 2016.

[47] T. Weber, J. Herbig, M. Mark, H.-C. Nagerl, and R. Grimm, "Bose-Einstein condensation of cesium", *Science*, vol. 299, no. 5604, pp. 232–235, 2003.

[48] C. Chin, R. Grimm, P. Julienne, and E. Tiesinga, "Feshbach resonances in ultracold gases", *Reviews of Modern Physics*, vol. 82, no. 2, pp. 1225–1286, 2010.

[49] C. d'Errico, M. Zaccanti, M. Fattori, *et al.*, "Feshbach resonances in ultracold ^{39}K", *New Journal of Physics*, vol. 9, no. 7, p. 223, 2007.

[50] T. Kraemer, M. Mark, P. Waldburger, *et al.*, "Evidence for Efimov quantum states in an ultracold gas of caesium atoms", *Nature*, vol. 440, no. 7082, pp. 315–318, 2006.

[51] J. M. Hutson and P. Soldan, "Molecule formation in ultracold atomic gases", *International Reviews in Physical Chemistry*, vol. 25, no. 4, pp. 497–526, 2006.

[52] G. Baym, "Cold quantum gases: Coherent quantum phenomena from Bose-Einstein condensation to BCS pairing of fermions", *Nuclear Physics A*, vol. 751, pp. 373–390, 2005.

[53] F. S. Cataliotti, E. A. Cornell, C. Fort, *et al.*, "Magneto-optical trapping of fermionic potassium atoms", *Physical Review A*, vol. 57, no. 2, p. 1136, 1998.

[54] S. Grego, M. Colla, A. Fioretti, J. Müller, P. Verkerk, and E. Arimondo, "A cesium magneto-optical trap for cold collisions studies", *Optics Communications*, vol. 132, no. 5-6, pp. 519–526, 1996.

[55] M. Gröbner, P. Weinmann, F. Meinert, K. Lauber, E. Kirilov, and H.-C. Nägerl, "A new quantum gas apparatus for ultracold mixtures of K and Cs and KCs ground-state molecules", *Journal of Modern Optics*, vol. 63, no. 18, pp. 1829–1839, 2016.

[56] G. D. Bruce, E. Haller, B. Peaudecerf, *et al.*, "Sub-Doppler laser cooling of ^{40}K with Raman gray molasses on the D2 line", *Journal of Physics B*, vol. 50, no. 9, p. 095 002, 2017.

[57] C. Salomon, J. Dalibard, W. Phillips, A. Clairon, and S. Guellati, "Laser cooling of cesium atoms below 3 μK", *Europhysics Letters*, vol. 12, no. 8, p. 683, 1990.

[58] V. Vuletić, C. Chin, A. J. Kerman, and S. Chu, "Degenerate Raman sideband cooling of trapped cesium atoms at very high atomic densities", *Physical Review Letters*, vol. 81, no. 26, p. 5768, 1998.

[59] E. Zohar, Y. Florshaim, O. Zilberman, A. Stern, and Y. Sagi, "Degenerate Raman sideband cooling of ^{40}K atoms", *Physical Review A*, vol. 106, no. 6, p. 063 111, 2022.

[60] M. Gröbner, P. Weinmann, E. Kirilov, and H.-C. Nägerl, "Degenerate Raman sideband cooling of ^{39}K", *Physical Review A*, vol. 95, no. 3, p. 033 412, 2017.

[61] T. Kishimoto, J. Kobayashi, K. Noda, K. Aikawa, M. Ueda, and S. Inouye, "Direct evaporative cooling of ^{41}K into a Bose-Einstein condensate", *Physical Review A*, vol. 79, no. 3, p. 031 602, 2009.

[62] A. Frisch, K. Aikawa, M. Mark, *et al.*, "Narrow-line magneto-optical trap for erbium", *Physical Review A*, vol. 85, no. 5, p. 051 401, 2012.

[63] H. J. Metcalf and P. van der Straten, "Laser cooling and trapping of atoms", *Journal of the Optical Society of America B*, vol. 20, no. 5, pp. 887–908, 2003.

[64] P. Van der Straten and H. Metcalf, *Atoms and molecules interacting with light: Atomic physics for the laser era*. Cambridge University Press, 2016.

[65] S. Chu, "Nobel lecture: The manipulation of neutral particles", *Reviews of Modern Physics*, vol. 70, pp. 685–706, 3 Jul. 1998.

[66] C. Savage, "Introduction to light forces, atom cooling, and atom trapping", *Australian Journal of Physics*, vol. 49, no. 4, pp. 745–764, 1996.

[67] T. Arpornthip, C. Sackett, and K. Hughes, "Vacuum-pressure measurement using a magneto-optical trap", *Physical Review A*, vol. 85, no. 3, p. 033 420, 2012.

[68] M. Mancini, A. Caires, G. Telles, V. S. Bagnato, and L. G. Marcassa, "Trap loss rate for heteronuclear cold collisions in two species magneto-optical trap", *The European Physical Journal D*, vol. 30, no. 1, pp. 105–116, 2004.

[69] J. Dobosz, "Development of a toolbox for high-precision spectroscopy of ultracold molecules", Ph.D. dissertation, University of Warsaw, 2025.

[70] W. Petrich, M. H. Anderson, J. R. Ensher, and E. A. Cornell, "Behavior of atoms in a compressed magneto-optical trap", *Journal of the Optical Society of America B*, vol. 11, no. 8, pp. 1332–1335, 1994.

[71] A. R. Gorges, A. J. Foxley, D. M. French, C. M. Ryan, and J. L. Roberts, "Suppression of reabsorption via modulation of light", *arXiv preprint physics/0607215*, 2006.

[72] B. Engeser, "A novel surface trapping apparatus for ultracold cesium atoms: And the investigation of an Efimov resonance", Ph.D. dissertation, University of Innsbruck, 2006.

[73] G. Salomon, L. Fouché, P. Wang, A. Aspect, P. Bouyer, and T. Bourdel, "Gray-molasses cooling of ^{39}K to a high phase-space density", *Europhysics Letters*, vol. 104, no. 6, p. 63 002, 2014.

[74] D. Wang, J. Qi, M. Stone, *et al.*, "Photoassociative production and trapping of ultracold KRb molecules", *Physical Review Letters*, vol. 93, no. 24, p. 243 005, 2004.

[75] P. D. Lett, R. N. Watts, C. I. Westbrook, W. D. Phillips, P. L. Gould, and H. J. Metcalf, "Observation of atoms laser cooled below the Doppler limit", *Physical Review Letters*, vol. 61, pp. 169–172, 2 Jul. 1988.

[76] J. Dalibard and C. Cohen-Tannoudji, "Laser cooling below the Doppler limit by polarization gradients: Simple theoretical models", *Journal of the Optical Society of America B*, vol. 6, no. 11, pp. 2023–2045, 1989.

[77] G. Colzi, G. Durastante, E. Fava, S. Serafini, G. Lamporesi, and G. Ferrari, "Sub-Doppler cooling of sodium atoms in gray molasses", *Physical Review A*, vol. 93, no. 2, p. 023 421, 2016.

[78] S. Rosi, A. Burchianti, S. Conclave, *et al.*, "Λ-enhanced grey molasses on the D2 transition of Rubidium-87 atoms", *Scientific Reports*, vol. 8, no. 1, p. 1301, 2018.

[79] D. Boiron, A. Michaud, P. Lemonde, *et al.*, "Laser cooling of cesium atoms in gray optical molasses down to 1.1 μK", *Physical Review A*, vol. 53, no. 6, R3734, 1996.

[80] M. Landini, S. Roy, L. Carcagní, *et al.*, "Sub-Doppler laser cooling of potassium atoms", *Physical Review A*, vol. 84, no. 4, p. 043 432, 2011.

[81] A. T. Grier, I. Ferrier-Barbut, B. S. Rem, *et al.*, "Λ-enhanced sub-Doppler cooling of lithium atoms in D1 gray molasses", *Physical Review A*, vol. 87, no. 6, p. 063 411, 2013.

[82] J. Dobosz, M. Bocheński, and M. Semczuk, "Bidirectional, analog current source benchmarked with gray molasses-assisted stray magnetic field compensation", *Applied Sciences*, vol. 11, no. 21, p. 10 474, 2021.

[83] NOAA National Centers for Environmental Information, *Geomagnetic field calculators*, Accessed: 2025-07-21, 2025. [Online]. Available: `https://www.ngdc.noaa.gov/geomag/calculators/magcalc.shtml`.

[84] M. Gröbner, P. Weinmann, E. Kirilov, *et al.*, "Observation of interspecies Feshbach resonances in an ultracold ^{39}K-^{133}Cs mixture and refinement of interaction potentials", *Physical Review A*, vol. 95, no. 2, p. 022 715, 2017.

[85] M. S. Hamilton, A. R. Gorges, and J. L. Roberts, "Influence of optical molasses in loading a shallow optical trap", *Physical Review A*, vol. 79, no. 1, p. 013 418, 2009.

[86] A. Ashkin, J. M. Dziedzic, J. E. Bjorkholm, and S. Chu, "Observation of a single-beam gradient force optical trap for dielectric particles", *Optics Letters*, vol. 11, no. 5, pp. 288–290, 1986.

[87] S. Chu, J. Bjorkholm, A. Ashkin, and A. Cable, "Experimental observation of optically trapped atoms", *Physical Review Letters*, vol. 57, no. 3, p. 314, 1986.

[88] S. Granade, M. Gehm, K. O'Hara, and J. Thomas, "All-optical production of a degenerate Fermi gas", *Physical Review Letters*, vol. 88, no. 12, p. 120 405, 2002.

[89] M. Barrett, J. Sauer, and M. Chapman, "All-optical formation of an atomic Bose-Einstein condensate", *Physical Review Letters*, vol. 87, no. 1, p. 010 404, 2001.

[90] J. Zirbel, K.-K. Ni, S. Ospelkaus, *et al.*, "Heteronuclear molecules in an optical dipole trap", *Physical Review A*, vol. 78, no. 1, p. 013 416, 2008.

[91] J. K. Chin, D. Miller, Y. Liu, *et al.*, "Evidence for superfluidity of ultracold fermions in an optical lattice", *Nature*, vol. 443, no. 7114, pp. 961–964, 2006.

[92] M. A. Norcia, C. Politi, L. Klaus, *et al.*, "Two-dimensional supersolidity in a dipolar quantum gas", *Nature*, vol. 596, no. 7872, pp. 357–361, 2021.

[93] R. Grimm, M. Weidemüller, and Y. B. Ovchinnikov, "Optical dipole traps for neutral atoms", in *Advances in Atomic, Molecular, and Optical Physics*, vol. 42, Elsevier, 2000, pp. 95–170.

[94] M. Schulz, "Tightly confined atoms in optical dipole traps", Ph.D. dissertation, University of Innsbruck, 2002.

[95] N. Zheng, W. Liu, J. Wu, Y. Li, V. Sovkov, and J. Ma, "Parametric excitation of ultracold sodium atoms in an optical dipole trap", in *Photonics*, MDPI, vol. 9, 2022, p. 442.

[96] C. Beulenkamp, K. P. Zamarski, R. C. Bird, *et al.*, "Formation of ultracold ^{39}K ^{133}Cs Feshbach molecules", *arXiv preprint arXiv:2506.16520*, 2025.

[97] E. Wille, "Preparation of an optically trapped Fermi-Fermi mixture of ^{6}Li and ^{40}K atoms and characterization of the interspecies interactions by Feshbach spectroscopy", Ph.D. dissertation, University of Innsbruck, Innsbruck, Austria, 2009. [Online]. Available: `https://www.ultracold.at/theses/2009-wille.pdf`.

[98] G. Reinaudi, T. Lahaye, Z. Wang, and D. Guéry-Odelin, "Strong saturation absorption imaging of dense clouds of ultracold atoms", *Optics Letters*, vol. 32, no. 21, pp. 3143–3145, 2007.

[99] P. Arciszewski, *WebBasedDataBrowser (WBDB). Internal lab project*, `https://github.com/pwarciszewski/WebBasedDataBrowser`, Accessed: 2025-07-28, 2024.

[100] K. Dinçer, "Observation of 'missing' vibrational levels and extending photoassociation spectra of excited ultracold cesium dimers", Ph.D. dissertation, University of Warsaw, 2024.

[101] P. Arciszewski, "An experimental apparatus for laser cooling of potassium and caesium", Master's thesis, University of Warsaw, Warsaw, 2019.

[102] A. Franzen, *Optical Component-library: A vector graphics library for illustrations of optics experiments*, Licensed under Creative Commons Attribution-NonCommercial 4.0 International, 2022.

[103] R. Trubko, M. D. Gregoire, W. F. Holmgren, and A. D. Cronin, "Potassium tune-out-wavelength measurement using atom interferometry and a multipass optical cavity", *Physical Review A*, vol. 95, p. 052 507, 5 May 2017.

[104] C. R. Cabrera Córdova, "Quantum liquid droplets in a mixture of Bose-Einstein condensates", Ph.D. dissertation, Universitat Politècnica de Catalunya, 2018.

[105] M. Bocheński and M. Semczuk, "Sub-doppler laser cooling and magnetic trapping of natural-abundance fermionic potassium", *Journal of Physics B*, vol. 57, no. 3, p. 035 301, 2024.

[106] T. Jeltes, J. M. McNamara, W. Hogervorst, *et al.*, "Comparison of the Hanbury Brown–Twiss effect for bosons and fermions", *Nature*, vol. 445, no. 7126, pp. 402–405, Jan. 2007, ISSN: 1476-4687.

[107] C. Cherfan, M. Denis, D. Bacquet, *et al.*, "Multi-frequency telecom fibered laser system for potassium laser cooling", *Applied Physics Letters*, vol. 119, no. 20, p. 204 001, Nov. 2021, ISSN: 0003-6951.

[108] R. A. Nyman, G. Varoquaux, B. Villier, *et al.*, "Tapered-amplified antireflection-coated laser diodes for potassium and rubidium atomic-physics experiments", *Review of Scientific Instruments*, vol. 77, no. 3, p. 033 105, Mar. 2006, ISSN: 0034-6748.

[109] R. S. Williamson III, P. A. Voytas, R. T. Newell, and T. Walker, "A magneto-optical trap loaded from a pyramidal funnel", *Optics Express*, vol. 3, no. 3, pp. 111–117, Aug. 1998.

[110] B. DeMarco, H. Rohner, and D. S. Jin, "An enriched ^{40}K source for fermionic atom studies", *Review of Scientific Instruments*, vol. 70, no. 4, pp. 1967–1969, Apr. 1999, ISSN: 0034-6748.

[111] G. Modugno, C. Benkő, P. Hannaford, G. Roati, and M. Inguscio, "Sub-Doppler laser cooling of fermionic ^{40}K atoms", *Physical Review A*, vol. 60, R3373–R3376, 5 Nov. 1999.

[112] V. Gokhroo, G. Rajalakshmi, R. K. Easwaran, and C. Unnikrishnan, "Sub-Doppler deep-cooled bosonic and fermionic isotopes of potassium in a compact 2D$^+$–3D MOT set-up", *Journal of Physics B*, vol. 44, no. 11, p. 115 307, 2011.

[113] W. Gunton, M. Semczuk, and K. W. Madison, "Realization of BEC-BCS-crossover physics in a compact oven-loaded magneto-optic-trap apparatus", *Physical Review A*, vol. 88, p. 023 624, 2 Aug. 2013.

[114] C.-H. Wu, I. Santiago, J. W. Park, P. Ahmadi, and M. W. Zwierlein, "Strongly interacting isotopic Bose-Fermi mixture immersed in a Fermi sea", *Physical Review A*, vol. 84, no. 1, p. 011 601, 2011.

[115] J.-L. Yang, Y. Long, W.-W. Gao, L. Jin, Z.-C. Zuo, and R.-Q. Wang, "Enhanced loading of ^{40}K from natural abundance potassium source with a high performance 2D$^+$ MOT", *Chinese Physics Letters*, vol. 35, no. 3, p. 033 701, Mar. 2018.

[116] C. Klempt, T. van Zoest, T. Henninger, *et al.*, "Ultraviolet light-induced atom desorption for large rubidium and potassium magneto-optical traps", *Physical Review A*, vol. 73, p. 013 410, 1 Jan. 2006.

[117] D. R. Fernandes, F. Sievers, N. Kretzschmar, S. Wu, C. Salomon, and F. Chevy, "Sub-Doppler laser cooling of fermionic ^{40}K atoms in three-dimensional gray optical molasses", *Europhysics Letters*, vol. 100, no. 6, p. 63 001, 2012.

[118] F. Sievers, N. Kretzschmar, D. R. Fernandes, *et al.*, "Simultaneous sub-Doppler laser cooling of fermionic ^{6}Li and ^{40}K on the D_1 line: Theory and experiment", *Physical Review A*, vol. 91, no. 2, p. 023 426, 2015.

[119] J. W. Park, C.-H. Wu, I. Santiago, *et al.*, "Quantum degenerate Bose-Fermi mixture of chemically different atomic species with widely tunable interactions", *Physical Review A*, vol. 85, p. 051 602, 5 May 2012.

[120] S. Aubin, S. Myrskog, M. Extavour, *et al.*, "Rapid sympathetic cooling to Fermi degeneracy on a chip", *Nature Physics*, vol. 2, no. 6, pp. 384–387, 2006.

[121] M. Greiner, I. Bloch, T. W. Hänsch, and T. Esslinger, "Magnetic transport of trapped cold atoms over a large distance", *Physical Review A*, vol. 63, p. 031 401, 3 Feb. 2001.

[122] G. Unnikrishnan, C. Beulenkamp, D. Zhang, K. P. Zamarski, M. Landini, and H.-C. Nägerl, "Long distance optical transport of ultracold atoms: A compact setup using a Moiré lens", *Review of Scientific Instruments*, vol. 92, no. 6, p. 063 205, Jun. 2021, ISSN: 0034-6748.

[123] Y. Bao, S. S. Yu, L. Anderegg, *et al.*, "Fast optical transport of ultracold molecules over long distances", *New Journal of Physics*, vol. 24, no. 9, p. 093 028, 2022.

[124] S. Falke, E. Tiemann, C. Lisdat, H. Schnatz, and G. Grosche, "Transition frequencies of the D lines of ^{39}K, ^{40}K, and ^{41}K measured with a femtosecond laser frequency comb", *Physical Review A*, vol. 74, p. 032 503, 3 Sep. 2006.

[125] J. Behr, A. Gorelov, T. Swanson, *et al.*, "Magneto-optic trapping of β-decaying ^{38}K^m, ^{37}K from an on-line isotope separator", *Physical Review Letters*, vol. 79, no. 3, p. 375, 1997.

[126] B. Bazak and D. S. Petrov, "Stable p-wave resonant two-dimensional Fermi-Bose dimers", *Physical Review Letters*, vol. 121, no. 26, p. 263 001, 2018.

[127] J. Ulmanis, S. Häfner, E. D. Kuhnle, and M. Weidemüller, "Heteronuclear Efimov resonances in ultracold quantum gases", *National Science Review*, vol. 3, no. 2, pp. 174–188, 2016.

[128] M. Bocheński, J. Dobosz, and M. Semczuk, "Magnetic trapping of an ultracold ^{39}K-^{40}K mixture with a versatile potassium laser system", *Optics Express*, vol. 32, no. 27, pp. 48 463–48 478, 2024.

[129] J. M. McNamara, T. Jeltes, A. S. Tychkov, W. Hogervorst, and W. Vassen, "Degenerate Bose-Fermi mixture of metastable atoms", *Physical Review Letters*, vol. 97, p. 080 404, 8 Aug. 2006.

[130] A. G. Truscott, K. E. Strecker, W. I. McAlexander, G. B. Partridge, and R. G. Hulet, "Observation of Fermi Pressure in a Gas of Trapped Atoms", *Science*, vol. 291, no. 5513, pp. 2570–2572, 2001.

[131] S. B. Papp, J. M. Pino, and C. E. Wieman, "Tunable miscibility in a dual-species Bose-Einstein condensate", *Physical Review Letters*, vol. 101, p. 040 402, 4 Jul. 2008.

[132] A. D. Lercher, T. Takekoshi, M. Debatin, *et al.*, "Production of a dual-species Bose-Einstein condensate of Rb and Cs atoms", *The European Physical Journal D*, vol. 65, no. 1, pp. 3–9, Nov. 2011.

[133] B. J. DeSalvo, K. Patel, J. Johansen, and C. Chin, "Observation of a Degenerate Fermi Gas Trapped by a Bose-Einstein Condensate", *Physical Review Letters*, vol. 119, p. 233 401, 23 Dec. 2017.

[134] I. Ferrier-Barbut, M. Delehaye, S. Laurent, *et al.*, "A mixture of Bose and Fermi superfluids", *Science*, vol. 345, no. 6200, pp. 1035–1038, 2014.

[135] U. Schlöder, C. Silber, T. Deuschle, and C. Zimmermann, "Saturation in heteronuclear photoassociation of ^{6}Li^{7}Li", *Physical Review A*, vol. 66, p. 061 403, 6 Dec. 2002.

[136] R. Chapurin, X. Xie, M. J. Van de Graaff, *et al.*, "Precision test of the limits to universality in few-body physics", *Physical Review Letters*, vol. 123, p. 233 402, 23 Dec. 2019.

[137] A. B. Deb and N. Kjærgaard, "Observation of Pauli blocking in light scattering from quantum degenerate fermions", *Science*, vol. 374, no. 6570, pp. 972–975, 2021.

[138] M. Landini, S. Roy, G. Roati, *et al.*, "Direct evaporative cooling of ^{39}K atoms to Bose-Einstein condensation", *Physical Review A*, vol. 86, p. 033 421, 3 Sep. 2012.

[139] G. Roati, M. Zaccanti, C. D'Errico, *et al.*, "^{39}K Bose-Einstein Condensate with Tunable Interactions", *Physical Review Letters*, vol. 99, p. 010 403, 1 Jul. 2007.

[140] G. Modugno, G. Ferrari, G. Roati, R. J. Brecha, A. Simoni, and M. Inguscio, "Bose-Einstein Condensation of Potassium Atoms by Sympathetic Cooling", *Science*, vol. 294, no. 5545, pp. 1320–1322, 2001.

[141] M. Tomza, "Energetics and control of ultracold isotope-exchange reactions between heteronuclear dimers in external fields", *Physical Review Letters*, vol. 115, p. 063 201, 6 Aug. 2015.

[142] E. Tiemann, P. Gersema, K. K. Voges, T. Hartmann, A. Zenesini, and S. Ospelkaus, "Beyond Born-Oppenheimer approximation in ultracold atomic collisions", *Physical Review Research*, vol. 2, p. 013 366, 1 Mar. 2020.

[143] M. Borkowski, A. A. Buchachenko, R. Ciuryło, *et al.*, "Weakly bound molecules as sensors of new gravitylike forces", *Scientific Reports*, vol. 9, no. 1, p. 14 807, Oct. 2019.

[144] A. Scherrer, F. Agostini, D. Sebastiani, E. K. U. Gross, and R. Vuilleumier, "On the Mass of Atoms in Molecules: Beyond the Born-Oppenheimer Approximation", *Physical Review X*, vol. 7, p. 031 035, 3 Aug. 2017.

[145] X. He, K. Wang, J. Zhuang, *et al.*, "Coherently forming a single molecule in an optical trap", *Science*, vol. 370, no. 6514, pp. 331–335, 2020.

[146] C. Sheng, J. Hou, X. He, *et al.*, "Defect-free arbitrary-geometry assembly of mixed-species atom arrays", *Physical Review Letters*, vol. 128, p. 083 202, 8 Feb. 2022.

[147] C. Chen, F. Yang, X. Wu, C. Shen, M. K. Tey, and L. You, "Two-color optical nonlinearity in an ultracold Rydberg atom gas mixture", *Physical Review A*, vol. 103, p. 053 303, 5 May 2021.

[148] M. Parniak, M. Mazelanik, A. Leszczyński, M. Lipka, M. Dąbrowski, and W. Wasilewski, "Quantum Optics of Spin Waves through ac Stark Modulation", *Physical Review Letters*, vol. 122, p. 063 604, 6 Feb. 2019.

[149] H. J. McGuinness, A. V. Rakholia, and G. W. Biedermann, "High data-rate atom interferometer for measuring acceleration", *Applied Physics Letters*, vol. 100, no. 1, p. 011 106, Jan. 2012.

[150] B. Adams, S. Kinge, K. Bongs, and Y. H. Lien, "Magneto-optical trap performance for high-bandwidth applications", *Physical Review A*, vol. 108, p. 063 111, 6 Dec. 2023.

[151] A. Bonnin, N. Zahzam, Y. Bidel, and A. Bresson, "Characterization of a simultaneous dual-species atom interferometer for a quantum test of the weak equivalence principle", *Physical Review A*, vol. 92, p. 023 626, 2 Aug. 2015.

[152] E. A. Donley, T. P. Heavner, F. Levi, M. O. Tataw, and S. R. Jefferts, "Double-pass acousto-optic modulator system", *Review of Scientific Instruments*, vol. 76, no. 6, p. 063 112, Jun. 2005, ISSN: 0034-6748.

[153] V. M. Valenzuela, S. Hamzeloui, M. Gutiérrez, and E. Gomez, "Multiple isotope magneto-optical trap from a single diode laser", *Journal of the Optical Society of America B*, vol. 30, no. 5, pp. 1205–1210, 2013.

[154] A. Banerjee and V. Natarajan, "Absolute-frequency measurements of the D_2 line and fine-structure interval in ^{39}K", *Physical Review A*, vol. 70, p. 052 505, 5 Nov. 2004.

[155] W. Bowden, I. R. Hill, P. E. G. Baird, and P. Gill, "Note: A high-performance, low-cost laser shutter using a piezoelectric cantilever actuator", *Review of Scientific Instruments*, vol. 88, no. 1, p. 016 102, Jan. 2017.

[156] R. S. Williamson III, "Magneto-optical trapping of potassium isotopes", Ph.D. dissertation, University of Wisconsin, Madison, 1997, p. 78.

[157] D. M. Farkas, K. M. Hudek, E. A. Salim, S. R. Segal, M. B. Squires, and D. Z. Anderson, "A compact, transportable, microchip-based system for high repetition rate production of Bose–Einstein condensates", *Applied Physics Letters*, vol. 96, no. 9, p. 093 102, 2010.

[158] H. Luo, K. Li, D. Zhang, T. Gao, and K. Jiang, "Multiple side-band generation for two-frequency components injected into a tapered amplifier", *Optics Letters*, vol. 38, no. 7, pp. 1161–1163, 2013.

[159] G. Dash, T. de Jongh, M. Dixmerias, C. Salomon, and T. Yefsah, "Simultaneous sub-Doppler laser cooling of ^{6}Li and ^{7}Li isotopes", *Physical Review A*, vol. 106, p. 033 105, 3 Sep. 2022.

[160] M. Gröbner, P. Weinmann, E. Kirilov, and H.-C. Nägerl, "Degenerate Raman sideband cooling of ^{39}K", *Physical Review A*, vol. 95, p. 033 412, 3 Mar. 2017.

[161] E. Zohar, Y. Florshaim, O. Zilberman, A. Stern, and Y. Sagi, "Degenerate Raman sideband cooling of ^{40}K atoms", *Physical Review A*, vol. 106, p. 063 111, 6 Dec. 2022.

[162] T. Klostermann, C. R. Cabrera, H. von Raven, *et al.*, "Fast long-distance transport of cold cesium atoms", *Physical Review A*, vol. 105, p. 043 319, 4 Apr. 2022.

[163] S. Falke, H. Knöckel, J. Friebe, M. Riedmann, E. Tiemann, and C. Lisdat, "Potassium ground-state scattering parameters and Born-Oppenheimer potentials from molecular spectroscopy", *Physical Review A*, vol. 78, p. 012 503, 1 Jul. 2008.

[164] J. J. Lutz and J. M. Hutson, "Deviations from Born-Oppenheimer mass scaling in spectroscopy and ultracold molecular physics", *Journal of Molecular Spectroscopy*, vol. 330, pp. 43–56, 2016, Potentiology and Spectroscopy in Honor of Robert Le Roy.

[165] V. Bolpasi and W. Von Klitzing, "Double-pass tapered amplifier diode laser with an output power of 1 W for an injection power of only 200 μW", *Review of Scientific Instruments*, vol. 81, no. 11, 2010.

[166] Z. Hadzibabic, C. Stan, K. Dieckmann, *et al.*, "Two-species mixture of quantum degenerate Bose and Fermi gases", *Physical Review Letters*, vol. 88, no. 16, p. 160 401, 2002.

[167] G. Roati, F. Riboli, G. Modugno, and M. Inguscio, "Fermi-bose quantum degenerate ^{40}K-^{87}Rb mixture with attractive interaction", *Physical Review Letters*, vol. 89, no. 15, p. 150 403, 2002.

[168] C. Cabrera, L. Tanzi, J. Sanz, *et al.*, "Quantum liquid droplets in a mixture of Bose-Einstein condensates", *Science*, vol. 359, no. 6373, pp. 301–304, 2018.

[169] I. Ferrier-Barbut, H. Kadau, M. Schmitt, M. Wenzel, and T. Pfau, "Observation of quantum droplets in a strongly dipolar Bose gas", *Physical Review Letters*, vol. 116, no. 21, p. 215 301, 2016.

[170] G. Ferioli, G. Semeghini, L. Masi, *et al.*, "Collisions of self-bound quantum droplets", *Physical Review Letters*, vol. 122, no. 9, p. 090 401, 2019.

[171] S. Jochim, M. Bartenstein, A. Altmeyer, *et al.*, "Bose-Einstein condensation of molecules", *Science*, vol. 302, no. 5653, pp. 2101–2103, 2003.

[172] M. Greiner, C. A. Regal, and D. S. Jin, "Emergence of a molecular Bose–Einstein condensate from a Fermi gas", *Nature*, vol. 426, no. 6966, pp. 537–540, 2003.

[173] S. L. Cornish, M. R. Tarbutt, and K. R. Hazzard, "Quantum computation and quantum simulation with ultracold molecules", *Nature Physics*, vol. 20, no. 5, pp. 730–740, 2024.

[174] A. Micheli, G. K. Brennen, and P. Zoller, "A toolbox for lattice-spin models with polar molecules", *Nature Physics*, vol. 2, no. 5, pp. 341–347, 2006.

[175] M. Baranov, K. Osterloh, and M. Lewenstein, "Fractional quantum Hall states in ultracold rapidly rotating dipolar Fermi gases", *Physical Review Letters*, vol. 94, no. 7, p. 070 404, 2005.

[176] G. Quéméner and P. S. Julienne, "Ultracold molecules under control!", *Chemical Reviews*, vol. 112, no. 9, pp. 4949–5011, 2012.

[177] M. Rockenhäuser, F. Kogel, T. Garg, S. A. Morales-Ramírez, and T. Langen, "Laser cooling of barium monofluoride molecules using synthesized optical spectra", *Physical Review Research*, vol. 6, no. 4, p. 043 161, 2024.

[178] E. Kuznetsova, M. Gacesa, P. Pellegrini, S. F. Yelin, and R. Côté, "Efficient formation of ground-state ultracold molecules via STIRAP from the continuum at a Feshbach resonance", *New Journal of Physics*, vol. 11, no. 5, p. 055 028, 2009.

[179] K.-K. Ni, S. Ospelkaus, M. De Miranda, *et al.*, "A high phase-space-density gas of polar molecules", *Science*, vol. 322, no. 5899, pp. 231–235, 2008.

[180] T. A. Schulze, T. Hartmann, K. K. Voges, *et al.*, "Feshbach spectroscopy and dual-species Bose-Einstein condensation of ^{23}Na-^{39}K mixtures", *Physical Review A*, vol. 97, no. 2, p. 023 623, 2018.

[181] K. Pilch, A. Lange, A. Prantner, *et al.*, "Observation of interspecies Feshbach resonances in an ultracold Rb-Cs mixture", *Physical Review A*, vol. 79, no. 4, p. 042 718, 2009.

[182] G. Thalhammer, G. Barontini, J. Catani, *et al.*, "Collisional and molecular spectroscopy in an ultracold Bose–Bose mixture", *New Journal of Physics*, vol. 11, no. 5, p. 055 044, 2009.

[183] N. Bigagli, W. Yuan, S. Zhang, *et al.*, "Observation of Bose–Einstein condensation of dipolar molecules", *Nature*, vol. 631, no. 8020, pp. 289–293, 2024.

[184] N. Zheng, W. Liu, J. Wu, Y. Li, V. Sovkov, and J. Ma, "Parametric excitation of ultracold sodium atoms in an optical dipole trap", *Photonics*, vol. 9, no. 7, 2022.

[185] A. Burchianti, G. Valtolina, J. Seman, *et al.*, "Efficient all-optical production of large ^{6}Li quantum gases using D1 gray-molasses cooling", *Physical Review A*, vol. 90, no. 4, p. 043 408, 2014.

[186] S.-K. Tung, K. Jimenez-Garcia, J. Johansen, C. V. Parker, and C. Chin, "Geometric scaling of Efimov states in a ^{6}Li-^{133}Cs mixture", *Physical Review Letters*, vol. 113, no. 24, p. 240 402, 2014.

[187] H. J. Patel, C. L. Blackley, S. L. Cornish, and J. M. Hutson, "Feshbach resonances, molecular bound states, and prospects of ultracold-molecule formation in mixtures of ultracold K and Cs", *Physical Review A*, vol. 90, no. 3, p. 032 716, 2014.

[188] K. K. Voges, P. Gersema, T. Hartmann, T. A. Schulze, A. Zenesini, and S. Ospelkaus, "A pathway to ultracold bosonic ^{23}Na^{39}K ground state molecules", *New Journal of Physics*, vol. 21, no. 12, p. 123 034, 2019.

[189] N. Bigagli, C. Warner, W. Yuan, *et al.*, "Collisionally stable gas of bosonic dipolar ground-state molecules", *Nature Physics*, vol. 19, no. 11, pp. 1579–1584, 2023.